


PH.D. IN ASTRONOMY, ASTROPHYSICS AND SPACE SCIENCE

CYCLE XXXII

THE SEARCH FOR PRIMORDIAL B-MODES IN THE POLARIZATION OF THE COSMIC MICROWAVE BACKGROUND WITH LSPE/SWIPE AND LITEBIRD

Fabio Columbro

A.Y. 2018/2019

Supervisor: P. de Bernardis

Coordinator: P. de Bernardis
Deputy Coordinator: N. Vittorio

Contents

Introduction

The most ambitious challenge in Experimental Cosmology today is the precision measurement of the polarized signal of the Cosmic Microwave Background (CMB). CMB was discovered in 1967 by Penzias and Wilson [1]. It is a snapshot of the primordial universe and represents an essential source of information about all epochs of the universe. This experimental thesis concerns the study of polarization measurement techniques and the development of a new superconducting magnetic bearing to continuously rotate a cryogenic half-wave plate (HWP). The chapter 1 of this thesis focuses on the fundamentals of the cold dark matter model (ΛCDM) which is a parametrization of the Big Bang cosmological model. It describes the constituents and the evolution of the universe. The ΛCDM model can be extended by adding cosmological inflation, a short period of exponential expansion in the very early universe. Inflation's basic predictions [2] regarding the universe large-scale geometry and structure have been borne out by cosmological measurements to date. Inflation makes an additional prediction as the existence of a background of gravitational waves, or tensor mode perturbations. At the recombination epoch, the inflationary gravitational waves (IGW) contribute to the anisotropy of the CMB in both total intensity and linear polarization, discussed deeply in the second part of the first chapter. The amplitude of tensors is conventionally parameterized by r, the tensor-to-scalar ratio at a fiducial scale, and its trace in the CMB polarization is a direct measure of the energy scale of inflation. Theoretical predictions of the value of r cover a very wide range. Conversely, a measurement of r can discriminate between models of inflation. The current upper limit is $r < 0.06$ at 95% confidence [3].

The chapter 2 presents the Large-Scale Polarization Explorer (LSPE) [4], an experiment composed of two instruments (the ground-based telescope STRIP and the balloon-borne counterpart SWIPE) which aims to measure the polarization of the CMB at large angular scale with a goal of $r = 0.01$. This thesis is mainly focused on the development of few important subsystems of SWIPE balloon.

The detection of this tiny signal requires a very large array of polarization-sensitive detectors coupled to an imaging optical system, to obtain a wide field of view, thus maximizing the mapping speed. SWIPE will focus the incoming radiation on two large curved focal planes (at a temperature of 0.3 K) hosting 326 multi-mode pixels with Transition Edge Sensor (TES) thermistors, divided in

the 3 frequency bands: 145 GHz (30% bandwidth), 210 GHz (20% bandwidth) and 240 GHz (10% bandwidth). Chapter 3 describes the tests performed on the multi-mode pixel assembly. A custom cryogenic neoprene absorber was developed to reduce the background on the detector at a level similar to the one expected in flight, allowing to measure the main beam of the pixel assembly. The measured FWHM of the pixel assembly is 21°, slightly narrower than the expected one (24°), due to vignetting produced by the filters stack.

Unfortunately this CMB polarization signal is well below the level of unpolarized foregrounds. This makes systematic errors due to temperature-to-polarization leakage particularly detrimental. Polarization modulators offer a solution to separate the polarized signal of interest from these unpolarized foregrounds. Many polarization modulation schemes exist, and a rapidly-rotating half-wave plate (HWP) is one of the most promising. The working principle of a polarimeter is discussed in chapter 4, where there is also an analysis of the main systematics introduced by a rotating HWP, particularly focused on HWP spurious signals and HWP wobbling.

Chapter 5 is focused on the SWIPE polarization modulator unit which operates at 1.6 K to reduce the background on the detector produced by the HWP emission. On the other hand rotating an object at cryogenic temperature is not trivial, in particular because the dissipation becomes an issue. The technology adopted is based on a superconducting magnetic bearing (SMB) which can significantly reduce the friction. After introducing the basics of superconductivity, the baseline design is described. A large number of tests were performed on a room temperature mockup to optimize the motor configuration while room and cryogenic temperature tests were performed on the clamp mechanism (necessary to hold the bearing at room temperature and release it below the superconductive transition). The total heat load expected from the polarization modulator unit is < 25 mW. This value has to be confirmed during cryogenic test of the whole system which is not performed yet due to delays in the cryostat fabrication. The expected heat load from the polarization modulator represents less than 15% of the total heat load on the superfluid He reservoir, and is fully compatible with the operation of the instrument.

Finally, chapter 6 presents LiteBIRD mission and the development of both polarization modulators of the medium and high frequency instruments. LiteBIRD is the next generation spacecraft [5], expected to be operative in ~ 10 years, and will map CMB polarization 20 times deeper than Planck, with a total error of $\delta r < 0.001$, conservatively assuming equal contributions of statistical error, systematic error, and margin. The use of 3 continuously rotating HWPs (for the 3 telescopes of LiteBIRD) mitigates important systematic errors already observed in Planck data. Their development is more challenging than for SWIPE due to the spacecraft requirements and the Technology Readiness Level (TRL) required. A scaled baseline design and an optimized configuration are discussed. We find that the optimized one will meet the power budget with a 100% of margin.

Chapter 1

The Cosmic Microwave Background radiation

1.1 The Big Bang model

The Big Bang is actually not a "theory" at all, but rather a scenario or model about the early moments of our universe, for which the evidence is overwhelming. It is a common misconception that the Big Bang was the origin of the universe. Indeed, the Big Bang scenario is completely silent about how the universe came into existence in the first place. In fact, the closer we look to time "zero", the less certain we are about what actually happened, as physical laws still result unable to describe such extremes of nature. The Big Bang scenario simply assumes that space, time, and energy already existed. But it tells us nothing about where they came from or why the universe was born hot and dense to begin with. In 1929, Edwin Hubble discovered that virtually every distant galaxy he observed was moving away from us, and the galaxies' recessional velocities v were roughly proportional to their distances d from us. This led to the famous Hubble-Lemaire law of the expansion of the universe:

$$v = H_0 d \tag{1.1}$$

where H_0 is the Hubble constant whose measurements have greatly improved over the last seventy years (see Fig. 1.1). Today, the Hubble constant is known with good accuracy, and the expansion of the universe producing the apparent recession of galaxies is convincingly confirmed. Moreover, the measurements have led to a determination of the deceleration parameter and the conclusion is that the expansion appears to be accelerating [6].

But if space and everything with it is expanding now, then the universe must have been much denser in the past. That is, all the matter and energy that we observe in the universe would have been compressed into a much smaller space in the past. Einstein's theory of gravity enables us to calculate the density that the universe must have had in the past. The result is that any chunk of

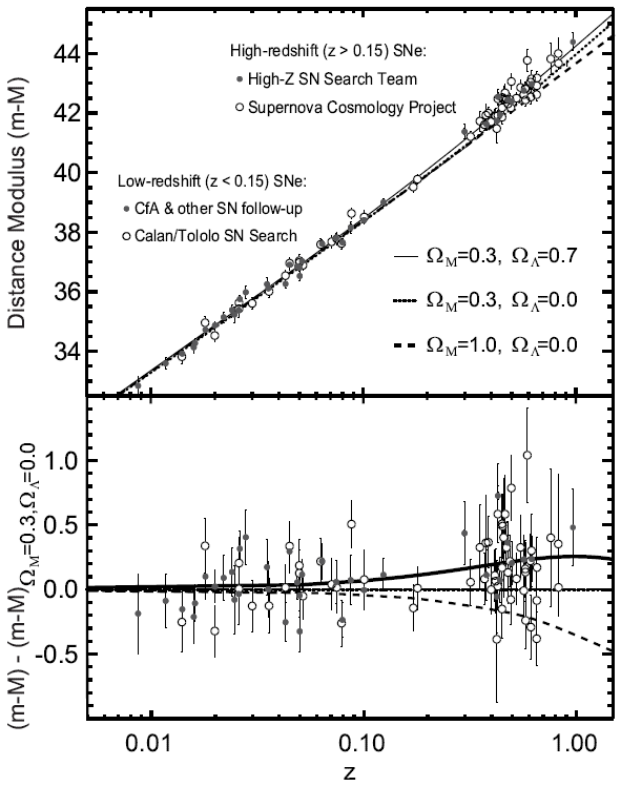

Figure 1.1: Hubble diagram of SNe Ia measured by the Supernova Cosmology Project and the High-z Supernova Team. Bottom panel shows residuals in distance modulus relative to an open universe with $\Omega_0 = \Omega_m = 0.3$ [6].

the universe we can observe must have expanded from an infinitesimally small volume of space. By determining how fast is the expansion of the universe, we are able to calculate its age. The result is that space started expanding 13.77 billion years ago. This number comes from measurements of the CMB, which have determined the values of the cosmological parameters with unprecedented accuracy thus allowing to estimate the age of the universe in the hot Big Bang model.

It is a common misconception that the Big Bang was an "explosion" that took place somewhere in space. Indeed, the Big Bang was an expansion of space itself. Every part of space participated in it. For example, the part of space occupied by the Earth, the Sun, and our Milky Way galaxy was once, during the Big Bang, incredibly hot and dense. The same holds true of every other part of the universe we can see. We observe that galaxies are rushing apart in just the way predicted by the Big Bang model. But there are other important observations that support the Big Bang.

Astronomers have detected, throughout the universe, two chemical elements that could only have been created during the Big Bang: hydrogen and helium. Furthermore, the estimates of the relative initial abundances of He, D, Li and ^{3}He are just the ones predicted to have been produced in the first minutes after the Big Bang. This is the nucleosynthesis of the light elements. This prediction is based on our well-established understanding of nuclear reactions. We can also detect the light left over from the Big Bang era, produced just 380000 years later. This is the origin of the cosmic microwave background radiation (see §1.3). This light is observed to have all the characteristics expected from the Big Bang scenario and from our understanding of heat and light.

The standard Hot Big Bang model also provides a framework to understand the collapse of matter which forms galaxies and other large-scale structures observed in the universe today. About 10,000 years after the Big Bang, the temperature had fallen to such an extent that the energy density of the universe began to be dominated by massive particles, rather than the light and other radiation which had predominated earlier. This change in the form of dominating energy density meant that the gravitational forces between the massive particles could begin to take effect and slowly accrete matter over initial seeds, so that density perturbations would grow. Today, $\sim$ 13.8 billion years later, we see the results of this coalescence in the structure and distribution of the galaxies.

1.2 ΛCDM cosmological model

The Λ Cold Dark Matter (ΛCDM) model is a parametrization of the Big Bang cosmological model in which the universe contains a cosmological constant, denoted by Λ, associated with dark energy, and cold dark matter (CDM). It also includes baryons, photons and neutrinos. The model assumes that general relativity is the correct theory of gravity on cosmological scales. The ΛCDM model can be extended by adding cosmological inflation, quintessence and other elements that are current areas of speculation and research in cosmology.

1.2.1 FLRW metric

First of all to use the general relativity we need a metric which describes the space. According to the hypothesis of homogeneous and isotropic universe, valid in our universe at large scales, the metric must be diagonal. As space is allowed to be curved, spherical coordinates (r, θ, Φ) are worthwhile to describe the metric. The center of the spherical coordinate system is the observer. The spatial part of the metric for flat space is:

$$ds^2 = dr^2 + r^2(d\theta^2 + \sin^2\theta d\Phi^2) = dr^2 + r^2 d\omega^2 \tag{1.2}$$

where $d\omega$ is the abbreviation of the term between brackets. It was proven by Friedmann, Lemaitre, Robertson and Walker that the only metric that obeys both isotropy and homogeneity is:

$$ds^2 = dr^2 + f_k(r)^2 d\omega^2 \tag{1.3}$$

where $f_k(r)$ is the curvature function given by:

$$f_k(r) = \begin{cases} k^{-1/2}\sin(k^{1/2}r), & \text{for } 0 < k \\ r, & \text{for } k = 0 \\ k^{-1/2}\sinh(k^{1/2}r), & \text{for } k > 0 \end{cases} \tag{1.4}$$

where k is the curvature constant which is related to the space radius of curvature by

$$R_{curv} = k^{-1/2}. \tag{1.5}$$

We can distinguish three different cases:

- k < 0: closed universe, two parallel geodesics[1] converge;
- k $= 0$: flat universe, two parallel geodetics remain parallel;
- k > 0: open universe, two parallel geodetics diverge.

The metric given in Eq. 1.3 can be rewritten, without any physical differences, by defining an alternative radius r as $r \equiv f_k(r)$. The metric becomes:

$$ds^2 = \frac{dr^2}{1 - kr^2} + r^2 d\omega^2. \tag{1.6}$$

We can now model our universe by taking for each point in time a Friedmann-Robertson-Walker (FRW) space (or metric). We allow the scale factor and the curvature of the RW space to vary with time. This gives the generic metric

$$ds^2 = -dt^2 + a(t)^2[d\chi^2 + f_k(\chi)^2\chi^2 d\omega^2]. \tag{1.7}$$

The function $a(t)$ corresponds to the scale factor that depends on time and which will describe the expansion (or contraction) of the universe and it is normalized such that at the present time we have by definition $a = 1$. We use the symbol χ instead of r because, as we shall see, the radial coordinate in this form no longer has a meaning as a true distance. Instead, the "true" distance r would be $r = a(t)\chi$, so only today we have $r = \chi$.

1.2.2 Friedmann's equations

We can assume both matter and radiation described as a continuum and treated as a uniform gas (compressible fluid) with the mass-energy density ρ and pressure P. The stress energy-momentum tensor for a perfect isotropic fluid is:

$$T^{\mu}_{\nu} = \begin{bmatrix} -\rho(t) & 0 & 0 & 0 \\ 0 & P(t) & 0 & 0 \\ 0 & 0 & P(t) & 0 \\ 0 & 0 & 0 & P(t) \end{bmatrix}. \tag{1.8}$$

[1] A geodesic is a locally length-minimizing curve, the path that a particle which is not accelerating would follow.

The relation between the metric and the matter-energy contents of the universe is described by the Einstein's equation:

$$R_{\nu\mu} - \frac{1}{2} R g_{\nu\mu} = \frac{8\pi G}{c^4} T_{\mu\nu} \tag{1.9}$$

where $R_{\nu\mu}$ is the Ricci tensor, R is the scalar curvature ($R \equiv g^{\nu\mu} R_{\nu\mu}$) and $g_{\nu\mu}$ the FRWL metric tensor. After substituting the metric and the energy-momentum tensor of ideal fluid into the Einstein's equations, one finds that out of these 16 equations only two are independent:

$$\left(\frac{\dot{a}}{a}\right)^2 = \frac{8\pi}{3} G\rho - \frac{Kc^2}{a^2}, \tag{1.10}$$

$$2\frac{\ddot{a}}{a} + \left(\frac{\dot{a}}{a}\right)^2 = -8\pi G \frac{P}{c^2} - \frac{Kc^2}{a^2}. \tag{1.11}$$

Eq. 1.10 is the Friedmann's first equation. Subtracting this equation from Eq. 1.11 one obtains the Friedmann's second equation (*acceleration equation*):

$$\frac{\ddot{a}}{a} = -\frac{4\pi G}{3}\left(\rho + 3\frac{P}{c^2}\right). \tag{1.12}$$

Finally if we use the Einstein equation with the cosmological term Λ

$$R_{\mu\nu} - \frac{1}{2} R g_{\mu\nu} = \frac{8\pi G}{c^4} T_{\mu\nu} - \frac{\Lambda}{c^2} g_{\mu\nu}, \tag{1.13}$$

the Friedmann and the acceleration equations respectively become

$$\left(\frac{\dot{a}}{a}\right)^2 = \frac{8\pi}{3} G\rho - \frac{Kc^2}{a^2} - \frac{\Lambda}{3}, \tag{1.14}$$

$$\frac{\ddot{a}}{a} = -\frac{4\pi G}{3}\left(\rho + 3\frac{P}{c^2}\right) + \frac{\Lambda}{3}. \tag{1.15}$$

It is useful to introduce adimensional densities (calculated today, for $t = t_0$) defined as

$$\Omega_i = \frac{\rho_i(t = t_0)}{\rho_{cr}} \tag{1.16}$$

where ρ_i are the energy densities of the different components ($i = m$ for non-relativistic matter, $i = R$ for radiation, $i = \Lambda$ for the cosmological constant) and ρ_{cr} is the critical density:

$$\rho_{cr} \equiv \frac{3H_0^2}{8\pi G} \sim 10^{-29} \mathrm{g\,cm^{-3}}. \tag{1.17}$$

Let us now analyze briefly these different energetic components of the universe. The universe contains non-relativistic matter in form of ordinary matter (called baryonic matter, including atoms, ions and electrons) and dark matter

as well, which interacts mainly through gravity. The energy of a non relativistic matter particle is equal to its rest mass energy, that remains constant with time, therefore the energy density of many particles is just their rest mass energy times their number density. In an expanding universe volumes are proportional to a^3, therefore the energy density of matter scales as a^{-3}. For what concerns radiation, its main components are the photons of the cosmic microwave background (CMB), that is the remnant of a hot state in the early universe, when matter was almost homogeneously and isotropically distributed and in thermal equilibrium. When the scale factor was smaller than today, the corresponding energy would have been larger by a factor $1/a$. Therefore the energy density of radiation, that is the average energy per particle times the number density, scales as a^{-4}. Similarly to the CMB, there is a cosmological background of neutrinos, but their energy, redshifted by the expansion of the universe, should be in the order of 10^{-3} eV today, almost impossible to measure. There is evidence from distant supernovae that there is another form of energy, called dark energy because of its unknown origin, besides ordinary matter and radiation. This new form of energy density remains constant with time, so it has been called the cosmological constant, and was first introduced by Einstein. The evidence of its existence is based on the difference between the luminosity distance (defined by the flux law $F = L/(4\pi d_L^2)$) in a (dark) matter or in a dark energy dominated universe. This has been tested by the measurements of high redshift Supernovae Type Ia (SNIa), and by the measurements of the CMB anisotropy [7]. The solution of the Friedmann Eq. 1.10 for a constant energy density provides an exponentially growing scale factor, so that objects of a given intrinsic brightness and distance will appear fainter if the universe is dominated by dark energy. This is indeed the case for the high redshift SNIa, which can be reconducted to standard candles and used for the test.

Finally we can define the curvature density parameter:

$$\Omega_K \equiv -\frac{K}{H_0^2} \tag{1.18}$$

and rewrite the first Friedmann's equation as:

$$\left(\frac{\dot{a}}{a}\right)^2 = \frac{\Omega_m}{a^3} + \frac{\Omega_R}{a^4} + \Omega_\Lambda + \frac{\Omega_K}{a^2}. \tag{1.19}$$

Computing at the present time, and defining $\Omega \equiv 1 - \Omega_k$ we derive:

$$\Omega = \Omega_m + \Omega_R + \Omega_\Lambda, \tag{1.20}$$

therefore if the universe is open $\Omega < 1$, while if it is closed $\Omega > 1$. Determining the spatial curvature of the universe implies therefore measuring its total energy density, and all the most recent data confirm that Ω is extremely close to 1 [8].

1.3 The Cosmic Microwave Background

During the first 380000 years, the universe was completely ionized, its primary baryonic matter components being free protons and electrons. The electrons

in the primordial universe continuously diffused the photons via Thomson scattering, allowing them to travel without interactions only for relatively short distances. This scattering of photons from free electrons kept electrons and photons in thermal equilibrium. Meanwhile the expansion of the universe was diluting the free electron number density ($\propto 1/a^3$) and accordingly the mean time between each scattering started to approach the characteristic time scale of the expansion of the universe, that is the Hubble time $\tau = 1/H(t)$. At the high energies of the primordial universe, the three species of neutrinos could be produced and created by the reaction:

$$\nu + \bar{\nu} \longleftrightarrow e^+ + e^-. \tag{1.21}$$

When the average energy per particle is reduced to $kT \sim 1\,\mathrm{MeV}$ the majority of electron-positron couples annihilate into photons:

$$e^+ + e^- \longrightarrow \gamma + \gamma. \tag{1.22}$$

With these annihilation reactions, and when neutrinos stop interacting among themselves forming e^+e^-, the number of photons increases, becoming higher than the number of neutrinos and electrons, giving rise to the epoch known as decoupling. When the universe had cooled to a temperature of about 3000 K, it was cold enough for electrons and protons to stick together as hydrogen atoms, without an energetic photon immediately reionizing them. This was the beginning of the era of recombination during which the universe rapidly went from ionized to neutral, and led to the release of CMB photons. This can be thought of as happening on a "surface in redshift space", which is commonly called the last scattering surface (LSS). LSS is a spherical surface, centered on the Earth, from which the CMB photons that arrive now to us underwent their last scattering and began their approximately undisturbed travel towards us, covering a distance equal to about 99.9% the size of the observable universe, in a time almost 99.997% the age of the universe [9].

Because the universe had undergone a period of thermal equilibrium in its history, the CMB was initially created with a blackbody spectrum. It can be shown that a blackbody radiation field in an expanding Universe retains its blackbody spectrum, but its characteristic temperature decreases as the inverse of the scale factor of the universe [10]. The spectrum of the CMB was measured by the FIRAS (Far-Infrared Absolute Spectrophotometer) instrument aboard the COBE (Cosmic Background Explorer) satellite in 1989 [11], as shown in Fig. 1.2. FIRAS measurement is the most accurate measurement of a blackbody ever performed. It corresponds to a temperature of $2.7253\,\mathrm{K} \pm 0.66\,\mathrm{mK}$.

1.3.1 CMB anisotropy

Direct measurements of the CMB detected the presence of temperature fluctuations, of the order of 1 part over 10^5 , with rms variations of a few tens of µK, in the brightness temperature of the CMB [12]. Theoretical models of structure formations were built to connect temperature fluctuations in the CMB to density

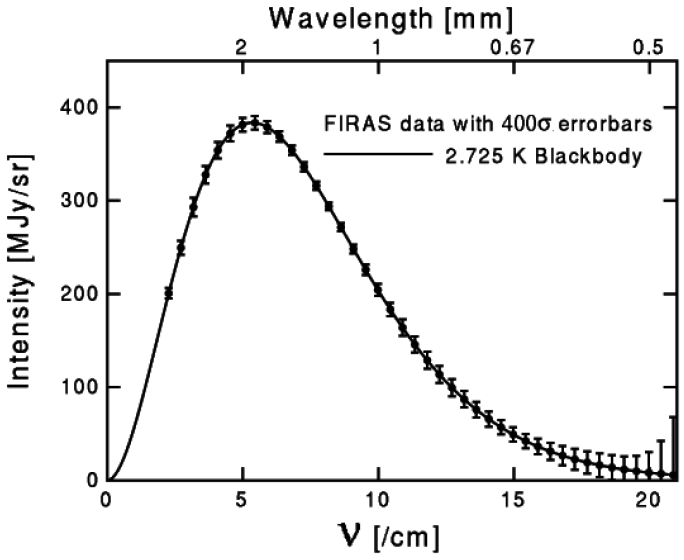

Figure 1.2: Specific brightness of the CMB radiation as measured by the FIRAS experiment aboard the COBE satellite. Note that the errorbars have been magnified 400 times with respect to the usual, otherwise would be invisible.

perturbations at the recombination epoch (and even to quantum fluctuations in the early universe), therefore it is possible to estimate the power spectrum of density fluctuations by measuring directly CMB fluctuations on the last scattering surface. The temperature anisotropy of the cosmic microwave background, in spherical coordinates θ and ϕ, can be decomposed in spherical harmonics:

$$\delta T(\theta,\phi) = T(\theta,\phi) - \langle T \rangle = \sum_{l=0}^{\infty} \sum_{m=-l}^{l} a_{lm} Y_{lm}(\theta,\phi) \tag{1.23}$$

where the index l is the multipole. $l = 0$ is the monopole, $l = 1$ corresponds to the dipole (angular variation $\theta = 180°$), $l = 2$ corresponds to the quadrupole ($\theta = 90°$) and so on. In general, the angular scale correspondent to the l-th term can be approximately expressed as:

$$\theta \simeq \frac{180^\circ}{l}. \tag{1.24}$$

If the fluctuations in the microwave background intensity are a Gaussian random variable, then all the information in anisotropy is included in the two-point autocorrelation function, $C(\theta)$, of the fluctuations:

$$C(\theta) = \left\langle \frac{\Delta T(\hat{n}_1)}{T_{cmb}} \frac{\Delta T(\hat{n}_2)}{T_{cmb}} \right\rangle \tag{1.25}$$

where $\Delta T(\hat{n})/T_{cmb}$ is the fractional deviation in the CMB temperature in the direction $\hat{n}$, and the average is over all pairs of directions on the sky $\hat{n}_1$ and $\hat{n}_2$ such that $\hat{n}_1 \cdot \hat{n}_2 = \cos\theta$. This function $C(\theta)$ then contains all the information present in the anisotropy, and can be expanded in terms of Legendre polynomials, where the information is stored in the C_l coefficients:

$$C(\theta) = \frac{1}{4\pi} \sum_l C_l P_l(\cos\theta). \tag{1.26}$$

The C_l's comprise the angular power spectrum of CMB anisotropies:

$$C_l = \frac{1}{2l+1} \sum_{-l}^{l} |a_{lm}|^2. \tag{1.27}$$

The CMB power spectrum, as reported in the Planck satellite results [13], is shown in Fig. 1.3. The $l = 1$ term in the Eq. 1.27 corresponds to the dipole

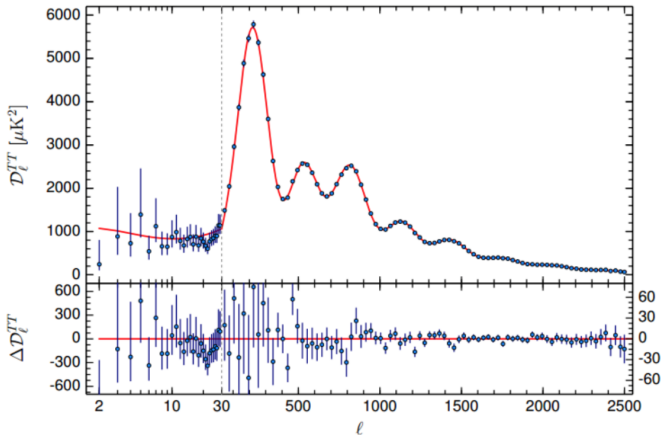

Figure 1.3: Planck 2015 temperature anisotropy angular power spectrum (measured data with error bars), compared to the base CDM model best fit (red line).The upper panel shows the power spectra, while the lower one shows the residuals. The blue vertical dashed line shows the "hybridization scale", at $l = 29$, where the horizontal scale changes from logarithmic to linear. The quantity D_l is connected to the C_l by $D_l = l(l+1)C_l/(2\pi)$.

anisotropy due to our motion with respect to the distant matter scattering the cosmic microwave background, causing a Doppler effect at a level $\beta = v/c \simeq 10^{-3}$. Starting from Lorentz transformations, one finds that the temperature as measured by an observer with peculiar velocity $\vec{v}$ with respect to the CMB is [14]:

$$T_{obs} = T_{rest} \frac{\sqrt{1-\beta^2}}{1-\beta\cos\theta} \simeq T_{rest}(1+\beta\cos\theta) \tag{1.28}$$

where T_{rest} is the CMB temperature as measured in a rest frame with respect to the LSS and θ is the angle between the line of sight and the peculiar velocity of the moving observer. Because the Earth's velocity with respect to comological matter is much smaller than the velocity of light we can use the second approximation. The measured CMB dipole amplitude [15] is $(3.358 \pm 0.001 \pm 0.0023)$mK in the direction $(l, b) = (264.31° \pm 0.04° \pm 0.16°, +48.05° \pm 0.02° \pm 0.09°)$ where the first uncertainties are statistical and the second include calibration and combined systematic uncertainties. Fig. 1.4 shows the CMB dipole.

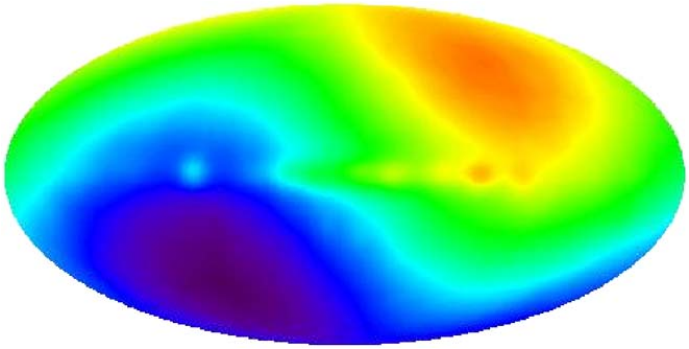

Figure 1.4: The CMB dipole, measured by the DMR experiment on board of the COBE satellite. Hotter areas (in orange) correspond to the Earth's motion direction with respect to the CMB, while colder areas (in purple) point towards the opposite direction. The horizontal line is due to the emission of astrophysical sources in the plane of our Galaxy.

In addition to the temperature anisotropy, the Earth's peculiar velocity produces also aberration and modulation effects in CMB anisotropies, which have been both detected by the Planck satellite [16]. These aberration effects consist in motions of anisotropy patches of about $4'$, and the modulation effect is of the order of few parts in 10^3, on an anisotropy that is already of the order of one part on 10^5. Both these effects have been measured by the Planck satellite, giving as a result a peculiar velocity of the Earth which is perfectly compatible with that measured by the Dipole anisotropy.

1.3.2 Secondary anisotropies

Temperature anisotropies observed in the CMB map which originated during the travel of photons from the last scattering surface towards us, at $0 \leq z \leq 1100$, are known as secondary anisotropies[2]. These anisotropies, unlike primary ones, do not have a primordial origin, but are due to the interaction of photons with the density, gravity and velocity fields during their propagation in the

[2]The redshift z is related to the scale factor at the time the object originally emitted that light as $a(t) = \frac{1}{1+z}$.

universe. Therefore an accurate knowledge is essential both to remove them from anisotropy maps to extract the real primordial fluctuations at the recombination and to have important information on the distribution of energy density in the universe, taking advantage of its interaction with CMB photons.

After their last scattering photons do not interact anymore with matter via Thomson scattering, but are still subject to the gravitational field of large-scale structures in the universe (like galaxy clusters, but also filaments between clusters, superclusters, etc.). The set of whole gravitational effects on CMB photons can be described with a time-varying gravitational potential ϕ and it is known as the *integrated Sachs-Wolfe effect* (ISW) [17]:

$$\frac{\delta T}{T} = \int \phi\,[r(t), T]\,dt. \tag{1.29}$$

Other anisotropies are due to gravitational lensing [18]. According to General Relativity, mass concentrations deflect light, and this deflection is described by geodesic lines following the curvature of the space-time. As a light ray follows the curvature, it is bent towards the mass which causes the space-time to be curved, and this leads to several important phenomena, such as the delay of light rays, the appearance of multiple images of the same source, its distortion and its magnification or demagnification. For example, if a pair of CMB photons forms initially an angle θ, because of this effect they will arrive to us forming an angle $\theta + \delta\theta$, with $\delta\theta/\theta \sim 0.1 - 0.2$ (weak gravitational lensing [19]). The corresponding effect on the CMB power spectrum at low angular scales is to blend its fluctuations, rounding both troughs and crests, at a level of few percent.

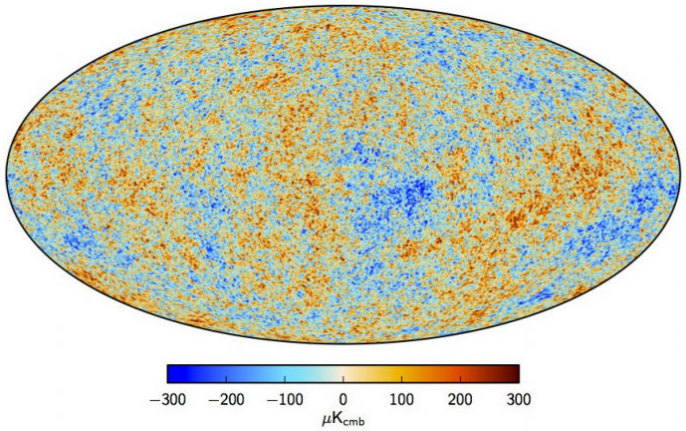

Figure 1.5: CMB temperature anisotropies map at $5'$ resolution, derived from the joint baseline analysis of Planck, WMAP, and 408 MHz observations [20]. A small strip of the Galactic plane (1.6% of the full sky), is filled in by a constrained realization with the same statistical properties of the rest of the sky [21].

Furthermore because of reionization, a fraction of CMB photons would have

been again affected by scattering after recombination, and will therefore arrive to an observer from a direction different from the one they had at last scattering. This mixing of CMB photons happens at large angular scales, roughly equal to the dimension of the cosmological horizon at the epoch of the diffusion. Finally two main effects of local reionization happen in galaxy clusters, and they both are known as Sunyaev-Zel'dovich effect (SZ), thermal and kinematic, introduced by Rashid Sunyaev and Yakov Zel'dovich in 1969 [22, 23]. Fig. 1.5 shows the map of the temperature anisotropies of the cosmic microwave background, as derived by the joint analysis of Planck, WMAP and 408 MHz observations [20].

1.3.3 Inflation

Cosmic inflation was originally proposed by Alan Guth, Alexei Starobinsky, Andrei Linde and Katsuhiko Sato [2, 24]. The inflation consists of a rapid exponential expansion of the early universe by a factor of at least 10^{78} in volume, driven by a negative pressure energy. Following the grand unification epoch (between 10^{-43} s and 10^{-36} s after the Big Bang), the inflationary epoch comprises the first part of the electroweak epoch. It lasted from 10^{-36} s to about 10^{-32} s. After that, the universe continued to expand at a rate that was much slower than inflation. While the detailed physics mechanism responsible for inflation is still unknown, inflation makes a number of predictions that have been confirmed by observations, such as CMB observations, galaxy surveys and 21 cm radiation measurements. Inflation is thus now considered to be an extension of the Big Bang theory. It resolves several problems in the Big Bang cosmology:

- The structure problem. How did clusters and super clusters of galaxies form? The Big Bang theory does not account for the needed initial fluctuations to produce the structure we see. Inflation gives a solution to this problem: Quantum fluctuations in the nearly-uniform density of the early universe expanded to cosmic scales during cosmic inflation. These fluctuations also would have left an imprint in the CMB radiation in the form of temperature fluctuations from point to point across the sky (the CMB anisotropy). The structures that we observe today grew from the gravitational pull of these fluctuations.

- The flatness problem. Observations show that the geometry of the current universe is nearly flat. However, under the nominal Big Bang theory, curvature grows with time. A universe as flat as we see it today would require an extreme fine-tuning of conditions in the past, which would be an unbelievable coincidence. Inflation provides a solution to this problem via the stretching of any initial curvature of the 3-dimensional universe to near flatness.

- The horizon problem. The uniformity of the CMB temperature implies that the entire observable universe must have been in causal contact in the past. But now two far regions in the sky could never have been in causal contact with each other because the light travel time is greater than the

age of the universe. Distant regions were actually much closer together prior to inflation than they would have been with only standard Big Bang expansion. Thus, such regions could have been in causal contact prior to inflation and could have reached a uniform temperature.

- The magnetic monopole problem. The Big Bang theory predicts that the early universe produced a very large number of heavy and stable magnetic monopoles. However, these magnetic monopoles have never been observed so far. The explanation from inflation is that, during this phase, the density of monopoles drops exponentially, so their abundance drops to undetectable levels.

To see in a simple way how inflation can solve the paradoxes, let's suppose that the primordial universe had a period of exponential growth at a certain epoch in the radiation dominated phase. Let's assume that this expansion starts immediately at $t = t_i$, and that lasts until a time $t = t_f$, when the exponential growth stops, and the universe gets back to a state of radiation dominated expansion. This exponential growth phase is called De Sitter phase, and in this simple case we can write the scale factor as:

$$a(t) = \begin{cases} a_i(\frac{t}{t_i})^{1/2}, & \text{for } t < t_i \\ a_i \exp H_i(t - t_i), & \text{for } t_i < t < t_f \\ a_i \exp H_i(t_f - t_i)(\frac{t}{t_f})^{1/2}, & \text{for } t > t_f \end{cases} \tag{1.30}$$

where $H_i = \sqrt{\Lambda_i/3}$ is the Hubble parameter, constant during inflation. Hence between the start time of inflation t_i and the final time t_f, the scale factor increases by a factor:

$$\frac{a(t_f)}{a(t_i)} = e^N \tag{1.31}$$

where $N \equiv H_i(t_f - t_i)$ is the *e-foldings number*. If the duration of inflation $t_f - t_i$ is long enough with respect to the Hubble time during inflation, then N is large ($\lesssim 100$) and the growth of the scale factor can be huge.

Inflation is the answer to the above paradoxes, but there are still some open questions, such as what triggers inflation at $t = t_i$ and what ends it at $t = t_f$. Another unanswered question is that if inflation dilutes the number density of unwanted cosmological relics, why it doesn't reduce also the number density of the particles we see today. Moreover, if inflation is so efficient to flatten the global curvature of the universe, we might ask the reason why it doesn't also flatten the local curvature due to energy density fluctuations. Indeed we know that the cosmic microwave background is not perfectly isotropic, and so the universe is not isotropic at small scales after the inflationary phase. To try to answer to these questions, suppose that the universe contains a single scalar field $\phi(t)$ whose value changes in time[3]. To this field a potential $V(\phi)$ is associated.

[3]Some implementations identify the inflaton with the Higgs field, that carries interactions between particles at energies higher than the GUT ones.

Now we want to understand if an homogeneous scalar field ϕ can give rise to an accelerated expansion. From the Lagrangian density of the inflaton, setting $\hbar = c = 1$, we can derive the energy density [25].

$$\rho = \frac{1}{2}\dot{\phi}^2 + V(\phi). \tag{1.32}$$

In this equation the first term is the kinetic energy density of the field while the second is its potential energy density. Therefore an homogeneous scalar field obeys the same dynamics of a particle moving under a given potential V. The pressure P of the inflation is

$$P = \frac{1}{2}\dot{\phi}^2 - V(\phi). \tag{1.33}$$

Then a negative pressure configuration is a configuration with a potential energy density larger than the kinetic energy density.

In Fig. 1.6 is shown an example of a scalar field ϕ trapped in a false vacuum, that is a local, but not global, minimum of the potential $V(\phi)$. Instead the global minimum of the potential is called the true vacuum because an homogeneous scalar field that is in the global minimum of the potential is in the ground state of the system. Since the scalar field is constant if it is trapped in the false vacuum, its energy density remains constant with time and has a negative pressure which gives rise to an accelerated expansion. Even if the universe is filled up at the beginning with a mixture of radiation, matter and energy of false vacuum, it will be soon dominated by the latter, because energy densities of matter and radiation gets quickly diluted during the expansion.

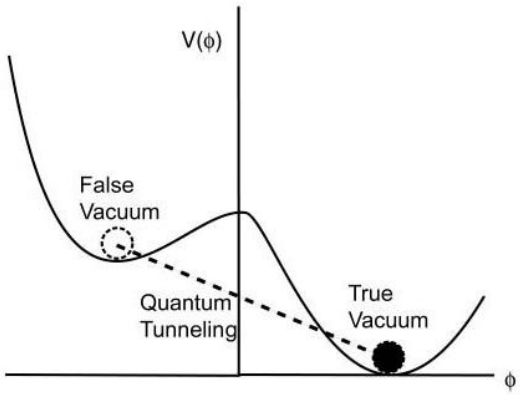

Figure 1.6: A scalar field trapped in a false vacuum.

This is the original formulation of inflation, but some problems arise: the only way to make the field evolve towards the true vacuum (to end the inflationary phase) is through quantum tunneling. Thus, initially small localized regions

tunnel from the false to the true vacuum, but these bubbles that get to the true vacuum must coalesce to allow the universe as a whole to move to the global minimum of the potential. Detailed calculations showed that this doesn't work, thus the true vacuum state of the universe is never attained. The new model of inflation is called *slow-roll inflation*. What changes here is the shape of the potential $V(\phi)$, chosen in such a way that the inflaton slowly rolls down along it.

1.3.4 Gravitational waves

One of the most striking predictions of General Relativity is the existence of gravitational waves. When a mass-energy distribution changes with time, the information related to these variations propagates in space in the form of waves. The tensor $g_{\mu\nu}$ corresponds both to the metric tensor and to the gravitational potential. These waves are also metric waves that change the geometry of space-time and therefore the proper distances between bodies. In the next chapter it will be shown that the primordial gravitational waves are potentially (and indirectly) detectable because they produce observable distortions in the CMB, especially at very large angular scales.

It is possible to consider tensor perturbations and scalar perturbations separately because of the *decomposition theorem*, that assures that scalar and tensor perturbations evolve completely independently. To characterize tensor perturbations we consider a perturbed metric:

$$ds^2 = -a^2[d\eta^2 - (\delta_{ij} + 2h_{ij})dx^i dx^j] \tag{1.34}$$

where $\eta \equiv \int_0^t dt'/a(t')$ is the conformal time and the slightly deviation from a flat metric h_{ij} is traceless and transverse. If we substitute this into Einstein equations and use modes[4] of the form $e^{ik_i x^i}$ we find:

$$\ddot{h}_{ij} + 2aH\dot{h}_{ij} + k^2 h_{ij} = 8\pi G\Sigma^T_{ij} \tag{1.35}$$

where Σ^T_{ij} is the transverse and traceless part of the anisotropic stress tensor. Expressing h_{ij} in terms of the two indipendent gravitational wave polarization coomponents h_+ and $h_\times$, we find two independent solutions:

$$h \propto \frac{1}{\eta^3}(\cos(k\eta)k\eta - \sin(k\eta)), \tag{1.36}$$

$$h \propto \frac{1}{\eta^3}(\cos(k\eta)k\eta + \sin(k\eta)). \tag{1.37}$$

If we go back in time, we can write for gravitational wave polarization components:

$$h_{+,\times}(\eta) = -\frac{3}{k^3\eta^3}(\cos(k\eta)k\eta - \sin(k\eta))h_{+,\times}(0). \tag{1.38}$$

[4]We are considering the wavevector $\vec{k}$ in the direction of the z-axis and the pertubations in the $x - y$ plane

We can show that this is the solution for scales entering the horizon well after matter domination. For large value of η the dependence is $\propto 1/\eta^2 \propto 1/t^{2/3} \propto 1+z$, so the gravitational perturbations redshift away inside the horizon, quite unlike the scalar perturbations.

Gravitational waves produce a quadrupolar distortion in the temperature of the CMB. We can define an angular power spectrum [26] for E-modes and B-modes (see §1.4.1 for more details):

$$C_{El}^T = (4\pi)^2 \int k^2 dk P_h(k) \left| \int d\tau g(\tau) \Psi(k,\tau) \left[-j_l(x) + \ddot{j}_l(x) + \frac{2j_l(x)}{x^2} + \frac{4\dot{j}_l(x)}{x} \right] \right|^2, \tag{1.39}$$

$$C_{Bl}^T = (4\pi)^2 \int k^2 dk P_h(k) \left| \int d\tau g(\tau) \Psi(k,\tau) \left[2\dot{j}_l(x) + \frac{4j_l}{x} \right] \right|^2 \tag{1.40}$$

where j_l is the spherical Bessel function of order l and $P_h(k)$ is the primordial power spectrum of gravitational waves.

1.4 Polarization

Though anisotropy studies have been remarkably successful, there is a third characteristic of the CMB that we have not yet discussed: its polarization. The first realistic measurements of the polarization of the CMB were undertaken by Lubin and Smoot [27] and Caderni [28] in the late 1970s; since then limits have improved by orders of magnitude, and experimentalists are inching ever closer to a full detection.

Before the recombination period, the radiation interacts with matter mainly through Compton scattering (relativistically) and Thomson scattering (classically). If we consider a non-polarized incident photons field, it is well-known the scattering can produce linear polarized radiation. We can imagine that CMB should not polarized because the direction of oscillation of radiation electric field should be randomized after several scattering, so the degree of polarization is averaged to zero. Despite this if we analyze small angular scales, of the order of photon mean free path, the number of scattering events decreases and radiation keeps some directional information. Furthermore a total isotropic incident radiation produces a non-polarized outgoing radiation because contributions which come from direction separated by 90° balanced out. If the radiation is not isotropic but has a quadrupole distribution, the effect is totally different (Fig. 1.7). So, CMB polarization comes from the quadrupolar component of the incident field seen by electrons at the last scattering surface, as expected from the theory of polarized Thomson scattering.

Defining σ_T the Thomson cross section, we can write the differential cross section:

$$\frac{d\sigma}{d\Omega} = \frac{3\sigma_T}{8\pi} \left| \hat{\boldsymbol{\epsilon}}' \cdot \hat{\boldsymbol{\epsilon}} \right|^2 \tag{1.41}$$

where $\hat{\boldsymbol{\epsilon}}'$ and $\hat{\boldsymbol{\epsilon}}$ are the polarization vectors orthogonal to the propagation direction of incident photon and scattered photon respectively (Fig. 1.8).

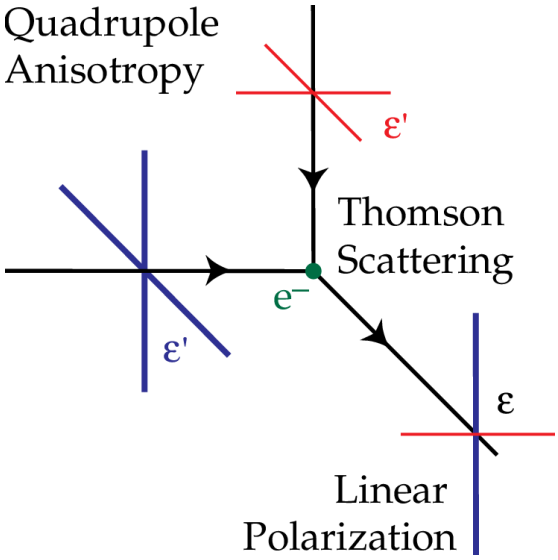

Figure 1.7: Thomson scattering of radiation with a quadrupole anisotropy generates linear polarization. Blue colors (thick lines) represent hot and red colors (thin lines) cold radiation. The unpolarized incoming photons are indicated with the apex.

In a reference frame with the electron resting in the origin we know the scattering Thomson matrix $\boldsymbol{T}$:

$$\boldsymbol{T} = \frac{3\sigma_T}{8\pi} \begin{pmatrix} (\hat{\epsilon}'_x \cdot \hat{\epsilon}_x)^2 & (\hat{\epsilon}'_y \cdot \hat{\epsilon}_x)^2 \\ (\hat{\epsilon}'_x \cdot \hat{\epsilon}_y)^2 & (\hat{\epsilon}'_y \cdot \hat{\epsilon}_y)^2 \end{pmatrix}. \tag{1.42}$$

The scattered intensities of unpolarized photons, which have intensities $I'_x = I'_y = I'$ for every choice of $\hat{x}$ and $\hat{y}$ are:

$$\begin{pmatrix} I_x \\ I_y \end{pmatrix} = \boldsymbol{T} \begin{pmatrix} I'_x \\ I'_y \end{pmatrix} = \frac{3\sigma_T}{8\pi} \begin{pmatrix} I'_x(\hat{\epsilon}'_x \cdot \hat{\epsilon}_x)^2 + I'_y(\hat{\epsilon}'_y \cdot \hat{\epsilon}_x)^2 \\ I'_x(\hat{\epsilon}'_x \cdot \hat{\epsilon}_y)^2 + I'_y(\hat{\epsilon}'_y \cdot \hat{\epsilon}_y)^2 \end{pmatrix} = \frac{3\sigma_T}{8\pi} \begin{pmatrix} I' \\ I' \cos^2\theta \end{pmatrix}. \tag{1.43}$$

If we introduce the Stokes parameters:

$$I = |E_x|^2 + |E_y|^2, \tag{1.44}$$
$$Q = |E_x|^2 - |E_y|^2, \tag{1.45}$$
$$U = 2\mathrm{Re}(E_x E_y^*), \tag{1.46}$$
$$V = -2\mathrm{Im}(E_x E_y^*) \tag{1.47}$$

where I describes the total intensity of light, Q the amount of horizontal/vertical linear polarization (along the x-axis or y-axis), U the amount of $\pm 45°$ linear

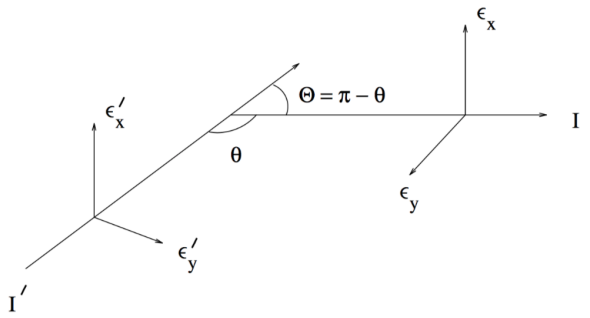

Figure 1.8: Scattering Thomson scheme between two photons with a generic scattering angle θ. The unpolarized incoming photon is indicated with the apex while the outgoing photon without. $\hat{z}$ and $\hat{z}'$ coincide with the propagation directions of photons.

polarization and V the amount of right/left circular polarization, we can obtain:

$$I = I_x + I_y = \frac{3\sigma_T}{8\pi} I'(1 + \cos^2\theta), \tag{1.48}$$

$$Q = I_x - I_y = \frac{3\sigma_T}{8\pi} I' \sin^2\theta \tag{1.49}$$

and the same about U in a reference frame rotated by 45°.

If we expand $I'(\hat{\boldsymbol{n}})$ in spherical harmonics $I'(\hat{\boldsymbol{n}}) = \Sigma_{lm} a_{lm} Y_l^m(\hat{\boldsymbol{n}})$ and integrate over all incident directions, we obtain the total Stokes parameters:

$$I = \frac{3\sigma_T}{16\pi}\left(\frac{8\sqrt{\pi}}{3} a_{00} + \frac{4}{3}\sqrt{\frac{\pi}{5}} a_{20}\right), \tag{1.50}$$

$$Q = \frac{3\sigma_T}{4\pi}\sqrt{\frac{2\pi}{15}} \Re a_{22}, \tag{1.51}$$

$$U = -\frac{3\sigma_T}{4\pi}\sqrt{\frac{2\pi}{15}} \Im a_{22}, \tag{1.52}$$

$$V = 0. \tag{1.53}$$

It is clear that polarization is strongly related to the presence of the quadrupole contribution in incident radiation. This model seems to suggest that scattering Thomson cannot produce V. Actually a more rigorous analysis shows that if at the beginning $V = 0$, circular polarization will not occur. Furthermore we have to consider other processes which can produce circular polarization, like the synchrotron originated by any primordial magnetic field. Nevertheless the resulting circular polatization turns out to be smaller than the linear component, so we will neglect it.

1.4.1 E-modes and B-modes

The Stokes formalism is not the best one to describe the general properties of the polarization field, because it depends on the choice of the reference frame. So it is useful to introduce scalar quantities, to reveal invariance properties of the field. The best choice is a linear combination $Q \pm iU$ which follows transformation's law

$$(Q \pm iU)' = e^{\pm 2i\phi}(Q \pm iU), \tag{1.54}$$

like spin weight $s = \pm 2$ harmonics [26]. Using the spinor spherical harmonics $Y_{s,lm}(\hat{\boldsymbol{n}})$, we have:

$$(Q + iU)(\hat{\boldsymbol{n}}) = \sum_{lm} a_{2,lm} Y_{2,lm}(\hat{\boldsymbol{n}}), \tag{1.55}$$

$$(Q - iU)(\hat{\boldsymbol{n}}) = \sum_{lm} a_{-2,lm} Y_{-2,lm}(\hat{\boldsymbol{n}}). \tag{1.56}$$

Like creation and annihilation operators, we can define $S_\pm$ operators which act on index s of a generic function f by rotating a spinor spherical harmonic in the previous or successive one in the following way:

$$(S_+ f)' = e^{-i(s+1)\phi} S_+ f, \tag{1.57}$$

$$(S_- f)' = e^{-i(s-1)\phi} S_- f. \tag{1.58}$$

If we apply operators twice in equations 1.55 and 1.56 we obtain the common spherical harmonics:

$$S_-^2 (Q + iU)(\hat{\boldsymbol{n}}) = \sum_{lm} a_{2,lm} \left[\frac{(l+2)!}{(l-2)!}\right]^{1/2} Y_l^m(\hat{\boldsymbol{n}}), \tag{1.59}$$

$$S_+^2 (Q - iU)(\hat{\boldsymbol{n}}) = \sum_{lm} a_{-2,lm} \left[\frac{(l+2)!}{(l-2)!}\right]^{1/2} Y_l^m(\hat{\boldsymbol{n}}). \tag{1.60}$$

So we can define two coefficients $a_{E,lm} = -\left[\frac{(l+2)!}{(l-2)!}\right]^{1/2} (a_{2,lm} + a_{-2,lm})/2$ and $a_{B,lm} = -i\left[\frac{(l+2)!}{(l-2)!}\right]^{1/2} (a_{2,lm} - a_{-2,lm})/2$ and introduce two quantities:

$$E(\hat{\boldsymbol{n}}) = -\frac{1}{2}\left[S_-^2 (Q + iU)(\hat{\boldsymbol{n}}) + S_+^2 (Q - iU)(\hat{\boldsymbol{n}})\right] = \sum_{lm} a_{E,lm} Y_l^m(\hat{\boldsymbol{n}}), \tag{1.61}$$

$$B(\hat{\boldsymbol{n}}) = \frac{i}{2}\left[S_-^2 (Q + iU)(\hat{\boldsymbol{n}}) - S_+^2 (Q - iU)(\hat{\boldsymbol{n}})\right] = \sum_{lm} a_{B,lm} Y_l^m(\hat{\boldsymbol{n}}). \tag{1.62}$$

These are the two scalar quantities we are looking for which describe E-modes and B-modes respectively. The respective power spectra are:

$$C_l^{EE} = \frac{1}{2l+1} \sum_m \langle a_{E,lm} a_{E,lm}^* \rangle, \tag{1.63}$$

$$C_l^{BB} = \frac{1}{2l+1} \sum_m \langle a_{B,lm} a_{B,lm}^* \rangle. \tag{1.64}$$

At this point it is interesting to study the behaviour of E and B modes under a parity transformation. By applying transformations $\hat{\boldsymbol{e}}'_\phi = -\hat{\boldsymbol{e}}_\phi$ and $\hat{\boldsymbol{e}}'_\theta = -\hat{\boldsymbol{e}}_\theta$, Stokes parameters become $Q'(\hat{\boldsymbol{n}}') = Q(\hat{\boldsymbol{n}})$ and $U'(\hat{\boldsymbol{n}}') = -U(\hat{\boldsymbol{n}})$. From equations 1.57 and 1.58 we have:

$$S^2_-(Q+iU)'(\hat{\boldsymbol{n}}') = S^2_+(Q-iU)(\hat{\boldsymbol{n}}), \tag{1.65}$$

$$S^2_+(Q-iU)'(\hat{\boldsymbol{n}}') = S^2_-(Q+iU)(\hat{\boldsymbol{n}}). \tag{1.66}$$

So we obtain:

$$E(\hat{\boldsymbol{n}}') = E(\hat{\boldsymbol{n}}), \tag{1.67}$$

$$B(\hat{\boldsymbol{n}}') = -B(\hat{\boldsymbol{n}}). \tag{1.68}$$

Another basic property concerns the pattern orientation in the space. If we indicate with $\boldsymbol{\theta}$ the angular variables (θ, ϕ) in polar coordinate system, we want to determine the expressions of $E(\boldsymbol{\theta})$ and $B(\boldsymbol{\theta})$ in order to analyze pattern properties explained in the next section. After a counterclockwise rotation of $\hat{x}$ and $\hat{y}$ axes by an angle ϕ', Stokes parameters follow Eq. 1.54:

$$\begin{pmatrix} Q' \\ U' \end{pmatrix} = \begin{pmatrix} \cos 2\phi & \sin 2\phi \\ -\sin 2\phi & \cos 2\phi \end{pmatrix} \begin{pmatrix} Q \\ U \end{pmatrix} = \begin{pmatrix} Q\cos 2\phi + U \sin 2\phi \\ -Q \sin 2\phi + U \cos 2\phi \end{pmatrix}. \tag{1.69}$$

Because the majority of CMB experiments studies a small region of sky (high value of l), we can consider the sky flat and replace spherical harmonics with Fourier space. For a generic observable f we have:

$$\sum a_{f,lm} Y_{lm}(\hat{\boldsymbol{n}}) \to \int d^2\boldsymbol{l} f(\boldsymbol{l}) e^{i\boldsymbol{l}\cdot\boldsymbol{\theta}}. \tag{1.70}$$

This approximation gives us the opportunity to simplify calculations, but it may be generalized for large angular scales. The new expressions of E and B modes are:

$$E(\boldsymbol{\theta}) = \frac{1}{2\pi} \int d^2\boldsymbol{l} E(\boldsymbol{l}) e^{i\boldsymbol{l}\cdot\boldsymbol{\theta}}, \tag{1.71}$$

$$B(\boldsymbol{\theta}) = \frac{1}{2\pi} \int d^2\boldsymbol{l} B(\boldsymbol{l}) e^{i\boldsymbol{l}\cdot\boldsymbol{\theta}}. \tag{1.72}$$

Using equations 1.71, 1.72 and the expressions of $E(\boldsymbol{l})$ and $B(\boldsymbol{l})$ in the Fourier

space[5] we can demonstrate [29]:

$$E(\boldsymbol{\theta}) = -\int d^2\boldsymbol{\theta}' w(\tilde{\theta})[Q(\boldsymbol{\theta}')\cos(2\tilde{\phi}) + U(\boldsymbol{\theta}')\sin(2\tilde{\phi})] = -\int d^2\boldsymbol{\theta}' w(\tilde{\theta}) Q_r(\boldsymbol{\theta}'), \tag{1.75}$$

$$E(\boldsymbol{\theta}) = -\int d^2\boldsymbol{\theta}' w(\tilde{\theta})[U(\boldsymbol{\theta}')\cos(2\tilde{\phi}) - Q(\boldsymbol{\theta}')\sin(2\tilde{\phi})] = -\int d^2\boldsymbol{\theta}' w(\tilde{\theta}) U_r(\boldsymbol{\theta}'), \tag{1.76}$$

where the variables $(\tilde{\theta}, \tilde{\phi})$ represent polar coordinates of vector $\boldsymbol{\theta} - \boldsymbol{\theta}'$ and $w(\tilde{\theta})$ is the window function[6]. Finally $Q_r(\boldsymbol{\theta}')$ and $U_r(\boldsymbol{\theta}')$ are Stokes parameters in the polar coordinates frame centered in θ and independent of system coordinate. With this notation it is clear that E-modes are scalar quantities and B-modes are pseudoscalar quantities. Moreover B-modes pattern locally represents a rotation of 45° of E-modes one.

1.4.2 Perturbations

It is interesting to analyze the structure of polarized pattern on the sky. We have to consider quadrupolar anisotropies ($l = 2$) in the CMB which could generate three different types of perturbations: scalar ($m = 0$), vector ($m = \pm 1$) and tensor ($m = \pm 2$), as shown in Fig. 1.9 [30].

Scalar Perturbations

Scalar modes represent perturbations in the density of the cosmological fluid at last scattering and are the only fluctuations which can form structure though gravitational instability.

The fluid can be schematized as a plane wave, with hot zones (crests) and cold zones (troughs). Imagining an observer located in a trough, the azimuthal symmetry in the problem requires $\boldsymbol{v} \parallel \boldsymbol{k}$ and irrotational flow $\boldsymbol{\nabla} \times \boldsymbol{v} = 0$. Hotter photons flow with a velocity $\boldsymbol{v}$ from the crests into the trough from $\pm\hat{\boldsymbol{k}}$ directions while cold photons surround the observer. To understand the dependence of polarization by Stokes parameters it is useful to study the intensity for varying θ related to the wave vector $\hat{\boldsymbol{k}}$ and to the observation direction $\hat{\boldsymbol{n}}$ by the relation

[5] The two generalizations are:

$$E(\boldsymbol{l}) = \int d^2\theta [Q(\boldsymbol{\theta})\cos(2\phi_l) + U(\boldsymbol{\theta})\sin(2\phi_l)] e^{-i\boldsymbol{l}\cdot\boldsymbol{\theta}} \tag{1.73}$$

$$B(\boldsymbol{l}) = \int d^2\theta [U(\boldsymbol{\theta})\cos(2\phi_l) - Q(\boldsymbol{\theta})\sin(2\phi_l)] e^{-i\boldsymbol{l}\cdot\boldsymbol{\theta}} \tag{1.74}$$

[6] Windoss function has the following trend:

$$w(\theta) = \begin{cases} \frac{1}{\pi\theta^2}, & \text{for } \theta \neq 0 \\ 0 & \text{for } \theta = 0 \end{cases} \tag{1.77}$$

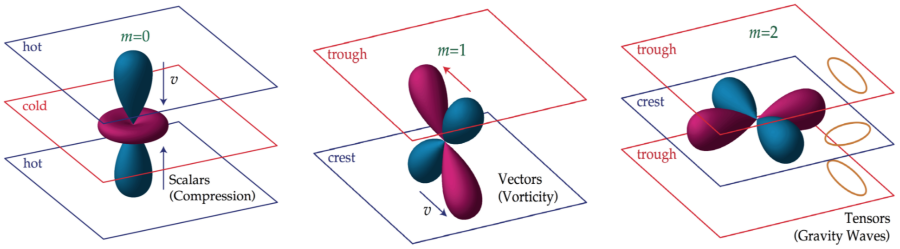

Figure 1.9: Blue colors represent hot lobes and red ones cold lobes for each type of quadrupolar anisotropies: scalar perturbations ($m = 0$) caused by density variations in the primordial fluid, vector perturbations ($m = \pm 1$) by vortical motion of matter and tensor perturbations ($m \pm 2$) by gravitational waves.

$\hat{\boldsymbol{n}} \cdot \hat{\boldsymbol{k}} = \cos\theta$. The final effect will come from polarization generated by Thomson scattering thanks to local quadrupolar anisotropies and modulated by a plane wave, $-Y_2^0(\hat{\boldsymbol{n}})e^{i\boldsymbol{k}\cdot\boldsymbol{x}}$, where the sign denotes the fact that photons flowing into cold regions are hot.

The polarization increases from $\theta = 0$ to $\theta = \pi/2$ (from pole to equator) and gives a field:

$$Q = \sin^2\theta, \qquad U = 0. \tag{1.78}$$

In different regions of space the sign of field could change, but not the direction. The overall pattern is shown in Fig. 1.10 where in orange is represented the real part of polarization (E-modes) and in purple the other possible configuration (B-modes), which is a rotation by 45° of the first one.

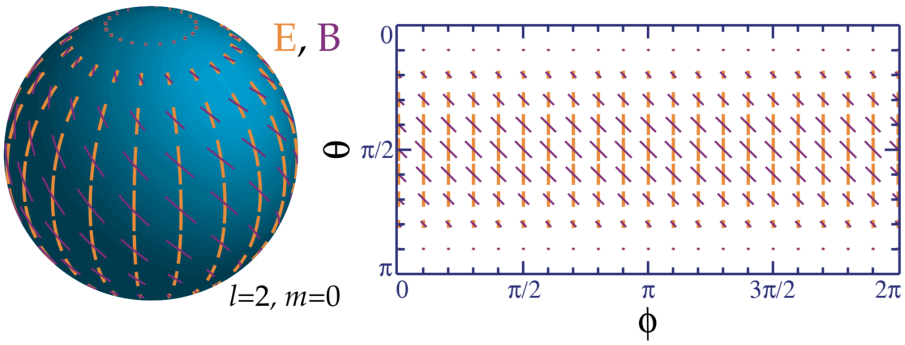

Figure 1.10: Polarization pattern for $l = 2$, $m = 0$. Both modes are ϕ independent and reach the maximum value for $\theta = \pi/2$ where there is also a pattern symmetry.

Vector Perturbations

Vector perturbations represent vortical motions of matter on which there is no associated density perturbation. The velocity field is $\boldsymbol{v} \perp \boldsymbol{k}$ and is null at maximum and minimum. Particles motion causes a Doppler effect which generates a dipole anisotropy in the radiation field. So the anisotropy is null in crest and trough while is maximum in the region with intermediate velocity. An observer sitting between crests and trough and looking up toward the trough will see the dipole pattern projected as a hot and cold spot across the zenith and looking down toward the crest will see the projected dipole reversed: the effect is a quadrupole pattern with $m = \pm 1$. The full polarization pattern is:

$$Q = -\sin\theta\cos\theta e^{i\phi}, \qquad U = -i\sin\theta e^{i\phi}, \tag{1.79}$$

and displayed clearly in Fig. 1.11.

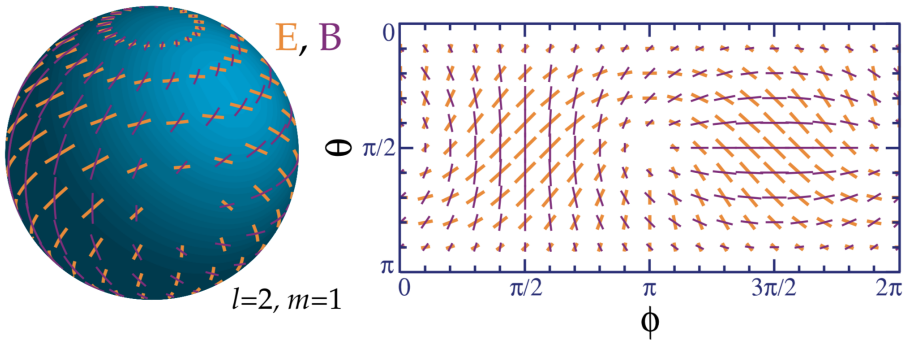

Figure 1.11: Polarization pattern for $l = 2$, $m = 1$. The main contribution comes from U especially closeness the equator ($\theta = \pi/2$).

A possible vector perturbation tends to decay quickly because they are not enhanced by fluctuations of gravitational field. Theories which describe universe at last scattering surface use only linear perturbations, but in this case tidal forces and high non linear perturbations are requested, surely not possible at recombination. This consideration together with the fast universe expansion lead to a negligible contribution of vector perturbations.

Tensor Perturbations

Tensor fluctuations are transverse-traceless perturbations to the metric, which can be viewed as gravitational waves. In this case the gravitational wave stretches the space in the plane of perturbation: a circle is distorted into an ellipse. So again the polarization is generated by Thomson scattering ($Y_2^{\pm 2}$). In contrast to other perturbations, the maximum of polarization is in the pole ($\theta = 0$). Stokes parameters are:

$$Q = (1 + \cos^2\theta)e^{2i\phi}, \qquad U = -2i\cos\theta e^{2i\phi}, \tag{1.80}$$

and the full pattern is shown in Fig. 1.12.

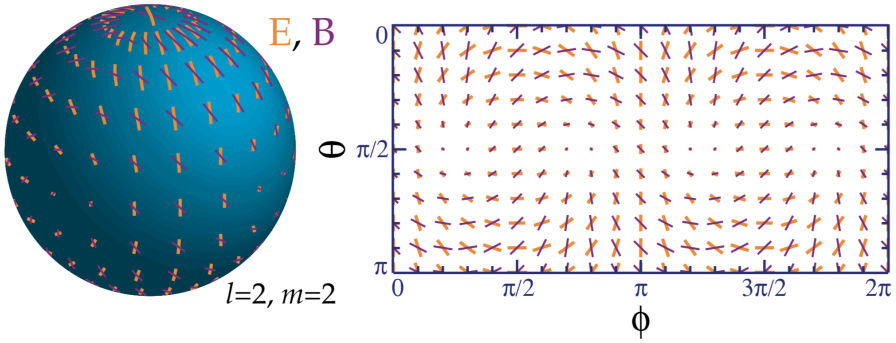

Figure 1.12: Polarization pattern for $l = 2$, $m = 2$. Q and U give approximately the same contribution.

1.4.3 Electric and Magnetic Modes

Every polarization pattern visible in the sky can be decomposed into electric (E) and magnetic (B) contribution: E and B modes are a rotation by 45° one to each other. The first conservation property is the parity: E-modes harmonics have $(-1)^l$ and B-modes have $(-1)^{l+1}$. Fig. 1.13 shows the invariance of E-modes and the inversion of B-modes for a transformation $\hat{\boldsymbol{n}} \to -\hat{\boldsymbol{n}}$ and $l = 2$. Thomson scattering can produce only E-modes because temperature perturbations are described by spherical harmonics with parity type $(-1)^l$.

The symmetries of temperature and polarization (intent as E-modes and B-modes) anisotropies allow four types of correlation. The autocorrelations of the temperature fluctuations, the E- and the B-modes are denoted, respectively, by TT, EE and BB, and the cross-correlation between temperature fluctuations and E-modes is denoted by TE. The other cross-correlations, TB and EB, vanish for symmetry reasons [31]. It is possible then to define the angular power spectrum for each correlation as:

$$C_l^{XY} = \frac{1}{2l+1} \sum_m \langle a^*_{X,lm} a_{Y,lm} \rangle, \tag{1.81}$$

where $X, Y = T, E, B$. The TT power spectrum (expressed as $D_l = l(l+1)C_l/(2\pi)$) is shown in Fig. 1.3, while Fig. 1.14 shows the TE and EE power spectra, as measured by Planck experiment [32].

Polarization also represents one of the most important tools to test the cosmic inflation scenario. In fact, one of the effects of inflation is to generate a spectrum of tensor perturbations (gravitational waves) which in turn produce quadrupole anisotropy at recombination, and thus a characteristic CMB polarization pattern including both E and B modes. On the other hand, scalar

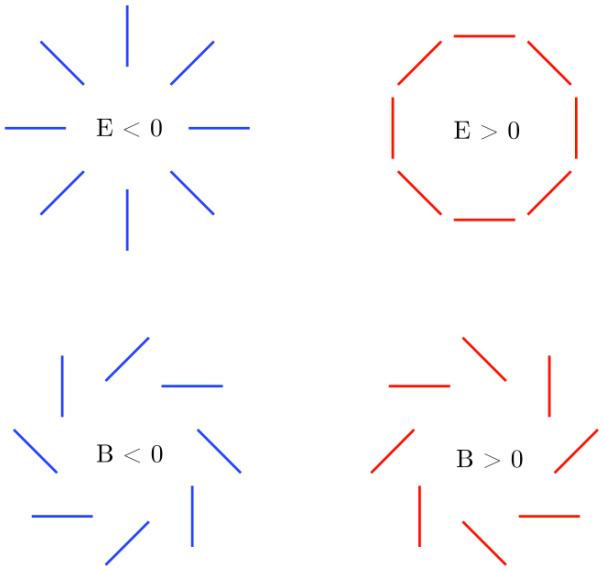

Figure 1.13: E and B polarization patterns. By applying a symmetry respect to any axis which pass through the center, E modes pattern remains unchanged while B modes one changes.

perturbations (density) only produce E modes. The amplitude of the peak in the BB power spectrum can be connected to the inflationary energy scale [33] by:

$$\left(\frac{l(l+1)}{2\pi}C_{BB}\right)^{1/2} = 0.024\left(\frac{E_{inflation}}{2\times10^{16}\,\mathrm{GeV}}\right)^{2}. \tag{1.82}$$

Models of cosmic inflation predict that gravitational waves induced effects could be observed in the polarization of the cosmic microwave background and having their origin in the early universe. Thus, the detection of B-modes supports the theory of inflation, and their strength can confirm and exclude different models of inflation. The parameter related to observable quantities is r, the ratio between tensor and scalar perturbations:

$$r \equiv \left.\frac{c_l^T}{c_l^S}\right|_{l=2} \simeq 0.1\left(\frac{E_{inflation}}{2\times10^{16}\,\mathrm{GeV}}\right)^{4}. \tag{1.83}$$

So far today there are only upper limits for the primordial part of the BB spectrum, but no detection [34]. The current status of B-modes detection of present and past experiments which contribute to set an upper limit on C_l^{BB} is shown in Fig. 1.15.

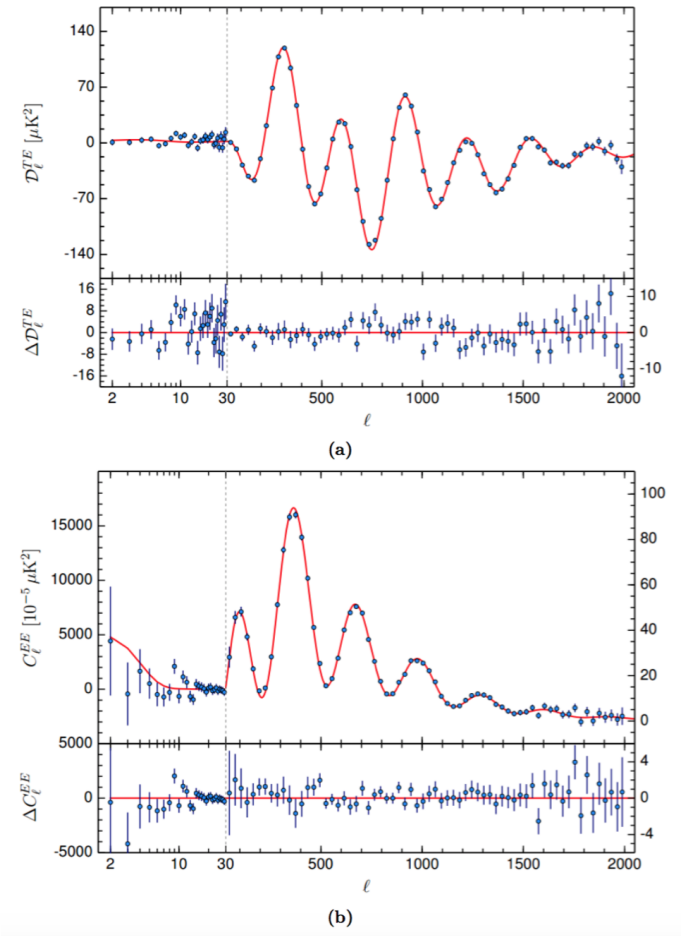

Figure 1.14: Planck 2015 TE (a) and EE (b) power spectra, compared with the base CDM fit to the Planck data (red line). The upper panels show the power spectra, while the lower ones show the residuals. The blue vertical dashed lines show the "hybridization scale", at $l = 29$, in correspondence of which the horizontal scale changes from logarithmic to linear. The quantity D_l is connected to the C_l by $D_l = l(l+1)C_l/(2\pi)$.

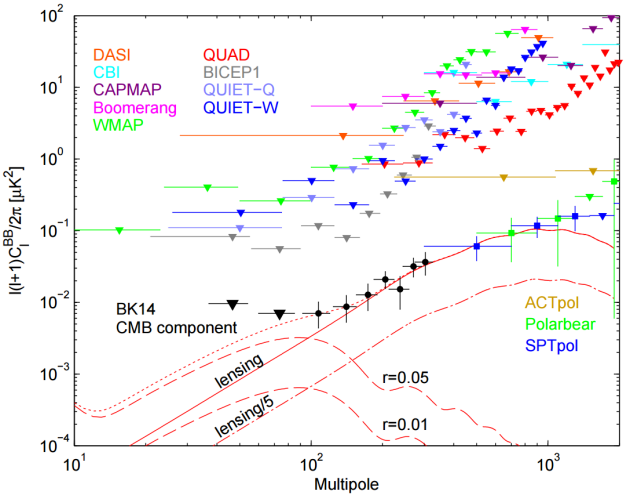

Figure 1.15: Upper limits on C_l^{BB} set by current experiments, no detection so far.

1.5 Foregrounds

The tiny CMB polarization signal is embedded in overwhelming polarized galactic foregrounds. This is especially true at larger angular scales where the amplitude of the CMB anisotropies is expected is expected to be very small, and several foregrounds are expected to have a decreasing power angular spectrum. To truly characterize foregrounds for polarization, we must understand them in terms of their E and B modes contributions, their behaviour in l-space, and their intensity and polarization dependence on frequency. The primary foregrounds to be concerned with at microwave frequencies are dust emission, free-free and synchrotron radiation. There is also the question of possible polarized emission by the Earth's atmosphere. There are strong features in the atmosphere that lead to significant emission at microwave frequencies. A polarization fraction of even one part in one million would lead to an emission of 20 µK which would entirely swamp the tiny cosmological signal from the CMB. As far as it is known, the mechanism producing the highest polarization level from the Earth's atmosphere is the Zeeman splitting of oxygen lines by the Earth's ∼0.5 G magnetic field [35], but Keating [36] shows that this leads to less than 10^{-8} fractional polarization. There is also the possibility of Faraday rotation of the plane of CMB (or foreground) polarization due to the magnetic field of the Earth, but this can be shown to be less than 0.01° at frequencies above 25 GHz [37], where most CMB observations occur. So we can neglect these contributions.

1.5.1 Synchrotron

Synchrotron emission arises from interactions between cosmic ray electrons and magnetic fields B in the Galaxy. The intensity and the spectrum depend on the magnetic field strength and cosmic ray energy, and therefore they show significant spatial variations on the sky. For electrons with a power-law energy distribution $N(E) \propto E^{-p}$ the spectrum of synchrotron emission [38] becomes $T_\nu \propto B^{(p+1)/2}\nu^\beta$ with $\beta = -(p+3)/2$. A typical value of β is $\beta \simeq -3.0$ at 10 GHz frequencies. Synchrotron emission from the Galaxy dominates the foreground in the lower frequency range [39].

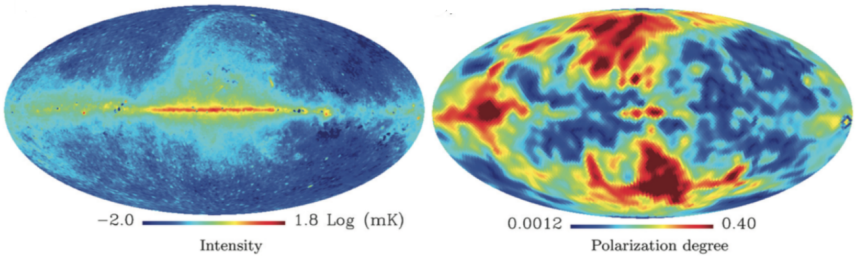

Figure 1.16: (Left) Synchrotron emission at 23 GHz in $\log_{10}$(mK) estimated in the WMAP nine-year analysis [40]. (Right) Polarization degree at 5° resolution.

The polarization degree at low Galactic latitudes may be small even if synchrotron emission is intrinsically strong there and these directions are not suitable for CMB observation anyway (Fig. 1.16) while the polarization degree can be as large as 40% at 23 GHz with higher values at higher galactic latitudes (Fig. 1.16). The larger polarization degrees at high Galactic latitudes are mostly attributed to the local structures, like the Fan region and the North Galactic Spur.

1.5.2 Free-Free

Free-free emission, also known as thermal bremsstrahlung, arises from electron–ion scattering in interstellar plasma. It is known that the emission can be traced with Hα line emission, both of which come dominantly from HII regions in the Galaxy. For optically thin plasma, the intensity of free-free emission is given by an integration along the line of sight as $I_\nu = \int j_\nu ds$, where [41]

$$j_\nu = \frac{g_{ff} Z_i^2 n_e n_i}{\sqrt{T_e}} e^{-\frac{h\nu}{kT_e}} 5.4 \times 10^{-16}\,\mathrm{Jy\,sr^{-1}\,cm^{-1}}, \tag{1.84}$$

n_e and n_i are the number densities of electrons and ions, Z_i the atomic number and $T_e \simeq 8000\,\mathrm{K}$ is the electron temperature. The Gaunt factor for free-free

emission and for our case ($h\nu \ll kT$) is approximately given by

$$g_{ff} = \frac{\sqrt{3}}{\pi}\left[\ln\frac{(2kT)^{3/2}}{\pi e\nu\sqrt{m_e}} - \frac{5\gamma}{2}\right] \tag{1.85}$$

where e is the electron charge, m_e is the electron mass and γ is the Euler constant.

Thermal free-free emission is intrinsically unpolarized because the scattering directions of electrons are isotropic and random. Magnetic fields can break the isotropy, but interstellar magnetic fields are too small to generate enough polarization at microwave frequencies. Some of the emitted photons are self-scattered by electrons through the Thomson scattering and can acquire polarization. The maximum level is $\sim 10\%$ for an optically thick cloud. Free-free emission is found to be unpolarized with an upper limit of 3.4% at the 95% confidence level [42].

1.5.3 Thermal Dust

The emission from interstellar dust in the far-infrared (FIR) to millimeter range is dominated by the emission from the biggest grains that are in thermal equilibrium with the local radiation field [43, 44]. In the optically thin limit, the emission from a uniform population of grains is well described, empirically, by a modified blackbody (MBB):

$$I_\nu = \tau_\nu B_\nu(T) \tag{1.86}$$

where I_ν is the specific intensity, B_ν is the Planck function for dust at temperature T and τ_ν is the frequency-dependent dust optical depth which is the product of dust opacity $\sigma_{e\nu}$ and gas column density $N_H : \tau_\nu = \sigma_{e\nu}N_H$. Although with an empirical fit, the best parametrization is:

$$I_\nu = \tau_n B_\nu(T_{obs})\left(\frac{\nu}{\nu_0}\right)^{\beta_{obs}} \tag{1.87}$$

where ν_0 is a reference frequency at which the optical depth τ_0 is estimated and β_{obs} would vary with frequency and/or grain size and/or grain temperature. Because at lower frequencies multicomponent models are favored, dust temperature should depend on the grain size and dust emission spectrum must be a superposition of the emissions from different size grains, therefore must vary with frequency and is not univocally determined.

Fig. 1.17 shows detailed all-sky maps of dust intensity and temperature released by Planck collaboration. Along the Galactic plane, a temperature gradient can be seen from the outer Galactic regions to the Galactic center from $T \approx 14 - 15\,\mathrm{K}$ to $19\,\mathrm{K}$.

Another problem related to the Galactic dust modelling is the subtraction of extragalactic sources, appearing as Cosmic Infrared Background (CIB). One way to subtract this contribution is to take cross correlations with the Galactic HI emission, determine the dust emissivity relative to HI column density, and read off the intercept as the offset due to the background light.

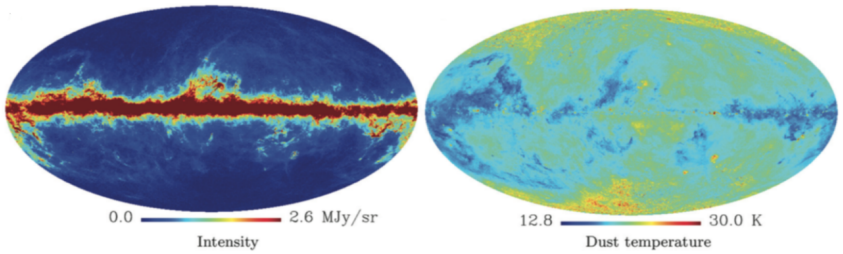

Figure 1.17: (Left) Thermal dust emission map at 353 GHz estimated by the Planck experiment. (Right) Dust temperature map estimated from modelling the IRIS 100 µm and the Planck-HFI emission at 857 GHz and 545 GHz [45].

1.6 CMB experiments

The measurements of CMB anisotropy have improved gradually from statistical samples of the microwave sky to real high resolution high sensitivity maps, first obtained by the BOOMERANG [46], MAXIMA [47], ARCHEOPS [48] and DASI [49] experiments in early 2000. These maps are analyzed and compared to models using their angular power spectrum C_ℓ. More recently the WMAP [50], SPT [51], ACT [52] experiments have provided wider maps and comprehensive measurement of the CMB power spectrum. Very recently the Planck satellite has produced a "definitive" precision measurement of CMB anisotropy [53], well extracted from the effect of local foreground emission, entering the era of *precision cosmology*.

Models of cosmic inflation predict that gravitational waves could be inferred from the polarization of the cosmic microwave background and having their origin in the early universe. Thus, the detection of B-modes supports the theory of inflation, and their strength can confirm and exclude different models of inflation.

Recent instruments of CMB experiments have sufficient sensitivity and angular resolution, so the main source of uncertainty is the contamination by foreground emissions from the Galaxy (or Earth atmosphere only for ground-based experiments), rather than instrument noise.

Synchrotron emission from the Galaxy dominates at low microwave frequencies (≤ 30 GHz) and thermal dust emission at higher frequencies (≥ 120 GHz). In the frequency range between these components, it has been argued that thermal free-free emission and non-thermal dust emission become important (Fig. 1.18). In addition, if the line of sight crosses molecular clouds or diffuse interstellar dust clouds, carbon monoxide (CO) lines starts to contaminate extremely sensitive observations like the Planck [53] ones.

Despite the importance of understanding the foregrounds, they do not represent a serious issue for observations of temperature anisotropies, because it is observationally evident that cosmological CMB photons dominate at high

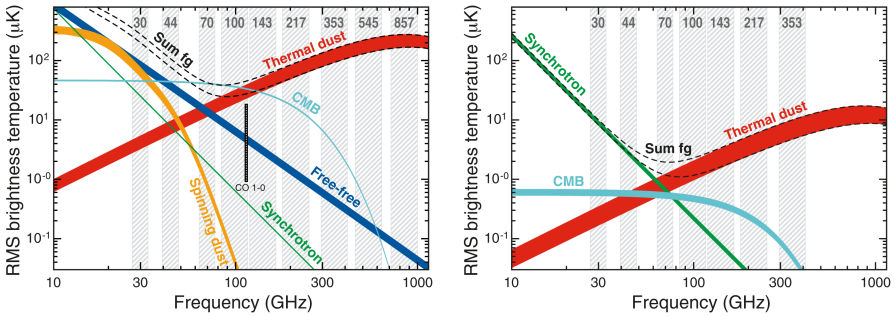

(a) Foreground emission. (b) Polarization anisotropy.

Figure 1.18: (a) Temperature anisotropy for the CMB and for sources of foreground emission. (b) Polarization anisotropy for the CMB and for main sources of foreground emission.

Galactic latitudes (Fig. 1.18a). Similar situations occur for E-mode observations, because both the foregrounds and the cosmological signal are polarized at $\sim 10\%$ levels. However, the primordial B-mode signal is expected to be $\leq 1\%$ of the foreground emission, and thus extraction of such a faint signal would be challenging. If the primordial B-mode signal turns out to be $\leq 10\%$ of the current upper limit, the Galactic foregrounds are always larger than the signal at all frequencies. Since the foreground emission is relatively smooth, it becomes more important on large angular scales. Therefore the development of foreground subtraction methods, based on data analyses at various frequencies with different frequency dependences of the astrophysical emission laws, has become increasingly more important.

Clearly, the solution to this issue is a multi-band instrument with a high number of detectors. To be foreground-limited we need to control first the efficiency of each detector (the responsivity could fluctuate or drift) and the $1/f$ noise. In order to measure the Stokes parameters Q and U with a single detector, some kind of modulation and extraction techniques of the polarized component are needed. There are several techniques to modulate polarization: rotating the instrument itself about its optical axis, specific scanning strategies, using a Stokes polarimeter with a rotating half-wave plate (see §4.1).

Current and forthcoming experiments are designed with a wide spectral coverage, thousands of detectors and a modulation technique, but each approach is quite different from the other depending on the location and the strategy. A partial list of current and planned CMB experiments is reported in Tab. **??**. This thesis is mainly focused on LSPE-SWIPE and LiteBIRD.

Experiment	**Basis**	**Location**	**Band** [GHz]	**HWP**
ABS [54]	Ground	Atacama Desert	150	Spin
Advanced ACT-Pol [52]	Ground	Atacama Desert	97, 148	Spin
BICEP3/Keck Array [55]	Ground	South Pole	95, 150, 220, 270	NO
CLASS [56]	Ground	Atacama Desert	28, 93, 148, 217	NO
EBEX [57]	Balloon	-	150, 250, 410	Spin
LiteBIRD [5]	Satellite	L2	40, 50, 60, 68, 78, 89, 100, 119, 140, 166, 195, 235, 280, 337, 402	Spin
LSPE [4]	Balloon/ Ground	-/ Tenerife	44, 90, 145, 210, 240	Spin
PIPER [58]	Balloon	-	200, 270, 350, 600	NO
POLARBEAR-2 [59]	Ground	Atacama Desert	95, 150, 220	Spin
QUBIC [60]	Ground	Puna de Atacama	$97, 150, 230$	Step
Spider [61]	Balloon	-	95, 150	Step
SPT-3G [51]	Ground	South Pole	95, 150, 220	NO

Table 1.1: Partial list of current and planned CMB experiments.

Chapter 2

The Large-Scale Polarizatin Explorer (LSPE)

The Large-Scale Polarization Explorer (LSPE) [4] is an experiment designed to measure the polarization of the CMB at large angular scales, in particular to constrain the B-modes produced by tensor perturbations. It is composed of two instruments: the ground-based telescope STRIP (Survey TeneRIfe Polarimeter) and the balloon-borne telescope SWIPE (Short Wavelength Instrument for the Polarization Explorer) which will provide high-precision complementary measurements of CMB polarization in the frequency range $44 - 240\,\mathrm{GHz}$ (Fig. 2.1).

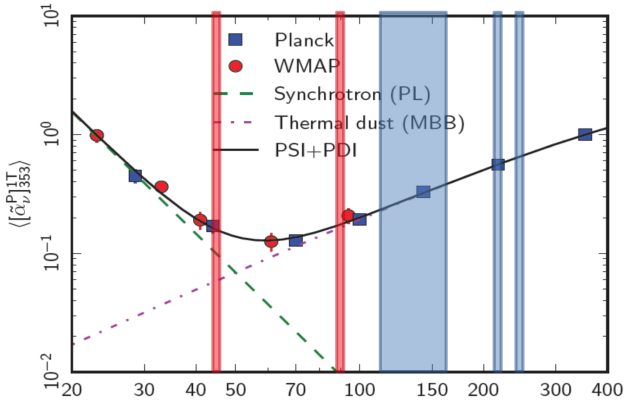

Figure 2.1: Frequency coverage of LSPE experiments: 44 GHz and 90 GHz for STRIP (red bands) and 145 GHz, 210 GHz and 240 GHz for SWIPE (blue bands).

The experiment is optimized for large angular scales and wide sky coverage. It is very challenging to measure sky polarization at these scales because the measurements require high stability of the instrument performance, stability of

the atmosphere over large volumes, and reduced, controlled telescope sidelobes over a wide range of angles. Moreover, the expected signal is very small with respect to E-modes and local foregrounds.

There is no theoretical forecast for the expected value of r, therefore it is essential to carry out pathfinder experiments, such as LSPE, before the development and the design of a third-generation space mission devoted to extremely precise measurements of the CMB polarization (see §1.6). The experiment has been designed in order to fulfill the following aspects:

- Sensitivity: greater sky survey sensitivity using arrays of photon-noise limited detectors (multimode for SWIPE §3) [62, 63]
- Systematic effects: their mitigation and control have been improved using several levels of modulation, and a polarization modulator (a HWP in the SWIPE instrument discussed in §4 and correlation radiometers in STRIP).
- Foregrounds: the frequency range covered by the two instruments brackets the region where the ratio between polarized CMB signal and polarized foregrounds is maximum. This allows us to use efficiently component separation techniques.

2.1 SWIPE observation strategy

The SWIPE payload will fly in a circumpolar long duration (15 days nominal) balloon mission during the polar night. Using the Earth as a giant solar shield, the instrument will spin in azimuth, observing a large fraction of the northern sky. The balloon will be launched from the Longyearbyen airport in Svalbard Islands at latitude 78°N. A demonstration flight was performed in 2011 and Fig. 2.2b shows the path of the test balloon, as performed by the Italian Space Agency (ASI), to test the stratospheric circulation near the North Pole. That flight was interrupted to avoid overflying over the Russian mainland, but the eastward path was demonstrated. Since then, a trajectory prediction tool has been developed and applied to historical stratospheric wind records, to obtain the trajectory of the balloon during the arctic winter. The results of these simulations show that the forecast of the tool is reliable, and that every winter there are occasions to launch LSPE-SWIPE, with optimal flight conditions for more than 2 weeks of measurements.

LSPE-SWIPE is expected to have a sky coverage of about 38% of the northern sky. On the other hand, the sky fraction observed by LSPE-STRIP depends strongly on telescope elevation as well as its sensitivity. We want at the same time to trade-off the sky coverage with the noise per pixel distribution and to maximize the overlap between the sky regions observed by the two LSPE instruments. In Figure 2.2a we represent the overlap, in ICRS (equatorial) coordinates, of the sky regions covered by SWIPE and STRIP (with zenith distance fixed to 20°).

The covered area is shown in Fig. 2.3 compared with PLANCK dust polarization map and to the area observed by BICEP [64]. The experiment spins

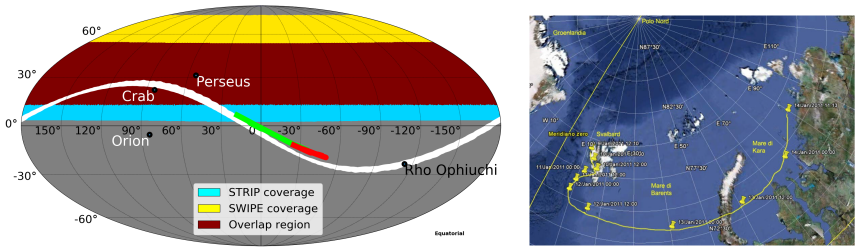

(a) SWIPE-STRIP overlap.

(b) SWIPE trajectory test flight.

Figure 2.2: (a) Map of the STRIP-SWIPE overlap when the STRIP zenith distance is set to 20°. The yellow area represents the SWIPE sky coverage, the cyan area represents the STRIP sky coverage, the dark-red area is the overlap. The maps also show the positions of the Crab and Orion nebulas, of the Perseus molecular cloud and the trajectories of Jupiter (green mark), Saturn (red mark) and the Moon (white curve). (b) Ground path of one of the test flights performed by ASI to test the stratospheric circulation near the North Pole. This flight was performed in the Arctic winter of 2011.

continuously around the local zenith axis (spin axis) at fixed angular velocity of $12.1\,\mathrm{mrad\,s^{-1}}$ to cover an altitude range from 35° to 55°, covering a large fraction of the sky in a single balloon flight

The main targets of the calibration observations (see Fig. 2.2a) are: Jupiter (the only planet with a usable signal to noise ratio) to map the main beam; the Crab Nebula (the most powerful polarized source observable at the LSPE frequencies and angular resolutions); the E-modes to calibrate the main axis of the polarimeters; the Moon to map sidelobes, and its limb can be measured to calibrate polarimeters. The Moon is observable only when it is opposite to the Sun, while Jupiter and the Crab Nebula are observable by all detectors with limited elevation changes. A fraction of time per day will be dedicated to the observation of calibration sources. The total equivalent time is one day of the mission.

The extreme environment of a polar-night stratospheric balloon flight poses important technical challenges in the areas of payload thermal management and the supply power for experiment and telemetry. During the polar night the temperature is around -80 °C and there is no solar radiation available to warm-up the payload. The most important impacts are on the electronic systems, which must be thermally insulated from the environment to achieve self-heating conditions (temperature $> -40°$). The second one regards the power requirement of SWIPE, which exceeds 700 W for 15 days. An electrical energy storage close to 1 GJ is needed. The simplest solution is to use lithium batteries, which feature high energy density and can operate in the vacuum and at very low temperatures, but still should be insulated from the external cold environment, and kept relatively warm by the heat dissipated by the instrument electronics.

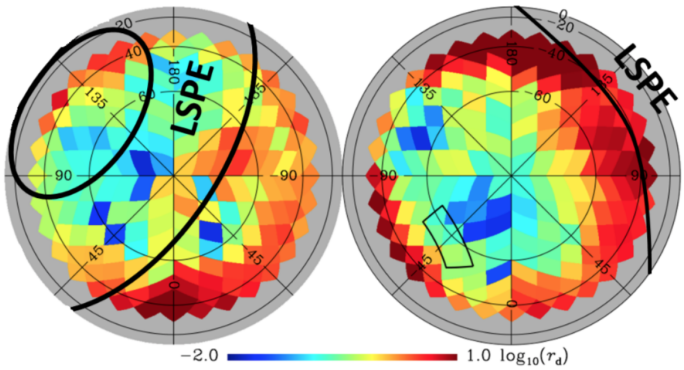

Figure 2.3: Map in orthographic projection of the 150 GHz D_l^{BB} amplitudes at $l = 80$, with l computed from the Planck 353 GHz data, extrapolated to 150 GHz, and then normalized by the CMB expectation for $r = 1$. The colors represent the estimated contamination from dust in r_d (the tensor-to-scalar ratio inferred from dust) units. The northern (southern) Galactic hemisphere is on the left (right). The small box is the area observed by BICEP while the covered area of the sky which will be scanned by LSPE is shown in thick black lines (Figure modified from [65]).

2.2 The SWIPE instrument

The main advantages of a balloon borne instrument are: almost null contribution of atmospheric noise, wide frequency coverage, large observable fraction of the sky during night-time with a stable environment and the possibility to reject ground spillover using very large ground-shields. As a matter of facts, most of the cosmological power of the LSPE comes from the SWIPE instrument, while STRIP has the very important role of low-frequency polarized foregrounds monitoring. In the following we focus on the SWIPE instrument, which is the subject of the experimental work carried out in this thesis activity. Main instrumental parameters of SWIPE are summarized in Tab. 2.1.

2.2.1 The telescope

The optical system of SWIPE has been optimized to achieve high instrumental polarization purity, which is essential for experiments aiming to constrain the B-modes signal. Moreover it is cooled cryogenically to reduce its emission on the TES detectors. The choice made is an axially symmetric refractive telescope, which has low cross-polarization ($< 0.2\%$ on axis), a controlled instrumental polarization and matches efficiently with multi-mode horns. High performances are maintained up to the edge of the field of view, that is $\pm 10^\circ$ off-axis, for all the three frequency bands, and the focal plane radius is limited by the constraint on the Strehl ratio ($> 90\%$). Regarding the off-axis pixels, the performances

	SWIPE		
Site	balloon		
Freq (GHz)	145	210	240
Bandwidth	30%	20%	10%
Angular resolution FWHM (arcmin)	85		
Detectors technology	TES multimoded		
Number of detectors $N_{\rm det}$	162	82	82
Detector NET ($\mu{\rm K}_{\rm CMB}\sqrt{\rm s}$)	12.7	15.7	30.9
Mission duration	15 days		
Duty cycle	90%		
Map sensitivity $\sigma_{Q,U}$ ($\mu{\rm K}_{\rm CMB}\cdot$ arcmin)	10	17	34

Table 2.1: SWIPE baseline instrumental parameters.

should be worse but the spurious polarization induced mainly by the off axis rays crossing the window should be small [66] and will be carefully characterized.

The optical system of SWIPE is composed by a single lens of 480 mm in diameter and a 420 mm diameter cold aperture stop, which result in an entrance pupil of 441 mm diameter. The optical ray tracing is shown in Fig. 2.4b. The lens has a maximum thickness of 62 mm and it is made of High Density Polyethylene, because it is easy to machine and has low losses in the SWIPE bands. The reflection loss is reduced by means of an antireflection coating. In conjunction with multimoded feedhorns (20 mm entrance diameter, see §3) in the focal plane, this simple telescope results in 1.5° FWHM beams in the sky, a resolution compatible with the large-scale polarization target of the instrument.

2.2.2 The cryostat

A large aluminum cryostat, installed in an aluminum gondola (Fig. 2.4a), suitable for balloon borne photometry [67] cools down the telescope and the detectors. In order to minimize the contribution to the emissivity of the system, the 600 mm diameter window has been designed in a similar way as used by the EBEX group [68]: a first thin vacuum window works at low ambient pressure ($\sim$ 3 mbar in the stratosphere) while a second movable and resealable window works at atmospheric pressure in addiction to the thinner one.

A stiff structure made of fiberglass tubes supports the toroidal ^{4}He tank, which is surrounded by two vapour cooled shields, at 170 K and 65 K. The total volume of the L^{4}He tank is approximately 250 L, the outer diameter of the system is approximately $\sim$ 140 cm, and it reaches a total height of $\sim$ 160 cm. A ^{3}He sorption fridge is used to cool-down the detectors arrays at a temperature of 0.3 K. Fig. 2.4b shows a section of the 3D SWIPE cryostat model realized using the software SOLIDWORKS, while Fig. 2.4c shows the external shell during a vacuum test. The total mass of the cryostat system, including the cold instrument, is around 300 kg.

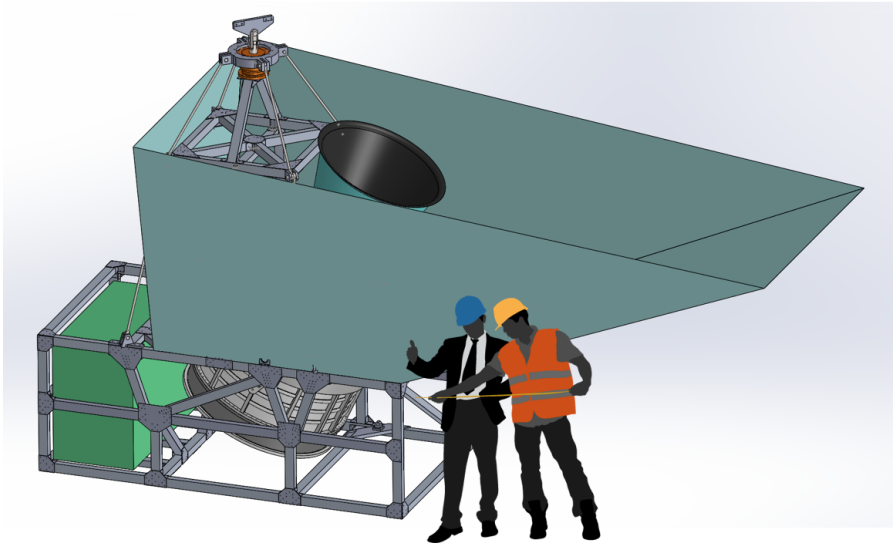

(a) SWIPE gondola.

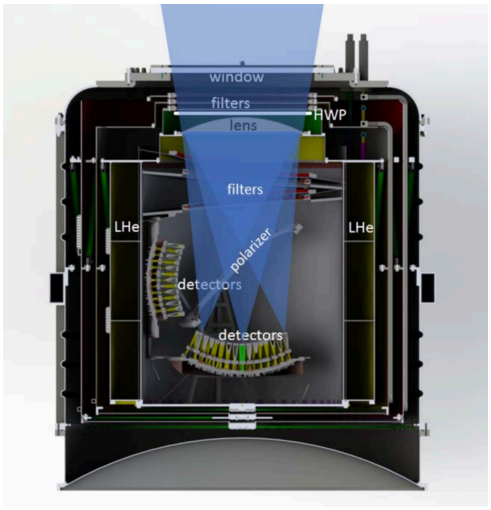

(b) Cryostat section.

(c) Cryostat external shell.

Figure 2.4: (a) SWIPE gondola design: a giant shield surrounds the cryostat; the electronics and batteries are in the same insulated box (left side). (b) Section of SWIPE cryostat with optical ray tracing. Most important elements are labelled in the figure. (c) External shell of SWIPE cryostat during vacuum test.

After the window, a sequence of three thermal mesh filters (at 170 K, 65 K and 1.6 K) reflect away the large optical load coming from the cryostat window and the external environment.

2.2.3 The polarimeter and the focal plane

The SWIPE instrument operates polarization separation before the radiation enters the detectors coupling pipeline; moreover, polarization modulation is performed before the radiation enters the telescope. In such a way the polarization properties of the antenna become irrelevant, and the polarization effects of the telescope which couples the focal plane to the sky are mitigated. This is obtained by means of a rotating half-wave plate and a large photolitographed wire-grid (500 mm in diameter) which acts as a polarization analyzer (for further details see §4). The wire-grid is titled at 45°, and splits the radiation into the two curved multi-frequency focal planes.

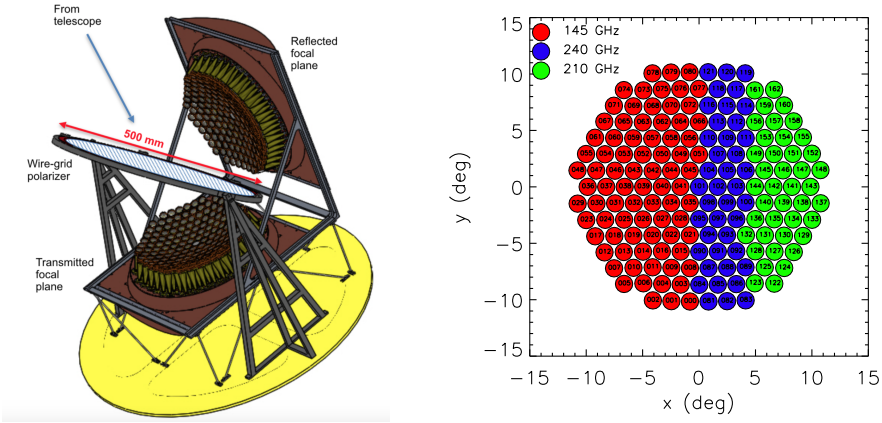

(a) Focal plane design.

(b) Pixels distribution.

Figure 2.5: (a) SWIPE transmitted and reflected focal plane with the large wire-grid polarizer. (b) Pixel distribution on each focal plane.

Fig. 2.5a shows the three-dimensional sketch of the curved focal planes of the SWIPE instrument, sustained by carbon-fiber bars. Each focal plane hosts 163 horns, for a total of 326 multi-mode pixels. Fig. 2.5b represents the position of the detectors, divided in the 3 frequency bands: 162 detectors at 145 GHz (width 30%), 82 detectors at 210 GHz (width 20%) and 82 detectors at 240 GHz (width 10%), respectively.

The horns designed for the SWIPE instrument couple efficiently with the telescope converging beam, and the dimensions of the circular waveguide allow the propagation of multi-modes beams of radiation. Moreover they ensure high suppression of stray radiation, through the incoherent superposition of the propagated modes at large angles.

The baseline detectors for the SWIPE instrument are spider-web bolometers with Transition Edge Sensors (TESs) thermistors. Thanks to the electrothermal feedback and the very light absorber, these detectors can reach very low time constants ($\sim 15 - 20\,\mathrm{ms}$), despite the larger absorber area needed to couple efficiently to a multi-mode beam [69].

The detectors (see §3) are designed to work at about 300 mK [70], with a thermal conductance of $\sim 10^{-10}\,\mathrm{W\,K^{-1}}$ and a NEP of $10^{-17}\,\mathrm{W\,Hz^{-1/2}}$ [71]. The spiderweb membrane is composed of 1 µm thick silicon nitride wires, with a mesh size of 250 µm onto which the gold absorber and the titanium/gold TES are grown. The diameter of the bolometers (8 mm) is chosen to minimize the cross section for incident cosmic rays present in the stratosphere [72], potentially very dangerous for CMB measurements. This is achieved carefully designing the spacing between the spider-web rays, which should be much greater than the wavelength of the cosmic rays. The critical superconducting transition temperatures ($\sim 550\,\mathrm{mK}$) of several devices were measured using a ^{3}He/^{4}He dilution cryostat, and all of them grouped around the working temperature, with transitions with a width of 2 mK or less.

The TES readout is performed by a 16-channel frequency-domain multiplexing (FDM). The cryogenic part of our 16-channel FDM readout chain features LC resonators composed of custom Nb superconducting inductors and SMD capacitors mounted on the boards next to the detector wafers, at 300 mK, while the SQUID board is at 1.6 K. Because of the SQUID magnetic field sensitivity, the SQUID board is enclosed in a tinned copper case to shield the residual magnetic field (see §2.2.4).

2.2.4 Magnetic shield

A key element is the ability to shield the detectors and the readout system from external magnetic field. In particular, there is the necessity to shield from static or low-frequency fields ($< 100\,\mathrm{Hz}$), indeed high-frequency fields ($> 1\,\mathrm{kHz}$) should not penetrate inside the cryostat. In order to select the right shielding factor, we have chosen to follow the prescription of SRON (Netherlands Institute for Space Research) [73] which suggests safe criteria that should be respected:

- The normal component of the static magnetic field on the TES/SQUID array should be less than $10^{-6}\,\mathrm{T}$.
- The maximum normal magnetic field noise on the focal plane array should be less than $0.2\,\mathrm{nT}/\sqrt{\mathrm{Hz}}$.

A passive shielding composed by a high-permeability material is used to block the external field thanks to the attenuation due to the skin effect and a second shield composed by superconductive materials which expels magnetic field thanks to the Meissner effect.

We simulated a high-permeability magnetic shield with the COMSOL Multiphysics software using the AC/DC module. We chose to simulate a static magnetic field which is the most suitable for studying the effect of steady or

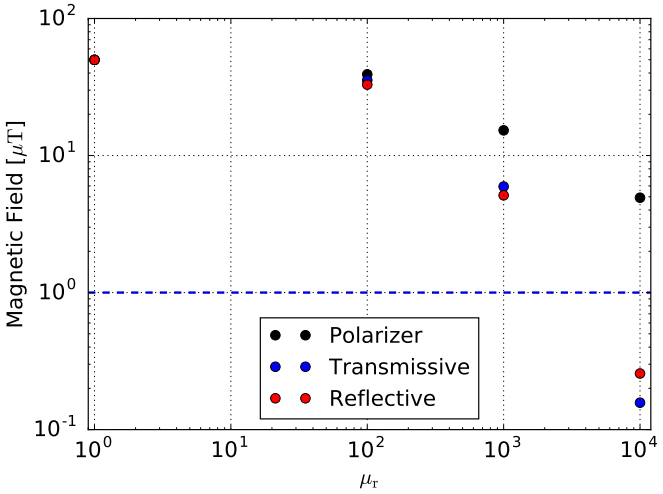

Figure 2.6: Geomagnetic field attenuated by the magnetic shield as a function of its permeability and calculated in the center of the polarizer, the trasmissive and reflective focal planes. The dotted line represents the threshold for the magnetic field on the detectors.

slowly variable magnetic field. The field considered is the geomagnetic field 5×10^{-5} T as a function of different magnetic permeability of the shield. The magnetic field is also computed in the center of the polarizer and in the center of both focal planes with a further attenuation of the superconductive shield (Fig. 2.6).

Compared to the threshold (dashed line in Fig. 2.6) the configuration with a permeability $\mu_r = 10^4$ is the most suitable one. We chose to use a 1 mm thick cyclinder as large as the Helium tank, surrounding both focal planes and made of *Cryoperm 10* which has a magnetic permeability $\mu_r > 10^4$, giving a safety margin.

The superconductive shield [74] is more complex and it will be made of copper with a thin film of tin (Fig. 2.7). This shield is composed by two different parts. The first one is a spherical cap, concentric with respect to the focal plane array, with 163 apertures, one for each horn. The diameter of the aperture is 24 mm, 1 mm more than the diameter of the external aperture of the horn. The second part is a section of a cylinder. Both parts will be screwed to the focal plane array. Moreover, in order to limit the weight of this shield it has been chosen to make both parts 1 mm thick.

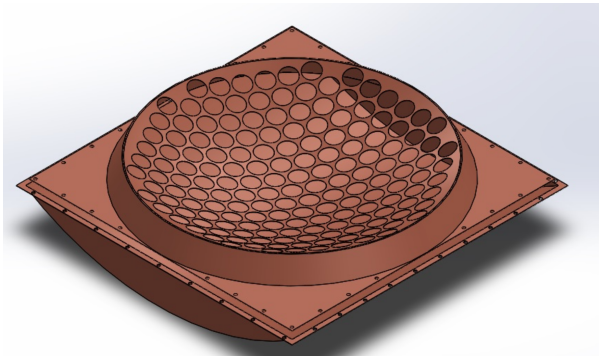

Figure 2.7: Supercondutive magnetic shield with focal plane composed by a spherical cap with 163 apertures (top) and a section of a cylinder (bottom). Both parts are 1 mm thick.

2.3 Sensitivity to tensor-to-scalar ratio

One way to assess the effectiveness of a planned CMB polarization experiment is to carry out end-to-end simulations. These include, as a first step, simulations of the time-ordered data collected by all the detectors, assuming the nominal sky observation strategy and the expected noise performance. Then, optimal maps for the Stokes parameters are built from the simulated data sets. A components separation process is carried out to extract the CMB component, and the power spectra of CMB anisotropy and polarization are estimated. Finally, the resulting power spectra are compared to a the theoretical power spectra, to estimate the values of the cosmological parameters.

The usual way to assess the effectiveness of the experiment is to give the limit on the parameter r, the tensor to scalar ratio, which is obtained as one of the outputs of the simulation process. Of course, this is only one, and arguably not the most important one, of the products of LSPE. Other important products will be the maps of the Stokes parameters at 44, 90, 145, 210, 240 GHz, featuring unprecedented sensitivity and accuracy over a wide fraction of the sky. Expecially the 240 GHz map will be quite unique, due to the difficulty to obtain these data from the ground.

This simulation activity is being carried out within the LSPE collaboration, and a summary paper is close to be released [75]. A simplified components separation has been carried out at map level, using a template fitting technique, where the 145 GHz channel is used to extract CMB polarization, while the other channels are used as foreground templates to remove the foregrounds. This approximate implementation is important to propagate the effect of detector noise from all the observation bands on the final CMB maps and power spectra.

The likelihood used in the parameter estimation is based on maps of Stokes parameters T, Q, U in `HEALPix` format. The polarization maps of the CMB component extracted by the components separation process are modelled as a

sum of CMB signal and instrumental Gaussian noise. The likelihood of obtaining the maps $\vec{m} \equiv T, Q, U$ under the hypothesis that the relevant power spectrum of the sky is C_ℓ is given by:

$$\mathcal{P}(\vec{m}|C_\ell) = \frac{1}{2\pi|\mathbf{C}(C_\ell)|^{1/2}} \exp\left(-\frac{1}{2}\vec{m}^{\mathsf{T}}\left[\mathbf{C}(C_\ell)\right]^{-1}\vec{m}\right), \tag{2.1}$$

where $\mathbf{C}$ is total covariance matrix. This is the sum of signal and noise:

$$\mathbf{C}(C_\ell) = \sum_{\ell=2}^{\ell_{\max}} \sum_{XY} \frac{2\ell+1}{4\pi} B_\ell^2 C_\ell^{XY} \mathbf{P}_\ell^{XY} + \mathbf{N}, \tag{2.2}$$

where B_ℓ is the beam window function, $\mathbf{P}_\ell^{XY}$ are the associated Legendre polynomials, and $\mathbf{N}$ is the pixel-pixel noise covariance matrix.

Assuming photon-noise limited performance and 20% sky coverage, the results of the likelihod analysis show that B-modes at a level $r = 0.01$ would be clearly detected (Fig. 2.8). This estimate does not include systematic uncertainties, and our job is to make sure that the effect of systematic errors is indeed negligible with respect to the effect of noise described above.

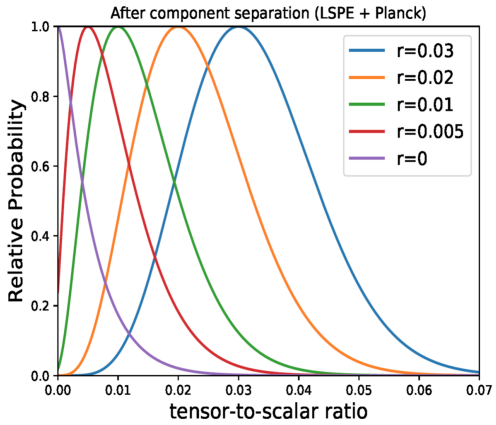

Figure 2.8: Likelihood of the detection of r at different levels.

In the following chapters, I will focus on experimental methods that I have investigated during this thesis work, exactly aimed at reducing many subtle systematic effects relevant for CMB polarization measurements.

Chapter 3

Detectors

The SWIPE instrument uses multi-mode detectors. This choice boosts the sensitivity of the instrument, at the expense of angular resolution (which is not required for a large-scale polarization survey), simplifying the readout and data processing. In this chapter we present beam pattern tests performed on the SWIPE multi-mode bolometric detector pixel assembly. In the focal plane, 20 mm aperture horns are coupled to large detector absorbers (10 mm mm diameter, see Fig. 3.1), with the TES sensor located on the side of the spider-web absorber. The pixel assembly has been checked at room temperature and tested at the bolometer base temperature of 300 mK, inside a custom cryogenic testbed, looking at a Gunn oscillator (128 GHz) located in the far field. We developed a custom cryogenic neoprene absorber, in addition to the stack of standard metal meshes low-pass filters. Such development reduced the background on the detector at a level similar to the one expected in flight, allowing to measure the main beam of the pixel assembly. The measured FWHM is 21°, slightly narrower than the one (24°) required for optimal coupling to the telescope lens, due to vignetting produced by the filters stack.

3.1 Horn and detector design

The key design guideline of SWIPE is to focus on the collection efficiency of microwave photons and on the polarization purity[70]. In order to optimize the collecting efficiency, we rely on a multi-moded coupling of the radiation to the detector. In our treatment of multi-mode systems, we assume that each of the modes transports the same fraction of the available radiative power from free space to the absorbing element of the detector, and that the individual contributions from the modes add incoherently to determine the total power collected by the system. Under these assumptions, a multi-mode system at frequency ν has a theoretical throughput, $A\Omega(\nu) = N_m(\nu)\lambda^2$, where A is the effective collection area, Ω is the effective solid angle of acceptance of the system, λ is the free-space wavelength of the photons and N_m the number of modes

collected. The signal-to-noise ratio of an individual detector scales as

$$SNR = \frac{\int B(\nu)\epsilon_{BP}(\nu)A\Omega(\nu)d\nu}{\sigma_{PNL}} \propto \langle N_m(\nu)\rangle^{1/2}, \tag{3.1}$$

where $B(\nu)A\Omega(\nu)d\nu$ is the power collected from a source of brightness B within a band $d\nu$ centered at frequency ν, ϵ_{BP} is the frequency-dependent bandpass efficiency, σ_{PNL} is the signal variance, and the brackets in the last term highlight a weighted average over the instrument passband. Therefore, an instrument with multi-moded coupling exhibits the same sensitivity per detector as N_m individual single-moded sensors, sacrificing high resolution (we obtain 1.4° FWHM, which, in our case, is perfectly adequate).

$\nu_{\rm eff}$ (GHz)	HPBW	$N_{\rm m}(\nu_{\rm eff})$	$N_{\rm m}(\nu_{\rm low})$	$N_{\rm m}(\nu_{\rm high})$	$A\Omega$ (cm^2 sr)
145	30%	13	10	17	0.56
210	20%	26	23	32	0.53
240	10%	34	32	39	0.53

Table 3.1: Basic parameters of the SWIPE pixels, including effective frequency, half-power bandwidth (HPBW), number of modes selected at the nominal frequency by the waveguide selector in the horn-cavity assembly, variation in the mode coupling at both edges of the band, and nominal system throughput.

The mode selection in the SWIPE pixels is performed by feeding radiation from a smooth conical horn into a cylindrical waveguide acting as a mode filter. A basic treatment of the cylindrical waveguide modes allows to tune the guide diameter in order to get the desired number of modes per channel. The SWIPE pixel assemblies employ 4.5 mm diameter, 10 mm long waveguides connecting the output of the horns to the tapered transition, which feeds a cylindrical cavity hosting the multi-mode absorber. With the chosen waveguide, the SWIPE detectors couple to different numbers of modes, as listed in Tab. 3.1. The characteristics of the antenna are shown in Fig. 3.1.

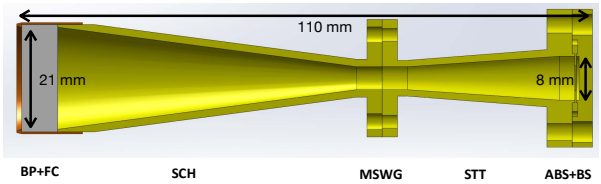

Figure 3.1: Schematic of the SWIPE pixel assembly, highlighting the bandpass filter and filter cap (BP+FC), the smooth conical horn antenna (SCH), the mode-selecting waveguide (MSWG) and the smooth tapered transition (STT) hosting the multi-mode spider-web absorber and its backshort (ABS+BS).

The multi-moded simulated beam pattern at 145 GHz (the frequency used during tests) is shown in Fig. 3.2a while Fig. 3.2b shows its cross-section. The FWHM is 20° and the working half aperture defined by the stop located just before the HWP is 30°.

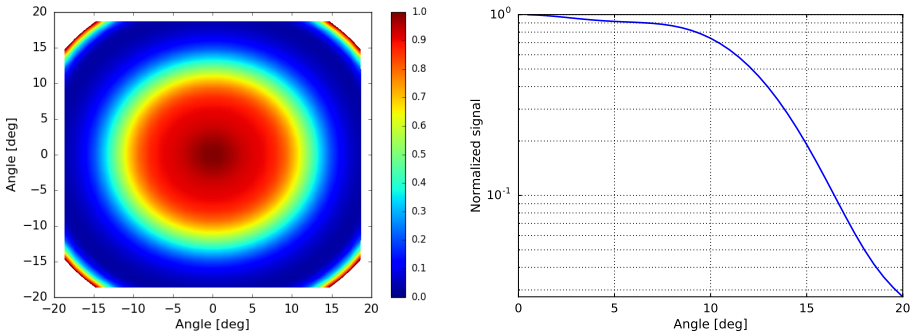

(a) Multi-moded beam pattern. (b) Beam cross section.

Figure 3.2: Simulated multi-moded beam pattern at 140 GHz (a) and its cross section (b).

The detector absorber [76] is a large (10 mm diameter) Si_3N_4 membrane with a mesh size of 250 µm, suspended with a thin legs structure (Fig. 3.3a) and designed to minimize its cross section for incident cosmic rays, which are potentially very dangerous for CMB measurements in the stratosphere. The transition-edge sensor (TES) is a Ti/Au bilayer with $T_c \sim 550$ mK (Fig. 3.3b), thermally coupled to a Bi/Au microwave absorber.

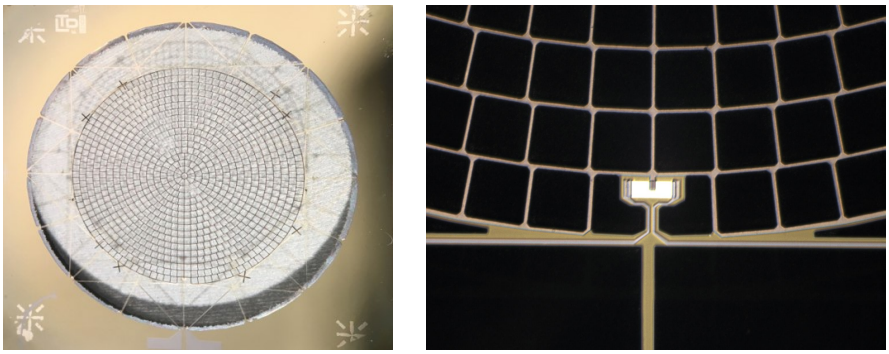

(a) Spiderweb. (b) TES.

Figure 3.3: (a) Detector absorber membrane (10 mm diameter). The detector is located in the bottom on the external ring. (b) Detail of the TES.

Near the transition temperature T_c, TES detectors exploit the sharp resistance variation of a thermistor which enables to measure extremely small

temperature variations occurring in an absorber upon absorption of a photon. Given the steepness of the R-T curve, it is convenient to introduce the logarithmic sensitivity α, defined as:

$$\alpha = \frac{d\log R}{d\log T} = \frac{T}{R}\frac{dR}{dT}. \tag{3.2}$$

The response of this kind of detector to an input power P is the result of the combined thermal and electrical interaction of different elements. Fig. 3.4 shows a scheme of both the thermal and electrical model of a TES. From the

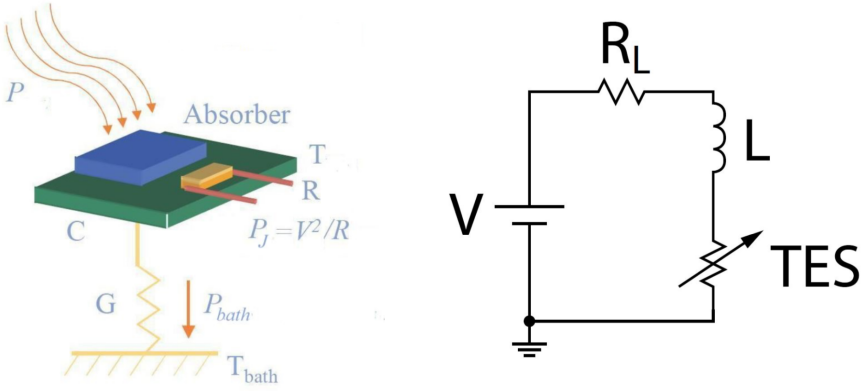

(a) Thermal model of a TES [77].

(b) Thevenin-equivalent electric circuit of a TES.

Figure 3.4: Thermal (a) and electrical (b) models of a TES.

electrical point of view the detector can be considered as a voltage-biased variable resistance R_{TES} in series with an inductance L and a load resistance R_L accounting for parasitic effects; in reality this condition is achieved by current-biasing a shunt resistance R_s in parallel with a series of R_{TES}, L and a parasitic resistance R_{PAR} (see §3.3.2). The evolution of this system is then described by two differential equations. The first one studies the thermodynamics of the system and reads:

$$C\frac{dT}{dt} = -P_{bath} + P_J + P \tag{3.3}$$

where C is the thermal capacity of the absorber, T is the temperature of the TES, P_{bath} is the cooling power of the thermal bath, P_J is the Joule power dissipated in the circuit. It is useful to define the thermal conductance of the link G as:

$$G = \frac{dP_{bath}}{dT}. \tag{3.4}$$

The second equation describes the evolution of the electrical circuit:

$$L\frac{dI}{dt} = V - IR_L + IR(T, I) \tag{3.5}$$

with V being the Thevenin-equivalent bias voltage, I the current flowing in the TES, R_L is the load resistance and $R(T, I)$ is the TES variable resistance. This two equations are coupled by the Joule power term P_J , through its dependency by $R(T, I)$. The voltage-bias condition is crucial to operate the TES in a condition of negative Electro-Thermal Feedback (ETF). Under this condition $P_J = \frac{V^2}{R}$ so, if the temperature varies by δT, the Joule dissipation decreases as:

$$\delta P_J = -\alpha P_J \frac{\delta T}{T} \tag{3.6}$$

providing a negative feedback that stabilizes the system, ensuring a constant total loading power $P_{opt} + P_J$ as the optical P_{opt} changes. For optical signals that change slowly ($\omega \ll 1/\tau$ where τ is the TES time constant), the variation in P_J will exactly compensate the changes in P_{opt}. In this strong-ETF limit, the sensitivity s results:

$$s \equiv \frac{dI}{dP_{opt}} \simeq -\frac{1}{V} \tag{3.7}$$

and the detector behaves linearly over a wide range of P_{opt} , independent of the bolometer's physical properties. The range in which the TES shows a linear response is then limited to $P_{tot} = P_{bias} + P_{opt} < P_{sat}$ where P_{sat} is the saturation power ($\sim 25\,\mathrm{pW}$ in the case of samples under testing).

3.2 Room temperature tests

In order to show that the pixel assembly optics does not introduce any beam distortion, we replaced the bolometer wafer holder with a white paper diffuser followed by a custom holder for a visible light photodiode. The system is mounted in a 2-axis rotation stage, and illuminated with a beam-expanded green light laser modulated by a mechanical chopper. The signal from the photodiode is demodulated with a lock-in and acquired versus the offset angle. The results of the measurements are reported in Fig. 3.5.

The pattern is reasonably circular and featureless, demonstrating that even in visible light the feedhorn assembly does not introduce any sharp feature or bump in the beam. Small residual asymmetries in the angular response are compatible with asymmetries in the illumination system.

Afterwards, the light photodiode was replaced with a room temperature platinum sensor (similar size of the final TES) located in the center of the final spiderweb, mounted in its holder and working in a vacuum environment. The antenna is illuminated by a 140 GHz Gunn oscillator modulated by a custom electronics and located in the antenna far field in an anechoic chamber. A beam splitter divides the emitted radiation which is monitored by means of a millimetric diode[1].Fig. 3.6 shows a sketch of the room temperature setup. The measurement has been very long due to the slow response of the detector ($\tau \sim$1-2 s). An example beam measurement is shown in Fig. 3.7.

[1] `http://www.pacificmillimeter.com/Detectors.html`

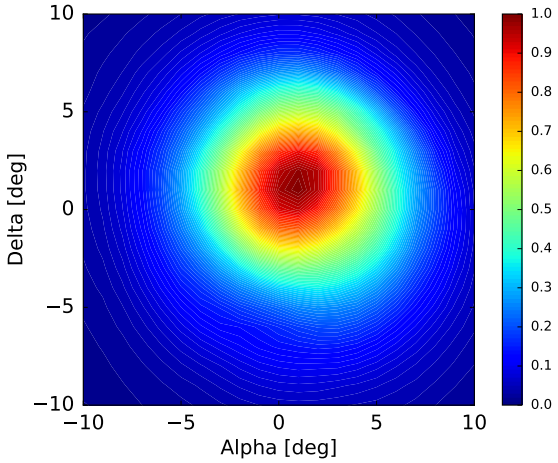

Figure 3.5: Normalized pixel assembly beam pattern obtained with a visible light source and a visible light photodiode.

Figure 3.6: Sketch of the room temperature setup. Black lines correspond to the eccosorb panels of the anechoic chamber. The pixel under testing (PUT) is illuminated by a modulated Gunn oscillator (GO) and is located in the antenna far field. A beam splitter (BS) divides the emitted radiation and the power emitted by the Gunn is monitored by means of a millimetric diode (PH).

The measured beam pattern of the entire pixel is found to be irregular, with features following the rotation of the detector around its axis and independent of the rotation of the feedhorn assembly around its optical axis. This fact points to a problem in the bolometer absorber.

One possible cause of this effect is the central position of the TES, requiring a radial signal connection on the spiderweb, breaking the azimuth symmetry of the absorber (black line in Fig. 3.7). Other possible causes of this effect could be a touch between the suspended absorber and the metal holder, or the thermal properties of the energy redistribution throughout the absorber, which are much more different at room temperature. In particular, the internal conduc-

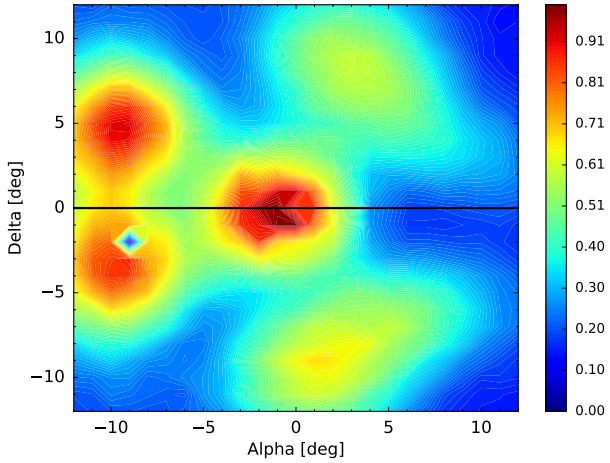

Figure 3.7: 2D beam pattern of the pixel assembly using the nominal feedhorn assembly and a platinum room bolometer located at the center of the absorber. The black line represents the thermistor tracks direction.

tivity of the absorber improves significantly at low temperature, warrantying the transport of the absorbed heat to the thermistor, without the possibility to be diverted towards the support legs and the thermal bath in a way depending on the absorbtion site.

For all these reasons we regard these results as not representative of the performance of the flight pixels. We decide to move the thermistor on the side of the absorber because the symmetry of the pattern coincides with the thermistor tracks and to improve support structure to enhance the thermal contact. However, it is not guaranteed that even in such implementation the measurements can be representative of the flight pixel operated at cryogenic temperature.

3.3 Cryogenic tests

The cryogenic measurements are more challenging than the room temperature ones because of multiple difficulties: the detector should be cooled down up to 300 mK; the background on the absorber should be reduced below the detector saturation power by means of a filter chain; the magnitude of standing waves introduced by the filters should be minimized as much as possible to neglect its impact in the beam pattern. Furthermore a detector sensitivity measurement is needed but this test is ongoing and it will not described in this thesis.

3.3.1 Testbed

The testbed used (Fig. 3.8b) is a three-stage dry cryostat composed by a pulse tube mechanical cryocooler[2] whose cold head cools down the first two stages to about 40 K and 4 K and a ^{4}He/^{3}He fridge to cool down the last stage to about 300 mK.

(a) Cryostat during tests.

(b) Overview of the cryostat.

Figure 3.8: (a) Cryostat installed on the aluminum frame looking at the Gunn oscillator (bottom) through a HR-10 Eccosorb cage. (b) Overview of the cryostat inner stages (upside down). The antenna is mounted on a copper plate on the evaporator while on the second stage is visible the SQUID series array box.

The external shield of the cryostat is made of an Al alloy similar to Al6016 (anticorodal) and provides the vacuum sealing. A 120 mm diameter and 6 mm thickness high-density-polyethylene (HDPE) window is located on the bottom of the shield. A thermal shader is mounted on internal side of the window to reject the far infrared radiation. The pulse tube (PT) cools down the first stage of the cryostat to an equilibrium temperature of ∼35 K in ∼12 h. The temperature is monitored by a DT-670 silicon diode[3] mounted on the copper plate. A low-

[2]Sumitomo Heavy Industries Ltd
[3]LakeShore Cryotronics

pass (LP) filter (cut-off frequency of $15\,\mathrm{cm}^{-1}$) is mounted on the bottom of the golden-plated cylindric aluminum shield. The second stage is cooled down to $\lesssim$ 4 K and hosts all the elements of the fridge: ^{3}He cryopump, ^{4}He cryopump, ^{3}He switch and ^{4}He switch, all monitored by DT-670 thermometers. On the bottom of the stage, a second LP filter (cut-off frequency of $12\,\mathrm{cm}^{-1}$) is mounted. The final stage is the evaporator where the detector is placed. The temperature is monitored by two thermometers optimized to operate in two different ranges: a Ruthenium oxide sensor from 4 K to 1 K and a Germanium sensor from 2 K to 0.3 K.

When the exchanger temperature goes below the ^{4}He condensation temperature, both cryopumps could be heated up. By applying a constant voltage to the heaters mounted on both cryopumps, they go up to $\sim$ 35 K. When the temperature is greater than $\sim$ 20 K the desorption of the gases starts and keeps around one hour to ensure complete desorption. After the desorption, the ^{4}He enters in thermal contact with the main plate and condenses inside the exchanger. At this point the ^{4}He heater is turned off and the relative switch turned on, connecting the main plate to the cryopump. The adsorption process causes a pressure decrease and subsequently a temperature decrease of the liquid ^{4}He, bringing the evaporator down to $\sim$0.8 K.

When a sharp drop in the CP4 temperature ($\sim$ 1 K) occurs, the grains' adsorption has been completed. At this point (usually about 5-6 h after the beginning of the cryopumping), the CP3 heater is turned off and the SW3 is closed to start pumping on the ^{3}He bath. It is mandatory to wait for the complete adsorption of ^{4}He, because otherwise its high heat capacity would waste the cooling power of the evaporating ^{3}He. The cryopumping on the ^{3}He bath brings finally the evaporator down to $\sim$ 300 mK in less than one hour: it will take about half an hour more for the detector thermalization.

In the first configuration (see §3.3.4) two neutral density filters (NDF) were mounted one at 40 K and one at 4 K while in the second one (see §3.3.5) both NDFs were removed and replaced by a neoprene absorber at 4 K and two additional filters ($10\,\mathrm{cm}^{-1}$ LP and FluoroGold) both on the same stage.

Fig. 3.9 displays the cryostat cooldown and a detail of the fridge cycle in the neoprene configuration. The typical time required to cool down the second stage is $\sim$48 h because of both thermal and optical properties of neoprene, while the evaporator temperature at equilibrium is $\sim$300 mK allowing measurements for $\sim$6-7 days.

The cryostat was installed on an aluminum (Fig. 3.8a) frame in a HR-10 Eccosorb[4] cage. The beam pattern measurements are performed by means of a tunable D-band Gunn oscillator, movable on graduated rails in an x-y plane located in the far field of the pixel assembly antenna under test (while the z axis is the optical symmetry axis of the antenna). The linear coordinates x, y were then converted to angular coordinates. The Gunn oscillator ($\sim$ 10 mW in the range 115 GHz-145 GHz) feeds a rectangular antenna (25 dB gain[5]) through

[4] `http://www.eccosorb.com/products-eccosorb-hr.htm`
[5] `http://www.aerowave.net/Catalog/28.pdf`

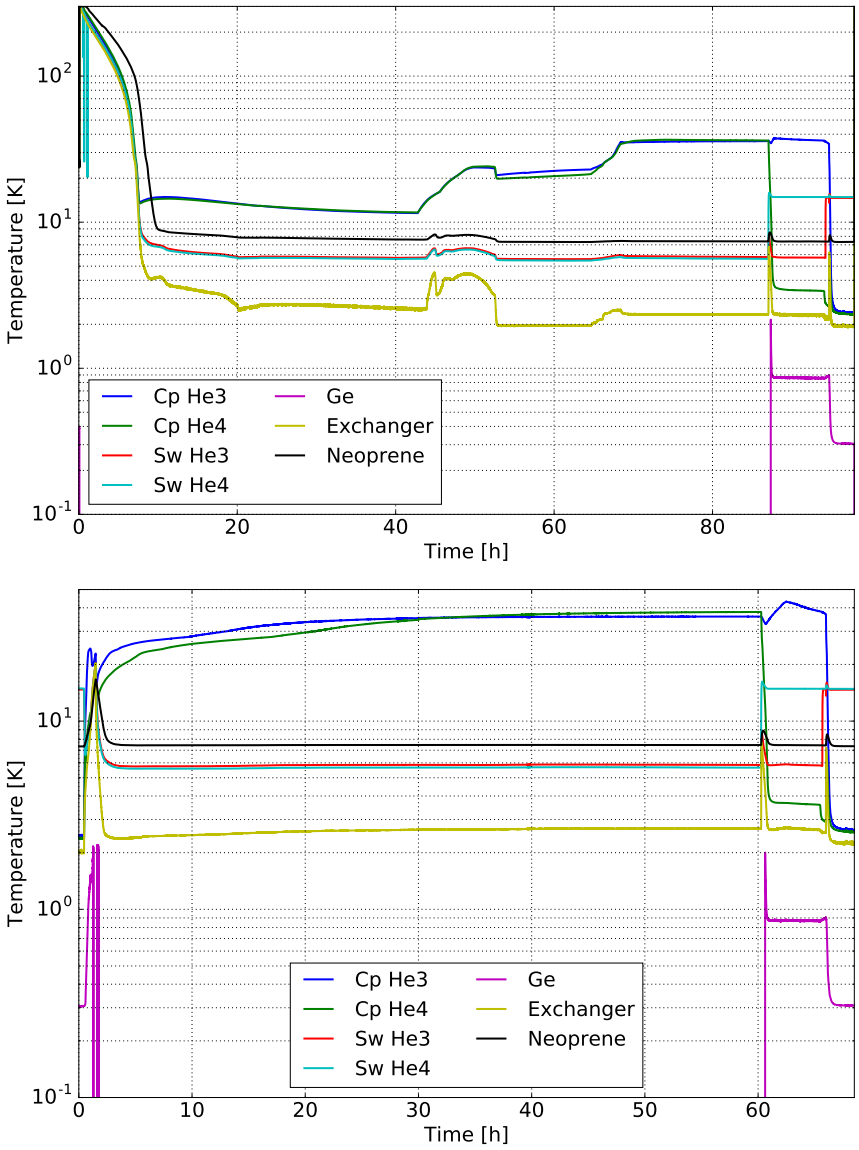

Figure 3.9: (*Top*) Temperatures of the first two stages and of the fridge during the cooldown. (*Bottom*) Detail of the fridge cycle: the cryopumps were kept at 35 K for 20 h (more than the required time of few hours) and after the closing of the ^{4}He switch the evaporator takes 7-8 h to reach 300 mK.

a variable attenuator, and is modulated according to an input reference coming from a function generator.

3.3.2 TES readout system

Close to the superconducting transition, the extremely low impedance of the TES (typically a few Ω) requires a low-impedance and low-noise amplifier in order to detect the really small currents flowing into the detector. The readout of the TESs bolometer uses an extremely sensitive magnetometer, called Superconducting Quantum Interference Device (SQUID). The SQUID used in the testbed (Fig. 3.10) is a SQUID Series Array (SSA) [78] manufactured by NIST[6]: it is composed of a chain of 100 SQUIDs installed in series that provide higher amplification of the signal by summing coherently the contribution of each SQUID.

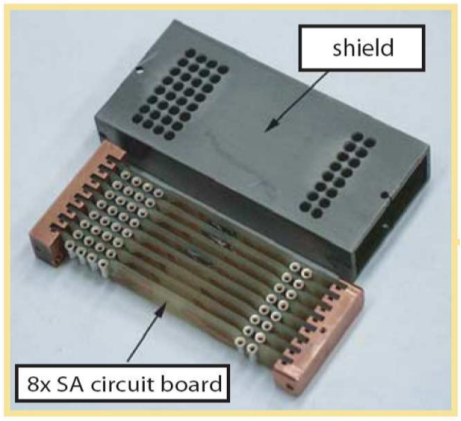

Figure 3.10: The model of Squid Series Array (SSA) built by NIST.

The SQUID is enclosed in a Nb case heat-sinked to the 4 K stage main plate: this ensures that all the magnetic field is kept outside by the Meissner effect when Nb becomes superconductor below ~ 9 K. Further shielding is provided by a layer of Cu-Sn tape and a foil of μ-metal that have been placed outside the 4 K stage shell.

Any residual magnetic field trapped within the SSA would cause the signal from each SQUID in the series array to sum incoherently with the others, resulting in a distorted $V - \Phi$ characteristic: if this is the case, it is possible to send a short current pulse to the SSA and heat it up to its transition temperature, so that the trapped field can be expelled without heating up the whole cryogenic stage.

Fig. 3.11 shows the wiring scheme of the TES/SQUID readout circuit with the relative temperature of each component. As described in the previous sec-

[6] http://cryogenics.nist.gov/

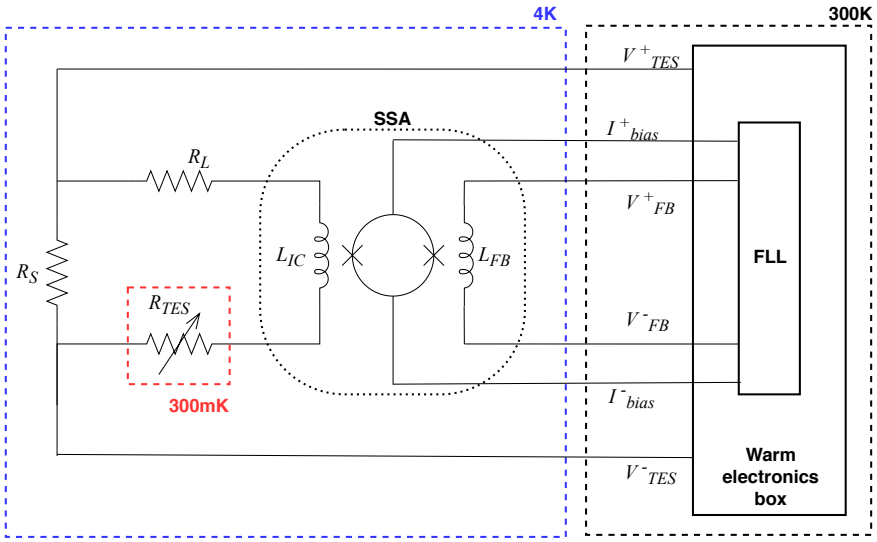

Figure 3.11: Scheme of the TES and SQUID readout circuit. For simplicity, the SQUID Series Array is represented as a single SQUID amplifier.

tion, the TES is voltage biased in order to provide a stable ETF; the voltage is supplied from the warm electronics box through ElectroMagnetic Interference (EMI) filters and via two manganin wires. The TES is represented as a variable resistor R_{TES} (12 kΩ at room temperature and ∼2 Ω after the transition) in series with the input coil L_{IC} and with the parasitic resistance R_L; these elements are in parallel with a shunt resistor R_S=20 mΩ. The TES wiring between the 4 K stage and the 300 mK evaporator is made of Nb, so that it becomes fully superconducting. The SSA assembly contains both the input and feedback coils (L_{IC}, L_{FB}); for the sake of simplicity, in Fig. 3.11 the series array of SQUIDS has been represented as just one SQUID element. Four manganin wires carry the DC bias current I_{bias} (40 µA-96 µA) and the feedback voltage V_{FB} circuit to the SSA.

The data readout system is controlled via a LabView interface: the signal first goes from the computer to a warm 12-bit Digital-Analog-Converter (DAC), located right outside the cryostat, which provides bias to TES detector and to the SQUID amplifier; the box also hosts the Flux-Locked Loop (FLL) electronics necessary for the SQUID readout. On the other way, the box splits the output signals into an analog and a digital channel: the analog signal goes to a lock-in amplifier which will demodulate the signal using the same reference of the Gunn oscillator; the digital one instead passes through a 12-bit Analog-Digital-Converter (ADC) unit and goes back to the LabView interface. The analog output channel is used to record the signal measured by the TES for different positions of the source, while the digital output channel is used to

check the SQUID performances and to easily produce time-series data of the non-modulated TES output signal.

3.3.3 Time constant

The TES time constant is one of the most important parameters for the development of the detectors because it should be enough to detect the 4 Hz modulation (1 Hz mechanical frequency) produced by the rotating HWP. This value is also necessary in order to properly tune the modulation frequency of the Gunn oscillator: a slow modulation may result in a saturation of the TES while, if the signal is modulated too fast, the detector may not detect the signal.

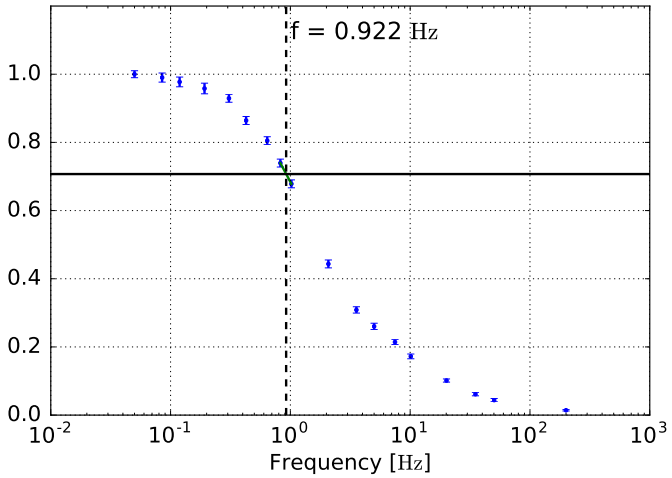

Figure 3.12: Measurement of the bolometer's time response: the data points represent the normalized voltage signal at different modulation frequencies of the source signal.

The source was placed on the optical axis and modulated at different frequencies f. Fig. 3.12 shows the TES response over a wide range of frequencies. We use the common definition of cutoff frequency f_c as the one at which the measured signal is $1/\sqrt{2}$ of its maximum value; converting to angular frequencies, the time constant will be $\tau = \frac{1}{2\pi f_c}$. We estimated that cutoff frequency of the TES prototype used in our setup is $f_c \simeq 0.922\,\text{Hz}$, resulting in a time constant $\tau = 170\,\text{ms}$.

If compared with the foreseen modulation frequency of the HWP, this time constant is too long, but it is still fine to use the TES detector for the beam characterization; an optimization of the fabrication process is currently undergoing to improve this parameter, increasing the number of supports for the spiderweb, so that the heat conductivity is increased (at constant heat capacity) and

the time constant is reduced. Moreover, the heat capacity of the absorber is being reduced using bismuth to metallize the absorber net to finally meet the requirement of $\tau = 20 - 25\,\mathrm{ms}$.

3.3.4 NDF configuration

In order to simulate the background expected on the detector during the flight ($\sim 10\,\mathrm{pW}$) [69], most of the incoming optical signal must be rejected. The most common technique consists in using a reflective neutral density filter (NDF) at room and/or cryogenic temperature. A first set of measurements was performed with a room temperature NDF located inside the cryostat (1% transmission) and a second one (0.3% transmission) mounted on the 4 K stage with the LP filter. In this configuration the background on the detector is $\ll 10\,\mathrm{pW}$ while the contribution of the Gunn is 200 nW at 128 GHz which saturates the TES response. A tunable attenuator was mounted between the Gunn and its antenna in order to reduce the power and adjust it to obtain the best signal to noise ratio.

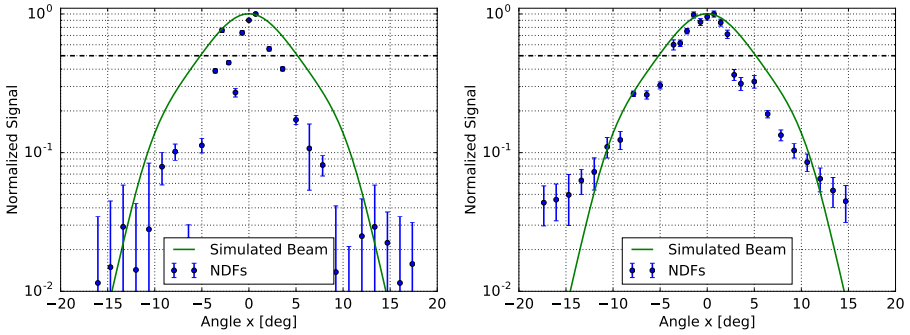

(a) Parallel NDFs configuration.

(b) Tilted NDFs configuration.

Figure 3.13: x-axis beam scan in the neutral density filters (NDFs) configuration.

Fig. 3.13a shows the x-axis beam scan in this configuration. The missing power in the main beam can be also found in the 2D map and is uncorrelated to room temperature setup systematics (e.g. eccosorb shield, diffraction on the window ring) which were deeply studied. This phenomenon is produced by the high reflectivity of NDFs which reflect back most of the radiation. Due to these reflections, using 2 parallel NDFs produces standing waves which can impact significantly on the beam pattern measurements.

The simplest way to solve this issue consists in tilting the filters, one with respect to each other, with a tilt across the filter surface of the order or larger than the test wavelength. However, in our setup, tilting the filters by few millimeters increases the distance between the horn and the window, reducing the free aperture of the system. Fig. 3.13b shows the same beam pattern of the parallel NDFs configuration. The beam has a more regular shape, still narrower

than the expected one. The beam tails are strongly affected by diffraction produced by the rings of the tilted filters stack (the 40 K filter is the aperture stop of the system).

3.3.5 Neoprene configuration

In order to effectively reduce standing waves, we selected neoprene (index of refraction $n = 2.4$) [79] as the substitute for the NDFs, due to its high absorption coefficient which allows for a total transmission comparable to the NDFs, obtained via absorbtion rather than via reflection. Using low reflectivity optical elements allows to improve the optical performance of the system reducing very significantly the standing waves. Fig. 3.14a shows the neoprene sample, while Fig. 3.14b shows its transmission as a function of its thickness, compared to the transmission produced by the two NDFs (dotted line) used in the previous configuration.

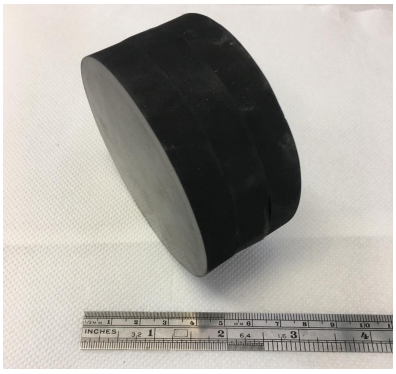

(a) Neoprene sample.

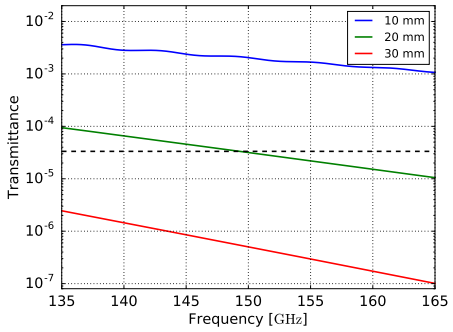

(b) Neoprene transmission.

Figure 3.14: (a) Neoprene sample installed in the cryostat without AR coating. (b) Neoprene transmission as a function of frequency and sample thickness. The dotted line corresponds to the transmission produced by two reflective neutral density filters.

The high absorption coefficient and low reflectivity of the neoprene make it a good candidate for a low-temperature optical chain. On the other hand the background produced is not negligible, and there is the difficulty of bonding it to a surface of well-defined temperature. In order to improve the thermal contact between the neoprene and the PT second stage, 3 copper braid links were added along the relative shield. In addition a $10\,\mathrm{cm}^{-1}$ LP filter was added to cut the radiative load and a FluoroGold filter to avoid radiation leaks above 1 THz.

Fig. 3.15 shows the optical setup scheme for the neoprene configuration while in the last two columns of Tab. 3.2 we report a summary of the contributions to the radiative background on the detector for both configurations, integrated

over the range of the final band-pass filter. If we also take into account that the background comes from the room temperature environment, we obtain a total background of 15 pW for the neoprene configuration and 2 pW for the NDFs configuration.

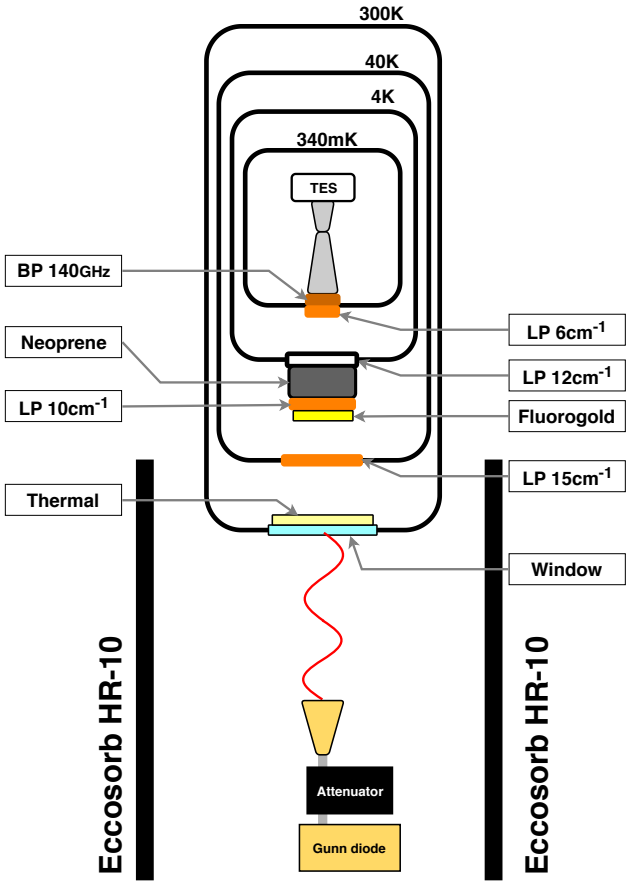

Figure 3.15: Optical setup scheme for the neoprene configuration.

Fig. 3.16 shows the measured beams in two orthogonal directions (x and y, parallel to the Gunn oscillator antenna sides, so that y corresponds to s-polarization and x corresponds to p-polarization). The simulated beam is combined with the angular response of the Gunn antenna:

$$AR_{Total}(\theta_x, \theta_y) = AR_{Gunn}(\theta_x, \theta_y) \cdot AR_{Antenna}(\theta_x, \theta_y). \tag{3.8}$$

Respect to the NDFs configuration beams, the measured beams do not present bumps or lacks of radiation and their shape is close to the expected

	T [K]	**Transm.**	**Emiss.**	**Load**	
				Neop. [pW]	**NDFs** [pW]
BP $4.7\,\mathrm{cm}^{-1}$	0.30	0.9	0.01	< 0.1	< 0.1
LP $6\,\mathrm{cm}^{-1}$	0.30	0.9	0.01	< 0.1	< 0.1
NDF	7.5	0.003	$\lesssim 0.01$	-	$\lesssim 1.2$
LP $12\,\mathrm{cm}^{-1}$	7.5	0.9	0.01	1.2	< 0.1
Neoprene	7.5	$\sim 10^{-6}$	~ 0.13	14	-
Fluorogold	7.5	0.85	0.02	< 0.1	-
LP $10\,\mathrm{cm}^{-1}$	7.5	0.95	0.01	< 0.1	-
NDF	40	0.01	< 0.01	-	< 0.1
LP $15\,\mathrm{cm}^{-1}$	40	0.95	0.01	< 0.1	< 0.1
Thermal	300	0.99	< 0.01	< 0.1	< 0.1
Window	300	~ 0.97	0.008	< 0.1	< 0.1

Table 3.2: Optical chain characteristics. In the last two columns we report a summary of the contributions to the radiative background on the detector for the neoprene and the NDFs configurations. A dash indicates the absence of the optical element in the corresponding configuration.

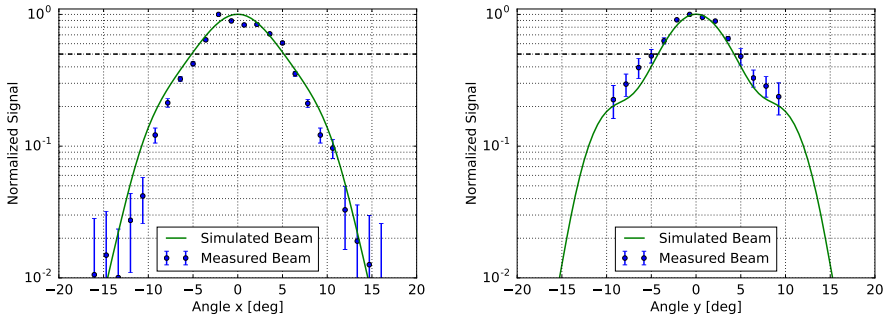

(a) x-axis beam scan (p-pol). (b) y-axis beam scan (s-pol).

Figure 3.16: Measured beam compared with the simulated beam (combined with the Gunn antenna response).

one but is not in full agreement: by using Eq. 3.8 where $AR_{Gunn}(\theta_x, \theta_y)$ is the angular response of the commercial Gunn horn, the measured antenna FWHM is 21° for the p-polarization beam, while the expected one is 24° (Fig. 6.1). A 2D beam map was performed (Fig. 3.17b) and compared with the expected one (Fig. 3.17a). The width of the main peak is similar but there are some features in the measured beam which are not expected. This discrepancy could be due to vignetting induced by the cryostat window and filters stack (geometrically seen as a ±12° stop). The issue will be solved by the measurements in the LHe SWIPE cryostat, where the 500 mm diameter aperture allows for pixel beam patterns without vignetting.

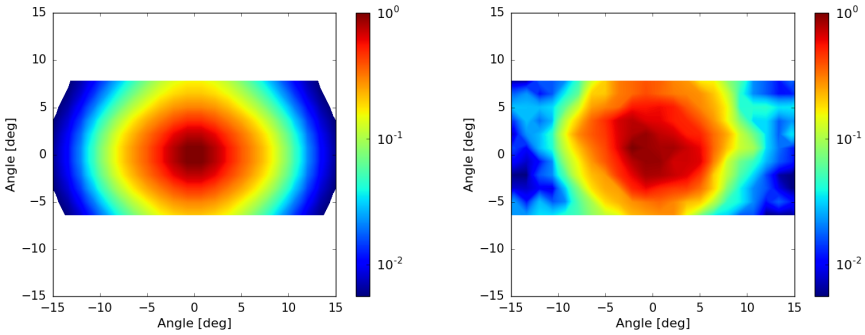

(a) Simulated beam. (b) Measured beam.

Figure 3.17: Measured beam (b) compared to the simulated beam (b) combined with the Gunn antenna response.

However, the results described here confirm the multi-mode nature of the pixel assembly by the main beam measurement which is compatible with the expected one and the goodness of the neoprene absorber, and represents and important step forward in the development of the instrument. The next step, before the final test in the SWIPE cryostat, will be a second beam pattern measurement with a faster bolometer which should reduce the fluctuation in the beam due to a possible gain drift during the scan.

Chapter 4

The Stokes polarimeter at mm wavelengths

This chapter describes the operation of a Stokes polarimeter [80, 81, 82] where the incoming radiation is analyzed by using an half-wave-plate (180° retarder, HWP) followed by a polarizer before arriving at the detector. A rotation of the half-wave plate (HWP) around the optical axis (orthogonal to the propagation of the radiation) induces a characteristic modulation if the radiation under analysis is linearly polarized, like CMB radiation. We first describe quantitatively the operation of the polarimeter, and in particular the operation of the SWIPE polarimeter. Then we investigate the main systematics induced by the presence of a rotating HWP.

4.1 Polarimeter

In order to estimate the Stokes parameters Q and U with a single detector sensitive to one of the two polarizations, some level of modulation with respect to the sky is needed. On the other hand, combining the signals coming from different detectors sensitive to orthogonal polarizations is prone to large systematic effects due to the small differences in the responses of the detectors, so we prefer to avoid it. The sky rotates by several degrees for polar balloon payload with an observing strategy similar to LSPE-SWIPE, so that provides some modulation. However, turning Q sensitivity completely into U sensitivity would require a rotation of 45°, therefore the sky scan and observation strategy need to be significantly improved using a different modulation technique. Rotating the instrument itself about its optical axis is one way to allow the same detector to measure both Q and U. A disadvantage of this technique consists in many undesired systematic effects in the instrument which rotate with the instrument and must be controlled accurately [83]. For LSPE, we chose to rotate the polarization sensitivity of the detectors using a Stokes polarimeter with a spinning HWP.

4.1.1 Stokes parameters

The polarization of light is due to the orientation of the electrical field vector. An electromagnetic wave is a three-dimensional object, it can be described by the superposition of its two orthogonal components oriented in a plane perpendicular to the propagation direction. When a beam of light propagates through space, the electric vector describes an ellipse in the wavefront plane, called *polarization ellipse*. The orientation angle is defined as the angle between the major axis of the ellipse and the x-axis, while the *ellipticity* is the ratio of the ellipse's major to minor axis. The polarization ellipse can be used only to describe completely polarized light, while usually light is either unpolarized or just partially polarized. Moreover the typical oscillation time of the electric field at optical wavelengths is $\simeq 10^{-15}$ s, not observable with current detectors. So to represent polarized light in terms of observables we must therefore use average values of the optical field, and this can be done using the *Stokes parameters*.

If we consider two monochromatic plane waves in $z = 0$ with orthogonal electric fields, we obtain:

$$E_x(t) = E_{0x}\cos(\omega t + \delta_x), \tag{4.1}$$
$$E_y(t) = E_{0y}\cos(\omega t + \delta_y), \tag{4.2}$$

where ω is the angular frequency and δ_i are the phase factors at time $t = 0$, both time-independent. By removing ωt in the equations and defining a phase delay between the two components $\delta(t) = \delta_y(t) - \delta_x(t)$, we can find the polarization ellipse:

$$\frac{E_x^2(t)}{E_{0x}^2} + \frac{E_y^2}{E_{0y}^2} - \frac{2E_x(t)E_y(t)}{E_{0x}E_{0y}}\cos\delta = \sin^2\delta. \tag{4.3}$$

Due to the short oscillation time of the electric field we must take an average over a single period of oscillation:

$$\langle E_i(t)E_j(t)\rangle = \lim_{T\to\inf}\frac{1}{T}\int_0^T E_i(t)E_j(t)dt \quad i,j = x,y \tag{4.4}$$

If we take the time average of Eq. 4.3, we obtain:

$$(E_{0x}^2 + E_{0y}^2)^2 = (E_{0x}^2 - E_{0y}^2)^2 + (2E_{0x}E_{0y}\cos\delta)^2 + (2E_{0x}E_{0y}\sin\delta)^2 \tag{4.5}$$

and now we can define the observables of the polarized field, the Stokes polarization parameters, as:

$$S_0 \equiv I \equiv \langle E_{0x}^2\rangle + \langle E_{0y}^2\rangle, \tag{4.6}$$
$$S_1 \equiv Q \equiv \langle E_{0x}^2\rangle - \langle E_{0y}^2\rangle, \tag{4.7}$$
$$S_2 \equiv U \equiv 2\langle E_{0x}E_{0y}\cos\delta\rangle, \tag{4.8}$$
$$S_3 \equiv V \equiv 2\langle E_{0x}E_{0y}\sin\delta\rangle, \tag{4.9}$$

and rewrite Eq. 4.5 as:

$$S_0^2 = S_1^2 + S_2^2 + S_3^2. \tag{4.10}$$

The parameter S_1 describes the amount of horizontal/vertical linear polarization (along the x-axis or y-axis), S_2 the amount of $\pm 45°$ linear polarization, S_3 the amount of right/left circular polarization and finally S_0 describes the total intensity of light. The Stokes parameters con be arranged in the *Stokes vector*:

$$S = \begin{pmatrix} S_0 \\ S_1 \\ S_2 \\ S_3 \end{pmatrix} = \begin{pmatrix} I \\ Q \\ U \\ V \end{pmatrix}. \tag{4.11}$$

If light is completely polarized Eq. 4.10 is valid, but in general, for partially polarized light, the relation is:

$$S_0^2 \geq S_1^2 + S_2^2 + S_3^2. \tag{4.12}$$

An other relevant parameter is the *degree of polarization* Π describing the fraction of polarized light I_{pol} with respect to the total intensity of light I_{tot}:

$$\Pi \equiv \frac{I_{pol}}{I_{tot}} = \frac{\sqrt{(S_1^2 + S_2^2 + S_3^2)}}{S_0} \tag{4.13}$$

which obviously is $\Pi = 1$ for completely polarized light and $\Pi = 0$ for unpolarized light.

4.1.2 Müller matrix

When light in arbitrary state of polarization propagates through a scattering medium or interacts with some optical element, its polarization properties are modified. The Müller formalism is required to study CMB experiments since we want to propagate partially polarized radiation through a polarimeter and extract the information about its polarization state. The *Müller matrix* M is used to describe the polarization-altering characteristics of a device which transforms an incident Stokes vector S into the exiting Stokes vector S'.

$$S' = \begin{pmatrix} S'_0 \\ S'_1 \\ S'_2 \\ S'_3 \end{pmatrix} = MS = \begin{pmatrix} m_{00} & m_{01} & m_{02} & m_{03} \\ m_{10} & m_{11} & m_{12} & m_{13} \\ m_{20} & m_{21} & m_{22} & m_{23} \\ m_{30} & m_{31} & m_{32} & m_{33} \end{pmatrix} \begin{pmatrix} S_0 \\ S_1 \\ S_2 \\ S_3 \end{pmatrix}. \tag{4.14}$$

The Müller matrix $M(k, \lambda)$ is a four-by-four matrix with real valued elements and is always a function of the direction of propagation k and wavelength λ. Moreover the Müller matrix is an appropriate formalism for characterizing polarization measurements because it contains within its elements all of the polarization properties.

We can define simply the Müller matrix of an optical element, called *polarizer*, which attenuates the orthogonal components of a light beam by introducing the coefficients p_i that relate the beam emerging from the polarizer to the incident beam:

$$E_i' = p_i E_i \qquad i = x, y, \tag{4.15}$$

where obviously $0 \leq p_i \leq 1$ and an ideal polarizer has trasmission along only one axis. Hence the Müller matrix for a polarizer [84] is:

$$M_P = \frac{1}{2}\begin{pmatrix} p_x^2 + p_y^2 & p_x^2 - p_y^2 & 0 & 0 \\ p_x^2 - p_y^2 & p_x^2 + p_y^2 & 0 & 0 \\ 0 & 0 & 2p_x p_y & 0 \\ 0 & 0 & 0 & 2p_x p_y \end{pmatrix}. \tag{4.16}$$

It is useful to redefine the vector $\vec{p} = (p_x, p_y)$ in a cylindrical coordinate system $\vec{p} = (p\cos\alpha, p\sin\alpha)$:

$$M_P(\alpha) = \frac{p^2}{2}\begin{pmatrix} 1 & \cos 2\alpha & 0 & 0 \\ \cos 2\alpha & 1 & 0 & 0 \\ 0 & 0 & \sin 2\alpha & 0 \\ 0 & 0 & 0 & \sin 2\alpha \end{pmatrix} \tag{4.17}$$

where $0^\circ \leq \alpha \leq 90^\circ$.

Finally the most general linear polarizer oriented at an angle θ is:

$$M_P(\theta) = \frac{1}{2}\begin{pmatrix} 1 & \cos 2\theta & \sin 2\theta & 0 \\ \cos 2\theta & \cos^2 2\theta & \cos 2\theta \sin 2\theta & 0 \\ \sin 2\theta & \cos 2\theta \sin 2\theta & \sin^2 2\theta & 0 \\ 0 & 0 & 0 & 0 \end{pmatrix}. \tag{4.18}$$

A *wave plate* or retarder is an optical device that alters the polarization state of a light wave travelling through it. A wave plate has a slow axis and a fast axis, both being perpendicular to the beam direction and also to each other. The phase velocity of light is slightly higher for polarization along the fast axis so it works by introducing a phase shift of ϕ between the two components of electric field. The Müller matrix for a perfect wave plate (neglecting transmission/reflection) is:

$$M_W(\phi) = \begin{pmatrix} 1 & 0 & 0 & 0 \\ 0 & 1 & 0 & 0 \\ 0 & 0 & \cos\phi & -\sin\phi \\ 0 & 0 & \sin\phi & \cos\phi \end{pmatrix}. \tag{4.19}$$

When $\phi = \frac{\pi}{2}$ the retarder is called a *quater wave plate* (QWP), while when $\phi = \pi$ the retarder is called a *half wave plate* (HWP).

Are you talking about the Muller rotation matrix or the polarization rotator device

The last useful element to understand the principle of a polarimeter is the *Müller rotation matrix*, which is an optical element that rotates the orthogonal electric field components through an angle θ. The Müller matrix for a rotator is:

$$M_R(\theta) = \begin{pmatrix} 1 & 0 & 0 & 0 \\ 0 & \cos 2\theta & \sin 2\theta & 0 \\ 0 & -\sin 2\theta & \cos 2\theta & 0 \\ 0 & 0 & 0 & 1 \end{pmatrix}. \tag{4.20}$$

4.1.3 Principle of operation of a rotating HWP

A standard wave plate can be obtained using a birefringent crystal that is cut in a disk shape, such that the ordinary and extraordinary axes lay in the plane of the disk, while the wave vector of the radiation is orthogonal to the disk, and propagates through its thickness. The phase difference ϕ between electric fields along ordinary and extraordinary axes is

$$\phi = 2\pi \frac{d(n_e - n_o)\nu}{c} \tag{4.21}$$

where d is the thickness of the wave plate, ν is the electromagnetic frequency of light, c is the speed of light and the two indices of refraction n_o and n_e are the ordinary and extraordinary indices. The general matrix of a rotated wave plate [84] is:

$$\begin{aligned} &M_{HWP}(\theta) = M_R(-\theta) M_W(\phi) M_R(\theta) = \\ &= \begin{pmatrix} 1 & 0 & 0 & 0 \\ 0 & \cos^2 2\theta + \cos\phi \sin^2 2\theta & (1-\cos\phi)\cos 2\theta \sin 2\theta & \sin 2\theta \sin\phi \\ 0 & (1-\cos\phi)\cos 2\theta \sin 2\theta & \cos\phi \cos^2 2\theta + \sin^2 2\theta & -\cos 2\theta \sin\phi \\ 0 & -\sin 2\theta \sin\phi & \cos 2\theta \sin\phi & \cos\phi \end{pmatrix} \end{aligned} \tag{4.22}$$

where θ is the angle of the fast axis. When $\phi = \pi$ the wave plate is called a HWP and hence $\Delta n = n_e - n_o = \frac{c}{2d\nu} = \frac{\lambda}{2d}$.

The Müller matrix of a rotating HWP is:

$$M_{HWP}(\theta) = M_R(-\theta) M_W(\phi = \pi) M_R(\theta) = \begin{pmatrix} 1 & 0 & 0 & 0 \\ 0 & \cos 4\theta & \sin 4\theta & 0 \\ 0 & \sin 4\theta & -\cos 4\theta & 0 \\ 0 & 0 & 0 & -1 \end{pmatrix}. \tag{4.23}$$

Hence the Stokes vector after a rotating HWP is:

$$S' = M_{HWP}(\theta)S = \begin{pmatrix} S_0 \\ S_1 \cos 4\theta + S_2 \sin 4\theta \\ S_1 \sin 4\theta - S_2 \cos 4\theta \\ -S_3 \end{pmatrix}. \tag{4.24}$$

4.1.4 SWIPE polarimeter

The SWIPE instrument is a polarimeter sensitive to linear polarization, composed of a HWP rotating at a frequency $f = 2\pi\omega = 2\pi\theta t$ followed by a steady polarizer placed in front of the detectors. By setting $p_x = 1$ and $p_y = 0$ in Eq. 4.16 we can obtain the Müller matrix of the linear polarizer:

$$M_P = \frac{1}{2}\begin{pmatrix} 1 & 1 & 0 & 0 \\ 1 & 1 & 0 & 0 \\ 0 & 0 & 0 & 0 \\ 0 & 0 & 0 & 0 \end{pmatrix}. \tag{4.25}$$

If S is the Stokes vector of the incident beam and S' the Stokes vector after the rotating HWP (Eq. 4.23), the Stokes vector S'' emerging from the polarimeter is:

$$S'' = M_P S' = \frac{1}{2}(S_0 + S_1 \cos 4\theta + S_2 \sin 4\theta)\begin{pmatrix} 1 \\ 1 \\ 0 \\ 0 \end{pmatrix} \tag{4.26}$$

and the intensity of the beam that hits the detector is:

$$I(\theta) = S_0'' = \frac{1}{2}(S_0 + S_1 \cos 4\theta + S_2 \sin 4\theta). \tag{4.27}$$

It is clear that monochromatic linearly unpolarized light passing through the polarimeter is just reduced in amplitude (by a factor 2) and emerges linearly polarized, while polarized light emerges linearly polarized but modulated at $4f$. A combination of the scanning speed of the telescope and the rotation frequency instability of the HWP, shifts the signal at the sideband of the $4f$. In this case we analyze this modulated intensity as a function of HWP angle to reconstruct the state of incoming polarized light. There are strong and multiple advantages of the rotating HWP polarimeter:

- The rotation frequency of the HWP can be chosen such that the signal frequency resides above the $1/f$ noise knee of the detector and readout system.
- The fact that the signal appears at known frequency $4f$ which is different from the rotation frequency of the HWP, providing us a strong tool to reject spurious signals with frequency $f' \neq 4f$.

- A single detector can fully reconstruct the state of incoming polarized light without the need of cross-calibrating very accurately multiple detectors.

In the next section some systematic effects due to the rotating HWP and relevant for CMB frequencies will be investigated.

4.2 Systematic effects

4.2.1 Real optical system

First of all we need a more rigorous formalism [85] to describe systematic effects. After rewriting the Stokes vector $S = (I, Q, U, V)$ and the general Müller matrix

$$M = \begin{pmatrix} m_{II} & m_{IQ} & m_{IU} & m_{IV} \\ m_{QI} & m_{QQ} & m_{QU} & m_{QV} \\ m_{UI} & m_{UQ} & m_{UU} & m_{UV} \\ m_{VI} & m_{VQ} & m_{VU} & m_{VV} \end{pmatrix} \tag{4.28}$$

we can redefine from Eq. 4.26 the total detected power P_d:

$$d = Im_{II} + Qm_{IQ} + Um_{IU} + Vm_{IV} \tag{4.29}$$

To better understand the impact of the physical inhomogeneity sources on the Müller matrix components, it is easier to start with the Jones formalism to describe the action of the optical system. The Jones matrix of a general retarder is

$$J_{ret}(f) = \begin{pmatrix} a(f) & \epsilon_1(f) \\ \epsilon_2(f) & b(f)e^{i\phi(f)} \end{pmatrix} \tag{4.30}$$

where $a(f)$, $b(f)$ and $\phi(f)$ are real and $\epsilon_1(f)$ and $\epsilon_2(f)$ are small and complex [86]. These values depend on frequency because the path length difference for polarization states traveling along the slow and fast crystal axes varies with frequency. The conversion between Müller matrix and Jones matrix is:

$$M_{ij} = \frac{1}{2} Tr(\sigma_i J \sigma_j J^\dagger) \tag{4.31}$$

where σ_i are the Pauli matrices.

For a single layer HWP, the two polarized states defined in the crystal axes cannot couple into each other, so $\epsilon_1(f) = \epsilon_2(f) = 0$. The Jones matrix becomes

$$J_{ret}(f) = \begin{pmatrix} a(f) & 0 \\ 0 & b(f)e^{i\phi(f)} \end{pmatrix} \tag{4.32}$$

and from Eq. 4.31 the Müller matrix of the retarder is

$$M_{ret}(f) = \begin{pmatrix} \frac{1}{2}(a^2+b^2) & \frac{1}{2}(a^2-b^2) & 0 & 0 \\ \frac{1}{2}(a^2-b^2) & \frac{1}{2}(a^2+b^2) & 0 & 0 \\ 0 & 0 & ab\cos(\phi) & -ab\sin(\phi) \\ 0 & 0 & ab\sin(\phi) & ab\cos(\phi) \end{pmatrix}. \tag{4.33}$$

For real Müller matrix we have to integrate against a CMB or foreground spectrum $S(f)$ and the detector passband $F_d(f)$. So the band averaged Müller matrix is

$$M_{HWP} = \frac{\int M_{ret}(f)S(f)F_d(f)df}{\int S(f)F(f)df} \tag{4.34}$$

The HWP Müller matrix can be rewritten as

$$M_{HWP} = \begin{pmatrix} T & \rho & 0 & 0 \\ \rho & T & 0 & 0 \\ 0 & 0 & c & -s \\ 0 & 0 & s & c \end{pmatrix} \tag{4.35}$$

where T, ρ, c and s can be calculated numerically from Eq. 4.34. Since the CMB is not expected to be circularly-polarized, in the case where the subsequent detector and optical system does not induce sensitivity to circular polarization the s parameter will not be relevant for CMB polarimetry.

We can turn Eq. 4.16 into the polarizer Müller matrix

$$M_{pol} = \begin{pmatrix} \frac{1}{2}(\eta^2+\delta^2) & \frac{1}{2}(\eta^2-\delta^2) & 0 & 0 \\ \frac{1}{2}(\eta^2-\delta^2) & \frac{1}{2}(\eta^2+\delta^2) & 0 & 0 \\ 0 & 0 & \eta\delta & 0 \\ 0 & 0 & 0 & \eta\delta \end{pmatrix} \tag{4.36}$$

where η and δ are the analogous of p_x and p_y introduced in Eq. 4.16.

Finally the addition of a HWP to the instrument can be modeled with the Müller matrix product

$$M = M_{pol}M_{\xi}M_{-\theta}M_{HWP}M_{\theta}M_{\xi} \tag{4.37}$$

where M_θ is the rotation matrix by the HWP angle θ_{HWP} and M_ξ is the rotation matrix by the detector orientation angle ξ_{det}, as shown in Fig. 4.1

From now on we consider only a single detector with $\xi_{det} = 0°$. The contributions of power detected (Eq. 4.29) are:

$$M_{II} = \frac{1}{2}[T(\eta^2+\delta^2) + \rho\cos(2\theta_{HWP})(\eta^2-\delta^2)], \tag{4.38}$$

$$M_{IQ} = F\sin(2\psi_{inst}) + G\cos(2\psi_{inst}), \tag{4.39}$$

$$M_{IU} = -F\sin(2\psi_{inst}) + G\cos(2\psi_{inst}), \tag{4.40}$$

$$M_{IV} = \frac{s}{2}\sin(2\theta_{HWP})(\eta^2-\delta^2) \tag{4.41}$$

where F and G are

$$F = -\frac{1}{4}(T-c)\sin(4\theta_{HWP})(\eta^2-\delta^2) - \frac{1}{2}\rho\sin(2\theta_{HWP})(\eta^2+\delta^2), \tag{4.42}$$

$$G = \frac{1}{4}[T+c+(T-c)\cos(4\theta_{HWP})](\eta^2-\delta^2) + \frac{1}{2}\rho\cos(2\theta_{HWP})(\eta^2+\delta^2). \tag{4.43}$$

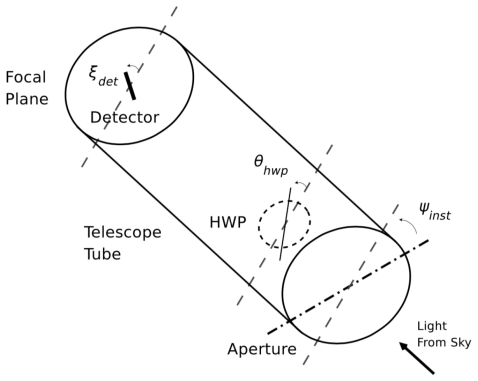

Figure 4.1: General scheme of a polarimeter. The detector angle ξ_{det} can be set to 0.

For a single-plate HWP, taking $\psi_{inst} = 0°$ and collecting the constant, $2f_{HWP}$ and $4f_{HWP}$ terms in Eq. 4.29 gives

$$\begin{aligned} d(\theta_{HWP}) =& [T\varepsilon I + \frac{1}{2}(T+c)\varepsilon\gamma Q] + [\frac{1}{2}(T-c)\varepsilon\gamma U]\sin 4\theta_{HWP} \\ &+ [\frac{1}{2}(T-c)\varepsilon\gamma Q]\cos 4\theta_{HWP} + [\rho\varepsilon\gamma I + \frac{1}{2}\rho\varepsilon Q]\cos 2\theta_{HWP} \\ &+ [s\varepsilon\gamma V + \frac{1}{2}\rho\varepsilon U]\sin 2\theta_{HWP} \end{aligned} \quad (4.44)$$

where $\varepsilon = \frac{1}{2}(\eta^2 + \delta^2)$ is the optical efficiency and $\gamma = \frac{\eta^2-\delta^2}{\eta^2+\delta^2}$ the polarization efficiency. This shows that only polarization information is contained in the $4f_{HWP}$ component of the detector timestream.

4.2.2 Step vs spin

In order to test the impact [87] of the HWP on CMB polarization measurements by SWIPE we use a simulator able to generate a realistic SWIPE scanning strategy in presence of spinning or stepped HWP. The main parameters are reported in Tab. 4.1. We complete this software with a map-making algorithm which collapses data timelines into maps.

We performed noise-free simulations of the observation of the CMB sky through the SWIPE scan strategy, to understand the effect of the application of a high-pass filter on the measured data to reconstruct the input sky map. The high-pass filter in fact is used to remove the contribution of $1/f$ noise, but also removes a fraction of the CMB sky signal.

As a first indicator, we compute the standard deviation of the difference between the output and the input maps. This provides an estimate of the quality of the reconstructed map. Fig. 4.2 shows the results as a function of

Strategy	HWP rotation [Hz]	Payload rotation [RPM]	Mission duration [days]
Step	$1.4\ 10^{-3}$	2.0	14
Spin	1.0	2.0	14

Table 4.1: Mission parameters for the scanning strategies adopted in the simulation pipeline.

the cut-off frequency of the high-pass filter (filter slope = $0.1\,\mathrm{mHz}^{-1}$). The stepped HWP case is represented by dotted lines while solid lines represent the continuously spinning HWP case.

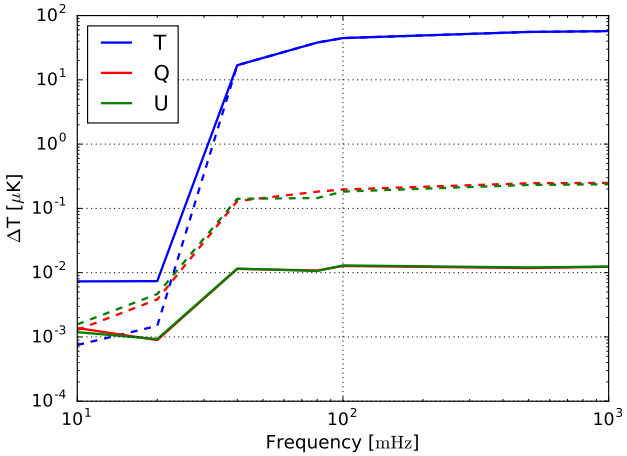

Figure 4.2: Standard deviations of the differences between the output and the input maps for T, Q and U, versus the cut-on frequency of a high-pass filter applied in the time-domain data. The smaller the standard deviation, the better the quality of the reconstruction. Solid lines correspond to spinning HWP ($f = 1\,\mathrm{Hz}$) while dashed lines correspond to stepped HWP ($f = 0.1\,\mathrm{Hz}$).

Smaller values of the standard deviation correspond to a better reconstruction of the input map. We find that cut-on frequencies higher than 10-20 mHz result in significant differences between the original and the reconstructed maps. The Q and U maps are reconstructed better for the spin case, where the standard deviation of the difference map is smaller by one order of magnitude with respect to the stepped case, for cut-on frequencies $> 30\,\mathrm{mHz}$.

Since the stepped rotation produces a modulated signal at frequencies $< 10\,\mathrm{mHz}$, the result above is already a strong indication in favour of the continuous spinning case.

The standard deviation indicator does not provide any information about the angular scales which are reconstructed better or worse. As a second, more informative indicator, we calculated the angular power spectra C_l.

We analyzed two extreme cases in opposite directions, with cut-ons at 10 mHz and at 500 mHz. Fig. 4.3a shows the reconstructed temperature power spectra (TT), compared to the power spectrum of the input map (green). We find that the TT signal is reconstructed well only for the lower cut frequency case, for both strategies. Fig. 4.3b shows the E-modes power spectra (EE): we find that with a step HWP we are able to reconstruct the spectrum if and only if the cut frequency is very low, while for the spinning case we can reconstruct the polarized signal regardless of the cut frequency.

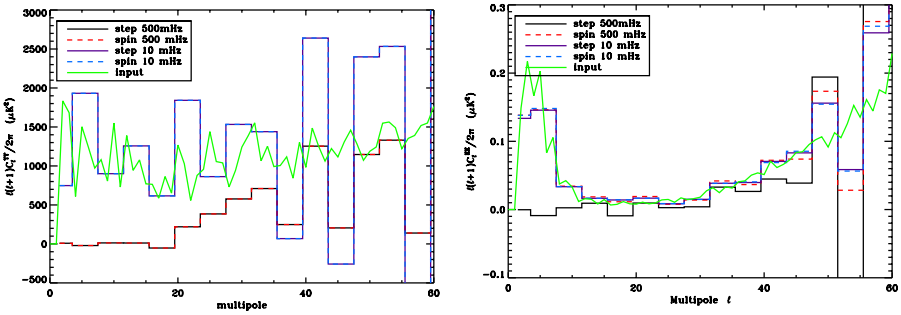

(a) TT power spectra. (b) EE power spectra.

Figure 4.3: Green lines represent the input power spectrum for TT and EE. (a) TT power spectra reconstructed better with lower cut frequency both for spin and step cases. (b) EE power spectra reconstructed well for a spin HWP independently of the cut frequency, while the step case works properly only for low cut frequency.

Figures 4.2 and 4.3 refer to unrealistic noiseless measurements. In a realistic noise scenario the most important contribution comes from $1/f$ noise, extremely high at lower frequencies. As we have just seen, with a stepped HWP configuration we have to set the cut frequency f_c <20 mHz. This means that if the knee frequency of the $1/f$ noise is comparable or higher respect to f_c, a lot of noise will contaminate our data. We conclude that a continuously spinning HWP is better suited to this kind of experiment, allowing to filter out very efficiently $1/f$ noise. In fact, in the continuously spinning HWP case, the cosmological signal is contained in a narrow band around $4f_{spin}$, allowing the use of a band-pass filter to reject all the noise outside this band.

4.2.3 HWP temperature

While a continuously rotating HWP is the best solution from the point of view of $1/f$ noise rejection, the choice of the operating temperature is not trivial. The spurious signals produced by the HWP, due to non-idealities in the HWP

itself and in the optical system of the polarimeter, is due at least in part to the emissions of the HWP and of the polarizer, which decrease with their temperature. However, the lower the temperature, the weaker the cooling power of the cryogenic system. So we need a trade-off, based on quantitative estimates.

Each detector sees the HWP as a grey-body with an emissivity $\epsilon_{HWP}(\nu)$ (assumed $\sim 3\%$ for all bands). The power load on the focal plane is:

$$P(\nu, T) = \int B(\nu, T)\, \epsilon_{HWP}(\nu)\, t_f(\nu)\, A\Omega\, d\nu \tag{4.45}$$

where $B(\nu, T)$ is the blackbody spectrum and $t_f(\nu)$ the transmission of the band-pass filters mounted on each detector. Fig. 4.4 shows the power load produced by the HWP for each band as a function of the HWP temperature. The color dashed lines correspond to the background power produced by the window ($\sim$5 pW at 145 GHz, $\sim$10 pW at 210 GHz and $\sim$10 pW at 240 GHz) which gives the greater contribution to the total power. The contribution of the HWP emission on the total power load should be as small as possible. At $\sim$10 K the power load produced by the HWP is comparable to the background power, while at 4 K or less the contribution becomes negligible.

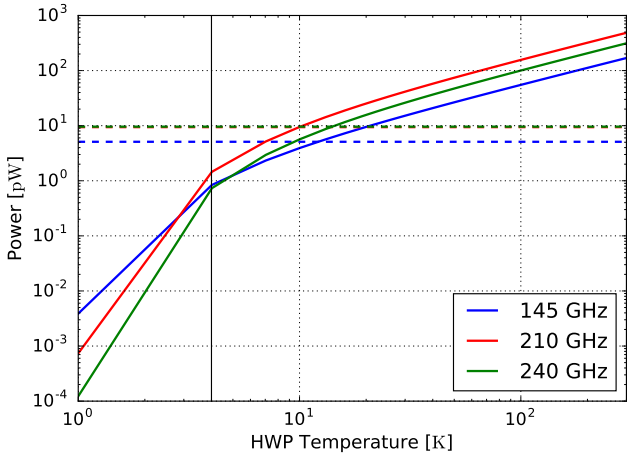

Figure 4.4: Power load produced by the HWP for each band as a function of the HWP temperature (color solid lines). The dashed lines correspond to the background power from the window. The vertical black line corresponds to the maximum temperature ($\sim$4 K) where the HWP contribution is negligible if compared with the window one.

4.2.4 Spurious signals

The most important spurious signals, in a Stokes polarimeter of this kind, come from polarized signals produced internally which can be confused with the cos-

mological signal modulated at $4f$ [88]. For a tensor to scalar ratio $r = 0.1$, the expected detected signal due to the CMB only, has a typical (rms) amplitude of about 0.7 µK. To convert the power emitted by each optical element into equivalent CMB fluctuations we use the following relation:

$$\Delta T_{CMB} = \frac{\int B(\nu, T_{opt\ elem})\, \epsilon_f(\nu)\, A\Omega\, d\nu}{\int \frac{\partial B(\nu, T_{CMB})}{\partial T}\, \epsilon_f(\nu)\, A\Omega\, d\nu} \tag{4.46}$$

Small differences in the absorption coefficient ($\sim 10^{-3}$) of the HWP produce a polarized emission; this radiation is modulated at $2f$ when is transmitted by the polarizer. This radiation could also be reflected by the polarizer, successively by the HWP and modulated at $4f$, the same frequency of the cosmological signal.

Fig. 4.5 shows the expected signals modulated at $2f$ (solid lines) and $4f$ (dashed lines). The large $2f$ contribution [89, 90] could be removed by using a high pass filter with a cut-on frequency between $2f$ and $4f$ to reject the entire spurious signal. On the other hand the $4f$ contribution could not be easily removed (a notch filter technique is under studying) but has to be carefully characterized or minimized by reducing and maintain constant the HWP temperature (the polarization modulator of SWIPE is cooled at 1.6 K).

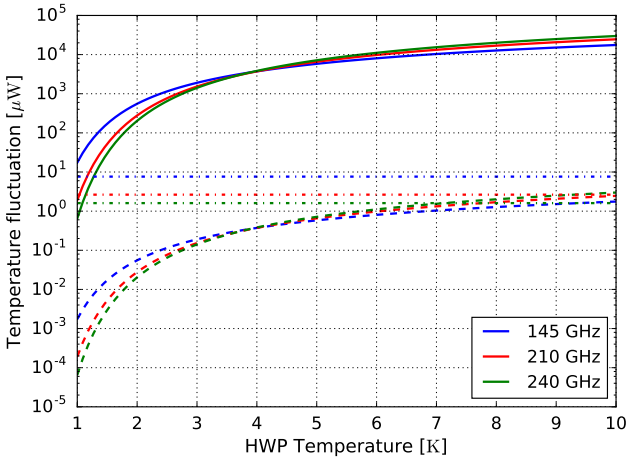

Figure 4.5: Solid lines: polarized emission of the HWP transmitted by the polarizer. Dashed lines: polarized emission of the HWP reflected by the polarizer and reflected again by the HWP. Dash-dot lines: polarized emission of the polarizer at 1.6 K reflected by the HWP.

Another critical element is the polarizer, because its linear polarized emission is reflected back by the rotating HWP (assuming the HWP to behave in reflection like a reflective-HWP), and transmitted by the polarizer itself, so that it is modulated at $4f$. If we assume 1.6 K as the temperature of the polarizer

(as in SWIPE), the signals of all three bands correspond to few µK, the same order of magnitude of the cosmological signal. Instead of the previous $4f$ signal, this one is simpler to characterize because the HWP reflectivity is basically independent of the temperature. Otherwise this spurious signal could be reduced dramatically by cooling down the polarizer below 1 K (i.e. connecting it at 0.3 K. This is not always possible due to the limited cooling power of sub-K fridges).

As we have seen, the easiest way to remove the largest $2f$ contribution is to use a band-pass filter around $4f$ to reject these spurious contributions. We studied [91] the case of a fast telescope scan speed ($12\,^\circ\,\mathrm{s}^{-1}$) as a function of HWP frequency for stepped and spinning strategy. Fig. 4.6 shows the signal power of temperature (red lines) and polarization (black lines). The temperature is strategy independent while the polarization depends drastically on the strategy. With a stepped wave-plate the signal is distributed in a wide range of frequencies but the rapid scan speed shifts the polarization signal beyond the $1/f$ knee frequency (the black vertical line at 0.1 Hz). On the contrary a continuous wave plate does not take advantage of the fast scan speed and only with a fast rotation (> 1 Hz) the signal is all beyond the knee frequency allowing to filter out the $1/f$ noise.

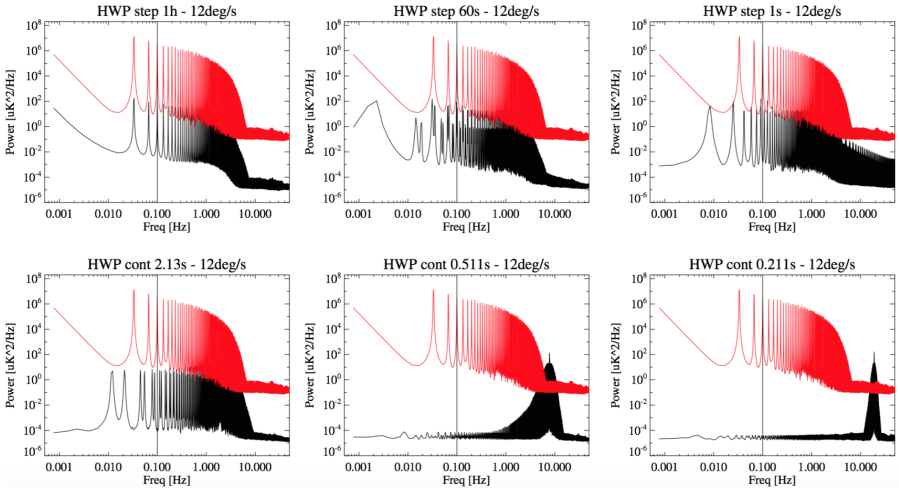

Figure 4.6: Power signal of temperature (red) and polarization (black) for a scan speed of $12\,^\circ\,\mathrm{s}^{-1}$. (Top panels) Stepped rotation every 1 h, 60 s and 1 s from left to right. (Bottom panels) Continuous rotation at ~ 0.5 Hz, ~ 2 Hz and ~ 5 Hz from left to right. (Courtesy of A. Buzzelli)

A lower scan speed of the telescope shrinks the polarization signal in a very narrow band around $4f$ allowing to remove the $2f$ component. The scan speed chosen for SWIPE payload is $f_{payload} = 2.08$ mHz. We are developing a specific pipeline to deal with any spurious term appearing at the frequency of the HWP

spin, or harmonics. This is based on application of notch filters, at the frequencies of interest. The notch filter applied at 4 times the HWP spin rate can remove some of the largest scales in the sky. This happens despite the payload spin rate is above the notch filter width. In fact, the sky signal is not exactly periodic, and part of the sky signal is spread below the spin rate frequency. This signal is recovered by a specifically designed iterative mapmaking.

4.2.5 Other effects

There are minor systematic effects produced by a rotating HWP which are minimized by a spinning modulation.

- Differential transmittance. A few per cent δ differential transmittance by the HWP of the two incoming linear polarization can be modelled using a non-ideal Jones matrix:

$$J_{HWP} = \begin{pmatrix} 1 & 0 \\ 0 & -(1+\delta) \end{pmatrix}. \tag{4.47}$$

  Propagating through the detected power, for the difference in output of the two detectors within a pixel, we find

$$d_1 - d_2 = \left[1 + \delta + \frac{\delta^2}{4}\right](Q\cos 4\phi + U \sin 4\phi) - \left[\delta + \frac{\delta^2}{2}\right] I \cos 2\phi + \frac{\delta^2}{4} Q. \tag{4.48}$$

  For reasonable values of δ ($\sim 1\%$) the mis-calibration is small and we can try to remove it during the likelihood analysis. Empirically we do not measure the power of each detector but its voltage, so the previous relation makes sense if and only if the responsivities of the two detectors are exactly the same.

- Polarized atmosphere. The $1/f$ component of the atmosphere could be polarized, so we have to add Q and U noise to the sky signal:

$$d_i = \frac{1}{2}[T + (Q + Q_i^{atms})\cos 2\phi_i + (U + U_i^{atms})\sin 2\phi_i] \tag{4.49}$$

  Both stepped and fast HWP does not remove the correlated $1/f$ atmospheric noise from the polarization analysis because it could be so strong that an extremely rapid rotation would be required. It can be removed completely by combining data from multiple detectors. At stratospheric ballon altitude the residual atmosphere is $\sim 1\%$ of the one from the ground so a continuous rotation and a data combination from different detectors allow an effective removal.

- Detector gain errors. There are two main types of gain errors. First, random errors in the gains that are constant in time and uncorrelated between detectors; second, drifts in the responsivity of each detector. The first should be removed by a good likelihood analysis in any case, but the

second is more complicated. We can have a random fluctuation around the nominal gain value with an RMS of few per cents, but in the most adverse case we can have a drift over all observation. Fast HWP modulation and low scan speed mitigate this effect because each detector observes every sky region only once (or few times) during all mission. So, during the observation of each region, the incoming signal is modulated many times and the responsivity remains mainly constant.

- Calibration errors. The typical error in calibration is a 1% gain mismatch between two detectors within each pixel. This corresponds to a $T \rightarrow Q$ leakage in the detector bias. The projection of this instrumental polarization onto the sky will therefore be suppressed if a wide range of sensitivity directions ϕ_i contribute to each sky pixel, as is the case for fast modulation. With a stepped HWP, one should be careful to design the stepping strategy because this systematic depends critically on direction and frequency of the HWP step.

4.2.6 3D formalism

In case of tilt of the HWP axis with respect to the incoming radiation beam (as is the case for peripheral pixels or for wobbling of the HWP itself), the simple Muller formalism described above is insufficient. In literature, a description of 3D extended Müller formalism is already existent [92, 93], though not yet applied to a Stokes polarimeter. Starting from 3D extended Jones matrices, the Jones matrix for an HWP with the fast axis at angle θ with respect to the horizontal axis is:

$$J_{HWP}(\theta) = \begin{bmatrix} \cos(2\theta) & \sin(2\theta) & 0 \\ \sin(2\theta) & -\cos(2\theta) & 0 \\ 0 & 0 & 1 \end{bmatrix} \tag{4.50}$$

and the matrix for a linear polarizer that transmits the horizontal component of a light beam is:

$$J_{pol} = \begin{bmatrix} 1 & 0 & 0 \\ 0 & 0 & 0 \\ 0 & 0 & 0 \end{bmatrix}. \tag{4.51}$$

From the Jones formalism, the $9x9$ Müller matrix corresponding to each optical element can be easily obtained from:

$$M_{ij} = tr(\sigma_i \cdot J \cdot \sigma_j \cdot J^{\dagger}), \tag{4.52}$$

where σ_n ($n = [0, ..., 8]$) are the trace-normalized Gell-Mann matrices 4.53:

$$\sigma_0 = \frac{1}{\sqrt{3}}\begin{bmatrix}1&0&0\\0&1&0\\0&0&1\end{bmatrix}, \quad \sigma_1 = \frac{1}{\sqrt{2}}\begin{bmatrix}0&1&0\\1&0&0\\0&0&0\end{bmatrix}, \quad \sigma_2 = \frac{1}{\sqrt{2}}\begin{bmatrix}0&0&1\\0&0&0\\1&0&0\end{bmatrix},$$
$$\sigma_3 = \frac{1}{\sqrt{2}}\begin{bmatrix}0&-i&0\\i&0&0\\0&0&0\end{bmatrix}, \quad \sigma_4 = \frac{1}{\sqrt{2}}\begin{bmatrix}1&0&0\\0&-1&0\\0&0&0\end{bmatrix}, \quad \sigma_5 = \frac{1}{\sqrt{2}}\begin{bmatrix}0&0&0\\0&0&1\\0&1&0\end{bmatrix},$$
$$\sigma_6 = \frac{1}{\sqrt{2}}\begin{bmatrix}0&0&i\\0&0&0\\-i&0&0\end{bmatrix}, \quad \sigma_7 = \frac{1}{\sqrt{2}}\begin{bmatrix}0&0&0\\0&0&-i\\0&i&0\end{bmatrix}, \quad \sigma_8 = \frac{1}{\sqrt{6}}\begin{bmatrix}1&0&0\\0&1&0\\0&0&-2\end{bmatrix} \tag{4.53}$$

By using the common polarization matrix:

$$\vec{P} = \langle \vec{E}\vec{E}^* \rangle = \begin{bmatrix}\langle E_x E_x^*\rangle & \langle E_x E_y^*\rangle & \langle E_x E_z^*\rangle \\ \langle E_y E_x^*\rangle & \langle E_y E_y^*\rangle & \langle E_y E_z^*\rangle \\ \langle E_z E_x^*\rangle & \langle E_z E_y^*\rangle & \langle E_z E_z^*\rangle\end{bmatrix}, \tag{4.54}$$

we can define the Stokes vector in the 3D formalism:

$$s = \begin{bmatrix}\Delta_0\\ \Delta_1\\ \Delta_2\\ \Delta_3\\ \Delta_4\\ \Delta_5\\ \Delta_6\\ \Delta_7\\ \Delta_8\end{bmatrix} = \begin{bmatrix}\frac{1}{\sqrt{3}}(\langle E_x E_x^*\rangle + \langle E_y E_y^*\rangle + \langle E_z E_z^*\rangle) \\ \frac{1}{\sqrt{2}}(\langle E_x E_y^*\rangle + \langle E_y E_x^*\rangle) \\ \frac{1}{\sqrt{2}}(\langle E_z E_x^*\rangle + \langle E_x E_z^*\rangle) \\ \frac{i}{\sqrt{2}}(\langle E_x E_y^*\rangle - \langle E_y E_x^*\rangle) \\ \frac{1}{\sqrt{2}}(\langle E_x E_x^*\rangle - \langle E_y E_y^*\rangle) \\ \frac{1}{\sqrt{2}}(\langle E_y E_z^*\rangle + \langle E_z E_y^*\rangle) \\ \frac{i}{\sqrt{2}}(\langle E_z E_x^*\rangle - \langle E_x E_z^*\rangle) \\ \frac{i}{\sqrt{2}}(\langle E_y E_z^*\rangle - \langle E_z E_y^*\rangle) \\ \frac{1}{\sqrt{6}}(\langle E_x E_x^*\rangle + \langle E_y E_y^*\rangle - 2\langle E_z E_z^*\rangle)\end{bmatrix}. \tag{4.55}$$

The conventional 2D Stokes parameters are related to the 3D Stokes parameters (optical ordering) by

$$T = \sqrt{\frac{2}{3}}\left(\Delta_0 + \frac{1}{\sqrt{2}}\Delta_8\right), \quad Q = \Delta_4, \quad U = \Delta_1, \quad V = \Delta_3. \tag{4.56}$$

From Eq. 4.52 we can find the analogous 3D Müller matrices for the Jones HWP matrix (Eq. 4.50) and for the Jones polarizer matrix (Eq. 4.51):

$$M_{pol\ x} = \begin{bmatrix}\frac{1}{3}&0&0&0&\frac{\sqrt{6}}{6}&0&0&0&\frac{\sqrt{2}}{6}\\ 0&0&0&0&0&0&0&0&0\\ 0&0&0&0&0&0&0&0&0\\ 0&0&0&0&0&0&0&0&0\\ \frac{\sqrt{6}}{6}&0&0&0&\frac{1}{2}&0&0&0&\frac{\sqrt{3}}{6}\\ 0&0&0&0&0&0&0&0&0\\ 0&0&0&0&0&0&0&0&0\\ 0&0&0&0&0&0&0&0&0\\ \frac{\sqrt{2}}{6}&0&0&0&\frac{\sqrt{3}}{6}&0&0&0&\frac{1}{6}\end{bmatrix}, \tag{4.57}$$

$$M_{HWP}(\theta) = \begin{bmatrix} 1 & 0 & 0 & 0 & 0 & 0 & 0 & 0 & 0 \\ 0 & -\cos(4\theta) & 0 & 0 & \sin(4\theta) & 0 & 0 & 0 & 0 \\ 0 & 0 & \cos(2\theta) & 0 & 0 & \sin(2\theta) & 0 & 0 & 0 \\ 0 & 0 & 0 & -1 & 0 & 0 & 0 & 0 & 0 \\ 0 & \sin(4\theta) & 0 & 0 & \cos(4\theta) & 0 & 0 & 0 & 0 \\ 0 & 0 & \sin(2\theta) & 0 & 0 & -\cos(2\theta) & 0 & 0 & 0 \\ 0 & 0 & 0 & 0 & 0 & 0 & \cos(2\theta) & -\sin(2\theta) & 0 \\ 0 & 0 & 0 & 0 & 0 & 0 & -\sin(2\theta) & -\cos(2\theta) & 0 \\ 0 & 0 & 0 & 0 & 0 & 0 & 0 & 0 & 1 \end{bmatrix}, \tag{4.58}$$

and by combining the previous matrices we can find the 3D polarimeter Stokes vector ($\eta = \xi = 0°$):

$$s_{out} = M_{pol\ x} \cdot M_{HWP}(\theta) \cdot s_{in} = M_{pol\ x} \cdot M_{HWP}(\theta) \cdot \begin{bmatrix} \Delta_0 \\ \Delta_1 \\ \Delta_2 \\ \Delta_3 \\ \Delta_4 \\ \Delta_5 \\ \Delta_6 \\ \Delta_7 \\ \Delta_8 \end{bmatrix} =$$

$$= \begin{bmatrix} \frac{1}{3}\Delta_0 + \frac{\sqrt{6}}{6}\sin(4\theta)\Delta_1 + \frac{\sqrt{6}}{6}\cos(4\theta)\Delta_4 + \frac{\sqrt{2}}{6}\Delta_8 \\ 0 \\ 0 \\ 0 \\ \frac{\sqrt{6}}{6}\Delta_0 + \frac{1}{2}\sin(4\theta)\Delta_1 + \frac{1}{2}\cos(4\theta)\Delta_4 + \frac{\sqrt{3}}{6}\Delta_8 \\ 0 \\ 0 \\ 0 \\ \frac{\sqrt{2}}{6}\Delta_0 + \frac{\sqrt{3}}{6}\sin(4\theta)\Delta_1 + \frac{\sqrt{3}}{6}\cos(4\theta)\Delta_4 + \frac{1}{6}\Delta_8 \end{bmatrix}. \tag{4.59}$$

Thanks to Eq. 4.56 we can derive the intensity:

$$I = \frac{T}{2} + \frac{Q}{2}\cos(4\theta) + \frac{U}{2}\sin(4\theta). \tag{4.60}$$

Note that the Eq. 4.60 is the common equation of a Stokes polarimeter.

4.2.7 HWP wobbling

One of the spurious signal arising from a rotating HWP is induced by possible wobbling of the rotor. Because a cryogenic fast rotation of the HWP can be performed only by using a magnetic bearing, this kind of system could be affected by a tilt of the HWP (i.e. small misalignment in the initial position, see §5 for further details). This effect has to be studied deeply because can induce a leakage from temperature to polarization.

We approximate the HWP as a cylindrically symmetric rigid body, like a coin, and we define a reference system $\hat{x}$-$\hat{y}$-$\hat{z}$ with the $\hat{x}$-$\hat{y}$ plane coincident with the base of the cylinder, see Fig. 4.7.

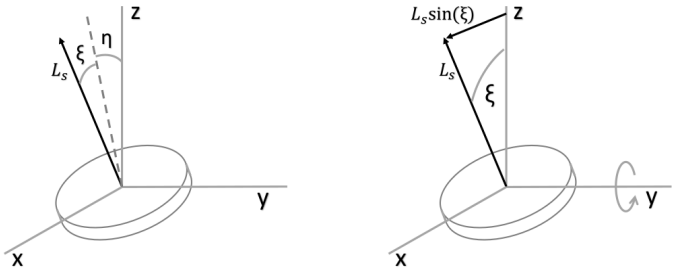

Figure 4.7: Illustration of rigid body precession where we can see the angular momentum dislocations respect to the $\hat{x}$ and $\hat{y}$ axes.

We hypothesize that the HWP has a large spin angular momentum $L_s = I_s\omega_s$ along the symmetry axis, where I_s and ω_s are respectively the moment of inertia and the angular velocity. In the unperturbed case L_s coincides with the $\hat{z}$ axis. The contribution to L_x due to the rotation about the x-axis is $L_x = \frac{d(I_{xx}\eta)}{dt} = I_{xx}\frac{d\eta}{dt}$. We can treat I_{xx} as a constant since moments of inertia about the principal axes are constant for small angular displacements. In addition, the rotation about the y-axis contributes to L_x by giving a component $L_s\sin(\xi)$ on the x-axis. Combining such contributions we get:

$$\begin{aligned} L_x &= I_{xx}\frac{d\eta}{dt} + L_s\sin(\xi)\ , \\ L_y &= I_{yy}\frac{d\xi}{dt} - L_s\sin(\eta). \end{aligned} \tag{4.61}$$

Since $I_{xx} = I_{yy} = I_\perp$ and exploring small angle first order approximation Equations 4.61 read:

$$\begin{aligned} L_x &= I_\perp\frac{d\eta}{dt} + L_s\xi\ , \\ L_y &= I_\perp\frac{d\xi}{dt} - L_s\eta. \end{aligned} \tag{4.62}$$

Furthermore, thanks to the same approximation $L_z = I_s\omega_s$. Since we are considering a torque-free system ($dL/dt = 0$), both L_s and ω_s are constant leading to:

$$\begin{aligned} I_\perp\frac{d^2\eta}{dt^2} + L_s\frac{d\xi}{dt} &= 0\ , \\ I_\perp\frac{d^2\xi}{dt^2} - L_s\frac{d\eta}{dt} &= 0. \end{aligned} \tag{4.63}$$

By introducing $\omega_x = \frac{d\eta}{dt}$ and $\omega_y = \frac{d\xi}{dt}$ Eq. 4.63 become:

$$\begin{aligned} I_\perp \frac{d\omega_x}{dt} + L_s\omega_y &= 0\ , \\ I_\perp \frac{d\omega_y}{dt} - L_s\omega_x &= 0. \end{aligned} \tag{4.64}$$

In order to solve this coupled system of differential equations we can differentiate one and substitute the other:

$$\frac{d^2\omega_x}{dt^2} + \gamma^2\omega_x = 0 \quad \text{with} \quad \gamma = \frac{L_s}{I_\perp} = \omega_s\frac{I_s}{I_\perp}\ . \tag{4.65}$$

The solution for the harmonic motion is (with A and ϕ arbitrary constants):

$$\omega_x = A\sin(\gamma t + \phi)\ . \tag{4.66}$$

While for ω_y we get:

$$\omega_y = -\frac{I_\perp}{L_s}\frac{d\omega_x}{dt} = -\frac{I_\perp}{I_s\omega_s}A\gamma\cos(\gamma t + \phi) = -A\cos(\gamma t + \phi)\ . \tag{4.67}$$

Integrating ω_x and ω_y we obtain:

$$\eta = -\frac{A}{\gamma}\cos(\gamma t + \phi) + \theta_{x_0}\ , \tag{4.68}$$

$$\xi = -\frac{A}{\gamma}\sin(\gamma t + \phi) + \theta_{y_0}\ . \tag{4.69}$$

In the small angle approximation we impose that $A/\gamma \ll 1$. Such equations reveal that the spin axis rotates around a fixed direction in space. If that direction is along the z-axis then $\theta_{x0} = \theta_{y0} = 0$. Assuming the initial conditions $\eta(t=0) = \theta_0$ and $\xi(t=0) = 0$, and assuming that $A/\gamma = \theta_0$ we get:

$$\eta = \theta_0\cos(\gamma t)\ , \tag{4.70}$$

$$\xi = \theta_0\sin(\gamma t)\ . \tag{4.71}$$

The last equations describe the torque-free precession of the spin axis that rotates in space at a fixed angle θ_0 respect to the z-axis with a frequency of the precession motion given by $\gamma = \omega_s I_s/I_\perp$ [94].
Considering a thin disc we get $I_s = 2I_\perp$ and so $\gamma = 2\omega_s$, thus the disc wobbles twice as fast as it spins.

Finally the apparent rate of a thin disc precession to an observer on the rigid body is:

$$\gamma' = \gamma - \omega_s = \omega_s(\frac{I_s - I_\perp}{I_\perp}) \sim \omega_s \tag{4.72}$$

In a torque-free precession we can identify two different rotations accordingly to the reference frame we consider. In the fixed laboratory frame, the angular velocity vector rotates around the fixed $\hat{z}$ axis (where the angular momentum vector lies), tracing the so-called "space cone". In the reference frame integral with the rotating body, we can see both angular momentum and angular velocity vector describing a circle around the symmetry axis of the cylinder, tracing the so-called "body cone" with a precession rate γ'.

For a wobbling HWP we need to calculate the Müller rotation matrices from Eq. 4.52:

$$M_{RotX}(\eta) = \begin{bmatrix} 1 & 0 & 0 & 0 & 0 & 0 & 0 & 0 & 0 \\ 0 & \cos(\eta) & 0 & 0 & 0 & \sin(\eta) & 0 & 0 & 0 \\ 0 & 0 & \cos(2\eta) & 0 & -\frac{1}{2}\sin(2\eta) & 0 & 0 & 0 & -\frac{\sqrt{3}}{2}\sin(2\eta) \\ 0 & 0 & 0 & \cos(\eta) & 0 & 0 & 0 & -\sin(\eta) & 0 \\ 0 & 0 & \frac{1}{2}\sin(2\eta) & 0 & \frac{1}{2}\cos^2(\eta)+\frac{1}{2} & 0 & 0 & 0 & -\frac{\sqrt{3}}{2}\sin^2(\eta) \\ 0 & -\sin(\eta) & 0 & 0 & 0 & \cos(\eta) & 0 & 0 & 0 \\ 0 & 0 & 0 & 0 & 0 & 0 & 1 & 0 & 0 \\ 0 & 0 & 0 & \sin(\eta) & 0 & 0 & 0 & \cos(\eta) & 0 \\ 0 & 0 & \frac{\sqrt{3}}{2}\sin(2\eta) & 0 & -\frac{\sqrt{3}}{2}\sin^2(\eta) & 0 & 0 & 0 & -\frac{3}{2}\sin^2(\eta)+1 \end{bmatrix}, \tag{4.73}$$

$$M_{RotY}(\xi) = \begin{bmatrix} 1 & 0 & 0 & 0 & 0 & 0 & 0 & 0 & 0 \\ 0 & \cos(\xi) & -\sin(\xi) & 0 & 0 & 0 & 0 & 0 & 0 \\ 0 & \sin(\xi) & \cos(\xi) & 0 & 0 & 0 & 0 & 0 & 0 \\ 0 & 0 & 0 & \cos(\xi) & 0 & 0 & -\sin(\xi) & 0 & 0 \\ 0 & 0 & 0 & 0 & \frac{1}{2}\cos^2(\xi)+\frac{1}{2} & \frac{1}{2}\sin(2\xi) & 0 & 0 & \frac{\sqrt{3}}{2}\sin^2(\xi) \\ 0 & 0 & 0 & 0 & -\frac{1}{2}\sin(2\xi) & \cos(2\xi) & 0 & 0 & \frac{\sqrt{3}}{2}\sin(2\xi) \\ 0 & 0 & 0 & \sin(\xi) & 0 & 0 & \cos(\xi) & 0 & 0 \\ 0 & 0 & 0 & 0 & 0 & 0 & 0 & 1 & 0 \\ 0 & 0 & 0 & 0 & \frac{\sqrt{3}}{2}\sin^2(\xi) & -\frac{\sqrt{3}}{2}\sin(2\xi) & 0 & 0 & -\frac{3}{2}\sin^2(\xi)+1 \end{bmatrix}. \tag{4.74}$$

And finally we can calculate the 3D Müller matrix for a Stokes polarimeter with a wobbling HWP:

$$M_{SP_{wob}} = M_{polx} \cdot M^{-1}_{RotY}(\xi) \cdot M^{-1}_{RotX}(\eta) \cdot M_{HWP}(\theta) \cdot M_{RotX}(\eta) \cdot M_{RotY}(\xi) =$$

$$= \begin{bmatrix} \frac{1}{3} & m_{01} & m_{02} & 0 & m_{04} & m_{05} & 0 & 0 & m_{08} \\ 0 & 0 & 0 & 0 & 0 & 0 & 0 & 0 & 0 \\ 0 & 0 & 0 & 0 & 0 & 0 & 0 & 0 & 0 \\ 0 & 0 & 0 & 0 & 0 & 0 & 0 & 0 & 0 \\ \frac{\sqrt{6}}{6} & \frac{\sqrt{6}}{2}m_{01} & \frac{\sqrt{6}}{2}m_{02} & 0 & \frac{\sqrt{6}}{2}m_{04} & \frac{\sqrt{6}}{2}m_{05} & 0 & 0 & \frac{\sqrt{6}}{2}m_{08} \\ 0 & 0 & 0 & 0 & 0 & 0 & 0 & 0 & 0 \\ 0 & 0 & 0 & 0 & 0 & 0 & 0 & 0 & 0 \\ 0 & 0 & 0 & 0 & 0 & 0 & 0 & 0 & 0 \\ \frac{\sqrt{2}}{6} & \frac{\sqrt{2}}{2}m_{01} & \frac{\sqrt{2}}{2}m_{02} & 0 & \frac{\sqrt{2}}{2}m_{04} & \frac{\sqrt{2}}{2}m_{05} & 0 & 0 & \frac{\sqrt{2}}{2}m_{08} \end{bmatrix}. \tag{4.75}$$

For the sake of clarity we define the following equations we will use from now on:

$$A = \sin^2(\eta)\sin^2(\xi) + \sin^2(\xi) - 1, \tag{4.76}$$
$$B = \sin(\eta)\sin(2\xi), \tag{4.77}$$
$$C = \sin(2\eta)\sin^2(\xi), \tag{4.78}$$
$$D = \sin(2\xi)\cos(\eta), \tag{4.79}$$
$$E = 3\sin^2(\eta)\sin^2(\xi) - 3\sin^2(\xi) + 1, \tag{4.80}$$

$$\begin{aligned} m_{01} = \frac{\sqrt{6}}{12}(&E\sin(2\eta)\sin(\xi) - 2(A\sin(4\theta) + B\cos(4\theta))\cos(\eta)\cos(\xi) \\ &-(-A\cos(4\theta) + B\sin(4\theta))\sin(2\eta)\sin(\xi) \\ &-2(C\sin(2\theta) + D\cos(2\theta))\sin(\eta)\cos(\xi) \\ &-2(C\cos(2\theta) - D\sin(2\theta))\sin(\xi)\cos(2\eta)) \end{aligned}$$

$$\begin{aligned} m_{02} = \frac{\sqrt{6}}{12}(&E\sin(2\xi)\cos^2(\eta) + 2(A\sin(4\theta) + B\cos(4\theta))\sin(\eta)\cos(2\xi) \\ &-\frac{1}{2}(A\cos(4\theta) - B\sin(4\theta))(3 - \cos(2\eta))\sin(2\xi) \\ &-2(C\sin(2\theta) + D\cos(2\theta))\cos(\eta)\cos(2\xi) \\ &+(C\cos(2\theta) - D\sin(2\theta))\sin(2\eta)\sin(2\xi)) \end{aligned}$$

$$\begin{aligned} m_{04} = \frac{\sqrt{6}}{12}(&E\left(\cos^2(\eta)\cos^2(\xi) - 2\cos^2(\eta) + 1\right) - \\ &(A\sin(4\theta) + B\cos(4\theta))\sin(\eta)\sin(2\xi) \\ &-(A\cos(4\theta) - B\sin(4\theta))\left(2\cos^2(\eta) + 2\cos^2(\xi) - \cos^2(\eta)\cos^2(\xi) - 1\right) + \\ &(C\sin(2\theta) + D\cos(2\theta))\sin(2\xi)\cos(\eta) \\ &+\frac{1}{2}(C\cos(2\theta) - D\sin(2\theta))(\cos(2\xi) - 3)\sin(2\eta)) \end{aligned}$$

$$\begin{aligned} m_{05} = \frac{\sqrt{6}}{12}(&-E\sin(2\eta)\cos(\xi) - 2(A\sin(4\theta) + B\cos(4\theta))\sin(\xi)\cos(\eta) + \\ &(-A\cos(4\theta) + B\sin(4\theta))\sin(2\eta)\cos(\xi) - \\ &2(C\sin(2\theta) + D\cos(2\theta))\sin(\eta)\sin(\xi) \\ &+2(C\cos(2\theta) - D\sin(2\theta))\cos(2\eta)\cos(\xi)) \end{aligned}$$

$$m_{08} = \frac{\sqrt{2}}{4}(E\left(\cos^2(\eta)\cos^2(\xi) - \frac{1}{3}\right) - (A\sin(4\theta) + B\cos(4\theta))\sin(\eta)\sin(2\xi) \\ - (A\cos(4\theta) - B\sin(4\theta))\left(2(\cos^2(\xi) - \cos^2(\eta)) - 1\right) \\ + (C\sin(2\theta) + D\cos(2\theta))\sin(2\xi)\cos(\eta) \\ + (C\cos(2\theta) - D\sin(2\theta))\sin(2\eta)\cos^2(\xi))$$

By assuming the field entering the polarimeter has $E_z = 0$, this is true only for the on-axis detectors and for all the focal plane assuming a telecentric optic system, we can find the general Stokes vector for a wobbling HWP:

$$s_{out} = M_{SP_{wob}} \cdot s_{in} = M_{SP_{wob}} \cdot \begin{bmatrix} \Delta_0 \\ \Delta_1 \\ 0 \\ 0 \\ \Delta_4 \\ 0 \\ 0 \\ 0 \\ \Delta_8 \end{bmatrix} = M_{SP_{wob}} \cdot \begin{bmatrix} \Delta_0 \\ \Delta_1 \\ 0 \\ 0 \\ \Delta_4 \\ 0 \\ 0 \\ 0 \\ \frac{1}{\sqrt{2}}\Delta_0 \end{bmatrix} = \\ = \begin{bmatrix} \frac{1}{3}\Delta_0 + m_{01}\Delta_1 + m_{04}\Delta_4 + m_{08}\frac{1}{\sqrt{2}}\Delta_0 \\ 0 \\ 0 \\ 0 \\ \frac{\sqrt{6}}{6}\Delta_0 + \frac{\sqrt{6}}{2}\left(m_{01}\Delta_1 + m_{04}\Delta_4 + m_{08}\frac{1}{\sqrt{2}}\Delta_0\right) \\ 0 \\ 0 \\ 0 \\ \frac{\sqrt{2}}{6}\Delta_0 + \frac{\sqrt{2}}{2}\left(m_{01}\Delta_1 + m_{04}\Delta_4 + m_{08}\frac{1}{\sqrt{2}}\Delta_0\right) \end{bmatrix}, \tag{4.81}$$

where we used $\Delta_8 = \frac{1}{\sqrt{2}}\Delta_0$, and thanks to Eq. 4.56 the equivalent intensity:

$$I = \left(\frac{1}{3} + \frac{\sqrt{2}}{2}m_{08}\right)T + \frac{\sqrt{6}}{2}m_{01}U + \frac{\sqrt{6}}{2}m_{04}Q. \tag{4.82}$$

Note that the components of the output Stokes vector which are not null (Eq. 4.81) are Δ'_0, Δ'_4, Δ'_8, so from the definition of the Stokes vector (Eq. 4.55) it is clearly $E_z^{out} = 0$. This happens because the polarizing grid does not permit $E_z^{out} \neq 0$ for on-axis rays. If we loose this assumption (i.e. for an off-axis detector) it is easy to verify that the output Stokes vector becomes a function of Δ_0, Δ_1, Δ_2, Δ_4, Δ_5, Δ_8, but the components of the output Stokes vector which are not null are always Δ'_0, Δ'_4, Δ'_8 (Eq. 4.83).

$$s_{out} = M_{SP_{wob}} \cdot s_{in} = M_{SP_{wob}} \cdot \begin{bmatrix} \Delta_0 \\ \Delta_1 \\ \Delta_2 \\ \Delta_3 \\ \Delta_4 \\ \Delta_5 \\ \Delta_6 \\ \Delta_7 \\ \Delta_8 \end{bmatrix} =$$

$$\begin{bmatrix} \frac{1}{3}\Delta_0 + m_{01}\Delta_1 + m_{02}\Delta_2 + m_{04}\Delta_4 + m_{05}\Delta_5 + m_{08}\Delta_8 \\ 0 \\ 0 \\ 0 \\ \frac{\sqrt{6}}{6}\Delta_0 + \frac{\sqrt{6}}{2}\left(m_{01}\Delta_1 + m_{02}\Delta_2 + m_{04}\Delta_4 + m_{05}\Delta_5 + m_{08}\Delta_8\right) \\ 0 \\ 0 \\ 0 \\ \frac{\sqrt{2}}{6}\Delta_0 + \frac{\sqrt{2}}{2}\left(m_{01}\Delta_1 + m_{02}\Delta_2 + m_{04}\Delta_4 + m_{05}\Delta_5 + m_{08}\Delta_8\right) \end{bmatrix}. \quad (4.83)$$

For a cylindrical HWP, including its support, with mass m, thickness h and radius R, the components of the moment of inertia respect to the principal axes are:

$$I_s = \frac{1}{2}mR^2; \quad (4.84)$$

$$I_\perp = \frac{1}{12}m\left(3R^2 + h^2\right), \quad (4.85)$$

where we are assuming a diagonal inertia tensor:

$$\mathbf{I} = \begin{bmatrix} I_\perp & 0 & 0 \\ 0 & I_\perp & 0 \\ 0 & 0 & I_s \end{bmatrix}. \quad (4.86)$$

The frequency for the precessional motion is directly linked to the HWP regular spin frequency f_s and to the ratio $I_\perp/I_s$ (Eq. 4.65).

We can note that this ratio depends only on the cylinder height and radius as:

$$I_\perp/I_s = 0.5 + \frac{1}{6}\left(\frac{h}{R}\right)^2. \quad (4.87)$$

We therefore explore different configurations as shown in Figure 4.8 where we show the fractional residual with respect to the ideal case. We consider input radiation horizontally polarized, a precession angle $\theta_0 = 1^\circ$, spin frequencies $f_s = [0.1, 0.5, 1.0, 2.0]$ Hz and $I_\perp/I_s = [0.501, 0.502, 0.506, 0.513]$. As an example, these values for the $I_\perp/I_s$ ratio correspond to an HWP with mass $m = 1\,\mathrm{kg}$,

radius $R = 16\,\mathrm{cm}$, and thickness $h \simeq [1.2, 1.7, 3.0, 4.5]$ cm; then I_s is fixed to $0.0128\,\mathrm{kg\,m^2}$. In practice the ratio of the components of the moment of inertia does not depend only on the plate thickness, but also on the structure of the HWP support.

The Fig. 4.8 shows the dependence of the effect from the HWP spinning speed and the inertia tensor: the simulation shows that a thinner HWP, $I_\perp/I_s \to 0.500$, has beats in the Intensity over an extended period while a thicker one has shorter beats. It is clear by looking the Fig. 4.8 from top to bottom. Anyway the value 0.5 is not possible since it corresponds to a null thickness.

The effect of different spinning speeds is to compress the beats. This is clear by looking the Fig. 4.8 from left to right. The maximum amplitude remains the same because it depends only on θ_0 that is fixed to 1° in this particular simulation.

In Fig. 4.9 we report the power spectra of the timelines for different ratios $I_\perp/I_s$. The spectra exhibit the effect discussed above, showing that the beats frequency moves to lower values as the ratio $I_\perp/I_s$ is reduced towards the minimum value of 0.5 (for $I_\perp/I_s = 0.513$ the period of the beats is 10 s, corresponding to a peak in the spectrum at 0.1 Hz).

In order to test the impact of the HWP precessional motion on CMB observations we build an algorithm able to generate a realistic satellite scanning strategy in presence of spinning HWP, producing data timelines. We complete this software with a map-making algorithm which collapses data timelines into maps. All simulations are noise-free, to better capture the impact of systematic effects.

The scan simulator takes as inputs the details of a Satellite scanning strategy, three spin rates and two angles (see [95] for a detailed description of the geometrical configuration), namely:

- Earth revolution velocity ω_1,
- precession velocity ω_2,
- satellite spin ω_3,
- precession angle α, i.e. the angle between the satellite spin axis and the sun-earth direction,
- boresight angle β, i.e. the angle between the focal plane direction and the spin axis.

We simulate only a single detector placed at the centre of the focal plane illuminating a spinning HWP with f_s frequency. The systematic affecting the HWP is included in the data at the timeline level and a simple re-binning map-making is used to average all the samples in T, Q, U Stokes parameters maps [96]. In this analysis we consider *Planck* , WMAP *COrE* and LiteBIRD [97] scanning strategies. The input parameters we employ for those scanning strategies are listed in Tab. 4.2. As sampling rate we use 60 Hz.

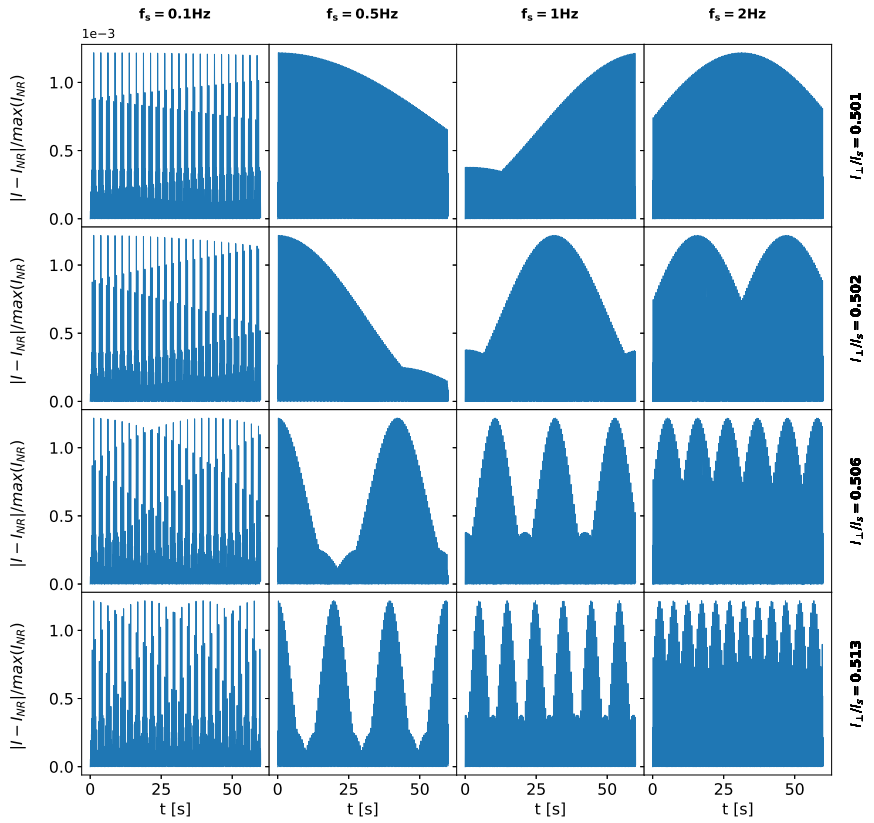

Figure 4.8: Fractional residual for different ratios $I_\perp/I_s$ and different HWP spinning frequencies. Each column shows a different f_s value while each row a different $I_\perp/I_s$ ratio. Note that a thinner HWP, $I_\perp/I_s \to 0.500$, has beats in the Intensity over an extended period while a thicker one has shorter beats. By looking the Figure from left to right it is clear how the spinning speed compress the beats. The maximum amplitude remains the same because it depends only on θ_0 that is fixed to 1° in this particular simulation.

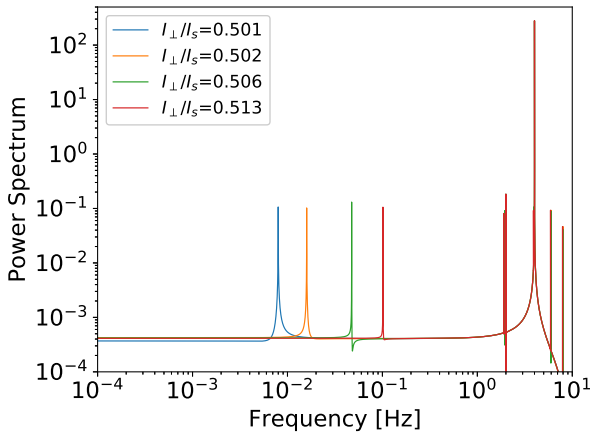

Figure 4.9: Power spectra extracted from timelines showing the shifting of the spurious peak at low frequencies. The simulation considers input light horizontally polarized, a precession angle θ_0 =1° and $I_\perp/I_s = [0.501, 0.502, 0.506, 0.513]$.

Scanning	α [deg]	β [deg]	$\omega_2[deg/min]$	$\omega_3[deg/min]$
Planck like	7.5	85.0	0.00139	360.0
WMAP like	22.5	70.5	6.0	167.0
COrE like	30.0	65.0	0.0625	180.0
LiteBIRD like	45.0	50.0	3.8709	36.0

Table 4.2: Parameters for the scanning strategies adopted in the simulation pipeline.

The input sky map, used for full-sky simulations, contains: Solar Dipole and Galactic diffuse foregrounds in temperature and a CMB realization, both in temperature and polarization. We decide to include foregrounds only in temperature in order to highlight the temperature to polarization leakage. The input $\mathcal{C}_\ell$ used for the CMB realization is compatible with the best fit of *Planck* 2015 release [98] with no tensor perturbations.

The foreground field is generated from the Commander solution delivered with the *Planck* 2015 release [21]. It includes the primary temperature emissions [99]: synchrotron, free-free, spinning dust, CO and thermal dust emission, without considering their polarization contribution.

Such map is modelled in order to highlight the temperature to polarization leakage induced by the HWP precession during the observations. We set the resolution parameter of the input map at `HEALPix` [100] resolution $N_{\rm side} = 256$, comfortable enough respect to the Gaussian beam with FWHM = 60′. In order to evaluate the impact of parameters chosen for the simulation, we have run a case with $N_{\rm side} = 128$, finding the same results in terms of angular power spectra

residual, except in the smaller scales, where the pixel size matters independently of the presence of systematic effects.

We perform several simulations with different configurations for the HWP. We vary the spin frequency, precession angle and $I_s/I_\perp$ ratio. For each simulation we compare input and output maps and compute the B-modes power spectrum. As visual example, we show in Fig. 4.10 (left panel) the output maps for a mission adopting a LiteBIRD-like scanning strategy and solving the Stokes parameters through an HWP with a spin frequency of 1 Hz, a precession angle of θ_0 =1° and $I_\perp/I_s = 0.514$.

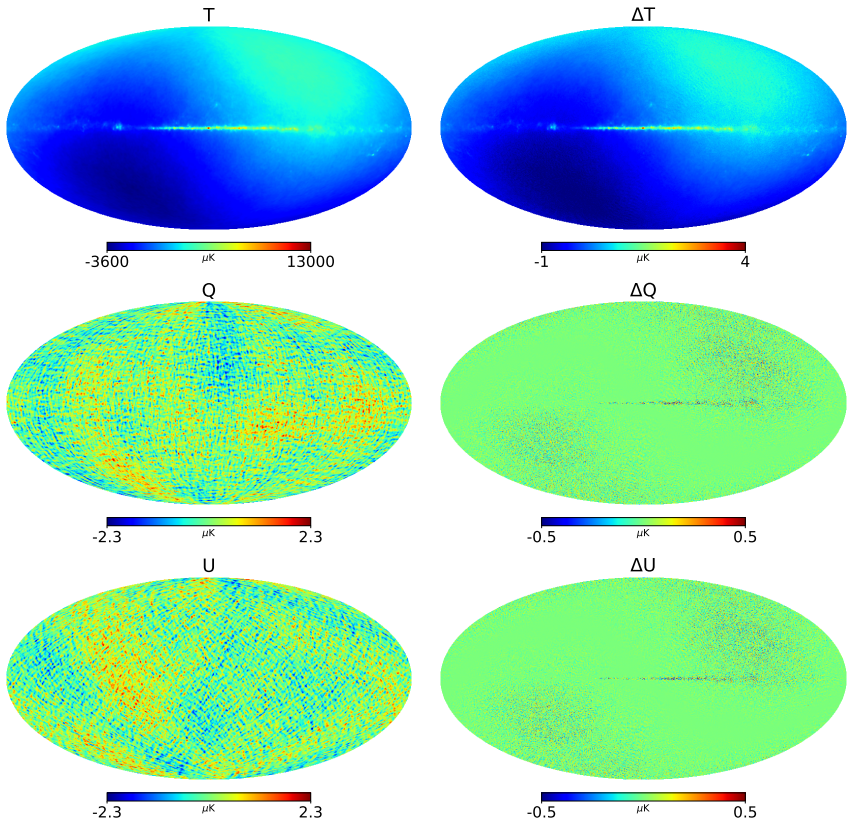

Figure 4.10: (*Left*) T, Q and U maps reconstructed through a Stokes polarimeter where the HWP wobbles. (*Right*) Difference between input and output T, Q and U maps showing the effect of the wave-plate precession on observed maps.

The residual maps (i.e. difference between output and input maps) in Fig. 4.10 (right panel) show the effect of the HWP wobble that induces variations of few percent with respect to the input map. The effect is noticeable close to the galactic plane and close to the maximum and minimum of the solar dipole, where the intensity emission is larger.

Since the effect on the maps is generated by the coupling between the satellite spin and the polarization modulation, affected by the precession, we decided to test several conditions. In particular, slowing the HWP spin speed down to 0.1 Hz the effect of the precession is emphasized as you can see in Fig. 4.11, where the systematic effect induced in the T, Q and U maps, reported in histogram equalized color scale, is at the same level of the input map.

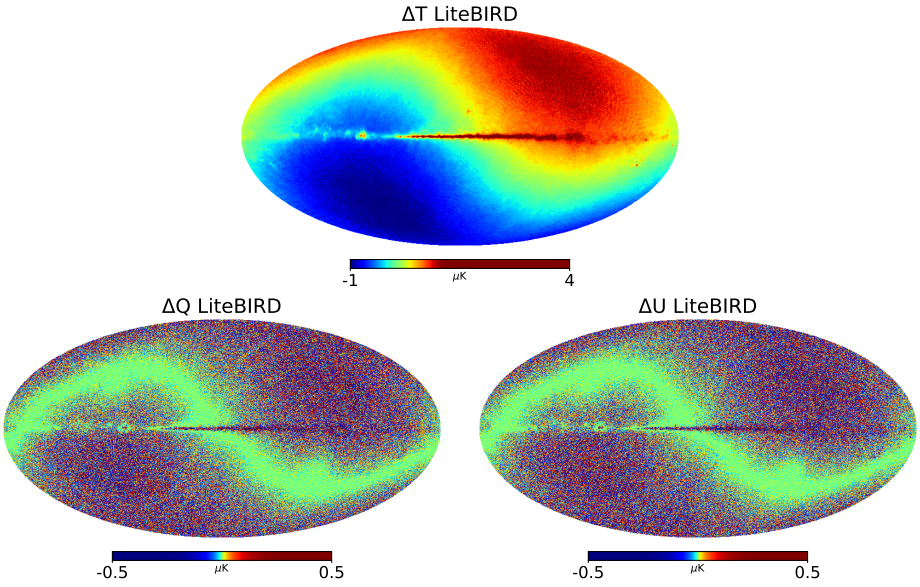

Figure 4.11: Temperature and polarization difference maps showing the effect of the wave-plate precession for a slow spinning modulator. Modulation parameters: f_s =0.1 Hz, θ_0 =1° , $I_\perp/I_s = 0.514$.

The angular power spectra from the output maps shown in Fig. 4.10 are reported up to $l \sim 200$, given the limit imposed by the beam. The relative variations, for both E and B-modes (Fig. 4.12), show the effect of the precession, combined with the satellite spin, that dominates at small angular scales ($l >$ 150).

If a 0.1 Hz spinning HWP is used, the synchronism with the satellite is slightly different and spurious B-mode polarization shows up at different angular scales ($l > 100$). What differs in these two cases is the matching between the systematic effect and the satellite spin (Fig. 4.13-(a)(b)).

The few simulations presented so far, assuming a LiteBIRD-like scanning strategy, show the effect of the HWP precession on full-sky maps and angular power spectra. Since the scan strategy can have a role in mitigating this systematic effect that couples temperature and B-mode polarization [101], we implemented simulations, as described previously, able to reproduce different satellite observational strategies. The results obtained analyzing those simula-

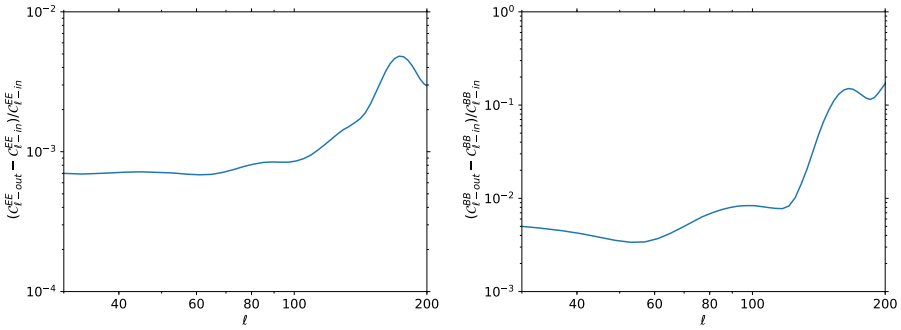

(a) EE power spectra (b) BB power spectra

Figure 4.12: Input minus output relative difference of EE and BB power spectra computed from the maps shown in Figure 4.10.

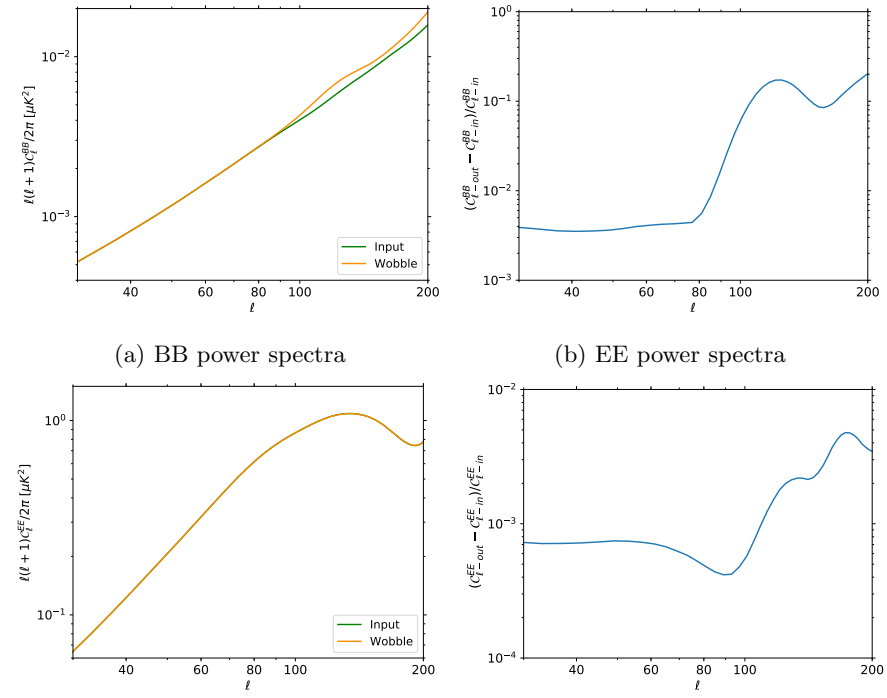

(a) BB power spectra (b) EE power spectra

(c) BB normalized difference (d) EE normalized difference

Figure 4.13: (a)-(c) BB and EE Power Spectra extracted from the input map and from the output map of Fig. 4.11, in (c) the two lines are overlapped. (b)-(d) Normalized difference between input and output power spectra.

tions are reported as residual maps (i.e. difference between output and input maps), shown in Fig. 4.14, as root mean square (hereafter RMS) of the residual maps, shown in Tab. 4.3, and as B-modes angular power spectra, shown in Fig. 4.15.

In Fig. 4.14 we report the Q residual maps, in histogram equalized color scale, for the case $f_s = 0.1\,\mathrm{Hz}$, $\theta_0 = 1^\circ$ (the U maps show variations with a similar pattern and similar dynamic range). We made the simulations with several HWP physical parameters. Here we report the results for the following values of the $I_\perp/I_s$ ratio as representative cases: 0.508 for *Planck*, 0.514 for *COrE*and LiteBIRD and 0.510 for WMAP.

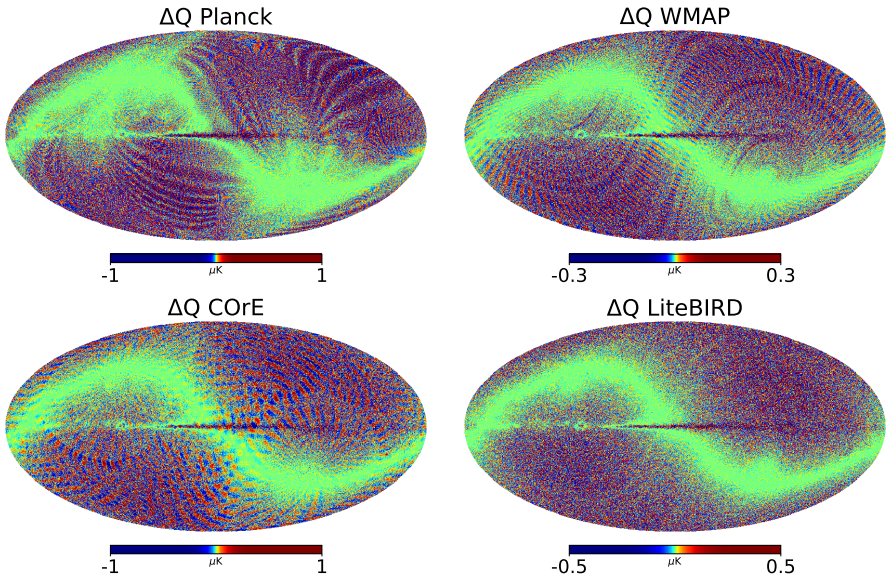

Figure 4.14: Difference between polarization Q-maps reconstructed through a Stokes polarimeter showing the direct effect of the wave-plate precession with different scan strategies. Modulation parameters: $f_s = 0.1\,\mathrm{Hz}$, $\theta_0 = 1^\circ$, $I_\perp/I_s = 0.508$ for *Planck*, $I_\perp/I_s = 0.514$ for *COrE*and LiteBIRD and $I_\perp/I_s = 0.510$ for WMAP. Scan strategy from the left to the right: *Planck*, WMAP, *COrE*, LiteBIRD.

The result of this analysis shows that the residual does not depend only on the scanning strategy, but mostly on the combination of scanning strategy, HWP rotation speed and $I_\perp/I_s$ ratio.

For example, all scanning strategy simulations show the largest effect in the case of an HWP spinning at 0.1 Hz, while they show the lowest residual in the case of 1 Hz spin frequency. This is also evident from the RMS value, reported in Tab. 4.3, and from the angular power spectrum in Fig. 4.15. Anyway, some strategies produce a spurious peak in the angular power spectrum possibly induced by a resonance between satellite spin and HWP wobbling, i.e. *COrE*

0.1 Hz at $\ell \sim 40$, WMAP 0.1 Hz at $\ell \sim 85$ or LiteBIRD 0.1 Hz at $\ell \sim 120$.

	Frequency 1.0 Hz			Frequency 0.1 Hz		
Strategy	T[μK]	Q[μK]	U[μK]	T[μK]	Q[μK]	U[μK]
Planck	0.600	0.032	0.032	0.600	0.050	0.050
WMAP	0.601	0.071	0.071	0.600	0.072	0.072
COrE	0.600	0.071	0.071	0.600	0.088	0.087
LiteBIRD	0.600	0.071	0.071	0.600	0.076	0.076

Table 4.3: RMS values in μK for intensity and polarization for different scan strategies. Maps correspond on the input/output difference maps for each case.

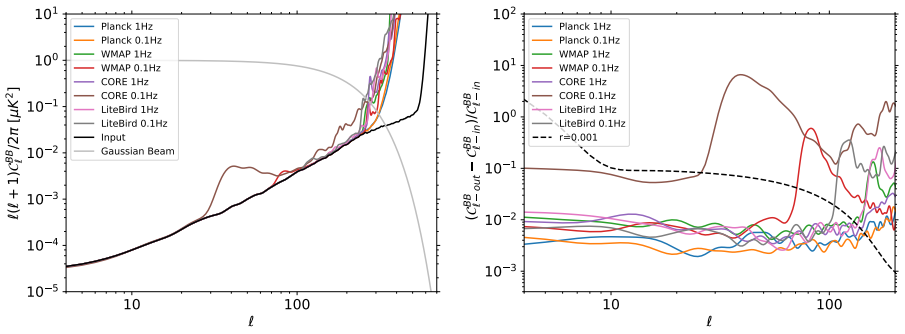

(a) BB power spectra

(b) BB normalized difference

Figure 4.15: B-mode power spectra (a) recovered from simulations including the systematic and the difference output minus input of BB power spectra (b) normalized respect to the input spectrum, when using the *Planck*, WMAP, *COrE* and LiteBIRD scan strategies with different HWP spinning speeds ($f_s = [0.1, 1]$ Hz). The dashed line represents the primordial B-modes angular power spectrum in the case $r = 0.001$, divided by the lensing only B-modes, assuming the other cosmological parameters from [102].

The *Planck*-like scanning strategy [103] does not create particular patterns or structures on larger angular scales, as can be seen in the BB power spectra orange and blue colored in Fig. 4.15.

On the other hand the *COrE*-like simulation (with slowly spinning HWP) shows the worst coupling between the satellite spin and wave-plate precession in terms of angular structures at large scales, as visible in terms of spurious B-modes (brown colored in Fig. 4.15). These simple cases show that the large scale patterns arising in the residual map are not related to the whole quality of the map better described by the angular power spectrum.

The power spectra and the maps recovered show the contaminations generated by the half-wave plate precession systematic, for a specified scan strategy. Repeating the analysis with different precession angles we conclude, as expected,

that the larger is the precession angle, the larger is the spurious B-mode signal; the higher is the HWP spin frequency, the greater is the mitigation of the systematic effect.

In terms of research for primordial B-modes, the faster rotation of the waveplate helps to mitigate the systematic effect induced by the precession of the modulating element in a Stokes polarimeter by moving the contamination at high ℓ. Fig. 4.15b illustrates the fractional residual B-modes due to observation with a wobbling HWP, in the case of no-tensor perturbations, but only lensing-induced B-modes. The fractional residual power is a good figure of merit of the contamination, given that next-generation CMB polarization experiment are designed to reach a sensitivity which is usually quantified as a fraction of the lensing-induced B-modes level.

Including in the input for the simulations a map with only temperature foregrounds, we can highlight the temperature-to-polarization leakage effect induced by the systematic for various scenarios. We verified that polarization foregrounds, removed with ideal component separation method, leave one order of magnitude lower residual in terms of P-P leakage.

The HWP wobble induces B-modes which amplitude is proportional to θ_0 as shown in Fig. 4.16 where we report the BB power spectra for different precession angles [0.5°, 1°, 1.5°, 2°] extracted from the maps scanned by a *COrE*-like satellite. The induced B-mode signal exceeds the gravitational lensing contribution already for $\theta_0 = 1°$.

The output polarization components Q and U are shown in Tab. 4.4.

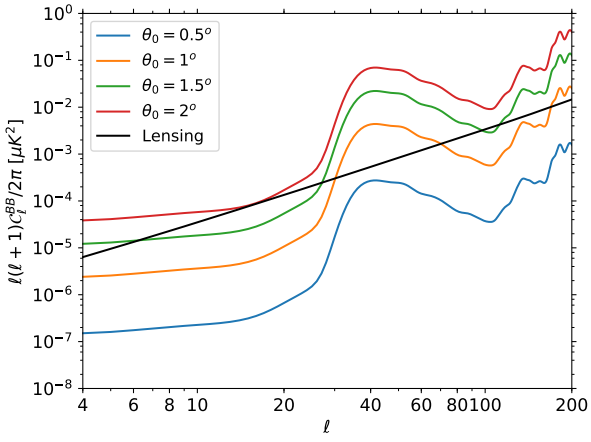

Figure 4.16: B-mode power spectra recovered from simulations including the systematic when using the *COrE* scan strategy with fixed HWP spinning speed ($f_s = 0.1$ Hz) and different precession angles. The input map includes only temperature contributions, the polarization contribution in the output map arises from the HWP precession.

θ_0 [°]	T[µK]	Q[µK]	U[µK]
0.5	0.150	0.533	0.531
1	0.600	0.540	0.537
1.5	1.350	0.569	0.569
2	2.401	0.640	0.640

Table 4.4: RMS values in µK for intensity and polarization residual maps considering a *COrE*-like scan strategy with the HWP spin speed at 0.1 Hz and with different precession angles.

The systematic effect induced by the wobbling can be mitigated by redundancy. Observing the same sky pixel with different phases of the wobbling plate averages out the contamination. This can be also obtained by the combination of multiple detectors, observing the same pixel at different times. In order to check this mitigation, we simulate the observation with two different detectors, pointing to different boresight angles β, shifted by 1°, for all the proposed scanning strategies. The modulation parameters used are:$f_s = 1\,\mathrm{Hz}$, $\theta_0 = 1°$, $I_\perp/I_s = 0.508$ for *Planck*, $I_\perp/I_s = 0.514$ for *COrE*and LiteBIRD and $I_\perp/I_s = 0.510$ for WMAP.

	β [°]	Q[nK]	U[nK]
Planck	85.0	31.9	32.0
	86.0	31.8	31.8
	combination	22.6	22.6
WMAP	70.5	70.7	70.8
	71.5	71.8	71.8
	combination	49.8	49.9
COrE	65.0	71.0	70.7
	66.0	72.6	72.6
	combination	50.9	50.5
LiteBIRD	50.0	70.9	70.9
	51.0	70.1	70.1
	combination	50.1	50.1

Table 4.5: RMS values, in µK, of the difference between the maps with and without the effect of the HWP wobbling. The RMS is calculated for the maps from the two detectors, and for the map from the two detectors combined. The RMS of the residual is reduced by a factor $\sim \sqrt{2}$ combining two detectors. Modulation parameters: $f_s = 1\,\mathrm{Hz}$, $\theta_0 = 1°$, $I_\perp/I_s = 0.508$ for *Planck* and *COrE*, $I_\perp/I_s = 0.514$ for LiteBIRD and $I_\perp/I_s = 0.510$ for WMAP.

The combination of the data from the two detectors results in a single map with a reduced contamination with respect to the single detector maps, as reported in Tab. 4.5. In the Table we report the RMS of the difference between

the map with and without the induced systematic effect. This RMS of the residual is very similar for the two single-detector maps, and is reduced in the map produced with their combination. The RMS of the residuals scales with a factor $\sim \sqrt{2}$, indicating that the contamination is rather uncorrelated among the two detectors.

LSPE scanning strategy is very similar to the *Planck* one which does not introduce any peculiar effects (like the *COrE* scanning strategy) and the wobbling angle expected for the SWIPE polarization modulator (see §5) is $< 0.2°$. Furthermore the large number of detectors will reduce the small wobbling contribution. For these reasons we expect that the wobbling effect will be negligible in the SWIPE case.

Chapter 5

The cryogenic HWP rotator for LSPE-SWIPE

In this chapter we present the cryogenic HWP rotator, based on a superconducting magnetic bearing (SMB) [81, 104, 105, 106] that we have developed for the SWIPE instrument of LSPE experiment. The goal is to rotate continuously a large HWP (500 mm) at ∼1.6 K with a power dissipation much smaller than the other heat loads on the superfluid helium bath of SWIPE. Tab. 5.1 summarizes the main requirements of the polarization modulator.

Parameter	**Requirement**
HWP diameter	500 mm
Mechanical frequency	1 Hz
Power budget	< 35 mW
Base temperature	1.6 K
Total mass	< 25 kg

Table 5.1: Requirements of SWIPE polarization modulator.

In the following, we deal with the basics of superconductivity theory and with the sources of friction which affect this kind of system, concluding with the description of all the tests.

5.1 Superconducting Magnetic Bearing principles

As we have seen a continuously rotating HWP is a better solution than a stepped one. However, a continuous mechanical rotation implies a high power dissipation inside the cryostat, reducing the hold time of the cryogen. A possible solution is to use a high-temperature superconducting (HTS) magnetic bearing to hold

a rotating HWP. Typically this support consists of a ring-shaped permanent magnet (PM) magnetized in the axial direction and an array of bulk HTS tiles. Field cooling (FC) process allows a stable levitation of PM above the array of HTSs. The levitating PM is stable in all degrees of freedom except in azimuthal direction. Thanks to the symmetry of the PM in geometry and magnetism about the axial direction, the PM can also rotate freely in azimuth with no contact and much reduced friction. This HTS magnetic bearing is very promising for use at cryogenic temperature, because has:

- Low Coefficient of Friction (COF) without stick-slip friction.
- Passive stable levitation without any active motion control.
- No wear and tear over long term use.
- Minimum energy deposit on the LHe temperature stage during the rotation (function of asymmetry of the magnetic field and of the drive mechanism),
- No extra-effort to cool HTSs to achieve levitation,

In the following we describe our design and tests of a superconducting magnetic bearing optimized for CMB polarimetry.

5.1.1 Superconductivity

Superconductivity was discovered by Heike Kamerlingh Onnes in 1911 [107] in Leiden while studying the electrical resistance of a sample of frozen mercury as a function of temperature. Superconductivity is an unusual property of certain metals, alloys, and ceramics in which electrical resistance drops to zero (Fig. 5.1) and the magnetic flux lines are expelled when the temperature is reduced below a critical value (T_c), also known as the transition temperature. In common materials electrical resistance decreases as the temperature is lowered but it does not disappear completely. But for superconductors the resistance is truly zero.

Locally the net force acting on the charge carriers in a normal metal is:

$$\frac{d(m\vec{v})}{dt} = e\vec{E} - \frac{m\vec{v}}{\tau} \tag{5.1}$$

where $\vec{v}$ is the drift velocity, m is the electron mass, e is the electron charge, $\vec{E}$ is the local electric field and τ is a phenomenological scattering time for the carrier which describes how long it takes the scattering to bring the velocity of the carrier to zero. In a common metal in steady state, the drift velocity achieves a constant value, meaning that the electric force and scattering forces balance, leading to

$$\vec{v} = \frac{e\tau}{m}\vec{E}. \tag{5.2}$$

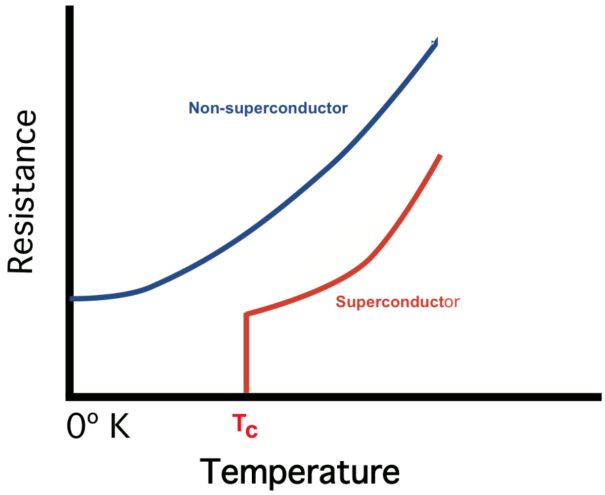

Figure 5.1: Electrical resistance as a function of temperature. Common materials reach a residual resistance at $T = 0\,\mathrm{K}$ while superconductors have zero resistance below the critical temperature T_c.

If there are n carriers per unit volume, the current density can be written as $\vec{J} = ne\vec{v}$, hence

$$\vec{J} = \frac{ne^2\tau}{m}\vec{E} = \sigma\vec{E} \tag{5.3}$$

which is the Ohm's law with the electrical conductivity σ.

There are two different approaches to model a superconductor: the first one is the Ginzburg-Landau theory [108] which is a mathematical physical theory used to describe macroscopical properties of superconductivity; the second one is the London approach which relates current to electromagnetic field inside and outside a superconductor. The latter is description of superconducting phenomena and this is the one we refer to in this thesis.

The main assumption by F. and H. London [109] in 1935 was the *two-fluid model* [110] in which all free electrons of the superconductor are divided into two groups: the electrons from a normal fluid of concentration n_n and a superfluid of concentration n_s, where the total density of free electrons is $n_n + n_s = n$. As the temperature increases from $0\,\mathrm{K}$ to the critical temperature T_c the density n_s decreases from n to 0. The superfluid electrons motion is not affected by scatterings, so, from the above equation, this means that the electrons will accelerate in an applied electric field. Therefore the equation of motion is:

$$m\frac{d\vec{v}}{dt} = e\vec{E}, \tag{5.4}$$

giving rise to the *first London equation*:

$$\frac{\partial \vec{J_s}}{\partial t} = \frac{n_s e^2}{m}\vec{E}. \tag{5.5}$$

This equation says that in order to create a variable current it is necessary to establish an electric field in the superconductor.

Starting from the previous equation we can define a new quantity

$$\frac{\partial \vec{J_s}}{\partial t} = \frac{1}{\mu_0 \lambda_L^2}\vec{E} \tag{5.6}$$

where

$$\lambda_L = \frac{m}{\mu_0 n_s e^2} \tag{5.7}$$

is the London penetration depth.

If we take the curl of both sides of Eq. 5.5 we have

$$\frac{\partial}{\partial t}(\nabla \times \vec{J}) = \frac{1}{\mu_0 \lambda_L^2}(\nabla \times \vec{E}) = -\frac{1}{\mu_0 \lambda_L^2}\frac{\partial \vec{B}}{\partial t} \tag{5.8}$$

where in the last equivalence we used the Maxwell's equation $\nabla \times \vec{E} = -\partial \vec{B}/\partial t$. So we can write:

$$\frac{\partial}{\partial t}\left(\nabla \times \vec{J} + \frac{1}{\mu_0 \lambda_L^2}\vec{B}\right) = 0. \tag{5.9}$$

This equation is just a basic consequence of the laws of electromagnetism, as applied to a perfect conductor. In principle, Eq. 5.9 allows for time-independent, but nonzero, magnetic field. This means that a perfect conductor with a magnetic field through it at $t = 0$ would retain that magnetism forever. The extra step taken by the London brothers was to assume that no time-independent solutions exist. This leads to the *second London equation*:

$$\nabla \times \vec{J} = -\frac{1}{\mu_0 \lambda_L^2}\vec{B}. \tag{5.10}$$

If this relation is correct, no magnetic field could exist in equilibrium in a superconductor. If a magnetic field initially existed in a metal that began to superconduct, the field would be dynamically expelled.

Furthermore the Eq. 5.10 leads immediately to the *Meissner effect*. Remembering the Ampere's Law

$$\nabla \times \vec{B} = \mu_0 \vec{J_s} + \mu_0 \epsilon_0 \frac{\partial \vec{E}}{\partial t} \tag{5.11}$$

and ignoring the displacement current in the low frequency region, we can take the curl of both parts and use the second London equation:

$$\nabla \times \nabla \times \vec{B} = \mu_0 \nabla \times \vec{J_s} = -\frac{1}{\lambda_L^2}\vec{B}. \tag{5.12}$$

Using the vector identity

$$\nabla \times \nabla \times \vec{B} = \nabla(\nabla \cdot \vec{B}) - \nabla^2 \vec{B} \tag{5.13}$$

and the fact that $\nabla \cdot \vec{B} = 0$, we arrive at

$$\nabla^2 \vec{B} = \frac{1}{\lambda_L^2} \vec{B}. \tag{5.14}$$

In the simple case where a magnetic field $\vec{B}_{apl} = B_{apl}\hat{y}$ is applied parallel to the surface the equation can simply be solved by

$$\vec{B}(x) = B_{apl}\hat{y}e^{-x/\lambda_L}, \quad for\ x \geq 0 \tag{5.15}$$

which implies that $\vec{B} \simeq 0$ for depths appreciably beyond λ_L (Fig. 5.2).

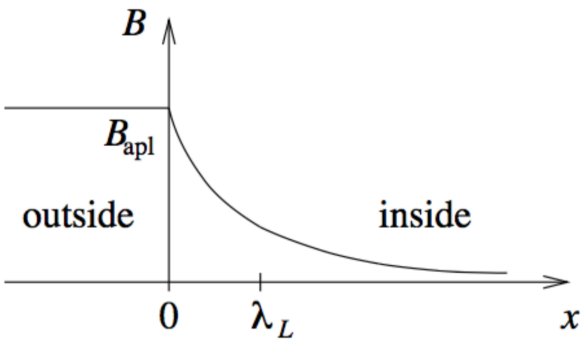

Figure 5.2: The trend of the magnetic field of a superconductor below his critical temperature T_c. The superconductor is placed in $x \geq 0$ and the magnetic field is ~ 0 for depths beyond the London penetration depth λ_L.

Meissner and Ochsenfeld [111] in 1993 showed by experiment that the field inside a superconductor is always zero, so Eq. 5.15 is perfectly in agreement with the experimental results.

The external magnetic field is dynamically expelled by screening currents set up inside the superconductor to cancel the magnetic field in the bulk, as shown in Fig. 5.3. This phenomenon is now called *Meissner Effect*. Assuming e.g., that the magnetic field is pointing along the z-axis, there is a current

$$\vec{J}_s(x) = -\frac{c}{4\pi\lambda_L} B_{apl}\hat{z}e^{-x/\lambda_L} \quad for\ x \geq 0 \tag{5.16}$$

within a screening length from the surface of the superconductor. This current produces a magnetic field that "screens" the external magnetic field inside the superconductor.

The supercurrent flows in the direction parallel to the surface and perpendicular to $\vec{B}$ and decreases into the bulk on the same scale λ_L. $\vec{J}_s$ can be understood as the *screening current* required to keep the magnetic field out of the bulk of the superconductor.

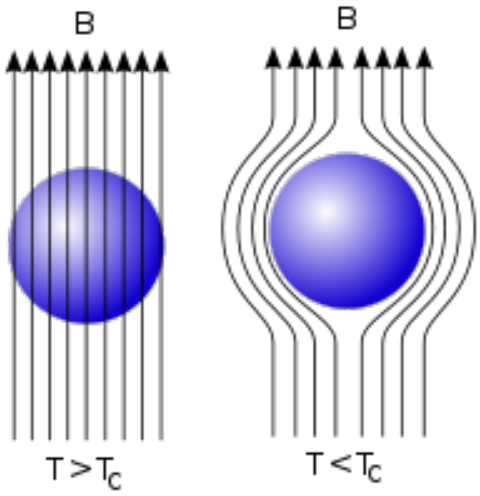

Figure 5.3: Meissner effect: magnetic field lines, represented as arrows, are expelled from a superconductor when it is below its critical temperature T_c.

5.1.2 Type I and II Superconductors

Type I and II superconductors exhibit different magnetic response to an external magnetic field. The left graph shown in Fig. 5.4 illustrates the internal magnetic field strength, B_i, with increasing applied magnetic field. It is found that the internal field is zero (as expected from the Meissner effect) until a critical external field, B_c, is reached where a sudden transition to the normal state occurs. This results in the penetration of the applied field into the interior. Superconductors that undergo this abrupt transition to the normal state above a critical magnetic field are known as type I superconductors. Type II superconductors, on the other hand, respond differently to an applied magnetic field, as shown in the right panel of Fig. 5.4. An increasing field from zero results in two critical fields, B_{c1} and B_{c2}. At B_{c1} the applied field begins to partially penetrate the interior of the superconductor. However, the superconductivity is maintained at this point. The superconductivity vanishes above the second, much higher, critical field, B_{c2}. For applied fields between B_{c1} and B_{c2}, the applied field is able to partially penetrate the superconductor, so the Meissner effect is incomplete, allowing the superconductor to tolerate very high magnetic fields.

Type II superconductors are the most technologically useful because the second critical field can be quite high ($> 20\,\mathrm{T}$). For our applications we choose type II superconductors, in particular the Yttrium barium copper oxide (YBCO) superconductor. It is a family of crystalline chemical compounds and the first material ever discovered to become superconducting above the boiling point

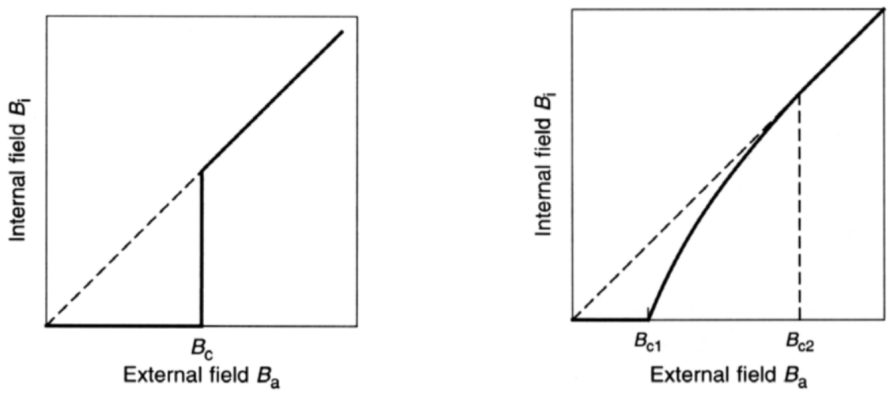

Figure 5.4: (Left) Type-I superconductor behaviour. (Right) Type-II superconductor behaviour.

of liquid nitrogen (77 K), at about 90 K. Many YBCO compounds have the general formula $YBa_2Cu_3O_{7-x}$ (also known as Y123). The material properties depend strongly on oxygen content x: only materials with $0 \leq x \leq 0.65$ are superconducting below T_c and when $x \sim 0.07$ the material superconducts at the highest temperature of 95 K [112]. The typical value for the penetration depth in YBCO is $\lambda_L \simeq 10^2$ nm, so we can think of a superconductor bulk as being a perfectly diamagnetic material. Turning on a magnetic field, internal currents which flow without resistance are generated and they cancel completely the field inside.

5.2 SMB design

A common demonstration of the Meissner effect is to cool a high T_c superconductor (like YBCO), then place a small and strong permanent magnet on top of it to demonstrate the repulsion of the magnetic field by the superconductor. This repulsion results in the levitation of the magnet. An explanation for this levitation is that the magnet "sees" a mirror image of itself in the superconductor, which is like a magnet floating on top of another identical magnet. If the superconductor is slightly larger than the magnet the force should be maximum.

In the SWIPE polarimeter we plan to use a SMB to rotate a large (500 mm) cryogenic (1.6 K) metal-mesh HWP. The modulator is conceptually similar to the EBEX one [57], but more challenging and ambitious because the size of the HWP (500 mm diameter) will make the SWIPE modulator the largest ever tested.

At variance with the most common design of a superconducting magnetic bearing, we choose a different SMB configuration (Fig. 5.5): the magnet ring and the superconductor are not stacked up but the internal rotating ring is the

magnetic one and the external is the superconductor one, in order to obtain a side face to face interaction and avoid any possible horizontal displacement

The selected superconductor (YBCO) is the type-II superconductor with the highest pinning force and critical current density ($\sim 10^5\,\mathrm{A\,mm^{-2}}$). Higher critical current means lower hysteresis losses [113]. Due to the high cost of large volume superconductors we decided to use a segmented ring of 18 YBCO tiles. The rotor is composed of 3 stacked rings, starting from the bottom:

- Groove ring: used to clamp the plate at room temperature or before the reheating.
- Magnetic ring: composed of 2 Neodymium magnetic rings and 3 thin iron rings to produce a more uniform magnetic field.
- Aluminum ring with three different functions: hold the HWP in the center, measure the angular position of the rotor with the encoder and hold the small magnets used as the motor.

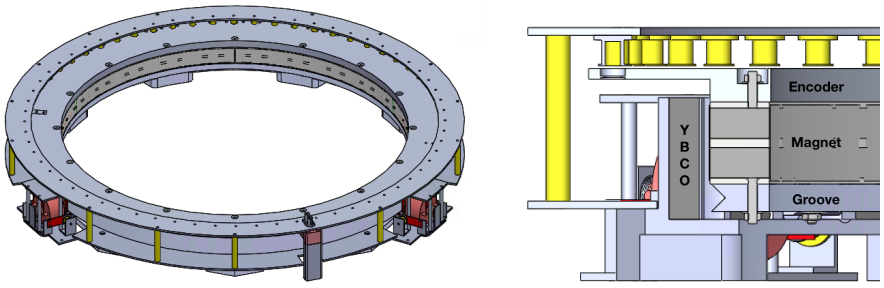

(a) Polarization modulator overview.

(b) Polarization modulator section.

Figure 5.5: (a) PMU overview. (b) PMU section. The inner ring is the rotor while the outer is the stator. On the top of the rotor there is the coils ring (yellow).

Three clamp and release systems evenly spaced on the external diameter are coupled with the groove ring and keep in position the rotor when the temperature is greater than the superconductor critical temperature.

In the next sections we investigate the properties of this system (stiffness, power loss, etc.) and present all the subsystems and the performed tests.

5.2.1 Stiffness

We can quantify the stiffness of a HTS bearing by modelling the system as a spring system with its spring constant. This assumption is true only for small displacement of the rotor respect to the motor, otherwise the relationship

becomes not linear. If we assume a dipole magnet that levitates above an infinite plane of type II superconductor we are able to estimate the spring constant of the system. When a dipole with the magnetization m is placed at the distance z above an infinite plane type II superconductor with FC, the flux due to the Meisner effect and trapped flux at a pinning center can be treated as two images, diamagnetic image (a mirror image of the levitating dipole at a distance z from the interface of the superconductor) and frozen image (an image at the same location as the diamagnetic image but with opposite magnetization). Assuming the magnetization direction of the levitating dipole is normal to the plane ($\vec{m} = m\hat{z}$) and treating the two images ($\vec{B}^{dia}$ and $\vec{B}^{frozen}$) as external magnetic field, we can calculate the magnetic interaction between external field and the real dipole and hence the spring constant:

$$k_z = -\frac{\partial F_z}{\partial z} = -m\left(4\frac{\partial^2 B_z^{dia}}{\partial z^2} + \frac{\partial^2 B_z^{frozen}}{\partial z^2}\right), \tag{5.17}$$

$$k_x = -\frac{\partial F_x}{\partial x} = -m\frac{\partial^2 B_x^{frozen}}{\partial x \partial z}, \tag{5.18}$$

$$k_y = -\frac{\partial F_y}{\partial y} = -m\frac{\partial^2 B_y^{frozen}}{\partial y \partial z}. \tag{5.19}$$

If we substitute the explicit expression of the magnetic field B produced by a magnetic ring, we obtain:

$$k_z = \frac{3\mu_0 m^2}{\pi(2z)^5}(2\cos^2\theta + \sin^2\theta), \tag{5.20}$$

$$k_x = \frac{3\mu_0 m^2}{\pi(2z)^5}(\cos^2\theta + \frac{3}{4}\sin^2\theta), \tag{5.21}$$

$$k_y = \frac{3\mu_0 m^2}{\pi(2z)^5}(\cos^2\theta + \frac{1}{4}\sin^2\theta). \tag{5.22}$$

The vertical stiffness is positive and indicates stability in the vertical direction. The horizontal stiffnesses are also positive, indicating stability in all directions. It is easy to demonstrate the relation:

$$k_x + k_y - k_z = 0 \quad \rightarrow \quad k_z = 2k_r \tag{5.23}$$

which shows that in this type of system (PM/HTS) the spring constants can all have simultaneously positive values. This substitutes the Earnshaw's theorem [114], which when applied to magnetic systems (PM/PM) can be written as:

$$k_x + k_y + k_z = 0. \tag{5.24}$$

The theorem shows that permanent magnets interaction cannot be stable because there is at least one negative stiffness.

Using this scheme we can associate a natural frequency to each degree of

freedom:

$$f_z = 2\pi\sqrt{\frac{k_z}{M}} \tag{5.25}$$

$$f_r = 2\pi\sqrt{\frac{k_r}{M}}. \tag{5.26}$$

These frequencies are very important in the design of the HTS bearing because the rotational frequency should be as far as possible from them, otherwise the two frequencies resonate and the rotor wobbles. Also, the previous equations show that a stronger magnet is recommended because the HTS bearing becomes stiffer.

5.2.2 Hysteresis loss

No physical contact between stator and rotor does not mean no friction. A spacial magnetic field inhomogeneity in the magnet becomes a time varying magnetic field with respect to the HTS tiles (the geometry discussed is introduced in §5.1). There are three types of inhomogeneities: azimuthal inhomogeneity derives from the joints between adjacent magnets of the ring (if the ring is segmented), radial and vertical from wobbling or vibration during the rotation (misalignment between the geometrical center and the magnetic center of the rotor).

The hysteresis can be produced in the YBCO superconductors by the trapped magnetic field of the rotor magnet or the drive magnets. Due to the distance between the drive magnets and the superconductors, their magnetic field is very low. On the other side the rotor magnetic field is huge but its magnetic field variation depends on the quality of the magnet and on the relative distance between the rotor and the superconductor. This variation of the magnetic field of the ring magnet drags flux through the type II superconductor as the rotor spins, creating hysteresis loss [115].

The current density in the superconductor is:

$$J = \begin{cases} J_c, & \text{if } 0 < z < \delta(t) \\ 0, & \text{if } z > \delta(t) \end{cases}$$

where $\delta(t) = H_0(t)/J_c$ is the relative penetration depth and H_0 is the value of the magnetic field at $z = 0$. Remembering the relation:

$$\frac{\partial E}{\partial z} = -\mu_0 \frac{\partial H}{\partial t}, \tag{5.27}$$

we can find the electric field

$$E = \begin{cases} \mu_0 J_c \dot{\delta}(t)[\delta(t) - z], & \text{if } 0 < z < \delta(t) \\ 0. & \text{if } z > \delta(t) \end{cases}$$

The power dissipated per unit surface area is

$$P_A = \int_0^{\delta(t)} JEdz = \frac{1}{2}\mu_0 J_c^2 \dot{\delta(t)}\delta^2(t) = \frac{\mu_0}{6J_c}\frac{d}{dt}H_0^3. \tag{5.28}$$

If we let the direction of motion at velocity v be x, the surface field is

$$H_0(x, y, t) = H_0(x - vt, y, 0) \tag{5.29}$$

and we can write $\frac{d}{dt}H_0(t) = -v\frac{\partial}{\partial x}H_0$. So the power dissipated per unit lenght is

$$P_L = \frac{5v\mu_0}{24J_c}H_{max}^3(y) \tag{5.30}$$

where $H_{max}^3(y)$ is the maximum magnetic field along a line in the y direction. By defining d the length of the magnet transverse to the direction of motion we can calculate the magnetic drag force

$$F_D = \frac{P}{v} = \frac{5\mu_0}{24J_c}\int_{-\infty}^{+\infty} H_{max}^3(y)dy \simeq \frac{5d(\mu_0 H_{max})^3}{24\mu_0^2 J_c}. \tag{5.31}$$

In order to reduce the drag force we can improve the quality of the magnet and so reduce ΔB but especially increase the critical current J_c by decreasing the temperature because the critical current is inversely proportional to temperature. For example the critical current increases by a factor of $20 - 30$ from 77 K to 4 K when the externally applied magnetic field is 1 T [116] [117]. The main point is that the hysteresis force does not depend on the frequency, so this is a constant contribution at all frequencies.

5.2.3 Eddy current loss

Eddy currents are loops of electrical current induced by a changing magnetic field in the conductor, due to Faraday's law of induction. They can be generated by a time varying magnetic field ΔB and dissipate as Joule heat. The power loss due to eddy currents per unit volume is:

$$P \propto \sigma(\Delta B)^2 d^2 f^2 \tag{5.32}$$

where σ and d are the conductivity and the thickness of the material. Eq. 5.32 represents a rough estimate of the power loss without considering the skin effect and derived using other approximations. Nevertheless the strong dependence on frequency, on the magnetic field inhomogeneities and on conductivity is clear. The main contribution comes from the HTS tiles holder because its distance from the magnet is a few millimeters, so the best solution could be the use of a dielectric material, like fiberglass, vespel or PEEK ($\sigma \sim 0\,\mathrm{S\,m^{-1}}$). On the other hand, thermalizing HTS tiles surrounded by these materials with a very low thermal conductivity coefficient could become a problem. At room temperature the best candidates are copper and aluminum ($\rho_{Cu} = 17.2\,\Omega\,\mathrm{nm}$

and $\rho_{Al} = 26.5\,\Omega\,\mathrm{nm}$), but at 4 K the best compromise is an aluminum support as the resistance ratio is $\frac{\rho(300\,\mathrm{K})}{\rho(4\,\mathrm{K})} \sim 2-3$ for aluminum and $\frac{\rho(300\,\mathrm{K})}{\rho(4\,\mathrm{K})} \sim 10-50$ for copper[1]. Despite the heat transfer of copper is twice as much as aluminum, the second has a lower electrical conductivity. The second important parameter is the magnetic field inhomogeneity. A more homogeneous main magnet ($\frac{\Delta B}{B} < 5\%$) helps to reduce drastically this contribution.

Other sources of eddy currents are the small magnets used in the motor. A dipole of moment m, oriented vertically, which is moving at height z_0 above a conductive plate produces a power loss[118]:

$$P = Fv = \frac{3\mu_0 m^2}{32\pi z_0^4} w \left[1 - \frac{1}{\sqrt{1 + \left(\frac{v}{w}\right)^2}}\right] \tag{5.33}$$

where v is the magnet velocity and $w = \frac{2}{\mu_0 \sigma \delta}$ related to the conductivity of the plate and to its thickness δ.

5.2.4 Harness

An important factor to achieve low base temperature is making sure that the power load on the colder stage is minimized. All the electrical wires required to drive the rotation and read its status also conduct heat from the warmer stage to the colder one.

The formula for heat flow is:

$$Q = \int_{T_1}^{T_2} \frac{A}{L} k(T) dt \tag{5.34}$$

where Q is the heat flow, $k(T)$ is the thermal conductivity of the material, A and L are the cross-sectional area and the length of the wire and T_1 and T_2 the temperatures gradient across the wire. The cross sectional area and the length of the wire can greatly affect the heat loss: too short of a wire will cause heating, too long of a wire will increase its resistance which may impact the circuit function and increase the power dissipated in the wire itself.

The choice of the wire material depends on the thermal conductivity and in particular on its dependence on temperature (Fig. 5.6). While the best choice for the thermal conductivity point of view is the manganin wire, the resistance is very high and can considerably increase the Joule loss:

$$P_J = Ri^2 \tag{5.35}$$

where R is the resistance and i the current.

In practice, for our polarization modulator unit we have a bundle of 16 cables for the motor: 8 carrying the driver coils currents (8 phases) and 8 for the return currents. We reduce electromagnetic interference by twisting

[1] `https://trc.nist.gov/cryogenics/materials/materialproperties.htm`

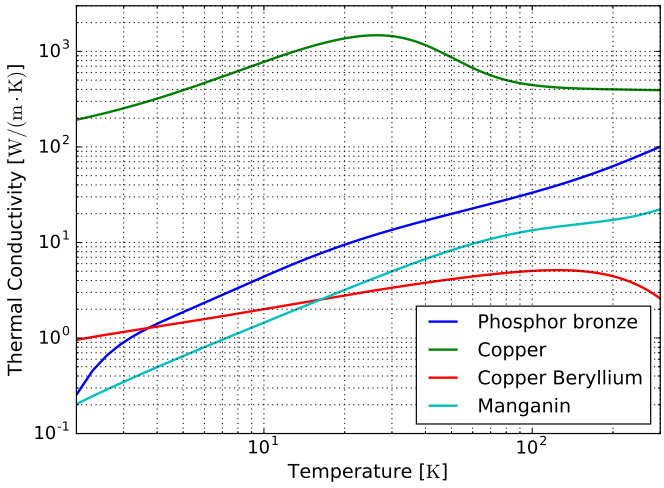

Figure 5.6: Thermal conductivity of most common materials used in cryogenic applications [119, 120].

the drive and return wires separately for each phase. The total heat load on the cold stage is the sum of the conduction loads and the power dissipation loads for all these wires. Fig. 5.7 shows the power load on the coldest stage (1.6 K) for different materials and currents as a function of the wire diameter. The Beryllium-Copper wire minimizes the heat load and the diameter chosen is 0.25 mm with 0.05 mm of Heavy Polyimide (HML) insulation[2].

The resulting heat load on the 180 K stage is 5-7 mW and 5-8 mW on the 65 K one. The total resistance for a single wire is 4.7 Ω (3 m length).

5.2.5 Motor design

The electromagnetic motor is based on the interaction between 8 small magnets placed on the rotor with 64 driving coils placed on the stator. By modulating the current in each coil we are able to simultaneously push/pull the nearest magnet

The choice of the magnets material is critical because of a possible modification of the demagnetization characteristics at cryogenic temperatures.. The Nd-FeB undergoes a spin reorientation as the temperature falls. Most reports [121] find a spin reorientation at 135 K due to an unusual combination of anisotropy constants and other factors. This demagnetization causes also a decrease of the magnetic field of about 20%. A possible solution to avoid both problems is to use Samarium Cobalt magnets ($SmCo_5$ or Sm_2Co_{17}) which are used without any issue below 2 K[122].

[2] `https://www.calfinewire.com/index.html`

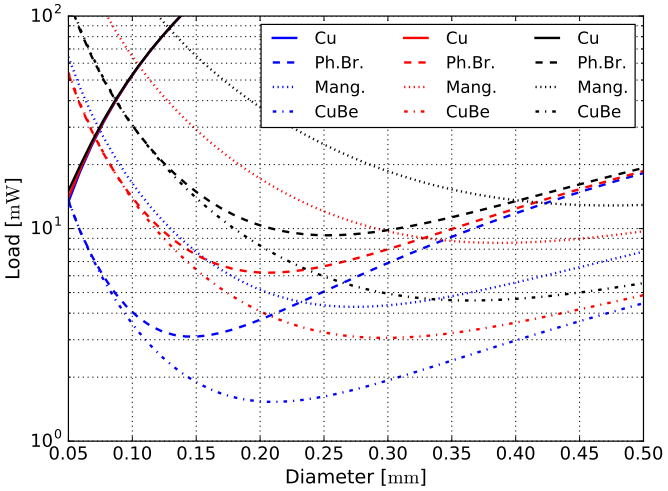

Figure 5.7: Heat load produced on the 1.6 K stage for different wire materials and different current values (20 mA in blue, 40 mA in red and 60 mA in black). In the most likely case (40 mA), the manganin (dotted lines) produces ~ 10 mW heat load while the behaviour of phosphor bronze (dashed lines) and Beryllium-Copper (dash-dotted lines) is very similar for lower wire diameters.

In the rotor of SWIPE we use 8 SmCo magnets evenly spaced at 45°, with 8 mm diameter and 2 mm thickness. The residual flux density is $B_{r_{max}} \approx 1.1$ T giving a magnetic dipole moment $m \approx 0.9\,\mathrm{A\,m^2}$.

In order to chose the best design to minimize friction produced by the small drive magnets, we simulate the eddy currents produced by their AC magnetic field variation using the COMSOL Multiphysics software. The parameters to optimize with the simulation are the height of the drive magnets (with respect to the bottom of the YBCO holder), and the radius where they are mounted on the rotor ring. Fig. 5.8 shows the trend of the power loss as a function of the magnets' height, for different values of the radius. As we expected the power loss is greater when magnets are close to the YBCO holder. As for the radius the safety condition corresponds to a value greater than 292 mm because of the interaction between the main magnet and the drive magnets (the distance should be > 30 mm). The values chosen for our design is $r = 296$ mm and height of 45 mm which correspond to an expected eddy current loss of 2.6 mW (assuming the ratio between the aluminum electrical conductivities $\frac{\sigma_{1.6\,\mathrm{K}}}{\sigma_{300\,\mathrm{K}}} = 2.8$) .

These magnets are coupled with the magnetic field produced by the solenoids. The axial magnetic field produced by an ideal solenoid is $B = Ni\mu$, where μ is the magnetic permeability, N is the number of turns and i is the current. Given an arbitrary value of the magnetic field, if we want to use the smallest possible current, we can both increase the number of turns (or modify the geometry of the coil) or increase the magnetic permeability. In case of air core coil, the mag-

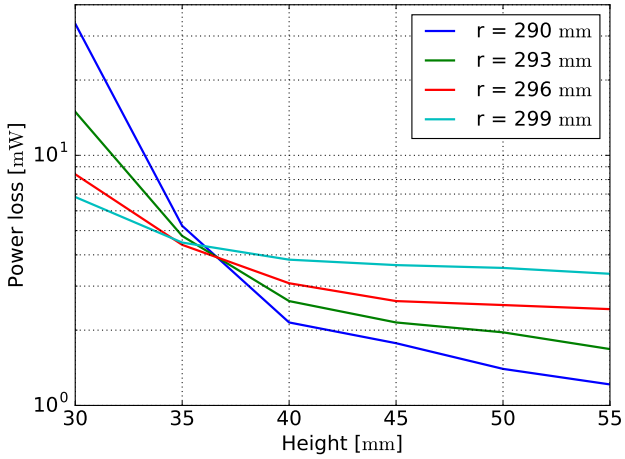

Figure 5.8: Power loss produced by eddy currents as a function of drive magnets height for various values of the radius.

netic permeability is $\mu = \mu_0$ while with a ferromagnetic core, the permeability increases by a factor μ_r. Because of the modulated current and the proximity of moving magnets, the ferromagnets should be magnetized and demagnetized. At low temperature the hysterisis loop is enlarged and so the ferromagnet could dissipate too much power or remain magnetized. For this reason we decided to use air coils with optimized geometry to increase the force and low resistance to minimize the Joule losses (see §5.2.7 for more details).

5.2.6 RRR measurement

RRR (Residual Resistivity Ratio) is a common index for measuring the quality of a metal at cryogenic temperatures and is usually defined as the ratio of the resistivity of a material at room temperature and at 0 K.

The RRR can vary quite strongly for a given material depending on the amount of impurities, it serves as a rough index of the purity and overall quality of a sample. A large RRR is associated with a pure sample because the resistivity usually increases as defect prevalence increases.

A theoretical RRR is defined:

$$RRR = \frac{\rho_{300\,\mathrm{K}}}{\rho_{0\,\mathrm{K}}} \simeq \frac{\rho_{300\,\mathrm{K}}}{\rho_{4\,\mathrm{K}}} \tag{5.36}$$

In the simplest case of a good metal that is free of scattering mechanisms, one would expect $\rho(0\,\mathrm{K}) = 0$, which would cause RRR to diverge. However, usually this is not the case because defects such as grain boundaries and impurities act as scattering sources that contribute a temperature independent ρ_0 value, giving a smaller RRR.

In order to select and validate the wire material for the coils, we performed a set of measurements of RRR with a custom experimental setup. A two-stage pulse tube cryocooler is used to achieve the low temperature environment. Its lowest cooling temperature is $\sim$ 6 K, thus meeting the measurement requirement. A DT-670 silicon diode[3] is used to monitor the temperature. The samples under testing are 2 copper wire coils:

1. 23 m long and 0.45 mm diameter
2. 56 m long and 0.20 mm diameter

We used a four-wires resistance measurement, with copper wires (R = 1.9 Ω) to increase the accuracy. Four-terminals sensing eliminates voltage drop in the measuring leads as a contribution to error. To increase accuracy further, the 2 couples of wires are twisted to prevent electromagnetic interference.

Bias current is injected by means of a room temperature load resistor ($R = 1015\,\Omega$) and a high precision function generator. The 1 V amplitude sine wave generated produces a peak to peak current amplitude of 2 mA $\pm$ 4 µA.

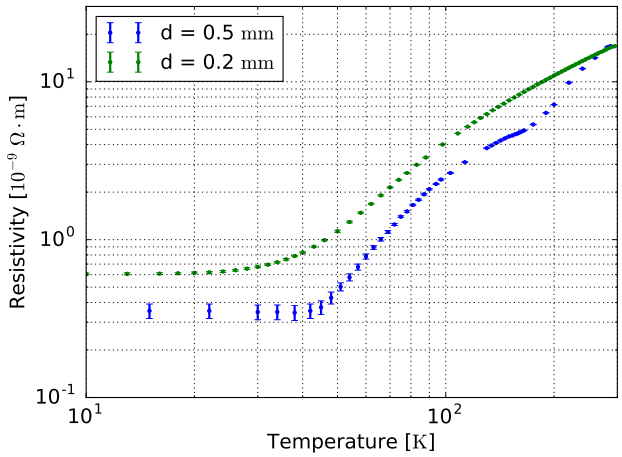

Figure 5.9: Measurement of copper resistivity as a function of temperature.

Fig. 5.9 shows the measured copper resistivity both for 0.5 mm and 0.2 mm diameter. The equivalent RRRs are ∼50 and ∼28, respectively. By assuming a 6-layer coil for 0.2 mm and a 2-layer coil for 0.5 mm, the total resistance at 4 K of each coil is

$$R = \frac{\rho_{300\,\mathrm{K}}}{RRR}\frac{2\pi a N}{S} \tag{5.37}$$

where a is the coil radius, N the number of turns and S the cross sectional

[3] https://www.lakeshore.com/products/categories/overview/temperature-products/cryogenic-temperature-sensors/dt-670-silicon-diodes

surface of the wire. The ratio between the two tested wires is

$$\frac{R_{0.2}}{R_{0.5}} = \frac{RRR_{0.5}}{RRR_{0.2}} \frac{n_{0.2}}{n_{0.5}} \frac{S_{0.5}}{S_{0.2}} \simeq 83. \tag{5.38}$$

5.2.7 Coil design optimization

In order to optimize the geometry of the coils we built an analytical model to define the force produced by a couple of coils as a function of the main coil parameters.

Considering a solenoid of length L and radius a, we can define a polar reference frame centered in the center of the solenoid where z, r and ϕ are the axial, radial and tangential components, respectively. The magnetic field is given in terms of the vector potential $\vec{A}$:

$$\vec{B} = \vec{\nabla} \times \vec{A} \tag{5.39}$$

where the only component different from zero is A_θ. Hence the only magnetic field components are:

$$B_r = -\frac{\partial A_\theta}{\partial z}, \tag{5.40}$$

$$B_z = \frac{1}{r}\frac{\partial (r A_\theta)}{\partial r}. \tag{5.41}$$

A typical coil composed by a series of n turns per unit length, with a flowing current i and composed by a core material with magnetic permeability μ_r ($\mu = \mu_r \mu_0$) has

$$A_\theta = \frac{a^2 \mu n i}{2\pi} \int_{\xi-}^{\xi^+} d\xi \int_0^\pi \frac{\cos\theta d\theta}{\sqrt{\xi^2 + r^2 + a^2 - 2ar\cos\theta}} \tag{5.42}$$

where $\xi = z - l$ ($\xi_\pm = z \pm L/2$) and l is the axial distance from the origin to the filament. If we integrate by parts, we find:

$$A_\theta = \frac{a^2 \mu n i r}{2\pi} \int_0^\pi \left[\frac{\xi \sin^2\theta d\theta}{(a^2 + r^2 - 2ar\cos\theta)\sqrt{\xi^2 + r^2 + a^2 - 2ar\cos\theta}} \right]_{\xi-}^{\xi_+}. \tag{5.43}$$

From Eq. 5.40 we can derive B_r component

$$B_r = -\frac{\partial A_\theta}{\partial z} = -\frac{a\mu n i}{2\pi} \int_0^\pi \left[\frac{\cos\theta d\theta}{\sqrt{\xi^2 + r^2 + a^2 - 2ar\cos\theta}} \right]_{\xi-}^{\xi^+}. \tag{5.44}$$

and from Eq. 5.41 the B_z component

$$B_z = \frac{1}{r}\frac{\partial (r A_\theta)}{\partial r} = \frac{a\mu n i}{2\pi} \int_0^\pi \left[\frac{\xi(a - r\cos\theta) d\theta}{(r^2 + a^2 - 2ar\cos\theta)\sqrt{\xi^2 + r^2 + a^2 - 2ar\cos\theta}} \right]_{\xi-}^{\xi_+}. \tag{5.45}$$

We can also rewrite Eq. 5.44 in a simpler way:

$$B_r = \frac{\mu n i}{\pi}\sqrt{\frac{a}{r}}\left[\frac{2-k^2}{2k}K(k) - \frac{E(k)}{k}\right]_{\xi_-}^{\xi^+} \tag{5.46}$$

where

$$k^2 = \frac{4ar}{\xi^2 + (a+r)^2} \tag{5.47}$$

and $E(k)$ and $K(k)$ are the standard elliptic integrals

$$E(k) = \int_0^{\pi/2} \sqrt{1 - k^2 \sin^2\theta}\, d\theta, \tag{5.48}$$

$$K(k) = \int_0^{\pi/2} \frac{d\theta}{\sqrt{1 - k^2 \sin^2\theta}}. \tag{5.49}$$

Similarly from Eq. 5.45 we find

$$B_z = \frac{\mu n i}{4}\left[\frac{\xi k}{\pi\sqrt{ar}}K(k) + \frac{(a-r)\xi}{|(a-r)\xi|}\lambda_0(\phi, k)\right]_{\xi_-}^{\xi_+} \tag{5.50}$$

where

$$\phi = \tan^{-1}\left|\frac{\xi}{a-r}\right|. \tag{5.51}$$

In addition $\lambda_0(\phi, k)$ is the Heuman function.

We can check the validity of these equations when $r \to 0$:

$$B_r = \frac{\mu n i}{4}\left[\frac{a^2 r}{(\xi^2 + a^2)^{3/2}}\right]_{\xi_-}^{\xi_+} = \frac{B_0}{4}\left[\frac{a^2 r}{(\xi^2 + a^2)^{3/2}}\right]_{\xi_-}^{\xi_+}, \tag{5.52}$$

$$B_z = \frac{\mu n i}{2}\left[\frac{\xi}{\sqrt{\xi^2 + a^2}}\right]_{\xi_-}^{\xi^+} = \frac{B_0}{2}\left[\frac{\xi}{\sqrt{\xi^2 + a^2}}\right]_{\xi_-}^{\xi^+} \tag{5.53}$$

which are the well-known expressions for the field produced far from a coil.

The normalized magnetic field for our motor coils geometry ($L = 8\,\text{mm}$, $r = 4.5\,\text{mm}$) is shown in Fig. 5.10.

By assuming the same radius $R = 296\,\text{mm}$ for all drag forces, we can find a rough estimate for the required force for a spin rate of 1 Hz:

$$F_{drag} = \frac{P}{v} = \frac{P}{2\pi f R_*} \simeq 5 \times 10^{-3}\,\text{N} = 8\,\text{mN} \tag{5.54}$$

where the assumed total power dissipated by the rotor is 15 mW.

The strongest force is required when a magnet is in the middle between two coils which is also the point where the force profile is minimum. In this configuration we can assume the magnet as a magnetic dipole $\vec{m} = m\hat{z}$ where

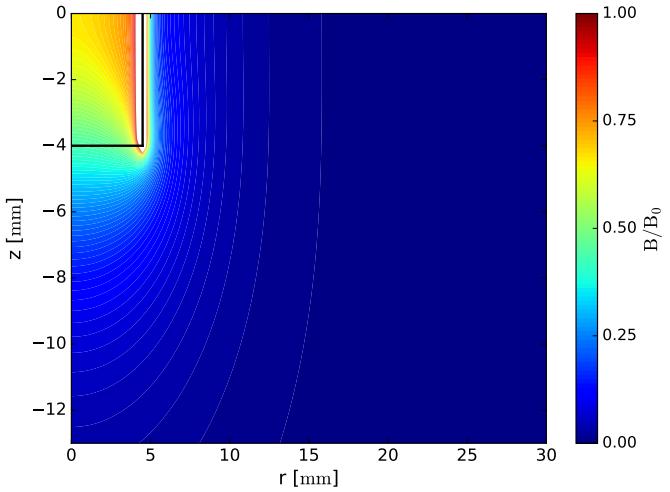

Figure 5.10: Normalized magnetic field ($B_0 = \mu ni$) produced by a finite air coil of length $L = 8\,\text{mm}$ and radius $r = 4.5\,\text{mm}$.

the magnetic dipole moment is related to the volume V and the residual flux density B_r of the magnet by

$$m = \frac{B_r V}{\mu_0}. \tag{5.55}$$

With this assumption, the force produced by one coil acting on the magnet is:

$$\vec{F} = \vec{\nabla}(\vec{m} \cdot \vec{B}) = m\vec{\nabla}B_z. \tag{5.56}$$

The radial component is the one which induces the rotation of the bearing rotor. Its magnitude is shown in Fig. 5.11a as a function of various coil geometries with a fixed distance and the same magnet dimension. Because of volume constrains (i.e. the encoder on the same diameter and the height of the room) the black point indicates the geometry chosen which is the only possible closer to the highest force region. Fig. 5.11b shows the force magnitude as a function of the magnet position between two nearest coils. The mean force per unit current given on a single magnet is $35\,\text{mN}\,\text{A}^{-1}$ which corresponds to a total force (8 magnets) of $280\,\text{mN}\,\text{A}^{-1}$ and requires an average current $\sim$30 mA (thanks to Eq. 5.54).

One coil is represented in Fig. 5.12a. The geometry chosen corresponds to 8 mm length and 7.8 mm diameter with 200 turns of 0.2 mm diameter copper wire. The resistance and inductance of all 70 coils were measured and both distributions are plotted in Fig. 5.12b. 4 coils (the ones on the left side) were rejected and the others were divided in 8 series with total resistance as homogeneous as possible ($\sim$27.6 Ω). After the assembly on the support ring the final resistance of each series becomes 28.6±0.1 Ω. The increased resistance is due to connections between coils and the connector on the stage.

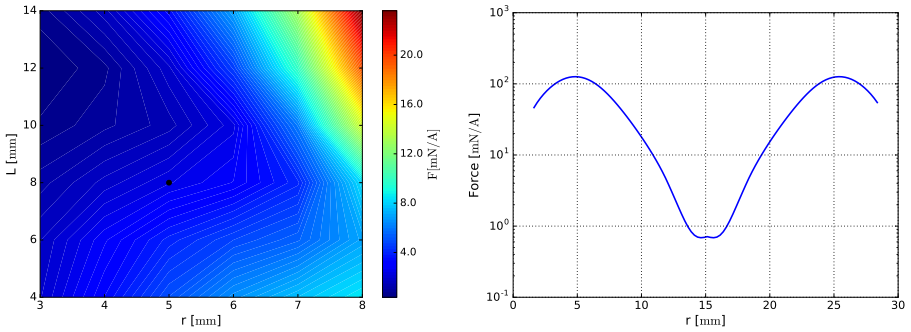

(a) (b)

Figure 5.11: (a) Radial component of force for various coil geometries. (b) Force magnitude as a function of the magnet position between two nearest coils.

The expected resistance in the cryogenic environment is $\frac{28.6\,\Omega}{RRR} = 1.0\,\Omega$. The circuit can be sketched as an RL series and the current in each coils is:

$$i = \frac{V_{in}}{R + j\omega L} \tag{5.57}$$

where V_{in} is the input voltage, $R \sim 9.5{+}1.0\,\Omega$ the resistance of the wires between room and cryogenic temperature and the resistance of one coil series and $L = 1.9\,\text{mH}$ the inductance of the series. Because the condition $R \gg \omega L$ is verified we expect a constant value of current for applied input voltage at different frequencies during the acceleration phase.

5.2.8 Encoder readout system

The readout position system for the PMU is based on optical encoder, based on light shining onto a photodiode through slits in the rotor. There are two different encoders: an absolute one with a single slit and a relative one composed by 64 evenly spaced slits (4 mm diameter). To avoid possible dissipation of LED or photodiode at cryogenic temperature, we use two pairs of optical fibers. Each pair consists in a fiber connected to a transmitter (HFBR-1412TMZ[4]) at room temperature, reaching the top surface of the encoder chopper ring, and a return fiber starting from the bottom surface of the optical chopper and reaching the detector (BPX61 photodiode[5]) at room temperature.

The transmitted signal is modulated at a frequency of 31 kHz produced by a quartz crystal oscillator circuit. The signal detected by the photodiodes is pre-amplified and then demodulated and amplified again by an AD630 lock-in, allowing to separate a small narrow-band signal from large amounts of uncorrelated noise produced by the significant light loss due to an air-gap of about

[4] https://it.rs-online.com/web/p/trasmettitori-a-fibre-ottiche/8019229/
[5] https://it.rs-online.com/web/p/fotodiodi/6547785/

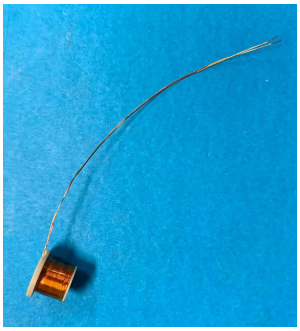

(a)

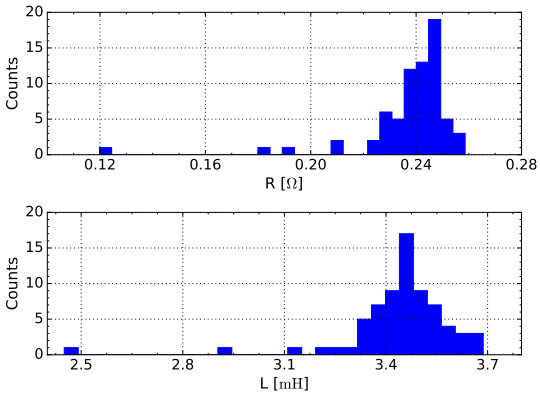

(b)

Figure 5.12: (a) Motor coil. (b) Distribution of the 70th coil resistances and inductances. The 4 coils (left) with measured values far from the distribution center were excluded.

$\sim$10 mm between the back-to-back optical fibers. The fibers are mounted in a PEEK holder (Fig. 5.13c) to nullify eddy currents due to the proximity to moving magnets. The signals produce high/low pulses which are transmitted to a single-board microcontroller. When the level of signal is above a threshold, a timestamp is settled with a µs resolution, giving an angular resolution greater than 0.01°. The conductive heat load produced by the 4 optical fibers is $\lesssim$ 50 µW.

5.3 Motor test

We developed a room temperature mockup to validate the motor, the relative driver/readout electronics, the eddy currents model, the main magnet inhomogeneities and the spinning frequency stablity. In place of the superconducting magnetic bearing we used a ball bearing[6] with low coefficient of friction.

Fig. 5.13a shows a section of the CAD model: in the center there are 2 ball bearings (blue) separated by an aluminum spacer. The umbrella support in the center keeps in position a lightened aluminum disk ($\sim$2 kg). The set of 64 coils (the smaller in yellow) is positioned on the top of the external part of the main disk and is coupled with 8 small Neodymium motor magnets (8 mm diameter) hosted in the rotating disk. On the same diameter there are 64 evenly spaced holes of the encoder readout system. Fig. 5.13b shows the assembled system.

First of all we mounted only the bearing and the encoder in order to quantify the friction of the bearing with and without the drive motor magnets. The friction is quantified in terms of power loss and measured by spinning the rotor

[6] `https://www.skf.com/it/index.html`

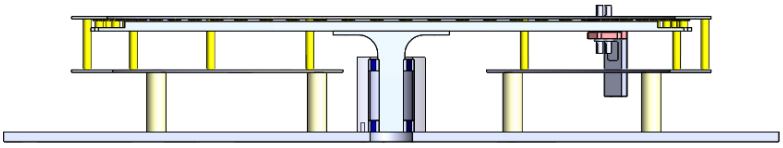

(a) Section of room temperature mockup design.

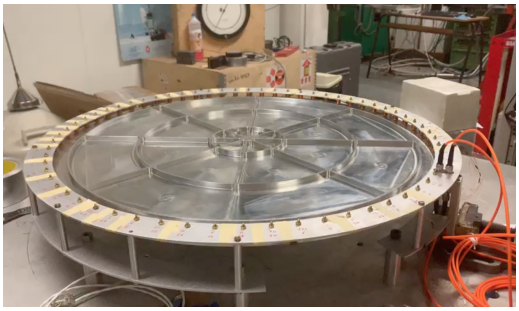

(b) Room temperature mockup.

(c) PEEK holder.

Figure 5.13: (a) CAD section of the room-temperature mockup, composed by 2 ball bearings (blue) separated by an aluminum spacer allowing to rotate an umbrella support which keeps in position a lightened aluminum disk (∼2 kg). (b) Picture of the room-temperature mockup rotating. The rotation is induced by a set of 64 coils mounted on the upper aluminum ring coupled with 8 small Neodymium motor magnets hosted in the rotating disk. (c) Detail of the PEEK encoder holder coupled with 64 evenly spaced holes on the rotor.

up to ∼1.6 Hz and then letting it free to slow down, while reading its angular position versus time with the optical encoder. The rotation of the system is described by the equation of motion:

$$\tau(i) - \tau_f(\omega) = I\frac{d\omega}{dt} \tag{5.58}$$

where τ is the external momentum applied to spin the rotor, τ_f is the momentum of friction forces, I is the moment of inertia of the rotating system and ω the angular velocity of the rotor we measure. When the bearing is free to slow down ($\tau = 0$) we can convert Eq. 5.58 into an equation for the dissipated power:

$$\tau_f(\omega) = \frac{P_f(\omega)}{\omega} \;\rightarrow\; P_f(\omega) = -\omega I\frac{d\omega}{dt}. \tag{5.59}$$

The measured values of the power dissipated for both configurations (P_0 for 0 magnets and P_8 for the 8 motor magnets) are reported in Fig. 5.14a. The small difference should be produced by eddy currents in the temporary iron support of the optical fibers holder, which will not be present in the final configuration.

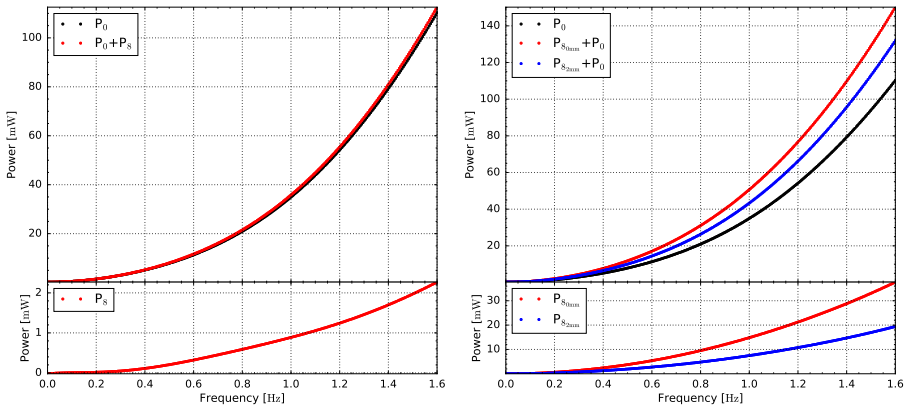

(a) (b)

Figure 5.14: Undersampled data of spin down tests processed by Eq. 5.59: (a) Power loss produced only by the rotor (P_0) and by the drive motor magnets (P_8). (b) Power loss produced by the drive motor magnets on the aluminum coil ring for the standard distance ($P_{8_{2\,mm}}$) and 2 mm closer ($P_{8_{0\,mm}}$).

After this test, all surrounding supports were mounted one by one, with negligible effects on total power loss, except for the aluminum ring which keeps in position the driving coils. Its contribution was measured for different distances, the nominal one ($P_{8_{2\,mm}}$) and 2 mm closer ($P_{8_{0\,mm}}$), and is clearly visible in Fig. 5.14b. As expected the power loss has a quadratic dependence of frequency, producing 7.4 mW at 1 Hz. In order to completely remove this contribution we decided to replace the aluminum ring supporting the coils with a G10 ring which is an electrical insulator.

5.3.1 Drive system

We developed a custom electronics (Fig. 5.16a) to control the spin of the rotor. All electrical components are qualified for the stratospheric pressure ($\sim$ mbar) and certified up to -40°. The electronic box will be heat sinked to a heater at a temperature $> -40°$ to remain warmer than the external environment ($\sim -70°$). The central idea of the drive system is a PI (Proportional-Integrated) feedback control composed by two optical encoders, an electronic platform, a voltage generator and the coils. A schematic diagram is shown in Fig. 5.15. The PI feedback controls both the frequency of pulses (allowing to spin up the rotor) and the magnitude of the current 8 times per round, to stabilize the rotation when the right frequency is reached. We decide to not use the classical PID controller with the derivative term because we do not expect fast variations of the rotational speed due to the high inertia of the system.

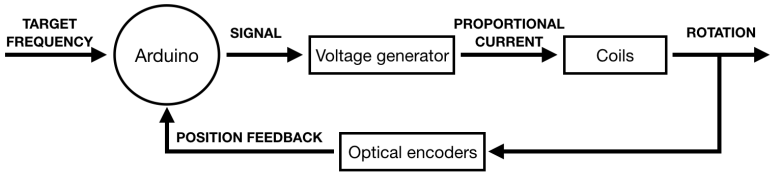

Figure 5.15: The PI feedback control: the user choses the target frequency, Arduino gives a signal to a current generator to control the amplitude and the frequency of the current in the coils. Two optical encoders monitor the position and the speed of the plate.

The electronic platform chosen is Arduino. The initial parameter given by the user at the beginning is the target frequency of the rotor which should be changed during the operation. Knowing the position of the 8 magnets (one every 8 slits), the relative phase of current in each series of coils is determined (Fig. 5.16b). The maximum value of the current is reached when the magnets are in the middle of two coils. There is another small phase dependent on the frequency, inserted to optimize the system.

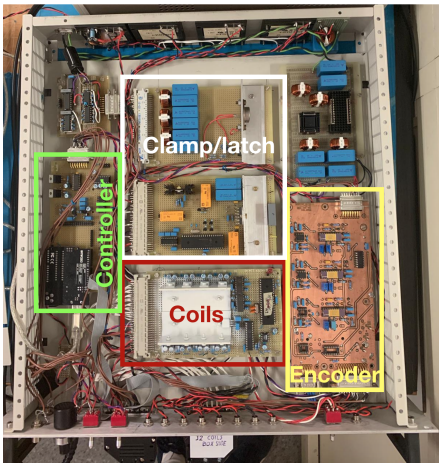

(a) Electronic box.

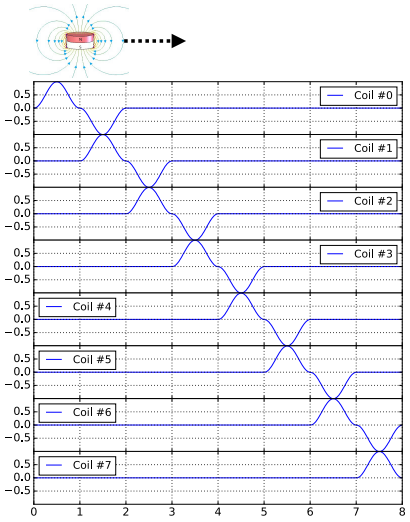

(b) Coil current shape.

Figure 5.16: (a) Electronics control box, composed mainly by 4 different boards: the microcontroller, the voltage generator, the clamp and latch (see §5.4) controller and the encoder readout. (b) Smooth current pulses generated to supply the driver coils and push/pull on the rotor magnets.

In the first version of the electronics we made a voltage generator with output voltage of 6.35 V_{PP} allowing a maximum average current of $\sim 55\,mA$ ($\sim 1\,A$ at

1.6 K). On the other hand, we measured a back electromotive force produced by the small magnets of $4\,V_{PP}Hz^{-1}$, so the effective current flowing in the coils is:

$$\bar{i}[A] \simeq \frac{0.25}{R[\Omega]}(V_{PP}[V] - 4f[Hz]) \tag{5.60}$$

For this reason we decided to switch to current generators, with the same voltage amplitude and high impedance ($\sim$ kΩ). The rotor, with the main magnet installed, can reach a maximum spin frequency of 0.59 Hz which means 17 mW of opposing friction force.

5.3.2 Magnet inhomogeneities

The main magnet was designed to maximize the magnetic field in proximity of the superconductors and minimize inhomogeneities. It is made of 2 neodymium rings sandwiched between three iron rings. Each neodymium ring is splitted in 32 segments and the junctions are out of phase to reduce the inhomogeneities (Fig. 5.17a).

The magnetic field is monitored by means of a Hall sensor[7] also suitable for cryogenic application. The power dissipation in the sensor is 180 µW with a bias current of 10 mA over a 1.8 Ω resistance. Measurements (Fig. 5.17b) are performed at different heights and distances from the steady magnet. Both peaks coincide with the upper and lower iron rings while the center ($\sim$ 0 mT) coincides with the middle.

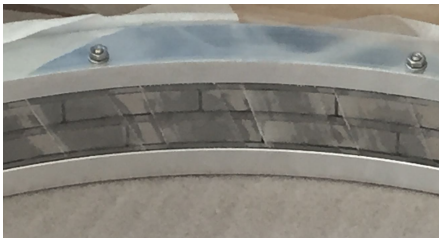

(a) Detail of the main magnet.

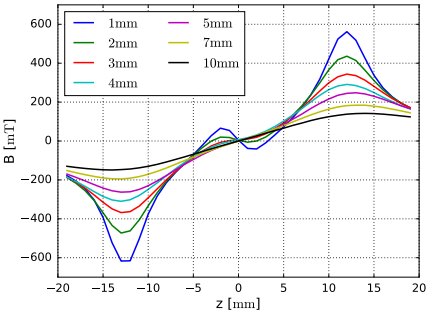

(b) Magnetic field.

Figure 5.17: (a) Detail of the main magnet structure.(b) Magnetic field as a function of height ($z = 0$ mm is the center of the middle iron ring) for various distances from the main magnet.

For the measurement of power dissipation from the main magnet, the main magnet is installed on the room temperature rotor and spins while the Hall sensor monitors the magnetic field for different heights at a fixed distance of a few mm. After a removal of sine component induced by a slight misalignment

[7] https://www.cryomagnetics.com/products/hall-effect-sensors/

of the rotation axis ($\sim 0.5°$), Fig. 5.18 shows the magnetic field average for each quote and the relative inhomogeneity. At the peak of the magnetic field, the relative inhomogeneity corresponds to $\lesssim 2\%$.

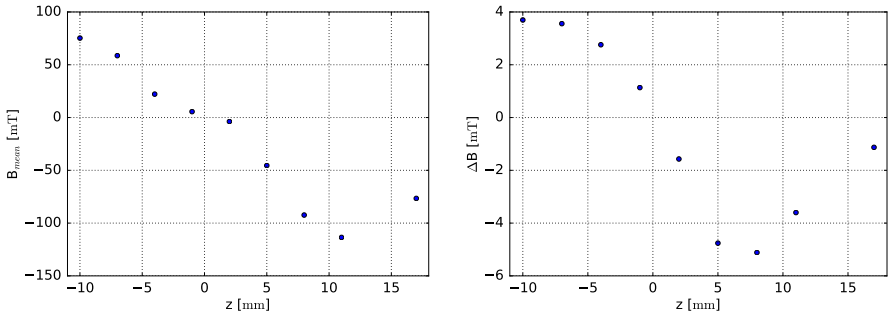

(a) Magnetic field average. (b) Magnetic field inhomogeneity

Figure 5.18: Magnetic field average (a) for different quotes at few mm from the magnet and the relative inhomogeneities (b).

After these tests, we evaluate the impact of these inhomogeneities in terms of friction produced in the whole setup (except the YBCO ring). If we compare the bottom panel of Fig. 5.19a with the blue line in the bottom panel of Fig. 5.14b we note a very similar trend. This means that the impact of the main magnet in terms of friction (except for the YBCO ring) is negligible.

At the end we installed the YBCO holder in the setup and removed all conductive materials. In this way the only contributions to friction comes from the eddy currents on the YBCO holder produced by the motor magnets and by the main magnet. As expected (see §5.2.5) the contribution of the motor magnets is low (0.8 mW at 1 Hz) while the friction produced by the main magnet is 6.2 mW.

5.3.3 Expected heat load performance

The performance we measured at 300 K and the performance we expect at 1.6 K (given the room temperature measurements), are summarized in Tab. 5.2 for a rotation frequency of 1 Hz. Material properties, such as electrical conductivity, thermal conductivity and YBCO critical current, were assumed to be the same as 4 K [123, 124].

In the first configuration the friction produced by the motor magnets is 9.2 mW. Most of this power comes from eddy currents produced on the aluminum ring which holds the coils in place. By replacing this ring with a G10 one the residual contribution is 0.8 mW. By assuming a RRR = 2.8 of aluminum (6082-T6) the expected contribution at cryogenic temperature is 2.2 mW, similar to the simulated one (see §5.2.5).

As for the friction produced by the main magnet inhomogeneities, we can reduce it from 6.2 mW to 1.3 mW by reducing the wobbling of the rotor in the

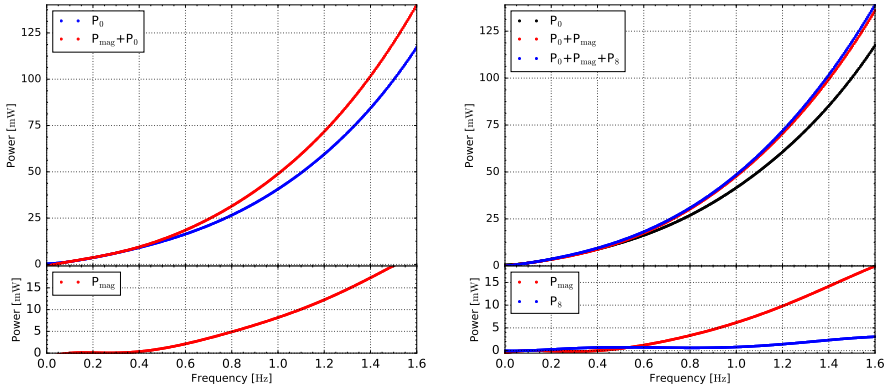

(a) (b)

Figure 5.19: Undersampled data of spin down tests processed by Eq. 5.59: (a) Friction measured removing all conductive materials nearby the rotor (P_0) and for the whole setup (P_{mag}) except the YBCO ring. (b) Same test but the YBCO aluminum holder was installed, with (P_8) and without (P_{mag}) the motor magnets.

	P [mW] - 300 K		**P** [mW] - 1.6 K
	Measured	**Optimized**	**Expected**
8 magnets	9.2	0.8	2.2
Main magnet	6.2	1.3	3.5
Hysteresis	-	-	10
Joule	1200	645	6.1
Harness	-	-	3.2
Bearing	41.5	41.5	-
Total	1260	690	25

Table 5.2: Performance measured at 300 K and performance expected at 1.6 K for a rotation frequency of 1 Hz.

room temperature mockup. The expected value of 3.5 mW should be reduced even more by the presence of the superconductor which will shield part of the magnetic field.

The hysteresis contribution will be tested only in the cryogenic environment. Since the mass of the rotor is 9.5 kg and the vertical spring constant of the system is 2-3 $\times 10^5$ N m^{-1}, we expect a fall of the rotor after the release < 0.5 mm. Starting from §5.2.2 and from the magnetic field profile we can estimate the hysteresis contribution which will be 5-10 mW.

Assuming the worst case the total friction during rotation at 1 Hz is 15 mW.

Considering the efficiency of the motor, we need $\bar{i} = 45\,\mathrm{mA}$ which produce a Joule heating of 6.1 mW. The total expected power load on the 1.6 K stage is $\sim 25\,\mathrm{mW}$ which is an acceptable contribution if compared to the total $\sim 180\,\mathrm{mW}$ present on the superfluid helium bath and does not considerably impact the duration of the flight ($\sim 15\,\mathrm{d}$).

5.4 Clamp and release system

For the SWIPE polarization modulator we developed a simple and reliable clamp/release system [125] which has: large rotor mass compliance ($\sim 10\,\mathrm{kg}$); zero power dissipation while holding the rotor, zero power dissipation when the rotor is released; fast ($\sim 40\,\mathrm{ms}$), balanced release and clamp actions, low power dissipation ($\sim 30\,\mathrm{J}$) on the cold stage during each operation; low cost; and high reliability over a very large number of operation cycles. We expect to clamp and release the rotor only once at the beginning of the flight, nevertheless the system was designed to be able to clamp and release the rotor as many times as necessary.

5.4.1 General design

The rotor is held above the stator by the clamp / release mechanism, keeping it in place during the cooldown process, until the transition temperature of the YBCO bulks is reached and the magnetic field is frozen. Thereafter, the rotor is kept in place by the magnetic field, the clamps can be released, and the electromagnetic motor can be activated to spin the rotor [126]. If for any reason the rotation has to be stopped (for example to cool-down the HWP), the mechanism can be activated to clamp the rotor back.

The clamp / release mechanism is composed of 3 linear actuators, radially oriented towards the center of the HWP ring, spaced 120° in azimuth, and pushing against a groove on the external side of the HWP rotor ring. Each of the 3 identical actuators, is composed of (i) a commercial customized linear actuator, (ii) a latch system and (iii) a Teflon head coupling with the groove on the rotor and clamping it.

Fig. 5.20 shows one of the three system completely assembled during tests while Fig. 5.21 shows its section from the CAD design.

The core of each linear actuator is a Low Profile Linear DC Solenoid produced by Johnson Electric. This type of solenoid is called linear solenoid due to the linear directional movement and action of the plunger. Linear pull-type solenoids are available in two basic design generally named “flat-face” and “conical-face”, which differ in the shape of the interface between the moving and the static parts. The three solenoids are connected in series to be activated simultaneously. When the supply current is turned “OFF” (de-energised) the magnetic field generated previously by the coil collapses and the plunger is free to move. When the supply current is turned “ON” an electrical current flows in the coils windings, behaving like an electromagnet, and the plunger is attracted

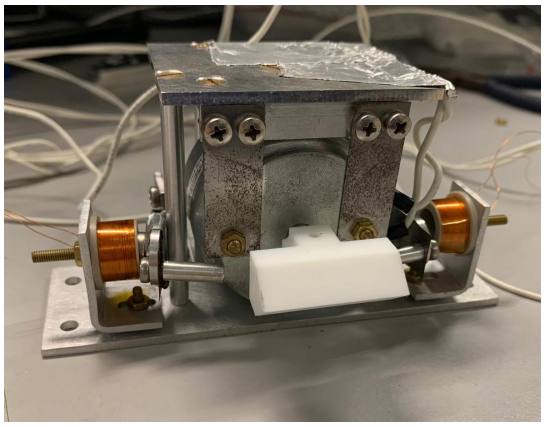

Figure 5.20: Assembly of the clamp / release system. For more details see Fig. 5.21.

towards the center of the coil by the magnetic flux. Usually the force and speed of the plungers movement is determined by the strength of the magnetic flux generated within the coil. With respect to the flat-face designs, which has higher efficiency but only for shorter strokes, a conical-faced designs extends the useful range of a solenoid, typically over 1.5 mm, and provides higher force for the same stroke.

The actuator we have selected[8] has a conical-face design with 1380 turns of copper wire AWG29 and a total resistance of 38 Ω at room temperature. To allow a frictionless movement of the plunger, we modified the actuator removing its central bushing, originally keeping in place and supporting the plunger shaft. The plunger shaft is now suspended by means of three flat springs obtained from thin sheets (thickness 0.3 mm) of spring steel. These can be bent, allowing for a frictionless linear movement of the plunger shaft along its axis ($\hat{r}$ direction; see Fig. 5.21).

The actuators are mounted so that at rest (no current in the coils) the Teflon heads press against the groove in the rotor, keeping it strongly in place. This rest position of the plunger corresponds to a stroke of ~ 3 mm with respect to the position where the flat springs are not bent. The hold force is produced by bending the flat springs, and is of the order of 30 N. This can be increased if needed, with the addition of a spring which can be added on the outer end of the shaft (opposite to the Teflon head).

When the actuator is turned ON, the plunger is retracted by 3 mm. At this point, we need a latch system, otherwise we would be forced to drive current through the coils during the whole duration of the measurements. The latch is composed of 2 small cylinders, moved by 2 electromagnets. These cylinders are introduced in the gap between the plunger disc and a static surface located

[8] Low Profile Linear DC Solenoids, model 5SFM. `https://www.johnsonelectric.com/en/product-technology/motion/solenoids/low-profile-linear-dc-solenoids`

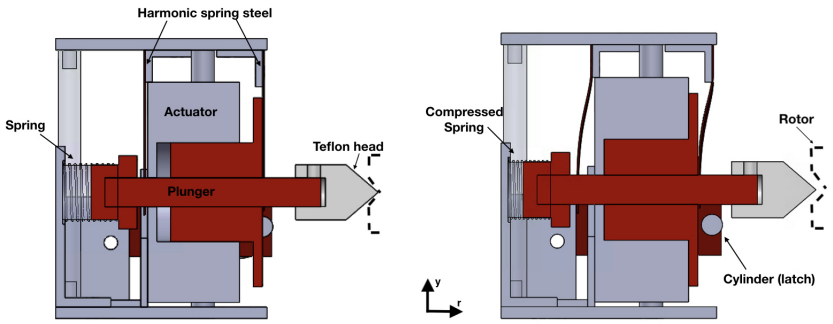

Figure 5.21: Cross sections of one of the 3 linear actuators composing the clamp/release system. The teflon head is mounted on the plunger shaft, which is kept in place by means of 3 flat springs made of harmonic steel (one on the plunger in the back and 2 on the plunger disk in the front). In the left panel, the actuator is holding the SMB rotor, with the teflon head engaging a complementary triangle-section groove on the outer side of the rotor. In the right panel, a current of $\sim$0.7 A is flown in the actuator coil, the plunger shaft is retracted by $\sim$3 mm in the radial direction, releasing the SMB rotor. Two small cylinders are inserted between the plunger disk and a fixed metal part, latching the head in the retracted position. At this point the current flow in the actuator coil can be interrupted, and the actuator can remain in the retracted position as long as needed.

in front of the actuator. Each cylinder is supported by another harmonic steel sheet (thickness 0.1 mm) and is free to move when the actuator is ON. A small Neodymium permanent magnet (8 mm in diameter and 2 mm thick) is attached on the external side of the cylinder. It is paired with an air coil (10 mm diameter) with a number of coils per unit length $n \sim 2 \cdot 10^5 m^{-1}$, wrapped on a thin empty fiberglass cylinder. By flowing current in both directions we are able to attract or repel the small magnet and so to insert/remove the small cylinder in/from the gap. If both cylinders are in the gap and we switch OFF the actuator, the springs try to bring the shaft back to the initial position but the cylinders work as a locking device between the two surfaces. In this way the end of the Teflon clamp is safely maintained $\sim$ 3 mm back with respect to the hold position. When we want to clamp back the rotor, we just need to switch ON the actuator, letting the cylinders free, retract them, and turn OFF the actuator.

5.4.2 Expected dynamic performance

To describe the release of one of the three clamps we can model the system as a 1D system subject to the force from the bearing ($-kx$) and the force from the actuator (F):

$$m\frac{d^2x}{dt^2} = F - kx \tag{5.61}$$

where $k = 10^5$ N/m is the estimated harmonic constant of our superconducting magnetic bearing, x the position of the rotor respect to the rest position and $F \sim 40\,\mathrm{N}$ corresponds to 4 times the minimal actuator force required to hold the rotor. Solving the equation we find the solution:

$$x(t) = \begin{cases} -\frac{F}{k}\cos(\omega t) + \frac{F}{k} & if \quad 0 \le t < t^* \\ \frac{v(t^*)}{\omega}\cos(\omega t) + x(t^*)\sin(\omega t) & if \quad t \ge t^* \end{cases}$$

where $\omega = \sqrt{k/m}$, $t = 0$ is the release time of two of the three actuators, and $t = t^*$ is the release of the delayed actuator. The delayed release of one of the actuators should be produced only by differences in manufacturing, which is accurate to a few %. If we assume a delay of 5% ($t^* = 2\,\mathrm{ms}$, see section 5.4.3), we can find the displacement induced on the rotor until the complete release, $x(t^*) = 8\,\mu\mathrm{m}$, and its velocity $v(t^*) = 8\,\mathrm{mm/s}$. After the complete release we have a simple harmonic oscillation, described in the second equation, with the initial conditions described above. The amplitude of the induced oscillation is thus $\simeq v(t^*)/\omega = 80\,\mu\mathrm{m}$. This can be considered as an upper limit, since the actuator force decreases during the delayed release as the actuator retracts. Moreover, due to the small residual friction, the oscillation will be damped to some extent. A lateral oscillation of the HWP can be dangerous mainly because it can induce a modulation of the background in beam sidelobes. For this reason, the edge of the HWP is optically masked by a $\sim$ cm narrower cold stop, which precludes its view from the detectors. We conclude that if the delay is, as expected, of the order of few ms, the induced $\sim 80\,\mu\mathrm{m}$ oscillation is masked and thus harmless.

5.4.3 Tests

Room temperature test

A load test at room temperature was performed loading the central test disk with lead masses of 1.5 kg (Fig. 5.22). The clamp/release system, even without the additional springs at the outer ends of the shafts, is able to hold a 10.5 kg rotor.

We measure the release time of the actuators by means of a red laser-diode beam going through the gap between the static and the moving part of one of the actuators, when the actuators are holding the disk. The laser light produces a negative current signal in a fast photodiode, placed on the opposite side of the actuator, which is monitored by an oscilloscope measuring the current through a $1000\,\Omega$ shunt (bottom trace in figure Fig. 5.23). The other channel of the oscilloscope measures the voltage across a $10\,\Omega$ resistor in series to the coils (top trace in Fig. 5.23), which is proportional to the current through the coils. When the actuator is turned ON, flowing current through the coils, the moving

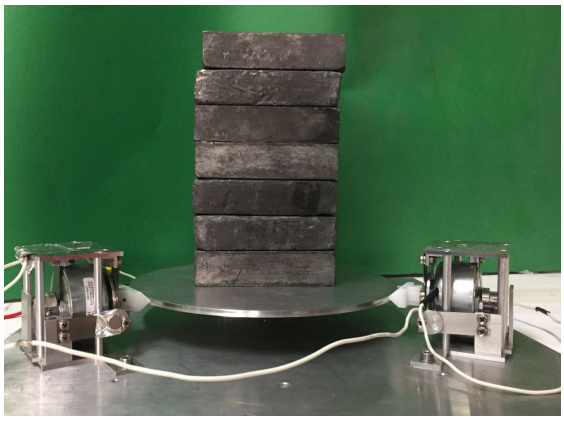

Figure 5.22: The clamp/release system is able to hold $\sim 10.5\,\mathrm{kg}$.

disc on the plunger retracts, and its disk interrupts the laser beam, so that the photodiode signal goes to zero. The two traces recorded in Fig. 5.23 demonstrate that the time needed to completely release the rotor is 40 ms.

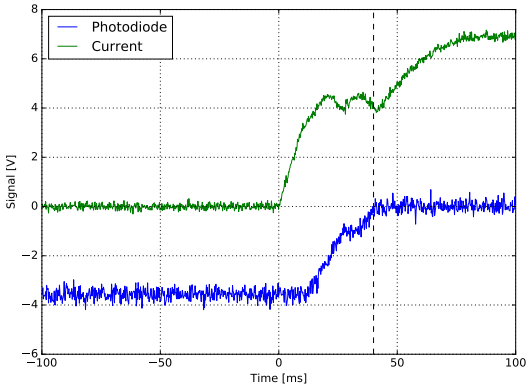

Figure 5.23: Measurement of the release time of the actuators (see text). The photodiode signal (bottom trace) goes to zero when the actuator is completely retracted. The delay between this event and the start of current flow in the coils (top trace, representing the voltage produced by the current in the coils across a $10\,\Omega$ series resistor) measures the release time of the system: about 40 ms.

Cryogenic test

One of the actuators was mounted in a test cryostat (Fig. 5.24), on a copper cold plate cooled to 4.8 K by a two-stage pulse-tube cryocooler. The temperature

of the system is monitored with four-wire-read DT-670 Series silicon diodes[9] mounted directly on the actuator and read out using commercial 10 µA current generators and a laboratory voltmeter.

To monitor the actuator during tests we installed in the cryostat a camera module[10] which includes white LEDs for subject illumination. The camera is not rated for cryogenic operation, so we mounted it on a fiberglass standoff, both to prevent electrical shorts on the back side of the printed circuit boards and to reduce the thermal conductance between the camera and the cold plate. In the vacuum environment inside the cryostat, there is no convective heat transfer, and radiative heat transfer is also negligible, so the camera remains operative thanks to its own power dissipation.

We use phosphorous-bronze wires (0.2 mm diameter, 3 m long) and copper wires (0.2 mm diameter, 4 m long) to carry the actuator and latch coil currents from room temperature to the 4 K stage of the cryostat. The wires are thermalized at an intermediate temperature (68 K). This results in negligible heat load (2 mW) on the coldest stage of the cryogenic system.

At 4.8 K the copper resistance of the actuator coil lowers to 6.5 Ω while the copper resistance of the latch coils becomes $< 1\,\Omega$. The actuator coil needs a current pulse of 0.7 A and the latch coils need a pulse of 0.9 A, with a duration <2 s, to activate the actuator and push the latch cylinders. The overall estimated heat load for each operation of the clamp / release system, for 3 actuators and the relative latch systems connected in series is 29 J in the coils, loading the 4 K stage, plus 9 J in the wires, distributed between the 68 K stage and the 4 K stage.

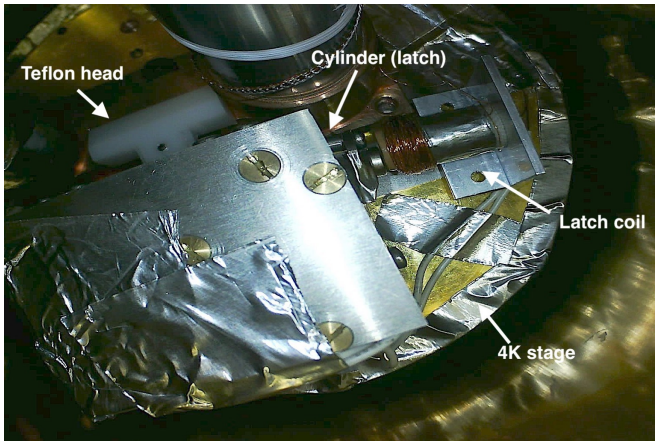

Figure 5.24: Image of the cryogenic test setup, taken with the internal CCD camera used to monitor the movement of the actuator head and latches.

[9] https://www.lakeshore.com/products/Cryogenic-Temperature-Sensors/Silicon-Diodes/DT-670/Pages/Overview.aspx

[10] https://shop.leopardimaging.com/searchquick-submit.sc?keywords=LI-OV5640-USB-72

The actuator has been activated hundreds times at different temperatures, without any failure and consistently moving the Teflon head and the two latches, as monitored continuously with the video camera.

Chapter 6

The cryogenic HWP rotator for LiteBIRD

Lite (Light) satellite for the studies of B-mode polarization and Inflation from cosmic background Radiation Detection (LiteBIRD) mission is the next step in the series of CMB space missions, COBE, WMAP, and Planck, each of which has given landmark scientific discoveries. A detection of primordial gravitational waves with LiteBIRD (at a level $r = 0.001$) would indicate that inflation occurred near the energy scale associated with grand unified theories, and would provide additional evidence in favor of the idea of the unification of forces. Additionally, the energy scale of inflation has important implications for other aspects of fundamental physics, such as axions and, in the context of string theory, the fields that control the shapes and sizes of the compact dimensions.

Furthermore, LiteBIRD's ability to measure the entire sky at the largest angular scales with 15 frequency bands is complementary to that of ground-based experiments which will focus on deep observations of low-foreground sky. LiteBIRD can provide valuable foreground information for ground- based experiments and ground-based experiments can improve LiteBIRD observations with high- resolution lensing data.

6.1 Instrumental overview

LiteBIRD will be launched on a H3 rocket from Japan in 2028 and it is composed of three instruments: the low frequency telescope (LFT), the medium frequency telescope (MFT) and the high frequency telescope (HFT).

The satellite works on a Lissajou orbit around the Sun-Earth L2 point. The observing strategy consists of a 0.05 RPM spin with telescope boresight offset 50° from the spin axis along with a precession of the spin axis that gives one observation of the entire sky every 6 months. The entire sky is observed 6 times during the 3-year mission lifetime (baseline).

An octagonal V-grooves system is used for passive radiative cooling and a

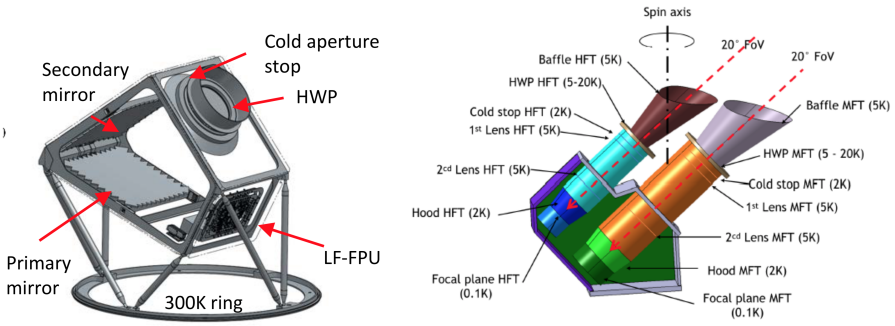

(a) Low frequency telescope (LFT). (b) Medium and high frequency telescopes (MHFT).

Figure 6.1: The LiteBIRD scientific payload composed by three instruments: the low frequency telescope (a) and the medium-high frequency telescope (b).

pulse-tube cooler provide a 20 K stage. Other mechanical cryocoolers (ESA) cool down the telescopes up to 5 K, an adiabatic demagnetization refrigerators (NASA) to 1.8 K, and a second-stage ADRs (CNES) to 0.1 K.

The first optical element in each telescope is a continuously rotating HWP based on a superconducting magnetic bearing to levitate the HWP. The LiteBIRD HWPs will be held using a launch lock and released during flight. The HWP will be radiatively cooled to the ambient 5 K. The HWP for LFT consists in an achromatic 9-layer sapphire HWP to achieve the required bandwidth [127]. A large bandwidth anti-reflection coating is required for this system. For MFT and HFT, meta-material technology is planned to be used for ultra-light HWPs.

The baseline design is a crossed-Dragone 40 cm aperture telescope for LFT and two refractive telescopes (Polyethylene lenses) with 30 cm (MFT) and 20 cm apertures (HFT).

The three focal planes for the LFT, MFT, and HFT are shown in Fig. 6.2. The focal-plane modules have 9 different staggered frequency schedules to observe at 15 frequency bands to characterize foregrounds accurately. The LFT and MFT will use broadband dual-polarized lenslet coupled sinuous antenna detector arrays. The detector architecture as shown in Fig. 6.2 has been developed at the University of California, Berkeley[128] . The sinuous is a planar broadband polarization-sensitive antenna, and the contacting anti-reflection-coated lenslet increases the forward gain of the antenna. On-chip bandpass filters partition the broadband RF signal into target frequency bands. Transition-Edge Sensor (TES) sensors on the bolometers are used to detect the RF power in the different bands.

The HFT will use orthomode transducer (OMT) coupled horn antenna detectors. The horn-coupled antenna detector was chosen for HFT for its maturity and the lower total sensitivity requirements in this frequency range. The horn-

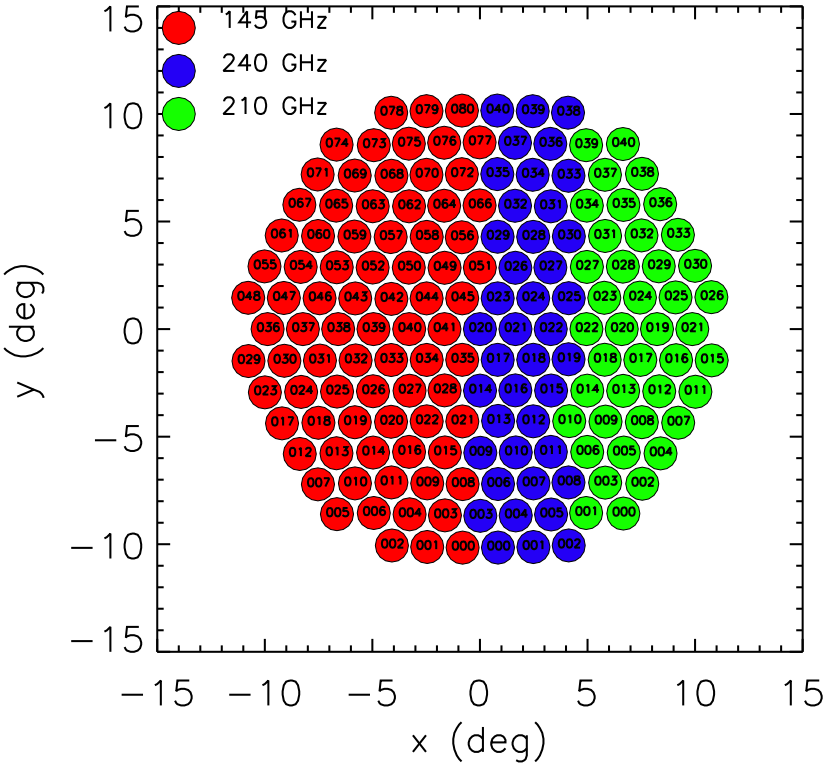

Figure 6.2: Detector focal planes. LFT focal plane will use broadband dual-polarized lenslet coupled sinuous antenna detector arrays while MHFT will use orthomode transducer coupled horn antenna detectors.

coupled antenna architecture has been developed at NIST. Horns and waveguides are fabricated by stacking multiple layers of microfabricated silicon wafers with gold plate coating. The RF is then coupled by probe "fins" that extende into the waveguide. Similar to a lensle-coupled detector, the RF is partitioned into bands by on-chip filters then detected by TES sensors.

6.2 Polarization modulator units

For the design of both polarization modulator units (PMUs) for MHFT the baseline is a continuously rotating HWP with lots of stringent requirements in terms of mass, dimension, stiffness, power dissipation, and TRL, for the levitation, driving and gripping mechanisms as well as position encoder. The most important for both PMUs are:

- spin rate of 39 rpm and 61 rpm for MFT and HFT;
- HWP diameter of 220 mm and 320 mm;
- temperature < 20 K for both HWPs;
- total power load on the 5 K stage < 4 mW;
- total mass < 20 kg.

In the next sections we analyze the baseline design, which consists in a scaled version of the SWIPE one, with further optimizations. These have been studied but not yet tested experimentally.

6.2.1 Baseline design

The baseline design of the bearing is a scaled version of the SWIPE one (see §5.2) with a permanent magnet ring (2 segmented neodymium rings and 3 iron rings) radially faced to a segmented YBCO ring (Fig. 6.3b). The total masses of both units are 14.5 kg and 8.5 kg

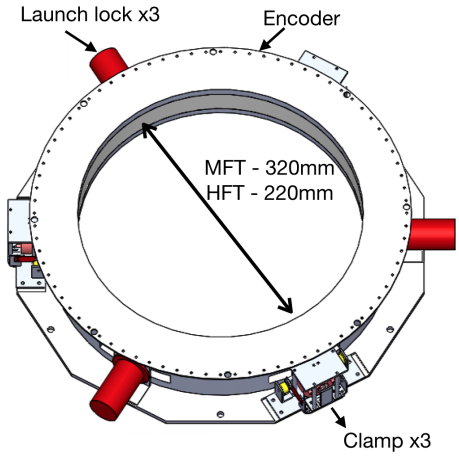

(a) Polarization modulator overview.

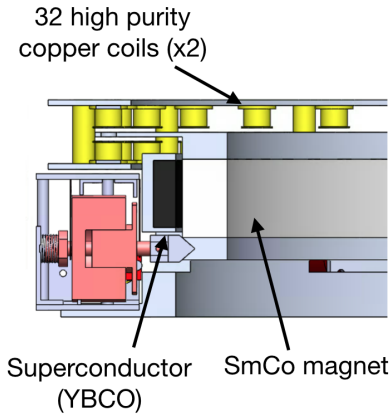

(b) Polarization modulator section.

Figure 6.3: (a) Overview of polarization modulator unit. Both systems have the same design with 3 clamp and release systems and 3 launch locks. (b) Section of the polarization modulator units. 2 coil rings surround the rotor.

There are 3 launch locks[1] to keep in position the rotor during the stress of the launch and release it still at room temperature. After the release, 3 clamp and release systems (Fig. 6.3a) continue to hold the rotor and have the function

[1] https://tiniaerospace.com/products/space-pinpuller/

of cooling down it before its release. We plan to perform a space qualification of the SWIPE clamp systems, and use them.

The concept of the motor is also very similar to the SWIPE one. We plan to use 8 SmCo magnets (2 mm thickness, 9 mm diameter) coupled with 2 rings of 32 coils each, on the top and on the bottom of the rotor to obtain a larger and more uniform force. The coils are connected in series (4 series of 16 coils each). The geometry parameters chosen are reported in Tab. 6.1 while Fig. 6.4 shows the force on each magnet produced by 4 coils (2 on the top and 2 on the bottom).

		MFT	**HFT**
Coil diameter	mm	6	5
Coil length	mm	10	10
n	mm^{-1}	25	25
Resistance (16 coils)	Ω	103	87

Table 6.1: Coils parameters for MFT and HFT. The diameter of the copper wire is 0.2 mm and the resistance reported is assumed at 300 K.

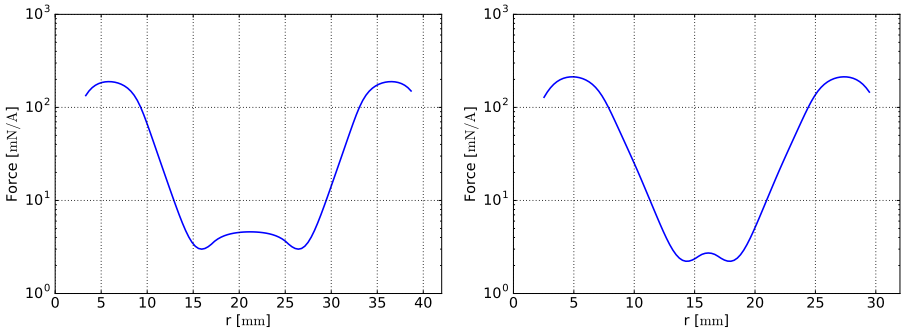

(a) Force for MFT.

(b) Force for HFT.

Figure 6.4: Force produced by 4 coils (2 on the top and 2 on the bottom of the rotor) on a single magnet for MFT (a) and HFT (b).

From the curves of Fig. 6.4, the resulting mean force for MFT (HFT) is $35\,\mathrm{mN\,A^{-1}}$ ($52\,\mathrm{mN\,A^{-1}}$) which corresponds to a total force for 8 magnets of $280\,\mathrm{mN\,A^{-1}}$ ($414\,\mathrm{mN\,A^{-1}}$). Because of the dependence on frequency and magnetic dipole (see Eq. 5.33) we can determine the expected power loss produced by the rotor eddy currents: 1.20 mW for MFT and 1.71 mW for HFT starting from the values we measured in the SWIPE mockup.

Considering the efficiency of the motor (see the performance measured in §5.3.1), to spin the rotor we need to use ~ 5 mA for MFT and ~ 4 mA for HFT producing 0.14 mW and 0.08 mW of Joule losses. The modulated current

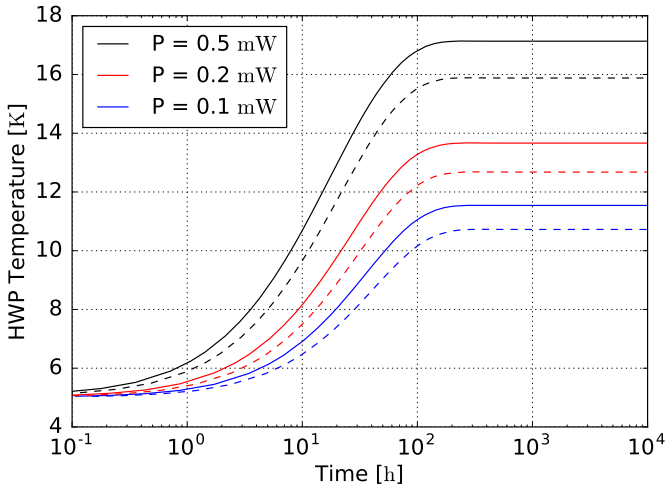

Figure 6.5: Thermal profile of the HWPs as a function of time for different values of power load on the rotor (0.1 mW is the most likely case). Dashed lines correspond to the MFT while continuous lines to the HFT.

in the coils will continuously heat up the rotor until it reaches the equilibrium temperature. This happens because it is not in thermal contact with the stator and the only cooling is by radiation, or by clamping it. The last solution should be avoided because such operation will reduce the total observing time.

We use Comsol Multiphysics to build a thermal model of the rotor surrounded by a 5 K environment. The HWP emissivities are 0.02 and 0.03 for MFT and HFT respectively while the assumed emissivity of aluminum is 0.5 reachable with a blackened surface. The expected dissipation on the rotor is ~ 0.1 mW. We have also analyzed more pessimistic cases (0.2 mW and 0.5 mW). Fig. 6.5 shows that in any case after few days the rotor (HFT continuous lines, MFT dashed lines) reaches the equilibrium temperature which is < 20 K.

As for the harness we need:

- Motor wires: 8 sets of coils are present, requiring 8 different current phases to operate. The current in each of these wires runs roughly for 1/4 of the time, and ranges from 300 mA at startup to less than 4-5 mA during operations. The resistance of the coils is negligible at low temperature, so the resistance of the wires must be minimized to maximize the energy efficiency of the system. We have selected Beryllium-Copper wires for these wires, since they feature a good electrical resistivity and a bad thermal conductivity. The diameter of the wire (0.25 mm) has been optimized as the best tradeoff between heat dissipated in the wire and heat conduction towards the coldest stage. Each wire is doubled for redundancy. So each telescope has 8 (phases) times 2 (go and return) times 2 (redundancy) =

32 wires, i.e. 64 wires for the two telescopes.

- Clamp/release coils wires: these are needed to drive the large current (0.7 A) required by the latch/release coils. Such a current is required for a short time (0.1 s) when actuating, and is zero for the rest of the time. For these wires we have selected the same wires as for the Coils currents. So each telescope has 2 (go and return) times 2 (redundancy) = 4 wires, i.e. 8 wires for the two telescopes.

- Latch coils wires: these are needed to drive the large current (0.7 A) required by the latch coils. Such a current is required for a short time (0.1 s) when actuating, and is zero for the rest of the time. For these wires we have selected the same wires as for the Coils currents. So each telescope has 2 (go and return) times 2 (redundancy) = 4 wires, i.e. 8 wires for the two telescopes.

- Launch Locks wires: these are needed to drive the large current ($\sim$ 1 A) required by the Launch Locks (TBC). Such a current is required for a short time when actuating, and is zero for the rest of the time. For these wires we have selected the same wires as for the Coils currents. So each telescope has 2 (go and return) times 2 (redundancy) = 4 wires, i.e. 8 wires for the two telescopes.

- Capacitive sensors: these are needed to monitor the wobbling of the rotor. Each telescope has 3 capacitive sensor wires (go and return) times 2 (redundancy) = 12 wires, i.e. 24 wires for the two telescopes.

- Hall sensors: these help in reading the position and monitor the wobbling if accurately calibrated. Hall sensors can be used as a redundancy for both systems. Here we take into account only the heat load produced by the wires when the system is turned off. Each telescope has 3 Hall sensors times 4 wires (power, go and return) times 2 (redundancy) = 24 wires, i.e. 48 wires for the two telescopes.

- Spare wires: necessary if something goes wrong. Each telescope has 4 spare wires, i. e. 8 wires for the two telescopes.

We decide to use manganin wires instead of CuBe wires for sensor wires. The total heat load expected for each telescope is shown in Fig. 6.6. The 3 CuBe curves represent different current values needed for the coils (2.5 mA, 5 mA and 10 mA). The total heat load produced by harness is 0.22 mW for each telescope.

We expect hysteresis losses to be very small. This is due both to the absence of gravity which keeps in position the rotor after the release and to the low inhomogeneities of the magnetic field which minimizes hysteresis in the superconductor. We estimate a contribution $\ll 0.5$ mW which will be neglect in our estimation but have to be measured during tests.

The total expected heat load (Tab. 6.2) is 3.73 mW (neglecting hysteresis losses) which is below 4 mW, but with a very small margin.

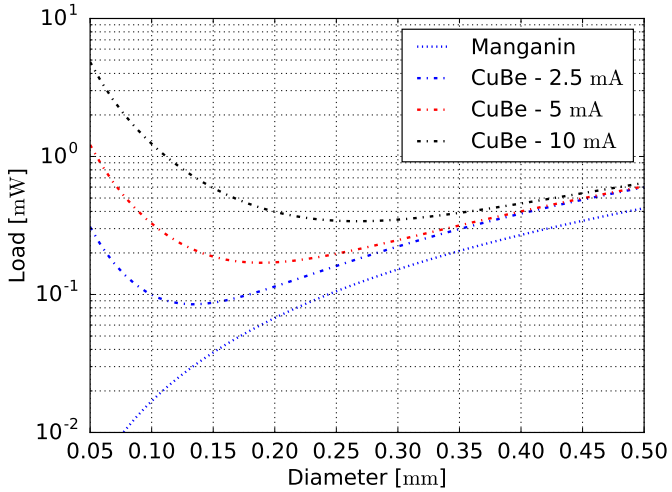

Figure 6.6: Power load produced by the harness of a single PMU. 3 cases of current used in coils were analyzed; the most likely corresponds to 5 mA.

	MFT [mW]	**HFT** [mW]
8 magnets	0.46	0.66
Main magnet	0.74	1.05
Hysteresis	< 0.5	< 0.5
Joule	0.14	0.08
Harness	0.22	0.22
Rotor emission	0.09	0.07
Total	1.65	2.08

Table 6.2: Expected heat load on the 5 K stage produced by PMUs. The contribution of hysteresis was not included in the total.

6.2.2 Optimized design

Simulations have shown that the eddy currents produced by the rotor could be responsible for most of the power dissipation. Minimize them is the first goal for an optimized design.

We propose two solutions:

- Reducing the inhomogeneities of the magnetic field from ∼2% to ∼1% will reduce the eddy currents by a factor 4. This is complicated but seems feasible because of the smaller dimension of the permanent magnets with respect to the SWIPE one. A further solution for HFT (due to the small radius of HFT magnet (212 mm)) consists in the use of a single magnet

with only one magnetization which will guarantee more uniformity.

- The main contribution of motor eddy currents comes from the holder of YBCO. Making the holder of electrical insulator like G10 will cancel eddy currents but will thermally insulate the superconductor ring. This solution becomes critical in terms of the superconductor cooling down. The possibility of using an electrical insulator for the upper part of the holder and a thermal conductor (aluminum) for the lower part is under study.
- Improve the RRR of the coils will reduce the Joule heating. The wire we used for SWIPE did not have any special treatment. The same wire with RRR = 100 should be used to reduce these losses by a factor 3.
- Reducing the diameter of the CuBe wires will reduce the conductive heat load.

If we consider only a reduction of the main magnet inhomogeneity, we will reduce the eddy currents power produced by the rotor for MFT (HFT) from 1.20 mW (1.71 mW) to 0.66 mW (0.92 mW), which means a current needed in each motor reduced by a factor ∼2. This reduction and the improvement of RRR make Joule losses negligible. Moreover the harness load will decrease (blue dash-dot curve of Fig. 6.6) and the diameter of the CuBe wires could be easily reduced to 0.2 mm.

	MFT [mW]	**HFT** [mW]
8 magnets	0.46	0.66
Main magnet	0.19	0.26
Hysteresis	< 0.1	< 0.1
Joule	0.01	<0.01
Harness	0.14	0.14
Rotor emission	0.06	0.05
Total	0.86	1.11

Table 6.3: Optimized configuration for both PMUs. The hysteresis contribution of hysteresis was neglected in the total.

The best achievable configuration is reported in Tab. 6.3 with a total heat load of ∼2 mW. This configuration is very optimistic because the hysteresis losses were neglected but we expect to meet the power budget requirement (< 4 mW) because the hysteresis losses are expected to be smaller and there is still a 100% of margin.

Conclusions

This thesis concerns the development of few important subsystems of LSPE-SWIPE and LiteBIRD. Both experiments are designed to measure the polarization of the CMB at large angular scale, in particular to constrain the B-modes produced by tensor perturbations.

SWIPE is the ballon-born counterpart of LSPE experiment which will fly from the north pole during the Antarctic night. The instrument is a large aperture Stokes polarimeter equipped with 326 multi-mode pixels with TES thermistors cooled down at 300 mK.

The SWIPE multi-mode pixel assembly was deeply tested both at room temperature and at cryogenic temperature. The warm tests demonstrate that in visible light the feedhorn assembly does not introduce any sharp feature or bump in the beam, reproducing the expected circular symmetry. For the cryogenic measurements, we developed a custom testbed, with a cold neoprene absorber to reduce the background on the detector at a level similar to the in-flight one. The measured beam is not in full agreement with the simulated one, with a narrower shape ($\sim 10\%$) due to vignetting produced by the filters stack. However, the main features of the pixel assembly (multi-mode response, wider than the single-mode one, and circularly symmetry) are validated. The next step is a more precise measurement, which will be carried out in a large-aperture cryostat.

The SWIPE polarization modulator was studied in terms of the requirements which will drive its design (modulation strategy, HWP temperature, rotation speed) and in terms of the main systematics introduced by this kind of system (spurious signals, wobbling). The strategy chosen corresponds to a continuously rotating (~ 1 Hz) HWP cooled at 1.6 K to reduce the radiative loading on the detector and minimize the amplitude of spurious signals.

Each subsystem of the polarization modulator unit was presented and tested: the HWP was mounted on a superconducting magnetic bearing based on magnetic levitation between a permanent magnet and a high temperature superconductor. A room temperature mockup allowed to validate the motor and the custom electronic box controller; the inhomogeneities of the main magnet were mapped; the clamp and release system was tested both at room temperature and in a cryogenic environment. The expected heat load during operation is < 25 mW, less than 15% of the total heat load on the superfluid He reservoir.

Finally the next generation LiteBIRD mission was presented and the de-

velopment of 2 out of 3 polarization units was discussed. Their developments were more challenging than for SWIPE, mainly due to the total power budget ($< 4\,\mathrm{mW}$). A baseline design and an optimized configuration were discussed. We have found that the optimized one will meet the power budget with a 100% of margin.

Appendix A

Publications

- **F. Columbro**, P. G. Madonia, L. Lamagna, E. S. Battistelli, A. Coppolecchia, P. de Bernardis, R. Gualtieri, S. Masi, A. Paiella, F. Piacentini, G. Presta, M. Biasotti, G. D'Alessandro, F. Gatti, L. Mele, B. Siri. *SWIPE multi-mode pixel assembly design and beam pattern measurements at cryogenic temperature*, Journal of Low Temperature Physics, (2019), accepted for publication.

- G. D'Alessandro, L. Mele, **F. Columbro**, L. Pagano, F. Piacentini, P. de Bernardis, S. Masi. *Systematic effects induced by half-wave plate precession into measurements of the cosmic microwave background polarization*, Astronomy and Astrophysics (2019), doi:10.1051/0004-6361/201834495.

- S. Masi, P. de Bernardis, A.Paiella, F. Piacentini, L. Lamagna, A. Coppolecchia, P. A. R. Ade, E. S. Battistelli, M. G. Castellano, I. Colantoni, **F. Columbro**, G. D'Alessandro, M. De Petris, S. Gordon, C. Magneville, P. Mauskopf, G. Pettinari, G. Pisano, G. Polenta, G. Presta, E. Tommasi, C. Tucker, V. Vdovin, A. Volpe, and D. Yvon. *Kinetic Inductance Detectors for the OLIMPO experiment: in-flight operation and performance*, Journal of Cosmology and Astroparticle Physics (2019), doi:10.1088/1475-7516/2019/07/003.

- A. Paiella, E. S. Battistelli, M. G. Castellano, I. Colantoni, **F. Columbro**, A. Coppolecchia, G. D'Alessandro, P. de Bernardis, S. Gordon, L. Lamagna, S. Masi, P. Mauskopf, G. Pettinari, F. Piacentini, and G. Presta. *Kinetic Inductance Detectors and readout electronics for the OLIMPO experiment*, Journal of Physics: Conference Series (2019), doi:10.1088/1742-6596/1182/1/012005.

- S. Masi, A. Coppolecchia, E. S. Battistelli, P. de Bernardis, **F. Columbro**, G. D'Alessandro, L. Lamagna, A. Paiella, F. Piacentini, and G. Presta. *Balloon-borne Cosmic Microwave Background experiments*, RICAP18 (2019), doi:10.1051/epjconf/201920901046.

- **F. Columbro**, E. S. Battistelli, A. Coppolecchia, G. D'Alessandro, P. de Bernardis, L. Lamagna, S. Masi, L. Pagano, A. Paiella, F. Piacentini and G. Presta. *The short wavelength instrument for the polarization explorer balloon-borne experiment: Polarization modulation issues*, Astronomical Notes (2019), doi:10.1002/asna.201913566.

- A. Mennella, et al. (QUBIC Collaboration). *QUBIC: Exploring the Primordial Universe with the Q and U Bolometric Interferometer*, Proceedings of ICNFP (2018), doi:10.3390/universe5020042.

- A. Paiella, A. Coppolecchia, L. Lamagna, P. A. R. Ade, E. S. Battistelli, M. G. Castellano, I. Colantoni, **F. Columbro**, G. D'Alessandro, P. de Bernardis, S. Gordon, S. Masi, P. Mauskopf, G. Pettinari, F. Piacentini, G. Pisano, G. Presta and C. Tucker. *Kinetic Inductance Detectors for the OLIMPO experiment: design and pre-flight characterization*, Journal of Cosmology and Astroparticle Physics (2019), doi:10.1088/1475-7516/2019/01/039.

- **F. Columbro**, P. de Bernardis and S. Masi. *A clamp and release system for superconducting magnetic bearings*, Review of Scientific Instruments (2018), doi:10.1063/1.5035332.

- P. de Bernardis, et al. (CORE Collaboration). *Exploring Cosmic Origins with CORE: The Instrument*, Journal of Cosmology and Astroparticle Physics (JCAP), April, (2018), doi:10.1088/issn.1475-7516.

- A. Paiella, E. S. Battistelli, **F. Columbro**, M. G. Castellano, I. Colantoni, S. Gordon, P. Mauskopf, A. Coppolecchia, G. D'Alessandro, P. de Bernardis, L. Lamagna, S. Masi, F. Piacentini. *Design and Electrical Performance of the Kinetic Inductance Detectors of the OLIMPO Experiment*, ISEC 2017 (2018), doi:10.1109/ISEC.2017.8314223.

- P. de Bernardis, et al. (QUBIC Collaboration). *QUBIC: Measuring CMB polarization from Argentina*, Boletin de la Asociacion Argentina de Astronomia La Plata Argentin (2018).

- A. J. May, et al. (QUBIC Collaboration). *Thermal architecture for the QUBIC cryogenic receiver*, Proceedings of SPIE (2018), doi:10.1117/12.2312085.

- Y. Sekimoto, et al. (LiteBIRD Collaboration). *Concept design of the LiteBIRD satellite for CMB B-mode polarization*, Proceedings of SPIE (2018), doi:10.1117/12.2313432.

- D. Burke, et al. (QUBIC Collaboration). *Optical modelling and analysis of the Q and U bolometric interferometer for cosmology*, Proceedings of SPIE (2018), doi:10.1117/12.2287158.

- C. O'Sullivan, et al. (QUBIC Collaboration). *Simulations and performance of the QUBIC optical beam combiner*, Proceedings of SPIE (2018), doi:10.1117/12.2313256.
- C. O'Sullivan, et al. (QUBIC Collaboration). *QUBIC: The Q and U bolometric interferometer for cosmology*, Proceedings of SPIE (2018), doi:10.1117/12.2313332.
- M. Salatino, et al. (QUBIC Collaboration). *Performance of NbSi transition-edge sensors readout with a 128 MUX factor for the QUBIC experiment*, Proceedings of SPIE (2018), doi:10.1117/12.2312080.
- B. R. Johnson, **F. Columbro**, D. Araujo, M. Limon, B. Smiley, G. Jones, B. Reichborn-Kjennerud, A. Miller, and S. Gupta. *A large-diameter hollow-shaft cryogenic motor based on a superconducting magnetic bearing for millimeter-wave polarimetry*, Review of Scientific Instruments, 88, 105102 (2017), doi:10.1063/1.4990884.
- A. Mennella, et al. (QUBIC Collaboration). *Qubic - The Q and U bolometric interferometer for cosmology - a novel way to look at the polarized cosmic microwave background*, Proceeding of Science (2017), doi:10.22323/1.314.0044.

Appendix B

Invited Talks & Conference Presentations

- F. Columbro on behalf of SWIPE team. "SWIPE multi-mode pixel assembly - Beam pattern measurement". *18th International Workshop on Low Temperature Detectors (LTD18)*, Milan, July 23, 2019.
- F. Columbro on behalf of LiteBIRD PMUs team. "LiteBIRD polarization modulators". *CNES - LiteBIRD collaboration meeting*, Toulouse, June 13, 2019.
- F. Columbro on behalf of LSPE collaboration. "The primordial B-modes search in the CMB polarization with LSPE/SWIPE". *8th International Workshop on Astronomy and Relativistic Astrophysics (IWARA2018)*, Ollantaytambo, September 10, 2018.
- F. Columbro on behalf of QUBIC collaboration. "The QUBIC Experiment". *15th Marcel Grossmann Meeting (MG15)*, Rome, July 2, 2018.
- F. Columbro on behalf of LSPE collaboration. "SWIPE-LSPE: Cosmic Microwave Background Polarimetry in the Polar Night". *XXXV SCAR Biennial Meetings (POLAR2018)*, Davos, June 19, 2018.

Bibliography

[1] A. A. Penzias and R. W. Wilson, "A measurement of excess antenna temper- ature at 4080 mc/s," *ApJ*, vol. 42, pp. 419–421, 1965.

[2] A. H. Guth, "Inflationary universe: A possible solution to the horizon and flatness problems," *Phys. Rev. Lett.*, vol. 23, pp. 347–356, Jan. 1981.

[3] Planck Collaboration, Y. Akrami, F. Arroja, M. Ashdown, J. Aumont, C. Baccigalupi, M. Ballardini, A. J. Banday, R. B. Barreiro, N. Bartolo, S. Basak, K. Benabed, J. P. Bernard, M. Bersanelli, P. Bielewicz, J. J. Bock, J. R. Bond, J. Borrill, F. R. Bouchet, F. Boulanger, M. Bucher, C. Burigana, R. C. Butler, E. Calabrese, J. F. Cardoso, J. Carron, A. Challinor, H. C. Chiang, L. P. L. Colombo, C. Combet, D. Contreras, B. P. Crill, F. Cuttaia, P. de Bernardis, G. de Zotti, J. Delabrouille, J. M. Delouis, E. Di Valentino, J. M. Diego, S. Donzelli, O. Doré, M. Douspis, A. Ducout, X. Dupac, S. Dusini, G. Efstathiou, F. Elsner, T. A. Enßlin, H. K. Eriksen, Y. Fantaye, J. Fergusson, R. Fernandez-Cobos, F. Finelli, F. Forastieri, M. Frailis, E. Franceschi, A. Frolov, S. Galeotta, S. Galli, K. Ganga, C. Gauthier, R. T. Génova-Santos, M. Gerbino, T. Ghosh, J. González-Nuevo, K. M. Górski, S. Gratton, A. Gruppuso, J. E. Gudmundsson, J. Hamann, W. Handley, F. K. Hansen, D. Herranz, E. Hivon, D. C. Hooper, Z. Huang, A. H. Jaffe, W. C. Jones, E. Keihänen, R. Keskitalo, K. Kiiveri, J. Kim, T. S. Kisner, N. Krachmalnicoff, M. Kunz, H. Kurki-Suonio, G. Lagache, J. M. Lamarre, A. Lasenby, M. Lattanzi, C. R. Lawrence, M. Le Jeune, J. Lesgourgues, F. Levrier, A. Lewis, M. Liguori, P. B. Lilje, V. Lindholm, M. Lpez-Caniego, P. M. Lubin, Y. Z. Ma, J. F. Macías-Pérez, G. Maggio, D. Maino, N. Mandolesi, A. Mangilli, A. Marcos-Caballero, M. Maris, P. G. Martin, E. Martínez-González, S. Matarrese, N. Mauri, J. D. McEwen, P. D. Meerburg, P. R. Meinhold, A. Melchiorri, A. Mennella, M. Migliaccio, S. Mitra, M. A. Miville-Deschênes, D. Molinari, A. Moneti, L. Montier, G. Morgante, A. Moss, M. Münchmeyer, P. Natoli, H. U. Nørgaard-Nielsen, L. Pagano, D. Paoletti, B. Partridge, G. Patanchon, H. V. Peiris, F. Perrotta, V. Pettorino, F. Piacentini, L. Polastri, G. Polenta, J. L. Puget, J. P. Rachen, M. Reinecke, M. Remazeilles, A. Renzi, G. Rocha, C. Rosset, G. Roudier, J. A. Rubiño-Martín, B. Ruiz-Granados, L. Salvati, M. Sandri, M. Save-

lainen, D. Scott, E. P. S. Shellard, M. Shiraishi, C. Sirignano, G. Sirri, L. D. Spencer, R. Sunyaev, A. S. Suur-Uski, J. A. Tauber, D. Tavagnacco, M. Tenti, L. Toffolatti, M. Tomasi, T. Trombetti, J. Valiviita, B. Van Tent, P. Vielva, F. Villa, N. Vittorio, B. D. Wandelt, I. K. Wehus, S. D. M. White, A. Zacchei, J. P. Zibin, and A. Zonca, "Planck 2018 results. X. Constraints on inflation," *arXiv e-prints*, p. arXiv:1807.06211, Jul 2018.

[4] The LSPE collaboration, S. Aiola, G. Amico, P. Battaglia, E. Battistelli, A. Baù, P. de Bernardis, M. Bersanelli, A. Boscaleri, F. Cavaliere, A. Coppolecchia, A. Cruciani, F. Cuttaia, A. D' Addabbo, G. D'Alessandro, S. De Gregori, F. Del Torto, M. De Petris, L. Fiorineschi, C. Franceschet, E. Franceschi, M. Gervasi, D. Goldie, A. Gregorio, V. Haynes, N. Krachmalnicoff, L. Lamagna, B. Maffei, D. Maino, S. Masi, A. Mennella, N. M. Wah, G. Morgante, F. Nati, L. Pagano, A. Passerini, O. Peverini, F. Piacentini, L. Piccirillo, G. Pisano, S. Ricciardi, P. Rissone, G. Romeo, M. Salatino, M. Sandri, A. Schillaci, L. Stringhetti, A. Tartari, R. Tascone, L. Terenzi, M. Tomasi, E. Tommasi, F. Villa, G. Virone, S. Withington, A. Zacchei, and M. Zannoni, "The Large-Scale Polarization Explorer (LSPE)," *arXiv e-prints*, Aug. 2012.

[5] Y. Sekimoto, P. Ade, K. Arnold, J. Aumont, J. Austermann, C. Baccigalupi, A. Banday, R. Banerji, S. Basak, S. Beckman, M. Bersanelli, J. Borrill, F. Boulanger, M. L. Brown, M. Bucher, E. Calabrese, A. Challinor, Y. Chinone, F. Columbro, A. Cukierman, D. Curtis, P. de Bernardis, M. de Petris, M. Dobbs, T. Dotani, L. Duband, A. Ducout, K. Ebisawa, T. Elleflot, H. Eriksen, J. Errard, R. Flauger, C. Franceschet, U. Fuskeland, K. Ganga, J. R. Gao, T. Ghigna, J. Grain, A. Gruppuso, N. Halverson, P. Hargrave, T. Hasebe, M. Hasegawa, M. Hattori, M. Hazumi, S. Henrot-Versille, C. Hill, Y. Hirota, E. Hivon, D. T. Hoang, J. Hubmayr, K. Ichiki, H. Imada, H. Ishino, G. Jaehnig, H. Kanai, S. Kashima, Y. Kataoka, N. Katayama, T. Kawasaki, R. Keskitalo, A. Kibayashi, T. Kikuchi, K. Kimura, T. Kisner, Y. Kobayashi, N. Kogiso, K. Kohri, E. Komatsu, K. Komatsu, K. Konishi, N. Krachmalnicoff, C. L. Kuo, N. Kurinsky, A. Kushino, L. Lamagna, A. T. Lee, E. Linder, B. Maffei, M. Maki, A. Mangilli, E. Martinez-Gonzalez, S. Masi, T. Matsumura, A. Mennella, Y. Minami, K. Mistuda, D. Molinari, L. Montier, G. Morgante, B. Mot, Y. Murata, A. Murphy, M. Nagai, R. Nagata, S. Nakamura, T. Namikawa, P. Natoli, T. Nishibori, H. Nishino, F. Noviello, C. O'Sullivan, H. Ochi, H. Ogawa, H. Ogawa, H. Ohsaki, I. Ohta, N. Okada, G. Patanchon, F. Piacentini, G. Pisano, G. Polenta, D. Poletti, G. Puglisi, C. Raum, S. Realini, M. Remazeilles, H. Sakurai, Y. Sakurai, G. Savini, B. Sherwin, K. Shinozaki, M. Shiraishi, G. Signorelli, G. Smecher, R. Stompor, H. Sugai, S. Sugiyama, A. Suzuki, J. Suzuki, R. Takaku, H. Takakura, S. Takakura, E. Taylor, Y. Terao, K. L. Thompson, B. Thorne, M. Tomasi, H. Tomida, N. Trappe, M. Tristram, M. Tsuji, M. Tsujimoto, S. Uozumi, S. Utsunomiya, N. Vittorio, N. Watanabe, I. Wehus, B. Westbrook, B. Winter, R. Yamamoto, N. Y. Yamasaki,

M. Yanagisawa, T. Yoshida, J. Yumoto, M. Zannoni, and A. Zonca, "Concept design of the LiteBIRD satellite for CMB B-mode polarization," in *Space Telescopes and Instrumentation 2018: Optical, Infrared, and Millimeter Wave*, vol. 10698 of *Society of Photo-Optical Instrumentation Engineers (SPIE) Conference Series*, p. 106981Y, Aug. 2018.

[6] M. Li, X.-D. Li, S. Wang, and Y. Wang, "Dark energy," *Communications in Theoretical Physics*, vol. 56, 03 2011.

[7] R. Amanullah, C. Lidman, D. Rubin, G. Aldering, P. Astier, K. Barbary, M. S. Burns, A. Conley, K. S. Dawson, S. E. Deustua, M. Doi, S. Fabbro, L. Faccioli, H. K. Fakhouri, G. Folatelli, A. S. Fruchter, H. Furusawa, G. Garavini, G. Goldhaber, A. Goobar, D. E. Groom, I. Hook, D. A. Howell, N. Kashikawa, A. G. Kim, R. A. Knop, M. Kowalski, E. Linder, J. Meyers, T. Morokuma, S. Nobili, J. Nordin, P. E. Nugent, L. Östman, R. Pain, N. Panagia, S. Perlmutter, J. Raux, P. Ruiz-Lapuente, A. L. Spadafora, M. Strovink, N. Suzuki, L. Wang, W. M. Wood-Vasey, N. Yasuda, and T. Supernova Cosmology Project, "Spectra and Hubble Space Telescope Light Curves of Six Type Ia Supernovae at 0.511 < z < 1.12 and the Union2 Compilation," *ApJ*, vol. 716, pp. 712–738, Jun 2010.

[8] Planck Collaboration, Ade, P. A. R., Aghanim, N., Arnaud, M., Ashdown, M., Aumont, J., Baccigalupi, C., Banday, A. J., Barreiro, R. B., Bartlett, J. G., Bartolo, N., Battaner, E., Battye, R., Benabed, K., Benoît, A., Benoit-Lévy, A., Bernard, J.-P., Bersanelli, M., Bielewicz, P., Bock, J. J., Bonaldi, A., Bonavera, L., Bond, J. R., Borrill, J., Bouchet, F. R., Boulanger, F., Bucher, M., Burigana, C., Butler, R. C., Calabrese, E., Cardoso, J.-F., Catalano, A., Challinor, A., Chamballu, A., Chary, R.-R., Chiang, H. C., Chluba, J., Christensen, P. R., Church, S., Clements, D. L., Colombi, S., Colombo, L. P. L., Combet, C., Coulais, A., Crill, B. P., Curto, A., Cuttaia, F., Danese, L., Davies, R. D., Davis, R. J., de Bernardis, P., de Rosa, A., de Zotti, G., Delabrouille, J., Désert, F.-X., Di Valentino, E., Dickinson, C., Diego, J. M., Dolag, K., Dole, H., Donzelli, S., Doré, O., Douspis, M., Ducout, A., Dunkley, J., Dupac, X., Efstathiou, G., Elsner, F., Enßlin, T. A., Eriksen, H. K., Farhang, M., Fergusson, J., Finelli, F., Forni, O., Frailis, M., Fraisse, A. A., Franceschi, E., Frejsel, A., Galeotta, S., Galli, S., Ganga, K., Gauthier, C., Gerbino, M., Ghosh, T., Giard, M., Giraud-Héraud, Y., Giusarma, E., Gjerløw, E., González-Nuevo, J., Górski, K. M., Gratton, S., Gregorio, A., Gruppuso, A., Gudmundsson, J. E., Hamann, J., Hansen, F. K., Hanson, D., Harrison, D. L., Helou, G., Henrot-Versillé, S., Hernández-Monteagudo, C., Herranz, D., Hildebrandt, S. R., Hivon, E., Hobson, M., Holmes, W. A., Hornstrup, A., Hovest, W., Huang, Z., Huffenberger, K. M., Hurier, G., Jaffe, A. H., Jaffe, T. R., Jones, W. C., Juvela, M., Keihänen, E., Keskitalo, R., Kisner, T. S., Kneissl, R., Knoche, J., Knox, L., Kunz, M., Kurki-Suonio, H., Lagache, G., Lähteenmäki, A., Lamarre, J.-M., Lasenby, A., Lattanzi, M., Lawrence, C. R., Leahy, J. P., Leonardi, R., Lesgourgues, J., Levrier,

F., Lewis, A., Liguori, M., Lilje, P. B., Linden-Vørnle, M., López-Caniego, M., Lubin, P. M., Macías-Pérez, J. F., Maggio, G., Maino, D., Mandolesi, N., Mangilli, A., Marchini, A., Maris, M., Martin, P. G., Martinelli, M., Martínez-González, E., Masi, S., Matarrese, S., McGehee, P., Meinhold, P. R., Melchiorri, A., Melin, J.-B., Mendes, L., Mennella, A., Migliaccio, M., Millea, M., Mitra, S., Miville-Deschênes, M.-A., Moneti, A., Montier, L., Morgante, G., Mortlock, D., Moss, A., Munshi, D., Murphy, J. A., Naselsky, P., Nati, F., Natoli, P., Netterfield, C. B., Nørgaard-Nielsen, H. U., Noviello, F., Novikov, D., Novikov, I., Oxborrow, C. A., Paci, F., Pagano, L., Pajot, F., Paladini, R., Paoletti, D., Partridge, B., Pasian, F., Patanchon, G., Pearson, T. J., Perdereau, O., Perotto, L., Perrotta, F., Pettorino, V., Piacentini, F., Piat, M., Pierpaoli, E., Pietrobon, D., Plaszczynski, S., Pointecouteau, E., Polenta, G., Popa, L., Pratt, G. W., Prézeau, G., Prunet, S., Puget, J.-L., Rachen, J. P., Reach, W. T., Rebolo, R., Reinecke, M., Remazeilles, M., Renault, C., Renzi, A., Ristorcelli, I., Rocha, G., Rosset, C., Rossetti, M., Roudier, G., Rouillé d´Orfeuil, B., Rowan-Robinson, M., Rubiño-Martín, J. A., Rusholme, B., Said, N., Salvatelli, V., Salvati, L., Sandri, M., Santos, D., Savelainen, M., Savini, G., Scott, D., Seiffert, M. D., Serra, P., Shellard, E. P. S., Spencer, L. D., Spinelli, M., Stolyarov, V., Stompor, R., Sudiwala, R., Sunyaev, R., Sutton, D., Suur-Uski, A.-S., Sygnet, J.-F., Tauber, J. A., Terenzi, L., Toffolatti, L., Tomasi, M., Tristram, M., Trombetti, T., Tucci, M., Tuovinen, J., Türler, M., Umana, G., Valenziano, L., Valiviita, J., Van Tent, F., Vielva, P., Villa, F., Wade, L. A., Wandelt, B. D., Wehus, I. K., White, M., White, S. D. M., Wilkinson, A., Yvon, D., Zacchei, A., and Zonca, A., "Planck 2015 results - xiii. cosmological parameters," *A&A*, vol. 594, p. A13, 2016.

[9] G. Tomen, "Dispense per il corso di cosmologia." 2002.

[10] P. J. E. Peebles, *Principles of Physical Cosmology*. Princeton Series in Physics, Princeton Univ Pr, 1993.

[11] N. W. Bogges, J. C. Mather, R. Weiss, *et al.*, "The COBE mission - Its design and performance two years after launch," *ApJ*, pp. 420–429, October 1992.

[12] E. L. Wright, "Theoretical Overview of Cosmic Microwave Background Anisotropy." arXiv:astro-ph/0305591, May 2003.

[13] Planck Collaboration, Aghanim, N., Arnaud, M., Ashdown, M., Aumont, J., Baccigalupi, C., Banday, A. J., Barreiro, R. B., Bartlett, J. G., Bartolo, N., Battaner, E., Benabed, K., Benoît, A., Benoit-Lévy, A., Bernard, J.-P., Bersanelli, M., Bielewicz, P., Bock, J. J., Bonaldi, A., Bonavera, L., Bond, J. R., Borrill, J., Bouchet, F. R., Boulanger, F., Bucher, M., Burigana, C., Butler, R. C., Calabrese, E., Cardoso, J.-F., Catalano, A., Challinor, A., Chiang, H. C., Christensen, P. R., Clements, D. L., Colombo, L. P. L., Combet, C., Coulais, A., Crill, B. P., Curto, A., Cuttaia, F.,

Danese, L., Davies, R. D., Davis, R. J., de Bernardis, P., de Rosa, A., de Zotti, G., Delabrouille, J., Désert, F.-X., Di Valentino, E., Dickinson, C., Diego, J. M., Dolag, K., Dole, H., Donzelli, S., Doré, O., Douspis, M., Ducout, A., Dunkley, J., Dupac, X., Efstathiou, G., Elsner, F., Enßlin, T. A., Eriksen, H. K., Fergusson, J., Finelli, F., Forni, O., Frailis, M., Fraisse, A. A., Franceschi, E., Frejsel, A., Galeotta, S., Galli, S., Ganga, K., Gauthier, C., Gerbino, M., Giard, M., Gjerløw, E., González-Nuevo, J., Górski, K. M., Gratton, S., Gregorio, A., Gruppuso, A., Gudmundsson, J. E., Hamann, J., Hansen, F. K., Harrison, D. L., Helou, G., Henrot-Versillé, S., Hernández-Monteagudo, C., Herranz, D., Hildebrandt, S. R., Hivon, E., Holmes, W. A., Hornstrup, A., Huffenberger, K. M., Hurier, G., Jaffe, A. H., Jones, W. C., Juvela, M., Keihänen, E., Keskitalo, R., Kiiveri, K., Knoche, J., Knox, L., Kunz, M., Kurki-Suonio, H., Lagache, G., Lähteenmäki, A., Lamarre, J.-M., Lasenby, A., Lattanzi, M., Lawrence, C. R., Le Jeune, M., Leonardi, R., Lesgourgues, J., Levrier, F., Lewis, A., Liguori, M., Lilje, P. B., Lilley, M., Linden-Vørnle, M., Lindholm, V., López-Caniego, M., Macías-Pérez, J. F., Maffei, B., Maggio, G., Maino, D., Mandolesi, N., Mangilli, A., Maris, M., Martin, P. G., Martínez-González, E., Masi, S., Matarrese, S., Meinhold, P. R., Melchiorri, A., Migliaccio, M., Millea, M., Mitra, S., Miville-Deschênes, M.-A., Moneti, A., Montier, L., Morgante, G., Mortlock, D., Mottet, S., Munshi, D., Murphy, J. A., Narimani, A., Naselsky, P., Nati, F., Natoli, P., Noviello, F., Novikov, D., Novikov, I., Oxborrow, C. A., Paci, F., Pagano, L., Pajot, F., Paoletti, D., Partridge, B., Pasian, F., Patanchon, G., Pearson, T. J., Perdereau, O., Perotto, L., Pettorino, V., Piacentini, F., Piat, M., Pierpaoli, E., Pietrobon, D., Plaszczynski, S., Pointecouteau, E., Polenta, G., Ponthieu, N., Pratt, G. W., Prunet, S., Puget, J.-L., Rachen, J. P., Reinecke, M., Remazeilles, M., Renault, C., Renzi, A., Ristorcelli, I., Rocha, G., Rossetti, M., Roudier, G., Rouillé d´Orfeuil, B., Rubiño-Martín, J. A., Rusholme, B., Salvati, L., Sandri, M., Santos, D., Savelainen, M., Savini, G., Scott, D., Serra, P., Spencer, L. D., Spinelli, M., Stolyarov, V., Stompor, R., Sunyaev, R., Sutton, D., Suur-Uski, A.-S., Sygnet, J.-F., Tauber, J. A., Terenzi, L., Toffolatti, L., Tomasi, M., Tristram, M., Trombetti, T., Tucci, M., Tuovinen, J., Umana, G., Valenziano, L., Valiviita, J., Van Tent, F., Vielva, P., Villa, F., Wade, L. A., Wandelt, B. D., Wehus, I. K., Yvon, D., Zacchei, A., and Zonca, A., "Planck 2015 results - xi. cmb power spectra, likelihoods, and robustness of parameters," *A&A*, vol. 594, p. A11, 2016.

[14] B. W. Carroll, *An Introduction to Modern Astrophysics*. Pearson, 2nd ed., July 2006.

[15] C. H. Lineweaver, L. Tenorio, G. F. Smoot, P. Keegstra, A. J. Banday, and P. Lubin, "The Dipole Observed in the COBE DMR 4 Year Data," *ApJ*, vol. 470, p. 38, Oct. 1996.

[16] Planck Collaboration, N. Aghanim, C. Armitage-Caplan, M. Arnaud, M. Ashdown, F. Atrio-Barandela, J. Aumont, C. Baccigalupi, A. J. Banday, R. B. Barreiro, J. G. Bartlett, K. Benabed, A. Benoit-Lévy, J.-P. Bernard, M. Bersanelli, P. Bielewicz, J. Bobin, J. J. Bock, J. R. Bond, J. Borrill, F. R. Bouchet, M. Bridges, C. Burigana, R. C. Butler, J.-F. Cardoso, A. Catalano, A. Challinor, A. Chamballu, H. C. Chiang, L.-Y. Chiang, P. R. Christensen, D. L. Clements, L. P. L. Colombo, F. Couchot, B. P. Crill, A. Curto, F. Cuttaia, L. Danese, R. D. Davies, R. J. Davis, P. de Bernardis, A. de Rosa, G. de Zotti, J. Delabrouille, J. M. Diego, S. Donzelli, O. Doré, X. Dupac, G. Efstathiou, T. A. Enßlin, H. K. Eriksen, F. Finelli, O. Forni, M. Frailis, E. Franceschi, S. Galeotta, K. Ganga, M. Giard, G. Giardino, J. González-Nuevo, K. M. Górski, S. Gratton, A. Gregorio, A. Gruppuso, F. K. Hansen, D. Hanson, D. L. Harrison, G. Helou, S. R. Hildebrandt, E. Hivon, M. Hobson, W. A. Holmes, W. Hovest, K. M. Huffenberger, W. C. Jones, M. Juvela, E. Keihänen, R. Keskitalo, T. S. Kisner, J. Knoche, L. Knox, M. Kunz, H. Kurki-Suonio, A. Lähteenmäki, J.-M. Lamarre, A. Lasenby, R. J. Laureijs, C. R. Lawrence, R. Leonardi, A. Lewis, M. Liguori, P. B. Lilje, M. Linden-Vørnle, M. López-Caniego, P. M. Lubin, J. F. Macías-Pérez, N. Mandolesi, M. Maris, D. J. Marshall, P. G. Martin, E. Martínez-González, S. Masi, M. Massardi, S. Matarrese, P. Mazzotta, P. R. Meinhold, A. Melchiorri, L. Mendes, M. Migliaccio, S. Mitra, A. Moneti, L. Montier, G. Morgante, D. Mortlock, A. Moss, D. Munshi, P. Naselsky, F. Nati, P. Natoli, H. U. Nørgaard-Nielsen, F. Noviello, D. Novikov, I. Novikov, S. Osborne, C. A. Oxborrow, L. Pagano, F. Pajot, D. Paoletti, F. Pasian, G. Patanchon, O. Perdereau, F. Perrotta, F. Piacentini, E. Pierpaoli, D. Pietrobon, S. Plaszczynski, E. Pointecouteau, G. Polenta, N. Ponthieu, L. Popa, G. W. Pratt, G. Prézeau, J.-L. Puget, J. P. Rachen, W. T. Reach, M. Reinecke, S. Ricciardi, T. Riller, I. Ristorcelli, G. Rocha, C. Rosset, J. A. Rubiño-Martín, B. Rusholme, D. Santos, G. Savini, D. Scott, M. D. Seiffert, E. P. S. Shellard, L. D. Spencer, R. Sunyaev, F. Sureau, A.-S. Suur-Uski, J.-F. Sygnet, J. A. Tauber, D. Tavagnacco, L. Terenzi, L. Toffolatti, M. Tomasi, M. Tristram, M. Tucci, M. Türler, L. Valenziano, J. Valiviita, B. Van Tent, P. Vielva, F. Villa, N. Vittorio, L. A. Wade, B. D. Wandelt, M. White, D. Yvon, A. Zacchei, J. P. Zibin, and A. Zonca, "Planck 2013 results. XXVII. Doppler boosting of the CMB: Eppur si muove," *A&A*, vol. 571, p. A27, Nov. 2014.

[17] R. K. Sachs and A. M. Wolfe, "Perturbations of a Cosmological Model and Angular Variations of the Microwave Background," *ApJ*, vol. 147, p. 73, Jan. 1967.

[18] R. Narayan and M. Bartelmann, "Lectures on Gravitational Lensing," *arXiv Astrophysics e-prints*, June 1996.

[19] A. Lewis and A. Challinor, "Weak gravitational lensing of the CMB," *Phys. Rep.*, vol. 429, pp. 1–65, Jun 2006.

[20] C. G. T. Haslam, C. J. Salter, H. Stoffel, and W. E. Wilson, "A 408 MHz all-sky continuum survey. II. The atlas of contour maps.," *A&A*, vol. 47, pp. 1–143, Jan 1982.

[21] Planck Collaboration, R. Adam, P. A. R. Ade, N. Aghanim, M. Arnaud, M. Ashdown, J. Aumont, C. Baccigalupi, A. J. Banday, R. B. Barreiro, and et al., "Planck 2015 results. IX. Diffuse component separation: CMB maps," *A&A*, vol. 594, p. A9, Sept. 2016.

[22] Y. B. Zeldovich and R. A. Sunyaev, "The Interaction of Matter and Radiation in a Hot-Model Universe," *Astrophys. Space Sci.*, vol. 4, pp. 301–316, July 1969.

[23] M. Birkinshaw, "The Sunyaev-Zel'dovich effect," *Phys. Rep.*, vol. 310, pp. 97–195, Mar. 1999.

[24] K. Sato, "Cosmological baryon-number domain structure and the first order phase transition of a vacuum," *Physics Letters B*, vol. 99, pp. 66–70, Feb 1981.

[25] G. Montani, "Astrophysics of the Primordial Universe," 2015.

[26] U. Seljak and M. Zaldarriaga, "Signature of Gravity Waves in the Polarization of the Microwave Background," *Physical Review Letters*, vol. 78, pp. 2054–2057, Mar. 1997.

[27] P. M. Lubin and G. F. Smoot, "Search for linear polarization of the cosmic background radiation," *Physical Review Letters*, vol. 42, pp. 129–132, Jan. 1979.

[28] N. Caderni, R. Fabbri, B. Melchiorri, F. Melchiorri, and V. Natale, "Polarization of the microwave background radiation. II. An infrared survey of the sky," *Phys. Rev. Lett.*, vol. 17, pp. 1908–1918, Apr 1978.

[29] M. Zaldarriaga, *Fluctuations in the Cosmic Microwave Background*. PhD thesis, MIT, May 1998.

[30] W. Hu and M. White, "A CMB polarization primer," *New Astronom.*, vol. 2, pp. 323–344, Oct. 1997.

[31] D. Baumann, "TASI Lectures on Inflaction." arXiv:0907.5424.

[32] Planck HFI Core Team, P. A. R. Ade, N. Aghanim, R. Ansari, M. Arnaud, M. Ashdown, J. Aumont, A. J. Banday, M. Bartelmann, J. G. Bartlett, E. Battaner, K. Benabed, A. Benoît, J.-P. Bernard, M. Bersanelli, R. Bhatia, J. J. Bock, J. R. Bond, J. Borrill, F. R. Bouchet, F. Boulanger, T. Bradshaw, E. Bréelle, M. Bucher, P. Camus, J.-F. Cardoso, A. Catalano, A. Challinor, A. Chamballu, J. Charra, M. Charra, R.-R. Chary, C. Chiang, S. Church, D. L. Clements, S. Colombi, F. Couchot, A. Coulais, C. Cressiot, B. P. Crill, M. Crook, P. de Bernardis, J. Delabrouille,

J.-M. Delouis, F.-X. Désert, K. Dolag, H. Dole, O. Doré, M. Douspis, G. Efstathiou, P. Eng, C. Filliard, O. Forni, P. Fosalba, J.-J. Fourmond, K. Ganga, M. Giard, D. Girard, Y. Giraud-Héraud, R. Gispert, K. M. Górski, S. Gratton, M. Griffin, G. Guyot, J. Haissinski, D. Harrison, G. Helou, S. Henrot-Versillé, C. Hernández-Monteagudo, S. R. Hildebrandt, R. Hills, E. Hivon, M. Hobson, W. A. Holmes, K. M. Huffenberger, A. H. Jaffe, W. C. Jones, J. Kaplan, R. Kneissl, L. Knox, G. Lagache, J.-M. Lamarre, P. Lami, A. E. Lange, A. Lasenby, A. Lavabre, C. R. Lawrence, B. Leriche, C. Leroy, Y. Longval, J. F. Macías-Pérez, T. Maciaszek, C. J. MacTavish, B. Maffei, N. Mandolesi, R. Mann, B. Mansoux, S. Masi, T. Matsumura, P. McGehee, J.-B. Melin, C. Mercier, M.-A. Miville-Deschênes, A. Moneti, L. Montier, D. Mortlock, A. Murphy, F. Nati, C. B. Netterfield, H. U. Nørgaard-Nielsen, C. North, F. Noviello, D. Novikov, S. Osborne, C. Paine, F. Pajot, G. Patanchon, T. Peacocke, T. J. Pearson, O. Perdereau, L. Perotto, F. Piacentini, M. Piat, S. Plaszczynski, E. Pointecouteau, R. Pons, N. Ponthieu, G. Prézeau, S. Prunet, J.-L. Puget, W. T. Reach, C. Renault, I. Ristorcelli, G. Rocha, C. Rosset, G. Roudier, M. Rowan-Robinson, B. Rusholme, D. Santos, G. Savini, B. M. Schaefer, P. Shellard, L. Spencer, J.-L. Starck, P. Stassi, V. Stolyarov, R. Stompor, R. Sudiwala, R. Sunyaev, J.-F. Sygnet, J. A. Tauber, C. Thum, J.-P. Torre, F. Touze, M. Tristram, F. van Leeuwen, L. Vibert, D. Vibert, L. A. Wade, B. D. Wandelt, S. D. M. White, H. Wiesemeyer, A. Woodcraft, V. Yurchenko, D. Yvon, and A. Zacchei, "Planck early results. IV. First assessment of the High Frequency Instrument in-flight performance," *A&A*, vol. 536, p. A4, Dec. 2011.

[33] M. C. Guzzetti, N. Bartolo, M. Liguori, and S. Matarrese, "Gravitational waves from inflation," *Nuovo Cimento Rivista Serie*, vol. 39, pp. 399–495, Sep 2016.

[34] BICEP2/Keck Collaboration, Planck Collaboration, P. A. R. Ade, N. Aghanim, Z. Ahmed, R. W. Aikin, K. D. Alexander, M. Arnaud, J. Aumont, C. Baccigalupi, and et al., "Joint Analysis of BICEP2/Keck Array and Planck Data," *Physical Review Letters*, vol. 114, p. 101301, Mar. 2015.

[35] S. Hanany and P. Rosenkranz, "Polarization of the atmosphere as a foreground for cosmic microwave background polarization experiments," *New Astron. Rev.*, vol. 47, pp. 1159–1165, Dec 2003.

[36] B. K. Keating, *A Search for the Large Angular Scale Polarization of the Cosmic Microwave Background*. PhD thesis, Brown University, 2000.

[37] B. Keating, P. Timbie, A. Polnarev, and J. Steinberger, "Large Angular Scale Polarization of the Cosmic Microwave Background Radiation and the Feasibility of Its Detection," *ApJ*, vol. 495, pp. 580–596, Mar. 1998.

[38] G. B. Rybicki and A. P. Lightman, *Radiative Processes in Astrophysics*. Wiley-VCH, revides edition ed., March 1985.

[39] N. Krachmalnicoff, E. Carretti, C. Baccigalupi, G. Bernardi, S. Brown, B. M. Gaensler, M. Haverkorn, M. Kesteven, F. Perrotta, S. Poppi, and L. Staveley-Smith, "S-PASS view of polarized Galactic synchrotron at 2.3 GHz as a contaminant to CMB observations," *A&A*, vol. 618, p. A166, Oct 2018.

[40] C. L. Bennett, D. Larson, J. L. Weiland, N. Jarosik, G. Hinshaw, N. Odegard, K. M. Smith, R. S. Hill, B. Gold, M. Halpern, E. Komatsu, M. R. Nolta, L. Page, D. N. Spergel, E. Wollack, J. Dunkley, A. Kogut, M. Limon, S. S. Meyer, G. S. Tucker, and E. L. Wright, "Nine-year Wilkinson Microwave Anisotropy Probe (WMAP) Observations: Final Maps and Results," *ApJ*, vol. 208, p. 20, Oct. 2013.

[41] L. Spitzer, *Physical processes in the interstellar medium*. Wiley, 1978.

[42] N. Macellari, E. Pierpaoli, C. Dickinson, and J. E. Vaillancourt, "Galactic foreground contributions to the 5-year Wilkinson Microwave Anisotropy Probe maps," *MNRAS*, vol. 418, pp. 888–905, Dec. 2011.

[43] K. Ichiki, "CMB foreground: A concise review," *Progress of Theoretical and Experimental Physics*, vol. 2014, p. 06B109, June 2014.

[44] N. Krachmalnicoff, C. Baccigalupi, J. Aumont, M. Bersanelli, and A. Mennella, "Characterization of foreground emission on degree angular scales for CMB B-mode observations . Thermal dust and synchrotron signal from Planck and WMAP data," *A&A*, vol. 588, p. A65, Apr 2016.

[45] Planck Collaboration, P. A. R. Ade, N. Aghanim, M. I. R. Alves, M. Arnaud, M. Ashdown, F. Atrio-Barandela, J. Aumont, C. Baccigalupi, A. Balbi, A. J. Banday, R. B. Barreiro, J. G. Bartlett, E. Battaner, L. Bedini, K. Benabed, A. Benoît, J.-P. Bernard, M. Bersanelli, A. Bonaldi, J. R. Bond, J. Borrill, F. R. Bouchet, F. Boulanger, C. Burigana, R. C. Butler, P. Cabella, J.-F. Cardoso, X. Chen, L.-Y. Chiang, P. R. Christensen, D. L. Clements, S. Colombi, L. P. L. Colombo, A. Coulais, F. Cuttaia, R. D. Davies, R. J. Davis, P. de Bernardis, G. de Gasperis, G. de Zotti, J. Delabrouille, C. Dickinson, J. M. Diego, G. Dobler, H. Dole, S. Donzelli, O. Doré, M. Douspis, X. Dupac, T. A. Enßlin, F. Finelli, O. Forni, M. Frailis, E. Franceschi, S. Galeotta, K. Ganga, R. T. Génova-Santos, T. Ghosh, M. Giard, G. Giardino, Y. Giraud-Héraud, J. González-Nuevo, K. M. Górski, A. Gregorio, A. Gruppuso, F. K. Hansen, D. Harrison, C. Hernández-Monteagudo, S. R. Hildebrandt, E. Hivon, M. Hobson, W. A. Holmes, A. Hornstrup, W. Hovest, K. M. Huffenberger, T. R. Jaffe, A. H. Jaffe, M. Juvela, E. Keihänen, R. Keskitalo, T. S. Kisner, J. Knoche, M. Kunz, H. Kurki-Suonio, G. Lagache, A. Lähteenmäki, J.-M. Lamarre, A. Lasenby, C. R. Lawrence, S. Leach, R. Leonardi, P. B. Lilje, M. Linden-Vørnle, P. M. Lubin, J. F. Macías-Pérez, B. Maffei, D. Maino, N. Mandolesi, M. Maris, D. J. Marshall, P. G. Martin, E. Martínez-González, S. Masi, M. Massardi, S. Matarrese, P. Mazzotta, A. Melchiorri,

A. Mennella, S. Mitra, M.-A. Miville-Deschênes, A. Moneti, L. Montier, G. Morgante, D. Mortlock, D. Munshi, J. A. Murphy, P. Naselsky, F. Nati, P. Natoli, H. U. Nørgaard-Nielsen, F. Noviello, D. Novikov, I. Novikov, S. Osborne, C. A. Oxborrow, F. Pajot, R. Paladini, D. Paoletti, M. Peel, L. Perotto, F. Perrotta, F. Piacentini, M. Piat, E. Pierpaoli, D. Pietrobon, S. Plaszczynski, E. Pointecouteau, G. Polenta, L. Popa, T. Poutanen, G. W. Pratt, S. Prunet, J.-L. Puget, J. P. Rachen, W. T. Reach, R. Rebolo, M. Reinecke, C. Renault, S. Ricciardi, I. Ristorcelli, G. Rocha, C. Rosset, J. A. Rubiño-Martín, B. Rusholme, E. Salerno, M. Sandri, G. Savini, D. Scott, L. Spencer, V. Stolyarov, R. Sudiwala, A.-S. Suur-Uski, J.-F. Sygnet, J. A. Tauber, L. Terenzi, C. T. Tibbs, L. Toffolatti, M. Tomasi, M. Tristram, L. Valenziano, B. Van Tent, J. Varis, P. Vielva, F. Villa, N. Vittorio, L. A. Wade, B. D. Wandelt, N. Ysard, D. Yvon, A. Zacchei, and A. Zonca, "Planck intermediate results. XII: Diffuse Galactic components in the Gould Belt system," *A&A*, vol. 557, p. A53, Sept. 2013.

[46] P. de Bernardis, P. A. R. Ade, J. J. Bock, J. R. Bond, J. Borrill, A. Boscaleri, K. Coble, B. P. Crill, G. De Gasperis, P. C. Farese, P. G. Ferreira, K. Ganga, M. Giacometti, E. Hivon, V. V. Hristov, A. Iacoangeli, A. H. Jaffe, A. E. Lange, L. Martinis, S. Masi, P. V. Mason, P. D. Mauskopf, A. Melchiorri, L. Miglio, T. Montroy, C. B. Netterfield, E. Pascale, F. Piacentini, D. Pogosyan, S. Prunet, S. Rao, G. Romeo, J. E. Ruhl, F. Scaramuzzi, D. Sforna, and N. Vittorio, "A flat Universe from high-resolution maps of the cosmic microwave background radiation," *Nature*, vol. 404, pp. 955–959, Apr. 2000.

[47] S. Hanany, P. Ade, A. Balbi, J. Bock, J. Borrill, A. Boscaleri, P. de Bernardis, P. G. Ferreira, V. V. Hristov, A. H. Jaffe, A. E. Lange, A. T. Lee, P. D. Mauskopf, C. B. Netterfield, S. Oh, E. Pascale, B. Rabii, P. L. Richards, G. F. Smoot, R. Stompor, C. D. Winant, and J. H. P. Wu, "MAXIMA-1: A Measurement of the Cosmic Microwave Background Anisotropy on Angular Scales of 10^{-5}°," *ApJ*, vol. 545, pp. L5–L9, Dec. 2000.

[48] A. Benoît and ARCHEOPS Collaboration, "ARCHEOPS: a balloon experiment for measuring the cosmic microwave background anisotropies," *Advances in Space Research*, vol. 33, pp. 1790–1792, Jan. 2004.

[49] E. M. Leitch, J. M. Kovac, N. W. Halverson, J. E. Carlstrom, C. Pryke, and M. W. E. Smith, "Degree Angular Scale Interferometer 3 Year Cosmic Microwave Background Polarization Results," *ApJ*, vol. 624, pp. 10–20, May 2005.

[50] C. L. Bennett, D. Larson, J. L. Weiland, N. Jarosik, G. Hinshaw, N. Odegard, K. M. Smith, R. S. Hill, B. Gold, M. Halpern, E. Komatsu, M. R. Nolta, L. Page, D. N. Spergel, E. Wollack, J. Dunkley, A. Kogut,

M. Limon, S. S. Meyer, G. S. Tucker, and E. L. Wright, "Nine-year Wilkinson Microwave Anisotropy Probe (WMAP) Observations: Final Maps and Results," *ApJ*, vol. 208, p. 20, Oct. 2013.

[51] B. A. Benson, P. A. R. Ade, Z. Ahmed, S. W. Allen, K. Arnold, J. E. Austermann, A. N. Bender, L. E. Bleem, J. E. Carlstrom, C. L. Chang, H. M. Cho, J. F. Cliche, T. M. Crawford, A. Cukierman, T. de Haan, M. A. Dobbs, D. Dutcher, W. Everett, A. Gilbert, N. W. Halverson, D. Hanson, N. L. Harrington, K. Hattori, J. W. Henning, G. C. Hilton, G. P. Holder, W. L. Holzapfel, K. D. Irwin, R. Keisler, L. Knox, D. Kubik, C. L. Kuo, A. T. Lee, E. M. Leitch, D. Li, M. McDonald, S. S. Meyer, J. Montgomery, M. Myers, T. Natoli, H. Nguyen, V. Novosad, S. Padin, Z. Pan, J. Pearson, C. Reichardt, J. E. Ruhl, B. R. Saliwanchik, G. Simard, G. Smecher, J. T. Sayre, E. Shirokoff, A. A. Stark, K. Story, A. Suzuki, K. L. Thompson, C. Tucker, K. Vanderlinde, J. D. Vieira, A. Vikhlinin, G. Wang, V. Yefremenko, and K. W. Yoon, "SPT-3G: a next-generation cosmic microwave background polarization experiment on the South Pole telescope," in *Millimeter, Submillimeter, and Far-Infrared Detectors and Instrumentation for Astronomy VII*, vol. 9153 of *Proceedings of the SPIE*, p. 91531P, July 2014.

[52] R. J. Thornton, P. A. R. Ade, S. Aiola, F. E. Angilè, M. Amiri, J. A. Beall, D. T. Becker, H.-M. Cho, S. K. Choi, P. Corlies, K. P. Coughlin, R. Datta, M. J. Devlin, S. R. Dicker, R. Dünner, J. W. Fowler, A. E. Fox, P. A. Gallardo, J. Gao, E. Grace, M. Halpern, M. Hasselfield, S. W. Henderson, G. C. Hilton, A. D. Hincks, S. P. Ho, J. Hubmayr, K. D. Irwin, J. Klein, B. Koopman, D. Li, T. Louis, M. Lungu, L. Maurin, J. McMahon, C. D. Munson, S. Naess, F. Nati, L. Newburgh, J. Nibarger, M. D. Niemack, P. Niraula, M. R. Nolta, L. A. Page, C. G. Pappas, A. Schillaci, B. L. Schmitt, N. Sehgal, J. L. Sievers, S. M. Simon, S. T. Staggs, C. Tucker, M. Uehara, J. van Lanen, J. T. Ward, and E. J. Wollack, "The Atacama Cosmology Telescope: The Polarization-sensitive ACTPol Instrument," *ApJ*, vol. 227, p. 21, Dec. 2016.

[53] Planck Collaboration, P. A. R. Ade, N. Aghanim, M. I. R. Alves, M. Arnaud, M. Ashdown, F. Atrio-Barandela, J. Aumont, C. Baccigalupi, A. Balbi, A. J. Banday, R. B. Barreiro, J. G. Bartlett, E. Battaner, L. Bedini, K. Benabed, A. Benoît, J.-P. Bernard, M. Bersanelli, A. Bonaldi, J. R. Bond, J. Borrill, F. R. Bouchet, F. Boulanger, C. Burigana, R. C. Butler, P. Cabella, J.-F. Cardoso, X. Chen, L.-Y. Chiang, P. R. Christensen, D. L. Clements, S. Colombi, L. P. L. Colombo, A. Coulais, F. Cuttaia, R. D. Davies, R. J. Davis, P. de Bernardis, G. de Gasperis, G. de Zotti, J. Delabrouille, C. Dickinson, J. M. Diego, G. Dobler, H. Dole, S. Donzelli, O. Doré, M. Douspis, X. Dupac, T. A. Enßlin, F. Finelli, O. Forni, M. Frailis, E. Franceschi, S. Galeotta, K. Ganga, R. T. Génova-Santos, T. Ghosh, M. Giard, G. Giardino, Y. Giraud-Héraud, J. González-Nuevo, K. M. Górski, A. Gregorio, A. Gruppuso, F. K. Hansen, D. Harri-

son, C. Hernández-Monteagudo, S. R. Hildebrandt, E. Hivon, M. Hobson, W. A. Holmes, A. Hornstrup, W. Hovest, K. M. Huffenberger, T. R. Jaffe, A. H. Jaffe, M. Juvela, E. Keihänen, R. Keskitalo, T. S. Kisner, J. Knoche, M. Kunz, H. Kurki-Suonio, G. Lagache, A. Lähteenmäki, J.-M. Lamarre, A. Lasenby, C. R. Lawrence, S. Leach, R. Leonardi, P. B. Lilje, M. Linden-Vørnle, P. M. Lubin, J. F. Macías-Pérez, B. Maffei, D. Maino, N. Mandolesi, M. Maris, D. J. Marshall, P. G. Martin, E. Martínez-González, S. Masi, M. Massardi, S. Matarrese, P. Mazzotta, A. Melchiorri, A. Mennella, S. Mitra, M.-A. Miville-Deschênes, A. Moneti, L. Montier, G. Morgante, D. Mortlock, D. Munshi, J. A. Murphy, P. Naselsky, F. Nati, P. Natoli, H. U. Nørgaard-Nielsen, F. Noviello, D. Novikov, I. Novikov, S. Osborne, C. A. Oxborrow, F. Pajot, R. Paladini, D. Paoletti, M. Peel, L. Perotto, F. Perrotta, F. Piacentini, M. Piat, E. Pierpaoli, D. Pietrobon, S. Plaszczynski, E. Pointecouteau, G. Polenta, L. Popa, T. Poutanen, G. W. Pratt, S. Prunet, J.-L. Puget, J. P. Rachen, W. T. Reach, R. Rebolo, M. Reinecke, C. Renault, S. Ricciardi, I. Ristorcelli, G. Rocha, C. Rosset, J. A. Rubiño-Martín, B. Rusholme, E. Salerno, M. Sandri, G. Savini, D. Scott, L. Spencer, V. Stolyarov, R. Sudiwala, A.-S. Suur-Uski, J.-F. Sygnet, J. A. Tauber, L. Terenzi, C. T. Tibbs, L. Toffolatti, M. Tomasi, M. Tristram, L. Valenziano, B. Van Tent, J. Varis, P. Vielva, F. Villa, N. Vittorio, L. A. Wade, B. D. Wandelt, N. Ysard, D. Yvon, A. Zacchei, and A. Zonca, "Planck intermediate results. XII: Diffuse Galactic components in the Gould Belt system," *A&A*, vol. 557, p. A53, Sept. 2013.

[54] Planck Collaboration, P. A. R. Ade, N. Aghanim, M. I. R. Alves, M. Arnaud, M. Ashdown, F. Atrio-Barandela, J. Aumont, C. Baccigalupi, A. Balbi, A. J. Banday, R. B. Barreiro, J. G. Bartlett, E. Battaner, L. Bedini, K. Benabed, A. Benoît, J.-P. Bernard, M. Bersanelli, A. Bonaldi, J. R. Bond, J. Borrill, F. R. Bouchet, F. Boulanger, C. Burigana, R. C. Butler, P. Cabella, J.-F. Cardoso, X. Chen, L.-Y. Chiang, P. R. Christensen, D. L. Clements, S. Colombi, L. P. L. Colombo, A. Coulais, F. Cuttaia, R. D. Davies, R. J. Davis, P. de Bernardis, G. de Gasperis, G. de Zotti, J. Delabrouille, C. Dickinson, J. M. Diego, G. Dobler, H. Dole, S. Donzelli, O. Doré, M. Douspis, X. Dupac, T. A. Enßlin, F. Finelli, O. Forni, M. Frailis, E. Franceschi, S. Galeotta, K. Ganga, R. T. Génova-Santos, T. Ghosh, M. Giard, G. Giardino, Y. Giraud-Héraud, J. González-Nuevo, K. M. Górski, A. Gregorio, A. Gruppuso, F. K. Hansen, D. Harrison, C. Hernández-Monteagudo, S. R. Hildebrandt, E. Hivon, M. Hobson, W. A. Holmes, A. Hornstrup, W. Hovest, K. M. Huffenberger, T. R. Jaffe, A. H. Jaffe, M. Juvela, E. Keihänen, R. Keskitalo, T. S. Kisner, J. Knoche, M. Kunz, H. Kurki-Suonio, G. Lagache, A. Lähteenmäki, J.-M. Lamarre, A. Lasenby, C. R. Lawrence, S. Leach, R. Leonardi, P. B. Lilje, M. Linden-Vørnle, P. M. Lubin, J. F. Macías-Pérez, B. Maffei, D. Maino, N. Mandolesi, M. Maris, D. J. Marshall, P. G. Martin, E. Martínez-González, S. Masi, M. Massardi, S. Matarrese, P. Mazzotta, A. Melchiorri, A. Mennella, S. Mitra, M.-A. Miville-Deschênes, A. Moneti, L. Montier,

G. Morgante, D. Mortlock, D. Munshi, J. A. Murphy, P. Naselsky, F. Nati, P. Natoli, H. U. Nørgaard-Nielsen, F. Noviello, D. Novikov, I. Novikov, S. Osborne, C. A. Oxborrow, F. Pajot, R. Paladini, D. Paoletti, M. Peel, L. Perotto, F. Perrotta, F. Piacentini, M. Piat, E. Pierpaoli, D. Pietrobon, S. Plaszczynski, E. Pointecouteau, G. Polenta, L. Popa, T. Poutanen, G. W. Pratt, S. Prunet, J.-L. Puget, J. P. Rachen, W. T. Reach, R. Rebolo, M. Reinecke, C. Renault, S. Ricciardi, I. Ristorcelli, G. Rocha, C. Rosset, J. A. Rubiño-Martín, B. Rusholme, E. Salerno, M. Sandri, G. Savini, D. Scott, L. Spencer, V. Stolyarov, R. Sudiwala, A.-S. Suur-Uski, J.-F. Sygnet, J. A. Tauber, L. Terenzi, C. T. Tibbs, L. Toffolatti, M. Tomasi, M. Tristram, L. Valenziano, B. Van Tent, J. Varis, P. Vielva, F. Villa, N. Vittorio, L. A. Wade, B. D. Wandelt, N. Ysard, D. Yvon, A. Zacchei, and A. Zonca, "Planck intermediate results. XII: Diffuse Galactic components in the Gould Belt system," *A&A*, vol. 557, p. A53, Sept. 2013.

[55] J. A. Grayson, P. A. R. Ade, Z. Ahmed, K. D. Alexander, M. Amiri, D. Barkats, S. J. Benton, C. A. Bischoff, J. J. Bock, H. Boenish, R. Bowens-Rubin, I. Buder, E. Bullock, V. Buza, J. Connors, J. P. Filippini, S. Fliescher, M. Halpern, S. Harrison, G. C. Hilton, V. V. Hristov, H. Hui, K. D. Irwin, J. Kang, K. S. Karkare, E. Karpel, S. Kefeli, S. A. Kernasovskiy, J. M. Kovac, C. L. Kuo, E. M. Leitch, M. Lueker, K. G. Megerian, V. Monticue, T. Namikawa, C. B. Netterfield, H. T. Nguyen, R. O'Brient, R. W. Ogburn, C. Pryke, C. D. Reintsema, S. Richter, R. Schwarz, C. Sorenson, C. D. Sheehy, Z. K. Staniszewski, B. Steinbach, G. P. Teply, K. L. Thompson, J. E. Tolan, C. Tucker, A. D. Turner, A. G. Vieregg, A. Wandui, A. C. Weber, D. V. Wiebe, J. Willmert, W. L. K. Wu, and K. W. Yoon, "BICEP3 performance overview and planned Keck Array upgrade," in *Millimeter, Submillimeter, and Far-Infrared Detectors and Instrumentation for Astronomy VIII*, vol. 9914 of *Proceedings of the SPIE*, p. 99140S, July 2016.

[56] T. Essinger-Hileman, A. Ali, M. Amiri, J. W. Appel, D. Araujo, C. L. Bennett, F. Boone, M. Chan, H.-M. Cho, D. T. Chuss, F. Colazo, E. Crowe, K. Denis, R. Dünner, J. Eimer, D. Gothe, M. Halpern, K. Harrington, G. C. Hilton, G. F. Hinshaw, C. Huang, K. Irwin, G. Jones, J. Karakla, A. J. Kogut, D. Larson, M. Limon, L. Lowry, T. Marriage, N. Mehrle, A. D. Miller, N. Miller, S. H. Moseley, G. Novak, C. Reintsema, K. Rostem, T. Stevenson, D. Towner, K. U-Yen, E. Wagner, D. Watts, E. J. Wollack, Z. Xu, and L. Zeng, "CLASS: the cosmology large angular scale surveyor," in *Millimeter, Submillimeter, and Far-Infrared Detectors and Instrumentation for Astronomy VII*, vol. 9153 of *Proceedings of the SPIE*, p. 91531I, July 2014.

[57] EBEX Collaboration, A. M. Aboobaker, P. Ade, D. Araujo, F. Aubin, C. Baccigalupi, C. Bao, D. Chapman, J. Didier, M. Dobbs, C. Geach, W. Grainger, S. Hanany, K. Helson, S. Hillbrand, J. Hubmayr, A. Jaffe, B. Johnson, T. Jones, J. Klein, A. Korotkov, A. Lee, L. Levinson,

M. Limon, K. MacDermid, T. Matsumura, A. D. Miller, M. Milligan, K. Raach, B. Reichborn-Kjennerud, I. Sagiv, G. Savini, L. Spencer, C. Tucker, G. S. Tucker, B. Westbrook, K. Young, and K. Zilic, "The EBEX Balloon-borne Experiment - Optics, Receiver, and Polarimetry," *ApJ*, vol. 239, p. 7, Nov. 2018.

[58] N. N. Gandilo, P. A. R. Ade, D. Benford, C. L. Bennett, D. T. Chuss, J. L. Dotson, J. R. Eimer, D. J. Fixsen, M. Halpern, G. Hilton, G. F. Hinshaw, K. Irwin, C. Jhabvala, M. Kimball, A. Kogut, L. Lowe, J. J. McMahon, T. M. Miller, P. Mirel, S. H. Moseley, S. Pawlyk, S. Rodriguez, E. Sharp, P. Shirron, J. G. Staguhn, D. F. Sullivan, E. R. Switzer, P. Taraschi, C. E. Tucker, and E. J. Wollack, "The Primordial Inflation Polarization Explorer (PIPER)," in *Millimeter, Submillimeter, and Far-Infrared Detectors and Instrumentation for Astronomy VIII*, vol. 9914 of *Proceedings of the SPIE*, p. 99141J, July 2016.

[59] A. Suzuki, P. Ade, Y. Akiba, C. Aleman, K. Arnold, C. Baccigalupi, B. Barch, D. Barron, A. Bender, D. Boettger, J. Borrill, S. Chapman, Y. Chinone, A. Cukierman, M. Dobbs, A. Ducout, R. Dunner, T. Elleflot, J. Errard, G. Fabbian, S. Feeney, C. Feng, T. Fujino, G. Fuller, A. Gilbert, N. Goeckner-Wald, J. Groh, T. D. Haan, G. Hall, N. Halverson, T. Hamada, M. Hasegawa, K. Hattori, M. Hazumi, C. Hill, W. Holzapfel, Y. Hori, L. Howe, Y. Inoue, F. Irie, G. Jaehnig, A. Jaffe, O. Jeong, N. Katayama, J. Kaufman, K. Kazemzadeh, B. Keating, Z. Kermish, R. Keskitalo, T. Kisner, A. Kusaka, M. L. Jeune, A. Lee, D. Leon, E. Linder, L. Lowry, F. Matsuda, T. Matsumura, N. Miller, K. Mizukami, J. Montgomery, M. Navaroli, H. Nishino, J. Peloton, D. Poletti, G. Puglisi, G. Rebeiz, C. Raum, C. Reichardt, P. Richards, C. Ross, K. Rotermund, Y. Segawa, B. Sherwin, I. Shirley, P. Siritanasak, N. Stebor, R. Stompor, J. Suzuki, O. Tajima, S. Takada, S. Takakura, S. Takatori, A. Tikhomirov, T. Tomaru, B. Westbrook, N. Whitehorn, T. Yamashita, A. Zahn, and O. Zahn, "The Polarbear-2 and the Simons Array Experiments," *Journal of Low Temperature Physics*, vol. 184, pp. 805–810, Aug. 2016.

[60] J. Aumont, S. Banfi, P. Battaglia, E. S. Battistelli, A. Baù, B. Bélier, D. Bennett, L. Bergé, J. P. Bernard, M. Bersanelli, M. A. Bigot-Sazy, N. Bleurvacq, G. Bordier, J. Brossard, E. F. Bunn, D. Buzi, A. Buzzelli, D. Cammilleri, F. Cavaliere, P. Chanial, C. Chapron, G. Coppi, A. Coppolecchia, F. Couchot, R. D'Agostino, G. D'Alessandro, P. de Bernardis, G. De Gasperis, M. De Petris, T. Decourcelle, F. Del Torto, L. Dumoulin, A. Etchegoyen, C. Franceschet, B. Garcia, A. Gault, D. Gayer, M. Gervasi, A. Ghribi, M. Giard, Y. Giraud-Héraud, M. Gradziel, L. Grandsire, J. C. Hamilton, D. Harari, V. Haynes, S. Henrot-Versillé, N. Holtzer, J. Kaplan, A. Korotkov, L. Lamagna, J. Lande, S. Loucatos, A. Lowitz, V. Lukovic, B. Maffei, S. Marnieros, J. Martino, S. Masi, A. May, M. McCulloch, M. C. Medina, S. Melhuish, A. Mennella, L. Montier, A. Murphy, D. Néel, M. W. Ng, C. O'Sullivan, A. Paiella, F. Pajot, A. Passerini,

A. Pelosi, C. Perbost, O. Perdereau, F. Piacentini, M. Piat, L. Piccirillo, G. Pisano, D. Prêle, R. Puddu, D. Rambaud, O. Rigaut, G. E. Romero, M. Salatino, A. Schillaci, S. Scully, M. Stolpovskiy, F. Suarez, A. Tartari, P. Timbie, M. Tristram, G. Tucker, D. Viganò, N. Vittori, F. Voisin, B. Watson, M. Zannoni, and A. Zullo, "QUBIC Technical Design Report," *arXiv e-prints*, Sept. 2016.

[61] R. Gualtieri, J. P. Filippini, P. A. R. Ade, M. Amiri, S. J. Benton, A. S. Bergman, R. Bihary, J. J. Bock, J. R. Bond, S. A. Bryan, H. C. Chiang, C. R. Contaldi, O. Doré, A. J. Duivenvoorden, H. K. Eriksen, M. Farhang, L. M. Fissel, A. A. Fraisse, K. Freese, M. Galloway, A. E. Gambrel, N. N. Gandilo, K. Ganga, R. V. Gramillano, J. E. Gudmundsson, M. Halpern, J. Hartley, M. Hasselfield, G. Hilton, W. Holmes, V. V. Hristov, Z. Huang, K. D. Irwin, W. C. Jones, C. L. Kuo, Z. D. Kermish, S. Li, P. V. Mason, K. Megerian, L. Moncelsi, T. A. Morford, J. M. Nagy, C. B. Netterfield, M. Nolta, B. Osherson, I. L. Padilla, B. Racine, A. S. Rahlin, C. Reintsema, J. E. Ruhl, M. C. Runyan, T. M. Ruud, J. A. Shariff, J. D. Soler, X. Song, A. Trangsrud, C. Tucker, R. S. Tucker, A. D. Turner, J. F. v. d. List, A. C. Weber, I. K. Wehus, D. V. Wiebe, and E. Y. Young, "SPIDER: CMB Polarimetry from the Edge of Space," *Journal of Low Temperature Physics*, vol. 193, pp. 1112–1121, Dec. 2018.

[62] M. Bersanelli, A. Mennella, G. Morgante, M. Zannoni, *et al.*, "A coherent polarimeter array for the Large Scale Polarization Explorer (LSPE) balloon experiment," *Proceedings of the SPIE*, September 2012.

[63] P. de Bernardis *et al.*, "SWIPE: a bolometric polarimeter for the Large-Scale Polarization Explorer," *SPIE Conference Series*, vol. 8452, p. 3, September 2012.

[64] P. A. R. Ade *et al.*, "Detection of B-Mode Polarization at Degree Angular Scales by BICEP2," *Phys. Rev. Lett.*, vol. 112, June 2014.

[65] Planck Collaboration, R. Adam, P. A. R. Ade, N. Aghanim, M. Arnaud, J. Aumont, C. Baccigalupi, A. J. Banday, R. B. Barreiro, J. G. Bartlett, N. Bartolo, E. Battaner, K. Benabed, A. Benoit-Lévy, J. P. Bernard, M. Bersanelli, P. Bielewicz, A. Bonaldi, L. Bonavera, J. R. Bond, J. Borrill, F. R. Bouchet, F. Boulanger, A. Bracco, M. Bucher, C. Burigana, R. C. Butler, E. Calabrese, J. F. Cardoso, A. Catalano, A. Challinor, A. Chamballu, R. R. Chary, H. C. Chiang, P. R. Christensen, D. L. Clements, S. Colombi, L. P. L. Colombo, C. Combet, F. Couchot, A. Coulais, B. P. Crill, A. Curto, F. Cuttaia, L. Danese, R. D. Davies, R. J. Davis, P. de Bernardis, G. de Zotti, J. Delabrouille, J. M. Delouis, F. X. Désert, C. Dickinson, J. M. Diego, K. Dolag, H. Dole, S. Donzelli, O. Doré, M. Douspis, A. Ducout, J. Dunkley, X. Dupac, G. Efstathiou, F. Elsner, T. A. Enßlin, H. K. Eriksen, E. Falgarone, F. Finelli, O. Forni, M. Frailis, A. A. Fraisse, E. Franceschi, A. Frejsel, S. Galeotta, S. Galli, K. Ganga, T. Ghosh, M. Giard, Y. Giraud-Héraud, E. Gjerløw,

J. González-Nuevo, K. M. Górski, S. Gratton, A. Gregorio, A. Gruppuso, V. Guillet, F. K. Hansen, D. Hanson, D. L. Harrison, G. Helou, S. Henrot-Versillé, C. Hernández-Monteagudo, D. Herranz, E. Hivon, M. Hobson, W. A. Holmes, K. M. Huffenberger, G. Hurier, A. H. Jaffe, T. R. Jaffe, J. Jewell, W. C. Jones, M. Juvela, E. Keihänen, R. Keskitalo, T. S. Kisner, R. Kneissl, J. Knoche, L. Knox, N. Krachmalnicoff, M. Kunz, H. Kurki-Suonio, G. Lagache, J. M. Lamarre, A. Lasenby, M. Lattanzi, C. R. Lawrence, J. P. Leahy, R. Leonardi, J. Lesgourgues, F. Levrier, M. Liguori, P. B. Lilje, M. Linden-Vørnle, M. López-Caniego, P. M. Lubin, J. F. Macías-Pérez, B. Maffei, D. Maino, N. Mandolesi, A. Mangilli, M. Maris, P. G. Martin, E. Martínez-González, S. Masi, S. Matarrese, P. Mazzotta, P. R. Meinhold, A. Melchiorri, L. Mendes, A. Mennella, M. Migliaccio, S. Mitra, M. A. Miville-Deschênes, A. Moneti, L. Montier, G. Morgante, D. Mortlock, A. Moss, D. Munshi, J. A. Murphy, P. Naselsky, F. Nati, P. Natoli, C. B. Netterfield, H. U. Nørgaard-Nielsen, F. Noviello, D. Novikov, I. Novikov, L. Pagano, F. Pajot, R. Paladini, D. Paoletti, B. Partridge, F. Pasian, G. Patanchon, T. J. Pearson, O. Perdereau, L. Perotto, F. Perrotta, V. Pettorino, F. Piacentini, M. Piat, E. Pierpaoli, D. Pietrobon, S. Plaszczynski, E. Pointecouteau, G. Polenta, N. Ponthieu, L. Popa, G. W. Pratt, S. Prunet, J. L. Puget, J. P. Rachen, W. T. Reach, R. Rebolo, M. Remazeilles, C. Renault, A. Renzi, S. Ricciardi, I. Ristorcelli, G. Rocha, C. Rosset, M. Rossetti, G. Roudier, B. Rouillé d'Orfeuil, J. A. Rubiño-Martín, B. Rusholme, M. Sandri, D. Santos, M. Savelainen, G. Savini, D. Scott, J. D. Soler, L. D. Spencer, V. Stolyarov, R. Stompor, R. Sudiwala, R. Sunyaev, D. Sutton, A. S. Suur-Uski, J. F. Sygnet, J. A. Tauber, L. Terenzi, L. Toffolatti, M. Tomasi, M. Tristram, M. Tucci, J. Tuovinen, L. Valenziano, J. Valiviita, B. Van Tent, L. Vibert, P. Vielva, F. Villa, L. A. Wade, B. D. Wandelt, R. Watson, I. K. Wehus, M. White, S. D. M. White, D. Yvon, A. Zacchei, and A. Zonca, "Planck intermediate results. XXX. The angular power spectrum of polarized dust emission at intermediate and high Galactic latitudes," *A&A*, vol. 586, p. A133, Feb 2016.

[66] P. F. Goldsmith, *Quasioptical Systems: Gaussian Beam Quasioptical Propogation and Applications* . Wiley-IEEE Press, 1st ed., 1998.

[67] S. Masi, P. Cardoni, P. de Bernardis, F. Piacentini, A. Raccanelli, and F. Scaramuzzi, "A long duration cryostat suitable for balloon borne photometry," *Cryogenics*, vol. 39, pp. 217–224, June 1999.

[68] K. Zilic, A. Aboobaker, F. Aubin, C. Geach, S. Hanany, N. Jarosik, M. Milligan, and I. Sagiv, "A double vacuum window mechanism for spaceborne applications," *Review of Scientific Instruments*, vol. 88, p. 045112, Apr. 2017.

[69] R. Gualtieri, E. S. Battistelli, A. Cruciani, P. de Bernardis, M. Biasotti, D. Corsini, F. Gatti, L. Lamagna, and S. Masi, "Multi-mode TES Bolome-

ter Optimization for the LSPE-SWIPE Instrument," *Journal of Low Temperature Physics*, vol. 184, pp. 527–533, Aug. 2016.

[70] S. Legg, L. Lamagna, G. Coppi, P. de Bernardis, G. Giuliani, R. Gualtieri, T. Marchetti, S. Masi, G. Pisano, and B. Maffei, "Development of the multi-mode horn-lens configuration for the LSPE-SWIPE B-mode experiment," in *Millimeter, Submillimeter, and Far-Infrared Detectors and Instrumentation for Astronomy VIII*, vol. 9914 of *Proceedings of the SPIE*, p. 991414, July 2016.

[71] M. Biasotti, D. Bagliani, D. Corsini, P. De Bernardis, F. Gatti, R. Gualtieri, L. Lamagna, S. Masi, G. Pizzigoni, and A. Schillaci, "Large Area Superconducting TES Spiderweb Bolometer for Multi-mode Cavity Microwave Detect," *Journal of Physics Conference Series*, vol. 507, p. 042004, May 2014.

[72] S. Masi, E. Battistelli, P. de Bernardis, L. Lamagna, F. Nati, L. Nati, P. Natoli, G. Polenta, and A. Schillaci, "On the effect of cosmic rays in bolometric cosmic microwave background measurements from the stratosphere," *A&A*, vol. 519, p. A24, Sept. 2010.

[73] H. J. van Weers, J. W. den Herder, B. D. Jackson, P. P. K. Kooijman, C. Bruineman, K. Ravensberg, M. P. Bruijn, B. Rangarajan, A. J. van der Linden, M. L. Ridder, M. Leeman, B. J. van Leeuwen, A. Gotink, S. Kwast, T. J. van der Velde, J. R. H. Diesveld, C. Werner, and R. F. M. M. Hamelinck, "TES-detector based focal plane assembly key-technology developments for ATHENA and SAFARI," in *Proceedings of the SPIE*, vol. 9144 of *Society of Photo-Optical Instrumentation Engineers (SPIE) Conference Series*, p. 91445R, Jul 2014.

[74] C. G., "Design and Development of the Focal Planes of the SWIPE Instrument on the Large Scale Polarization Explorer," Master's thesis, University of Rome, La Sapienza, 2015.

[75] F. Piacentini and LSPE Collaboration, "The large scale polarization explorer (lspe) for cmb measurements: performance forecast," *In prep.*, 2019.

[76] M. Biasotti *et al.*, "Large Area Superconducting TES Spiderweb Bolometer for Multi-mode Cavity Microwave Detect," *JPCS*, vol. 507, no. 4, 2014.

[77] M. D. Niemack, *Towards dark energy: Design, development, and preliminary data from ACT*. PhD thesis, Princeton University, Jan. 2008.

[78] R. P. Welty and J. M. Martinis, "A series array of DC SQUIDs," *IEEE Transactions on Magnetics*, vol. 27, pp. 2924–2926, Mar. 1991.

[79] M. Halpern, H. P. Gush, E. Wishnow, and V. de Cosmo, "Far infrared transmission of dielectrics at cryogenic and room temperatures - Glass, Fluorogold, Eccosorb, Stycast, and various plastics," *Journal of Applied Physics*, vol. 25, pp. 565–570, Feb. 1986.

[80] G. Savini, G. Pisano, and P. A. R. Ade, "Achromatic half-wave plate for submillimeter instruments in cosmic microwave background astronomy: modeling and simulation," *Appl. Opt.*, vol. 45, pp. 8907–8915, Dec 2006.

[81] T. Matsumura, *A cosmic microwave background radiation polarimeter using superconducting magnetic bearings*. PhD thesis, University of Minnesota, Minnesota, USA, Jan 2006.

[82] T. Essinger-Hileman, *Probing Inflationary Cosmology: The Atacama B-Mode Search (ABS)*. PhD thesis, Princeton University, Jan 2011.

[83] M. Crumrine, P. A. R. Ade, Z. Ahmed, R. W. Aikin, K. D. Alexander, D. Barkats, S. J. Benton, C. A. Bischoff, J. J. Bock, R. Bowens-Rubin, J. A. Brevik, I. Buder, E. Bullock, V. Buza, J. Connors, J. Cornelison, B. P. Crill, M. Dierickx, L. Duband, C. Dvorkin, J. P. Filippini, S. Fliescher, J. A. Grayson, G. Hall, M. Halpern, S. A. Harrison, S. R. Hildebrand t, G. C. Hilton, H. Hui, K. D. Irwin, J. H. Kang, K. S. Karkare, E. Karpel, J. P. Kaufman, B. G. Keating, S. Kefeli, S. A. Kernasovskiy, J. M. Kovac, C. L. Kuo, N. A. Larsen, K. Lau, E. M. Leitch, M. V. Lueker, K. G. Megerian, L. Moncelsi, T. Namikawa, C. B. Netterfield, H. T. Nguyen, R. O'Brient, R. W. Ogburn, S. Palladino, C. Pryke, B. Racine, S. Richter, R. Schwarz, A. Schillaci, C. D. Sheehy, A. Soliman, T. St. Germaine, Z. K. Staniszewski, B. Steinbach, R. V. Sudiwala, G. P. Teply, K. L. Thompson, J. E. Tolan, C. E. Tucker, A. D. Turner, C. Umiltà, A. G. Vieregg, A. Wandui, A. C. Weber, D. V. Wiebe, J. Willmert, C. L. Wong, W. L. K. Wu, E. Yang, K. W. Yoon, and C. Zhang, "BICEP Array cryostat and mount design," in *Proceedings of the SPIE*, vol. 10708 of *Society of Photo-Optical Instrumentation Engineers (SPIE) Conference Series*, p. 107082D, Jul 2018.

[84] E. Collet, *Polarized Light, Fundamentals and Applications*. CRC Press, December 1992.

[85] S. A. Bryan, T. E. Montroy, and J. E. Ruhl, "Modeling dielectric half-wave plates for CMB polarimetry using a Mueller matrix formalism," *Applied Optics*, vol. 49, no. 32, pp. 6313–6323, 2010.

[86] A. O'Dea *et al.*, "Systematic errors in cosmic microwave background polarization measurements," *Mon. Not. R. Astron. Soc.*, vol. 376, pp. 1767–1783, April 2007.

[87] F. Columbro, E. S. Battistelli, A. Coppolecchia, G. D'Alessandro, P. de Bernardis, L. Lamagna, S. Masi, L. Pagano, A. Paiella, F. Piacentini, and G. Presta, "The short wavelength instrument for the polarization explorer balloon-borne experiment: Polarization modulation issues," *Astronomische Nachrichten*, vol. 340, pp. 83–88, Jan 2019.

[88] M. Salatino, P. de Bernardis, and S. Masi, "A cryogenic waveplate rotator for polarimetry at mm and submm wavelengths," *A&A*, vol. 528, p. A138, Apr. 2011.

[89] J. Didier, D. Chapman, A. Aboobaker, D. Araujo, W. Grainger, S. Hanany, K. Helson, S. Hillbrand, A. Korotkov, M. Limon, A. Miller, B. Reichborn-Kjennerud, I. Sagiv, G. Tucker, and Y. Vinokurov, "A high-resolution pointing system for fast scanning platforms: The EBEX example," *arXiv e-prints*, p. arXiv:1602.03249, Feb 2016.

[90] S. Takakura, M. Aguilar, Y. Akiba, K. Arnold, C. Baccigalupi, D. Barron, S. Beckman, D. Boettger, J. Borrill, S. Chapman, Y. Chinone, A. Cukierman, A. Ducout, T. Elleflot, J. Errard, G. Fabbian, T. Fujino, N. Galitzki, N. Goeckner-Wald, N. W. Halverson, M. Hasegawa, K. Hattori, M. Hazumi, C. Hill, L. Howe, Y. Inoue, A. H. Jaffe, O. Jeong, D. Kaneko, N. Katayama, B. Keating, R. Keskitalo, T. Kisner, N. Krachmalnicoff, A. Kusaka, A. T. Lee, D. Leon, L. Lowry, F. Matsuda, T. Matsumura, M. Navaroli, H. Nishino, H. Paar, J. Peloton, D. Poletti, G. Puglisi, C. L. Reichardt, C. Ross, P. Siritanasak, A. Suzuki, O. Tajima, S. Takatori, and G. Teply, "Performance of a continuously rotating half-wave plate on the POLARBEAR telescope," *J. Cosmol. Astropart. Phys.*, vol. 2017, p. 008, May 2017.

[91] A. Buzzelli, P. de Bernardis, S. Masi, N. Vittorio, and G. de Gasperis, "Optimal strategy for polarization modulation in the LSPE-SWIPE experiment," *A&A*, vol. 609, p. A52, Jan. 2018.

[92] C. J. R. Sheppard, M. Castello, and A. Diaspro, "Three-dimensional polarization algebra," *J. Opt. Soc. Am. A*, vol. 33, pp. 1938–1947, Oct 2016.

[93] M. Samim, S. Krouglov, and V. Barzda, "Nonlinear stokes-mueller polarimetry," *Phys. Rev. A*, vol. 93, p. 013847, Jan 2016.

[94] D. Kleppner and R. Kolenkow, *An Introduction To Mechanics*. Cambridge University press, 1973.

[95] S. Das and T. Souradeep, "Leakage of power from dipole to higher multipoles due to non-symmetric beam shape of the CMB missions," *JCAP*, vol. 1505, no. 05, p. 012, 2015.

[96] M. Tegmark, "How to make maps from CMB data without losing information," *Astrophys. J.*, vol. 480, pp. L87–L90, 1997.

[97] Y. Sekimoto, P. Ade, K. Arnold, J. Aumont, J. Austermann, C. Baccigalupi, A. Banday, R. Banerji, S. Basak, S. Beckman, M. Bersanelli, J. Borrill, F. Boulanger, M. L. Brown, M. Bucher, E. Calabrese, A. Challinor, Y. Chinone, F. Columbro, A. Cukierman, D. Curtis, P. de Bernardis, M. de Petris, M. Dobbs, T. Dotani, L. Duband, A. Ducout, K. Ebisawa, T. Elleflot, H. Eriksen, J. Errard, R. Flauger, C. Franceschet, U. Fuskeland, K. Ganga, J. R. Gao, T. Ghigna, J. Grain, A. Gruppuso, N. Halverson, P. Hargrave, T. Hasebe, M. Hasegawa, M. Hattori, M. Hazumi, S. Henrot-Versille, C. Hill, Y. Hirota, E. Hivon, D. T. Hoang, J. Hubmayr, K. Ichiki, H. Imada, H. Ishino, G. Jaehnig, H. Kanai, S. Kashima,

Y. Kataoka, N. Katayama, T. Kawasaki, R. Keskitalo, A. Kibayashi, T. Kikuchi, K. Kimura, T. Kisner, Y. Kobayashi, N. Kogiso, K. Kohri, E. Komatsu, K. Komatsu, K. Konishi, N. Krachmalnicoff, C. L. Kuo, N. Kurinsky, A. Kushino, L. Lamagna, A. T. Lee, E. Linder, B. Maffei, M. Maki, A. Mangilli, E. Martinez-Gonzalez, S. Masi, T. Matsumura, A. Mennella, Y. Minami, K. Mistuda, D. Molinari, L. Montier, G. Morgante, B. Mot, Y. Murata, A. Murphy, M. Nagai, R. Nagata, S. Nakamura, T. Namikawa, P. Natoli, T. Nishibori, H. Nishino, F. Noviello, C. O'Sullivan, H. Ochi, H. Ogawa, H. Ogawa, H. Ohsaki, I. Ohta, N. Okada, G. Patanchon, F. Piacentini, G. Pisano, G. Polenta, D. Poletti, G. Puglisi, C. Raum, S. Realini, M. Remazeilles, H. Sakurai, Y. Sakurai, G. Savini, B. Sherwin, K. Shinozaki, M. Shiraishi, G. Signorelli, G. Smecher, R. Stompor, H. Sugai, S. Sugiyama, A. Suzuki, J. Suzuki, R. Takaku, H. Takakura, S. Takakura, E. Taylor, Y. Terao, K. L. Thompson, B. Thorne, M. Tomasi, H. Tomida, N. Trappe, M. Tristram, M. Tsuji, M. Tsujimoto, S. Uozumi, S. Utsunomiya, N. Vittorio, N. Watanabe, I. Wehus, B. Westbrook, B. Winter, R. Yamamoto, N. Y. Yamasaki, M. Yanagisawa, T. Yoshida, J. Yumoto, M. Zannoni, and A. Zonca, "Concept design of the LiteBIRD satellite for CMB B-mode polarization," in *Proceedings of the SPIE*, vol. 10698 of *Society of Photo-Optical Instrumentation Engineers (SPIE) Conference Series*, p. 106981Y, Aug 2018.

[98] Planck Collaboration, P. A. R. Ade, N. Aghanim, M. Arnaud, M. Ashdown, J. Aumont, C. Baccigalupi, A. J. Banday, R. B. Barreiro, R. Barrena, and et al., "Planck 2015 results. XXVII. The second Planck catalogue of Sunyaev-Zeldovich sources," *A&A*, vol. 594, p. A27, Sept. 2016.

[99] Planck Collaboration ES, *The Explanatory Supplement to the Planck 2015 results,* `http://wiki.cosmos.esa.int/planckpla2015`. ESA, 2015.

[100] K. M. Gorski, E. Hivon, A. J. Banday, B. D. Wandelt, F. K. Hansen, M. Reinecke, and M. Bartelman, "HEALPix - A Framework for high resolution discretization, and fast analysis of data distributed on the sphere," *Astrophys. J.*, vol. 622, pp. 759–771, 2005.

[101] C. G. R. Wallis, M. L. Brown, R. A. Battye, and J. Delabrouille, "Optimal scan strategies for future CMB satellite experiments," *Mon. Not. Roy. Astron. Soc.*, vol. 466, no. 1, pp. 425–442, 2017.

[102] Planck Collaboration, Y. Akrami, F. Arroja, M. Ashdown, J. Aumont, C. Baccigalupi, M. Ballardini, A. J. Banday, R. B. Barreiro, N. Bartolo, S. Basak, R. Battye, K. Benabed, J. P. Bernard, M. Bersanelli, P. Bielewicz, J. J. Bock, J. R. Bond, J. Borrill, F. R. Bouchet, F. Boulanger, M. Bucher, C. Burigana, R. C. Butler, E. Calabrese, J. F. Cardoso, J. Carron, B. Casaponsa, A. Challinor, H. C. Chiang, L. P. L. Colombo, C. Combet, D. Contreras, B. P. Crill, F. Cuttaia, P. de Bernardis, G. de Zotti, J. Delabrouille, J. M. Delouis, F. X. Désert, E. Di

Valentino, C. Dickinson, J. M. Diego, S. Donzelli, O. Doré, M. Douspis, A. Ducout, X. Dupac, G. Efstathiou, F. Elsner, T. A. Enßlin, H. K. Eriksen, E. Falgarone, Y. Fantaye, J. Fergusson, R. Fernandez-Cobos, F. Finelli, F. Forastieri, M. Frailis, E. Franceschi, A. Frolov, S. Galeotta, S. Galli, K. Ganga, R. T. Génova-Santos, M. Gerbino, T. Ghosh, J. González-Nuevo, K. M. Górski, S. Gratton, A. Gruppuso, J. E. Gudmundsson, J. Hamann, W. Hand ley, F. K. Hansen, G. Helou, D. Herranz, E. Hivon, Z. Huang, A. H. Jaffe, W. C. Jones, A. Karakci, E. Keihänen, R. Keskitalo, K. Kiiveri, J. Kim, T. S. Kisner, L. Knox, N. Krachmalnicoff, M. Kunz, H. Kurki-Suonio, G. Lagache, J. M. Lamarre, M. Langer, A. Lasenby, M. Lattanzi, C. R. Lawrence, M. Le Jeune, J. P. Leahy, J. Lesgourgues, F. Levrier, A. Lewis, M. Liguori, P. B. Lilje, M. Lilley, V. Lindholm, M. López-Caniego, P. M. Lubin, Y. Z. Ma, J. F. Macías-Pérez, G. Maggio, D. Maino, N. Mand olesi, A. Mangilli, A. Marcos-Caballero, M. Maris, P. G. Martin, E. Martínez-González, S. Matarrese, N. Mauri, J. D. McEwen, P. D. Meerburg, P. R. Meinhold, A. Melchiorri, A. Mennella, M. Migliaccio, M. Millea, S. Mitra, M. A. Miville-Deschênes, D. Molinari, A. Moneti, L. Montier, G. Morgante, A. Moss, S. Mottet, M. Münchmeyer, P. Natoli, H. U. Nørgaard-Nielsen, C. A. Oxborrow, L. Pagano, D. Paoletti, B. Partridge, G. Patanchon, T. J. Pearson, M. Peel, H. V. Peiris, F. Perrotta, V. Pettorino, F. Piacentini, L. Polastri, G. Polenta, J. L. Puget, J. P. Rachen, M. Reinecke, M. Remazeilles, A. Renzi, G. Rocha, C. Rosset, G. Roudier, J. A. Rubiño-Martín, B. Ruiz-Granados, L. Salvati, M. Sandri, M. Savelainen, D. Scott, E. P. S. Shellard, M. Shiraishi, C. Sirignano, G. Sirri, L. D. Spencer, R. Sunyaev, A. S. Suur-Uski, J. A. Tauber, D. Tavagnacco, M. Tenti, L. Terenzi, L. Toffolatti, M. Tomasi, T. Trombetti, J. Valiviita, B. Van Tent, L. Vibert, P. Vielva, F. Villa, N. Vittorio, B. D. Wandelt, I. K. Wehus, M. White, S. D. M. White, A. Zacchei, and A. Zonca, "Planck 2018 results. I. Overview and the cosmological legacy of Planck," *arXiv e-prints*, p. arXiv:1807.06205, Jul 2018.

[103] J. Tauber, M. Bersanelli, J. M. Lamarre, G. Efstathiou, C. Lawrence, F. Bouchet, E. Martinez-Gonzalez, S. Matarrese, D. Scott, M. White, *et al.*, "The Scientific programme of Planck." astro-ph/0604069, 2006.

[104] J. Klein, A. Aboobaker, P. Ade, F. Aubin, C. Baccigalupi, C. Bao, J. Borrill, D. Chapman, J. Didier, M. Dobbs, B. Gold, W. Grainger, S. Hanany, J. Hubmayr, S. Hillbrand, J. Grain, A. Jaffe, B. Johnson, T. Jones, T. Kisner, A. Korotkov, S. Leach, A. Lee, L. Levinson, M. Limon, K. MacDermid, T. Matsumura, A. Miller, M. Milligan, E. Pascale, D. Polsgrove, N. Ponthieu, K. Raach, B. Reichborn-Kjennerud, I. Sagiv, R. Stompor, H. Tran, M. Tristram, G. S. Tucker, A. Yadav, M. Zaldarriaga, and K. Zilic, "A cryogenic half-wave plate polarimeter using a superconducting magnetic bearing," in *Proceedings of the SPIE*, vol. 8150 of *Society of Photo-Optical Instrumentation Engineers (SPIE) Conference Series*, p. 815004, 2011.

[105] C. A. Hill, A. Kusaka, P. Barton, B. Bixler, A. G. Droster, M. Flament, S. Ganjam, A. Jadbabaie, O. Jeong, A. T. Lee, A. Madurowicz, F. T. Matsuda, T. Matsumura, A. Rutkowski, Y. Sakurai, D. R. Sponseller, A. Suzuki, and R. Tat, "A Large-Diameter Cryogenic Rotation Stage for Half-Wave Plate Polarization Modulation on the POLARBEAR-2 Experiment," *Journal of Low Temperature Physics*, vol. 193, pp. 851–859, Dec 2018.

[106] Y. Sakurai, T. Matsumura, T. Iida, H. Kanai, N. Katayama, H. Imada, H. Ohsaki, Y. Terao, T. Shimomura, H. Sugai, H. Kataza, R. Yamamoto, and S. Utsunomiya, "Design and Thermal Characteristics of a 400 mm Diameter Levitating Rotor in a Superconducting Magnetic Bearing Operating Below at 10 K for a CMB Polarization Experiment," *IEEE Transactions on Applied Superconductivity*, vol. 28, p. 2797302, Jun 2018.

[107] H. Kamerlingh Onnes, "Further experiments with Liquid Helium. D. On the change of Electrical Resistance of Pure Metals at very low Temperatures, etc. V. The Disappearance of the resistance of mercury," *Koninklijke Nederlandse Akademie van Wetenschappen Proceedings Series B Physical Sciences*, vol. 14, pp. 113–115, 1911.

[108] V. L. Ginzburg and L. D. Landau, "To the Theory of Superconductivity," *Zh. Eksp. Teor. Fiz.*, vol. 20, p. 1064, 1950. [This paper is available in English in L. D. Landau, *Collected Papers*. Pergamon Press, Oxford, 1965].

[109] F. London, *Superfluids*, vol. 1. Wiley, 1950.

[110] J. Bardeen, L. N. Cooper, and J. R. Schrieffer, "Theory of Superconductivity," *Physical Review*, vol. 108, pp. 1175–1204, Dec. 1957.

[111] W. Meissner and R. Ochsenfeld, "Ein neuer Effekt bei Eintritt der Supraleitfähigkeit," *Naturwissenschaften*, vol. 21, pp. 787–788, Nov. 1933.

[112] N. N. Greenwood and A. Earnshaw, *Chemistry of the Elements*. Butterwoth-Heinemann, 2nd ed., December 1997.

[113] C. P. Bean, "Magnetization of High-Field Superconductors," *Reviews of Modern Physics*, vol. 36, pp. 31–38, Jan 1964.

[114] S. Earnshaw, "On the Nature of the Molecular Forces which Regulate the Constitution of the Luminiferous Ether," *Transactions of the Cambridge Philosophical Society*, vol. 7, p. 97, 1848.

[115] L. C. Davis, E. M. Logothetis, and R. E. Soltis, "Stability of magnets levitated above superconductors," *Journal of Applied Physics*, vol. 64, pp. 4212–4218, Oct. 1988.

[116] T. Habisreuther, M. Zeisberger, D. Litzkendorf, O. Surzhenko, and W. Gawalek, "Developing melt-textured YBCO," *JOM - Journal of the Minerals, Metals and Materials Society*, vol. 52, pp. 26–28, June 2000.

[117] M. Zeisberger and W. Gawalek, "Losses in magnetic bearings," *Materials Science and Engineering: B*, vol. 53, no. 1, pp. 193 – 197, 1998.

[118] J. R. Reitz, "Forces on Moving Magnets due to Eddy Currents," *Journal of Applied Physics*, vol. 41, pp. 2067–2071, Apr. 1970.

[119] R. W. Powell, C. Y. Ho, and P. E. Liley, *Thermal conductivity of selected materials*, vol. 1. National Bureau of Standards, 1966.

[120] J. Tuttle, E. Canavan, and M. DiPirro, "Thermal and Electrical Conductivity Measurements of Cda 510 Phosphor Bronze," *Transactions of the International Cryogenic Materials Conference-ICMC: Advances in Cryogenic Engineering Materials*, vol. 1219, pp. 55–62, 2010.

[121] L. M. García, J. Chaboy, F. Bartolomé, and J. B. Goedkoop, "Orbital Magnetic Moment Instability at the Spin Reorientation Transition of $Nd_2Fe_{14}B$," *Physical Review Letters*, vol. 85, pp. 429–432, July 2000.

[122] S. R. Trout and C. D. Graham, "High field magnetic measurements on sintered SmCo5 permanent magnets," *American Institute of Physics Conference Series*, vol. 29, pp. 608–609, May 1976.

[123] F. R. Fickett, *Electrical Properties of Materials and Their Measurement at Low Temperatures* . , 1st ed., 2018.

[124] T. J. Haugan, F. J. Baca, M. J. Mullins, N. A. Pierce, T. A. Campbell, E. L. Brewster, P. N. Barnes, H. Wang, and M. D. Sumption, "Temperature and Magnetic Field Dependence of Critical Current Density of YBCO With Varying Flux Pinning Additions," *IEEE Transactions on Applied Superconductivity*, vol. 19, pp. 3270–3274, Jun 2009.

[125] F. Columbro, P. de Bernardis, and S. Masi, "A clamp and release system for superconductive magnetic bearings," *Review of Scientific Instruments*, vol. 89, Dec 2018.

[126] B. R. Johnson, F. Columbro, D. Araujo, M. Limon, B. Smiley, G. Jones, B. Reichborn-Kjennerud, A. Miller, and S. Gupta, "A large-diameter hollow-shaft cryogenic motor based on a superconducting magnetic bearing for millimeter-wave polarimetry," *Review of Scientific Instruments*, vol. 88, no. 10, p. 105102, 2017.

[127] K. Komatsu, T. Matsumura, H. Imada, H. Ishino, N. Katayama, and Y. Sakurai, "Demonstration of the broadband half-wave plate using the nine-layer sapphire for the CMB polarization experiment," *J. Astron. Telesc. Instrum. Syst.*, vol. 5(4), May 2019.

[128] A. Suzuki, *Multichroic Bolometric Detector Architecture for Cosmic Microwave Background Polarimetry Experiments*. PhD thesis, University of California, Berkeley, 2013.